The Self-Assembly, Optical Response and Stretch Tunability of Plasmonic Nanoparticle Monolayers

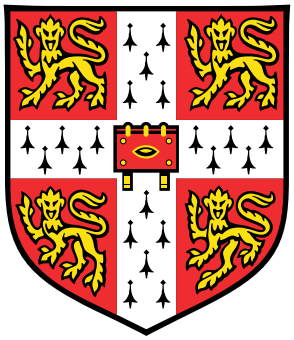

Matthew George Millyard

Cavendish Laboratory, Department of Physics

University of Cambridge

This thesis is submitted for the degree of Doctor of Philosophy

Queens College

October 2020

Declaration

This thesis is the result of my own work and includes nothing which is the outcome of work done in collaboration except as declared in the Preface and specified in the text. It is not substantially the same as any that I have submitted, or, is being concurrently submitted for a degree or diploma or other qualification at the University of Cambridge or any other University or similar institution except as declared in the Preface and specified in the text. I further state that no substantial part of my thesis has already been submitted, or, is being concurrently submitted for any such degree, diploma or other qualification at the University of Cambridge or any other University or similar institution except as declared in the Preface and specified in the text. It does not exceed the prescribed word limit for the relevant Degree Committee.

Matthew George Millyard
October 2020

Abstract: The Self-Assembly, Optical Response and Stretch Tunability of Plasmonic Nanoparticle Monolayers

Matthew George Millyard

The optical properties of self-assembled plasmonic nanoparticle monolayers of varying densities are explored. These particles are sensitive to changes in their local environment and proximity to other particles. By altering these factors, the appearance of nanoparticle assemblies is changed, enabling their measurement optically. Additionally, the manipulation of near-field enhancement between particles via the application of strain increases the degree of enhancement observed in surface enhanced Raman spectroscopy.

By manipulating forces such as interfacial tension and by tuning the electrostatic repulsion exhibited by charge stabilised nanoparticles, the fabrication of long-range organised structures can be directed. Self-assembly methods are used here to fabricate different densities of nanoparticle monolayers. Spin coating methods are used to fabricate sparsely packed nanoparticle monolayers. These methods are investigated as a potential high intensity scattering film with minimal surface coverage. An alternative fabrication method using capillary aided deposition on vertically aligned substrates is also detailed. Interfacial trapping is explored as a means to fabricate large-scale close-packed nanoparticle monolayers.

By fabricating close-packed nanoparticle mats onto elastomeric substrates, interparticle distances can be manipulated with strain, creating a dynamic and tunable plasmonic material. An anisotropic polarisation dependent response to uniaxial strain is observed in the optical behaviour of these mats. Perpendicular to the strain axis, particles are able to move closer together due to contraction in this plane. The dependence of the optical response on nanoparticle surfactant is explored as well as the sensitivity to local refractive index changes. In addition to the optical response, stretch tunable near-field enhancement is explored via its effects on surface enhanced Raman spectroscopy. A relative enhancement of the SERS signal is observed with applied strain. By changing the refractive index medium between particles, the resonance position can be changed and therefore the behaviour under strain altered.

For Donald Frederick Leech, as thanks for gifting his playful sense of curiosity,

for Scarlett, who I shall endeavour to pass it on to next,

and for Katherine, who went the extra five thousand miles.

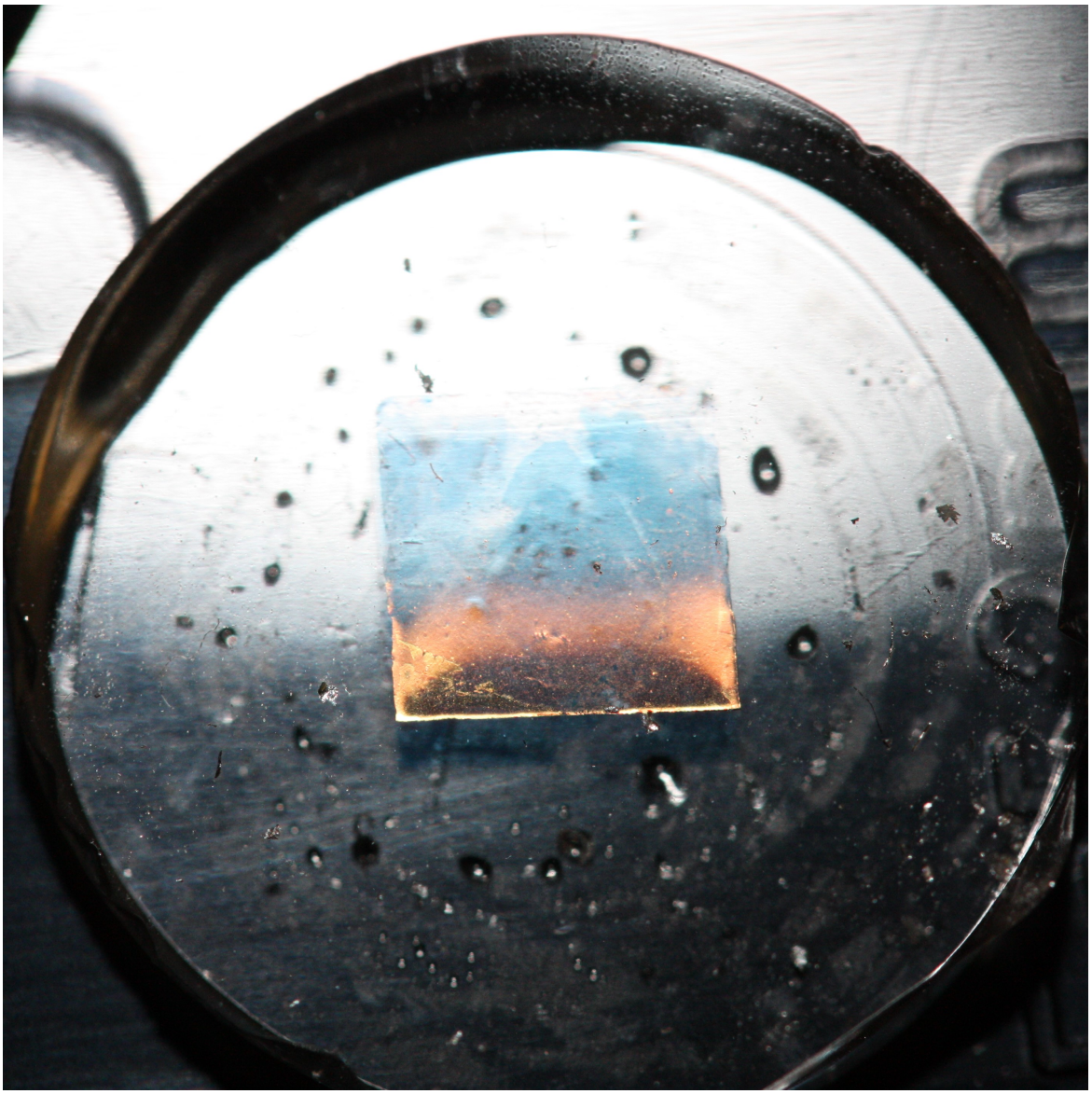

Fig. 1 A Nano Sunrise: simultaneous reflection, transmission and scattering from a 20nm gold nanoparticle mat.

Acknowledgements

The following work could not have been performed without the help and guidance of a great many people. Firstly I would like to thank the Nokia Research Centre Cambridge for the use of their facilities and for their assistance in driving forward the assembly of some of the structure performed here. In particular the insights of Richard White, Elisabetta Spigone and Jani Kiviola who were instrumental in the development of our close-packed nanoparticle mats. Similarly I would to thank Cambridge Display Technology Ltd. for funding the investigation of the spun nanoparticle monolayers detailed in this thesis.

Although a doctorate can be solitudinous it rarely felt so due to the great many people who worked along side me over the course of this work providing their encouragement, thought provoking discussion and insight in equal measures. Therefore I would like to thank Lindsey Ibbotson, Wendy Niu, Qibin Zhao, Richard Taylor, Peter Cristofolini, James Hugall, Jan Mertens, Andrew Haines, Alan Sanders, Gen Kamita, Daniel Sigle, Richard Bowman, Ventislav Valev, Silvia Vignolini, Ahu Gümrah Dumanli, Uli Stiener, Fumin Huang, Tao Ding, Niraj Lal, Kevin Savage, Matthew Hawkeye, and Laura Brooks for their time, friendship, guidance and inspiration.

In particular, a special thanks goes to Daniel Sigle, for his time and assistance with the Raman microscope, Sam Jones for his guidance on nanoparticle chemistry and synthesis as well as Lars Herrmann and Fumin Huang for assistance preparing theoretical FDTD and BEMAX calculations respectively.

Finally, I would like to thank Professor Jeremy Baumberg for his influence, intellect and above all kindness that helped make this work possible, Mark Graves and Julia May for their help in pushing this thesis over the finish line, as well as my parents Steve and Jackie Millyard and in-laws Beth, Michael, and Berthie Marcheschi, for their equal parts of faith, cajoling, and support. Last of all, I would like to thank Katherine, whose patience I would prefer to think I helped to improve (in the same way that running a marathon would help

improve ones endurance).

Perhaps one more: a thank you to Scarlett, for being a constant ray of hope and light. Daddy did it!

List of Publications and Conferences

Publications

Matthew G. Millyard et al., 'Stretch-induced plasmonic anisotropy of self-assembled gold nanoparticle mats', Applied Physics Letters, 100 (7), 2012.

Fumin Huang, Matthew G. Millyard et al. 'Zero-Reflectance Metafilms for Optimal Plasmonic Sensing', Advanced Optical Materials, 4 (2), 2016.

Patent

Jeremy J., Baumberg, Fumin Huang, Matthew G Millyard, Optical Device, 2012, US Patent App. 14/117,876

Conference Posters and Talks

"Tunable Plasmons on Stretch Tuneable Substrates", Meta 14, London, UK, 2014

"Inducted plasmonic anisotropy of stretched elastic gold nanoparticle mats", SPP6, Ottawa, Canada, 2013

"Self Assembled Metal Nanoparticle Mats For Sensing Applications", SET for Britain, London, UK, 2012

Contents

List of Figures

List of Tables

Chapter 1

Introduction

Although the study of nanoplasmonics is a recent field, the classic example of plasmonic based nanotechnology sits not in a laboratory but a specialised case in the British Museum. The Roman antiquity named the Lycurgus Cup (figure 1.1) dates from around the fourth century. The cup's distinguishing feature is revealed by its display case, which alternates between front and back lighting. The manner of illumination changes the appearance of the glass; with transmitted light the cup appears a striking red, however reflected light shows a dull green. The origin of this colour change is embedded in the glass shell of the cup, nanoscopic chunks of gold and silver that interact with the incident light, absorbing and scattering different wavelengths resulting in an optical appearance that is dependent upon the incoming direction of light [1].

Despite the use of noble metal nanoparticles as far back as the Romans it was not until the 1800's that a scientific description arrived. Michael Faraday reported the optical behaviour of colloidal gold, that is to say gold nanoparticles suspended in a liquid, as part of the 1857 Bakerian lecture. In particular, he reported [2];

> *Occasionally some of the fluids containing the very finest particles in suspension, when illuminated by the sun's rays and a lens, appeared to give a fine green reflexion, but whether this is a true colour as compared to white light, or only the effect of contrast with the bright ruby in the other parts of the fluid, I am not prepared to say.*

Here perhaps is the first direct description of the green scattered light from gold nanoparticles, long before work explaining the phenomena was proposed by Gustav Mie 60 years

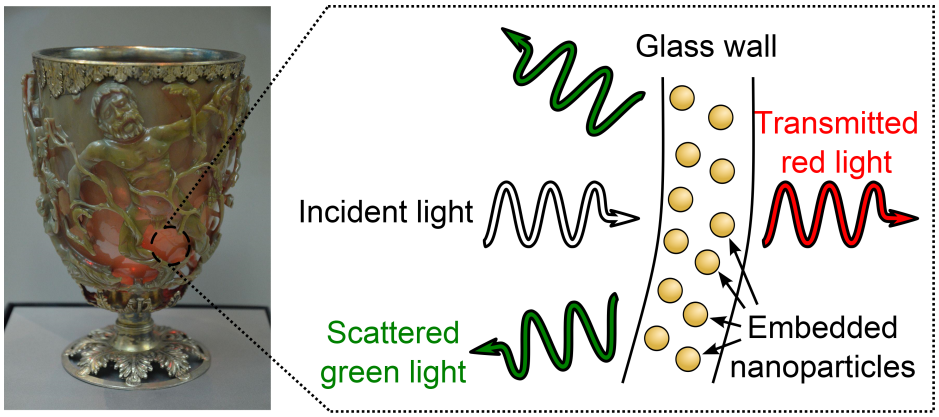

Fig. 1.1 The Lycurgus cup, dating from the 4th century, featuring gold and silver nanoparticles embedded within the glass. This results in different apparent colouring depending whether light is scattered off the surface (green, top left of the cup) or transmitted through it (red, bottom right). Image copyright of and used with permission from Wikipedia Commons [4]

later [3]. In short, a metallic nanoparticle is able to interact with incident light despite a length-scale well below the associated diffraction limit. This is due to the presence of free electrons within the particle and their subsequent polarisability due to the incoming oscillating electric field. This effect, coupled with the resulting restoring force, enables a resonant condition that results in the scattering of incident photons of specific wavelengths. Colloidal gold scatters green light resulting in the optical effect observed by Faraday.

The response of the free elections in metals to incident light is not limited within nanoscopic volumes. The study of the interaction between so called plasmonic materials and light, as well as the propagation of the resulting plasma oscillation through the material [5], has led to a proliferation of studies into the field now known as plasmonics. This research covers a wide range of different structures varying from thin metal films to complex gratings and antennae. Differing designs aid a wide range of applications such as extraordinary transmission through films [6], waveguides [7] or molecular sensing [8]. A comprehensive overview of these can be found elsewhere [9]. This work is concerned with the interactions between light and plasmonic nanoparticles, in particular the interactions between large assemblies of nanoparticles.

As the optical response of a plasmonic nanoparticle arises as a function of its polarisability, the resonance condition is strongly affected by the presence of other nearby particles. Particle separation is therefore a key factor that defines the optical appearance of metal nanoparticles. Additionally, the coupling between particles in this manner results in dramatic field

enhancements close to the particle surface. This leads to increased sensitivity to the molecular make-up of the particle surroundings, allowing for potential sensing applications based upon the illumination of the structure.

A significant issue preventing the mass implementation of plasmonic sensing applications is that the fabrication at nanoscopic length scales often relies on lithographic methods. These are often slow and complicated, preventing scalability and mass production. However alternative methods can be used in order to quickly assemble long-range ordered structures by manipulating the fundamental forces that exist between individual nanoparticles and their environment; this is known as self-assembly. Such techniques offer a potential route for fast large-scale fabrication of structures with nanoscopic length-scales and show great promise in the mass production of nanotechology.

1.1 Thesis structure

This thesis will detail methods for assembling varying densities of nanoparticle monolayers and explore their differing optical properties. Over the next two chapters the theoretical grounding of the following work will be detailed. Chapter 2 will explain the origin of the localised surface plasmon resonance within noble metal nanoparticles before discussing the interactions between nanoparticles, the environmental properties that affect their optical response and the resultant enhancement in the near-field in their proximity. The subsequent chapter will describe the forces that can be manipulated in order to stimulate and control the assembly of these particles, as well as detail multiple examples of self-assembled structures. Chapter 4 will provide an overview of the experimental methods and equipment used in our practical investigations.

After this theoretical grounding, the subsequent chapters will detail the experimental work performed. The main focus of this thesis is the fabrication of large-scale two-dimensional arrays of noble metal nanoparticles with separations well below those of a particle's diameter. These are assembled onto elastic substrates allowing the control of interparticle spacings via the application of strain, altering the plasmonic resonances of the structure.

The fabrication methods employed in the manufacture of closely-packed nanoparticle mats is detailed in Chapter 5, before a discussion of the optical properties of closely-packed mats, including their stretch tunable optical response, is discussed in Chapters 6 and 7. Additionally Chapter 7 also details the influence of changing refractive index and different

particle surfactants on the optical response.

Chapter 8 will focus on the enhancement of near-field light in the gaps between closely-packed nanoparticle mats and use this to greatly magnify the interaction between photons and molecular vibrations. In this manner the enhancement of Raman scattering from close-packed nanoparticle arrays is explored. The experimental chapters draw to close with a examination of assembly methods and and optic properties of lower density nanoparticle mats in chapter 9, before conclusions and suggestions of future work are discussed in Chapter 10.

The theoretical basis of plasmonics will now be explored, starting with the origins of the localised surface plasmon polariton that defines the optical response of a metal nanoparticle.

Chapter 2

Plasmonic Theory

In this chapter the theory of plasmon polaritons in bulk metals is reviewed in order to explain the origin of the localized surface plasmon polaritons in metal nanoparticles. The optical behaviour of these particles is explored, as well as how the interactions between them change this optical response, building to an explanation of the optical properties of large-scale nanoparticle arrays. Finally this chapter ends by discussing a consequence of these interactions; where the focusing of light in the near-field around plasmonic structures increases the intensity of Raman scattering from molecules in their surroundings and how this phenomenon can be used for molecular sensing.

2.1 The interaction of light and metals

Light propagation through a material is defined by the interaction between its molecular structure and the coupled oscillation of electric and magnetic fields that make up light. Crucially the response is frequency dependent. For example, whilst opaque within the visible area of the spectrum, large thicknesses of metals are transparent at ultraviolet frequencies. This is due to the increased frequency of the electric field oscillation which varies too fast for the electrons within the material to respond. This results in minimal interaction between them, low absorption and therefore transparency.

Within a metal the interaction between the incident field and the free electrons within the bulk provide the fundamental basis for modelling its optical behaviour. In practise these simple models fail due to the interband transitions of electron states at visible wavelengths. Using gold as an example, incident photons excite electrons from the filled d band to the

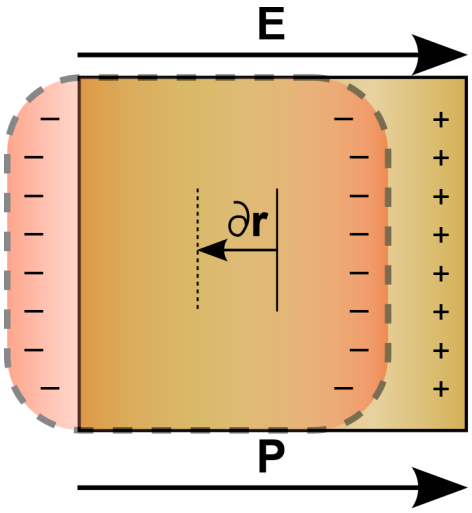

Fig. 2.1 In a metal with an incident electric field, **E**, a free electron gas is displaced within the bulk by a distance $\partial \mathbf{r}$ within, resulting in a polarization **P**.

partially filled *s* band at around 2.5eV ($\approx$ 500nm). This accounts for the typical yellow sheen of gold, as below this wavelength photon absorption occurs. Initially these effects are ignored, with the optical behaviour of a metal considered purely as originating from the movement of a free electron gas, before these added complications are considered.

2.1.1 A model of the free electron gas

The plasma model, or the Drude-Sommerfeld model, describes the response of the electrons to an incident electric field as a damped harmonic oscillator [10]. The electrons in the conduction band are considered as a free moving mass, made up of a number n_e of electrons. Under an incident electric field, **E**, this results in the displacement of the electron gas and a subsequent polarisation, **P** (figure 2.1). This polarisation can be described macroscopically as a physical displacement of the electrons with the equation

$$\mathbf{P}(\mathbf{r},t) = -n_e e \mathbf{r}(\omega) \tag{2.1}$$

where n_e is the number density of free electrons, e is their charge and **r** is their position vector. The dependence on the position vector is key, as it results in the electron gas oscillating under the harmonic electric field of light. By considering the motion of the free electrons

being driven by an oscillating electric field, their time dependant motion can be modelled as

$$m_e \frac{\partial^2 \mathbf{r}}{\partial t^2} + m_e \Gamma \frac{\partial \mathbf{r}}{\partial t} = e\mathbf{E} \tag{2.2}$$

where m_e is the effective mass of an electron. The damping term Γ arises from collisions within the material. This is estimated by dividing an electron's Fermi velocity by its mean free path, $\Gamma = v_f/l \approx 100\text{THz}$ [11].

In order to describe the varying electric field and the resultant oscillation of an electron, time-dependent harmonic relations are used with $\mathbf{E}(t) = \mathbf{E}_0 e^{-i\omega t}$ and $\mathbf{r}(t) = \mathbf{r}_0 e^{-i\omega t}$ where $\mathbf{E}_0$ and $\mathbf{r}_0$ are the maximum amplitude of $\mathbf{E}$ and $\mathbf{r}$ respectively and ω is the frequency of the incident light. By substituting these relations into equation 2.2 and combining the solution with equation 2.1, a new equation for the polarization of the free electron gas is reached in terms of the frequency of the incident electric field

$$\mathbf{P} = -\frac{n_e e^2}{m(\omega^2 + i\Gamma\omega)}\mathbf{E}(t). \tag{2.3}$$

By considering the macroscopic polarisation $\mathbf{D} = \varepsilon_0\mathbf{E} + \mathbf{P}$ and the constitutive relation for a linear and isotropic media $\mathbf{D} = \varepsilon\varepsilon_0\mathbf{E}$, an expression for the dielectric constant ε in terms of $\mathbf{P}$ and $\mathbf{E}$ can be formulated as

$$\varepsilon = 1 + \frac{\mathbf{P}}{\varepsilon_0 \mathbf{E}} \tag{2.4}$$

By substituting 2.4 into equation 2.1, the frequency dependent ε of a Drude metal is returned as

$$\varepsilon(\omega) = 1 - \frac{\omega_p^2}{\omega^2 + i\Gamma\omega} \tag{2.5}$$

where $\omega_p^2 = \frac{n_e e^2}{m_e \varepsilon_0}$ is the plasma frequency, the resonant frequency of the free electron gas. Below ω_p the electron gas cannot sustain the transmission of incident transversely polarised light and the electric field is strongly attenuated. Above ω_p, light can pass through the medium as the incident field frequency is faster than the electrons can effectively respond to.

2.1.2 Interband transitions

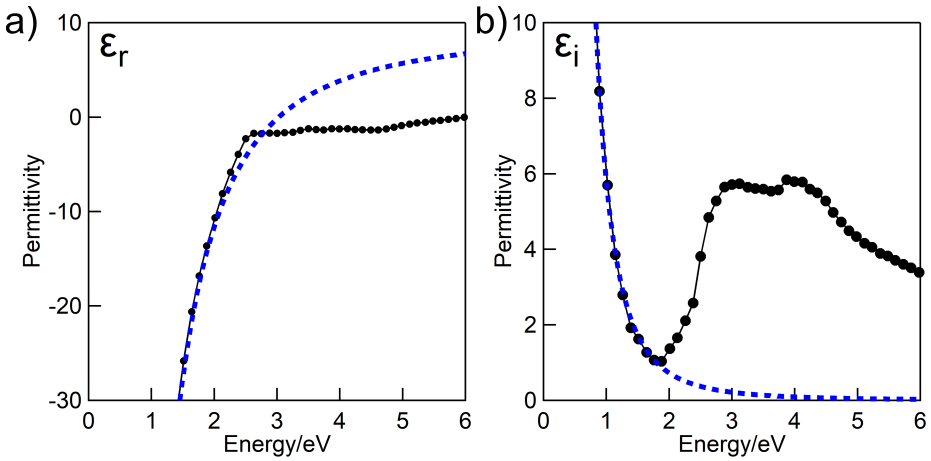

Fig. 2.2 The a) real and b) imaginary permittivity of gold modelled as a free electron gas using the Drude-Sommerfeld model (blue dash), compared with literature values for the permittivity (black) [12]. Above 2.5e V the model falls down, due to the excitation of interband transitions.

By using equation 2.5, the permittivity of a metal can be modelled. Figure 2.2 shows a comparison of the model to the experimental values of the permittivity of gold [12]. Above 2.5eV the model falls down, with the experimental values diverging from the theoretical. This is due to the introduction of the interband transitions at these energies, the first of which for gold occurs at a wavelength of 450nm. In real metals a correction factor, ε_∞, replaces unity in equation 2.5 to account for the additional polarisation caused by the displaced valance electrons. Typically for noble metals $1 \leq \varepsilon_\infty \leq 10$. However this does not account for the additional absorption from these interband transitions. A second equation of motion can be formulated for the bound electrons, with an additional term added to equation 2.2 to account for the restoring force

$$m\frac{\partial^2 \mathbf{r}}{\partial t^2} + m\gamma\frac{\partial \mathbf{r}}{\partial t} + m_e\omega_0^2\mathbf{r} = e\mathbf{E} \tag{2.6}$$

where γ is the damping constant and ω_0 is the resonance frequency of the bound electron under an electric field. In the same manner as with equation 2.2, an expression for the dielectric function of the metal from these interband transitions is returned as

$$\varepsilon_{Interband}(\omega) = 1 + \frac{\tilde{\omega_p}^2}{(\omega_0^2 - \omega^2) - i\gamma\omega}. \tag{2.7}$$

where $\tilde{\omega}_p = \sqrt{\frac{\tilde{n_e}e^2}{m_e\varepsilon_0}}$ is the resonant frequency of bound charge oscillation, dependent upon the bound electron density $\tilde{n_e}$, and is analogous to the plasma frequency of a free electron gas in equation 2.2. Summing together equations 2.5 and 2.7 can result in a limited model of the dielectric function of a noble metal that takes into account both free and bound electrons [13]. However, additional terms are required to account for each interband transition to adequately model a metal's permittivity [11].

Through study of these plasma movements it was discovered that incident TM polarized light, with the electric field normal to the plane of incidence, can cause a surface wave to propagate at the interface between a metal and a dielectric. These excitations, known as surface plasmon polaritons, were first theorised by Richie in 1957 [5], and the study of this phenomena has grown to explore many different methods of coupling light into a metal surface in order to generate them [6].

Plasmonic behaviour of materials can be changed by structuring them to influence how the plasmon can move in the material. These plasmonic metamaterials can be used to enhance transmission through what would classically be opaque metal thicknesses [14]. By specifically tuning the resonance of the structure it is possible to get a considerable amount of colour control over light transmission, allowing for application such as plasmonic based colour filtering [15].

However, this work is not concerned with propagating surface plasmons manipulated in this manner. Instead, using this understanding of electron movement in metals, the optical properties of plasma movements spatially confined to nanoscopic metal volumes is now discussed.

2.2 Localised surface plasmon polaritons

Incident light excites the electrons of small nanosized metal particles in the same manner as it would do to a large volume. However, as they are confined to a set volume they are no longer able to move freely. Instead the electrons move in response to the field to each side of the particle, oscillating with the varying electric field as shown in figure 2.3. Because of the disparity in charge across the particle, the electrons experience a restoring force. At a certain frequency a resonant condition will arise that is dependent upon the charge distribution within the particle. This resonance results in a maximum of absorption and scattering that dominates the optical behaviour of the nanoparticle, meaning that a nanoparticle's ap-

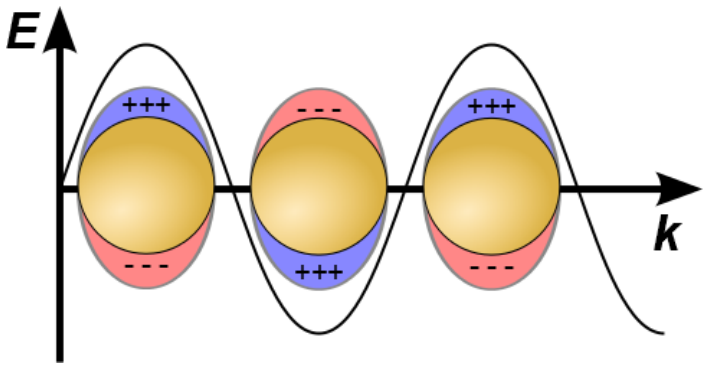

Fig. 2.3 Electron movement in a metal nanoparticle due to an incident electric field over time. As the field varies the electrons move from one side of the particle to another, resulting in a rapidly varying state of polarisation.

pearance is dependent upon factors that affect this, such as size and morphology.

In order to understand the origin of this resonance, as well the consequence it has on the optical appearance of metal nanoparticles, a spherical metal particle with a diameter much smaller than the incident wavelength of light is considered. Defining the particle diameter, D, as much smaller than the incident wavelength allows a quasistatic approximation for the electron behaviour of the particle. This is due to the phase of the electron oscillation in the particle being uniform across its volume. This particle is configured as in figure 2.4, with a radius R, dielectric function $\varepsilon(\omega)$, sitting in a dielectric medium with dielectric function ε_d.

Due to the spherical symmetry of the system a general solution to the Laplace equation can be used to find the potentials both inside and outside of the particle.

$$\Phi_{in} = -\frac{3\varepsilon_d}{\varepsilon(\omega)+2\varepsilon_d} E_0 r\cos\theta \tag{2.8}$$

$$\Phi_{out} = -E_0 r\cos\theta + \frac{\varepsilon(\omega)-\varepsilon_d}{\varepsilon(\omega)+2\varepsilon_d} E_0 a^3 \frac{\cos\theta}{r^2} \tag{2.9}$$

The two components that make up Φ_{out} in equation 2.9 describe the applied field and an oscillating dipole centred on the particle. Φ_{out} can be rewritten in terms of a dipole moment $\mathbf{p}$;

$$\Phi_{out} = -E_0 r\cos\theta + \frac{\mathbf{p}\cdot\mathbf{r}}{4\pi\varepsilon_0\varepsilon_d r^3}. \tag{2.10}$$

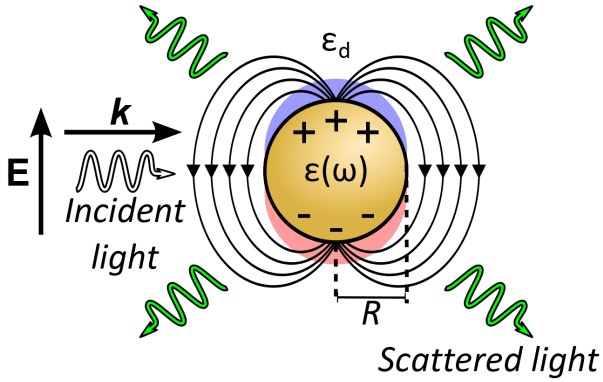

Fig. 2.4 A Metal nanoparticle with radius, R, and dielectric function, $\varepsilon(\omega)$, within a dielectric material with dielectric function ε_d. With incident light with wavevector, **k**, the electrons in the particle respond to the electric field component, **E**, becoming polarised as an oscillating dipole (for particles R< 50nm). At the resonant frequency of electron oscillation the intensity of light scattered from the particle is maximised.

where **p** is defined as;

$$\mathbf{p} = 4\pi\varepsilon_0\varepsilon_d R^3 \frac{\varepsilon(\omega)-\varepsilon_d}{\varepsilon(\omega)+2\varepsilon_d}\mathbf{E}_0 \tag{2.11}$$

As polarisability α is related to the dipole moment by $\mathbf{p} = \varepsilon_0\varepsilon_d\alpha\mathbf{E}_0$, an expression can be found from the above equation for the polarisability of a spherical nanoparticle,

$$\alpha = 4\pi R^3 \frac{\varepsilon(\omega)-\varepsilon_d}{\varepsilon(\omega)+2\varepsilon_d}. \tag{2.12}$$

At the maximum value of polarisability the amplitude of electron oscillation is at a maximum; this is the resonant frequency of the nanoparticle. The magnitude of scattered light is also maximised in this state due to the absorption and re-emission of incident photons at this frequency. This condition is met when $|\varepsilon(\omega)+2\varepsilon_d|$ is at a minimum, so when $Re[\varepsilon(\omega)] = -2\varepsilon_d$. For a Drude metal with a dielectric function as shown in equation 2.5, this condition is met when $\omega_0 = \omega_p/\sqrt{3}$ [11].

Subsequently, equations for the absorption and scattering cross sections of the nanoparticle can be found by calculating the Poynting vector of an oscillating electric dipole. This results

in the following two relations;

$$\sigma_{scattering} = \frac{k^4}{6\pi}|\alpha|^2 = \frac{8\pi}{3}k^4R^6|\frac{\varepsilon(\omega)-\varepsilon_d}{\varepsilon(\omega)+2\varepsilon_d}|^2 \tag{2.13}$$

$$\sigma_{absorption} = kIm[\alpha] = 4\pi kR^3 Im[\frac{\varepsilon(\omega)-\varepsilon_d}{\varepsilon(\omega)+2\varepsilon_d}] \tag{2.14}$$

.

where $k = 2\pi/\lambda$. These relations demonstrate how the scattering from a nanoparticle is heavily dependent on size. Scattering is proportional to the square of the polarisability and therefore R^6. As absorption is proportional to R^3, the scattering from a nanoparticle dominates the optical response as particle radius increases, with absorption playing a more important role in vanishingly small radii particles. Both scattering and absorption contribute to the optical extinction of a particle, with the extinction cross section being defined as the sum of the scattering and absorption cross section, $\sigma_{extinction} = \sigma_{scattering} + \sigma_{absorption}$.

The argument above is dependent upon the polar symmetry of the particle. By modelling a sphere, complications that arise from geometric asymmetry can be ignored. Different particle shapes can be sensitive to the manner of illumination. For example, an infinitely long nanowire would behave similarly to a metal film when the electric field component of the illuminating light is parallel to the length axis of the wire. With the E field aligned across its width, a localised surface plasmon would arise as a result of the structural boundary. Therefore, morphology is a crucial component to the optical appearance of a nanosized metal object.

The theory above is limited to particles with diameters below 100nm by the dipole approximation [11]. Above this size more complicated resonances, such as quadrapoles, begin to affect the radiated field and therefore cause additional scattering due to the additional resonant condition. A more detailed electrodynamic theory, covering these further terms, was described by Gustav Mie in 1908 [3]. The dipolar results detailed above are established in the first order terms of an expanded power series detailing the normal modes of the internal and scattered fields, with more complex terms for higher order modes following these. Mie theory can therefore be used to predict the optical behaviour of noble metal nanoparticles. For a comprehensive treatise of Mie theory the reader is directed to the work by Kreibig and Vollmer [16].

Using Mie theory, the scattering cross section of particles can be calculated (figure 2.5a).

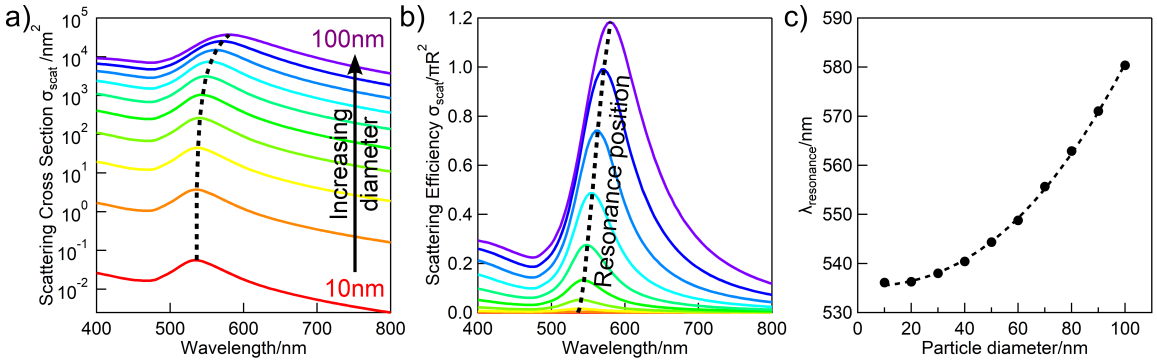

Fig. 2.5 Mie calculations of a) the scattering cross section σ_{scat} and b) the scattering efficiency ($\sigma_{scattering}/\pi R^2$) for a gold nanoparticle in water (n= 1.33) for particles with diameters $10-100$nm. As particle size increases the scattering cross section and the scattering efficiency increases. The resonance position is tracked by the dashed black line. c) The single particle plasmon scattering resonance wavelength for increasing particle diameter.

As the particle diameter increases, the resonance position redshifts and the scattering cross section increases by a factor of 10^5 from a diameter of 10 to 100nm. To more practically display this information, scattering efficiency can be used, which is a ratio of the scattering cross section to the geometric cross section, $\sigma_{scat}/\pi R^2$ (figure 2.5b). This shows that the scattering efficiency increases with particle diameter. The resonance position also shifts as the diameter increases (figure 2.5c).

The resonant frequency is not only dependant upon particle size and morphology, but also the environment in which it is in. As the polarisability of a medium in equation 2.12 is set by ε_d, the optical response of the nanoparticle is affected by the dielectric constant of the surrounding medium. The sensitivity of the scattering cross section is shown in figure 2.6. As the refractive index increases, the resonance position redshifts. As particle diameter increases, this sensitivity also rises demonstrating that larger particles are more sensitive to refractive index changes (figure 2.6b). This sensitivity enables localised plasmon resonances to be used for refractive index sensing [17, 18].

Nanoparticle resonances are sensitive to their size, morphology and environment. When one of these particles is positioned in close proximity to another, the interaction between the electric fields of both also influences their optical response. This interaction between closely-spaced particles will now be discussed.

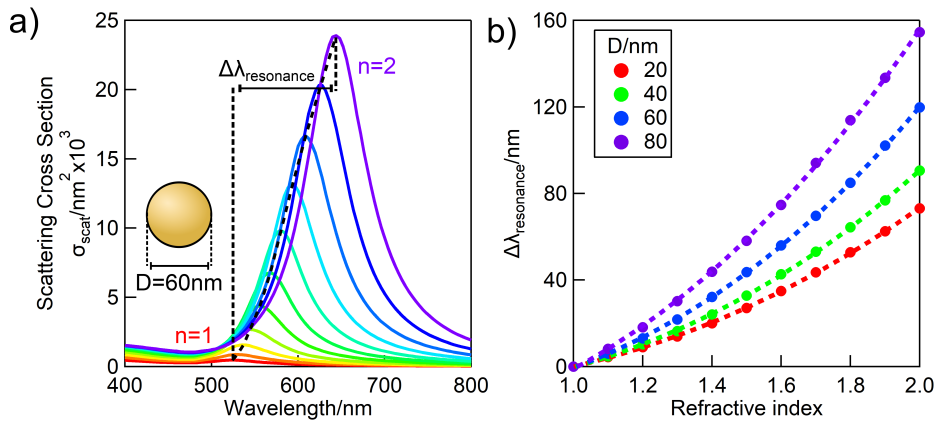

Fig. 2.6 a) Calculated Mie model scattering cross sections for a 60nm diameter gold nanoparticle embedded in different refractive index media from n= 1 to n= 2. As the refractive index increases, the resonance wavelength $\lambda_{resonance}$ redshifts. b) The shifts in the plasmon resonance $\Delta\lambda_{resonance}$ from n= 1 with increasing embedded medium refractive index values for different diameter nanoparticles. As the refractive index and particle diameter increase, the magnitude of $\Delta\lambda_{resonance}$ rises.

2.2.1 Coupling between nanoparticles: Nanoparticle chains

As illuminated small ($D < 100$nm) metal nanoparticles behave as electrical dipoles, the electric fields that they exhibit interact with one another, resulting in a coupling of their resonances. This in turn will result in a change in the optical properties of the particles. This manifests as a shift of the resonant frequency and therefore a change in the particle's optical appearance, with an associated increase in the scattering cross section of the assembly.

The shift in resonance from coupled metal nanoparticles is dependent on the interparticle separation, d. It is important to distinguish between two different forms of interaction, which arise depending on whether or not the interparticle separation is much smaller than a wavelength. For larger separations, the nanoparticles interact in the far-field only [11], however when $d \ll \lambda$ the interaction is dominated by a near-field coupling between nanoparticles.

In order to analyse the effect proximal particles have on each other, the E field of an individual nanoparticle is initially considered. Evaluating the electric potential of the particle (equations 2.8 and 2.9) using $\mathbf{E} = -\nabla\Phi$ can give us the electrostatic result for the electric field for when $r \ll \lambda$;

$$\mathbf{E}_{out} = \frac{3\mathbf{n}(\mathbf{n}\cdot\mathbf{p}) - \mathbf{p}}{4\pi\varepsilon_0\varepsilon_d}\frac{1}{r^3} \tag{2.15}$$

The key result of equation 2.15 is that the magnitude of the electric field falls by the cubic relation r^{-3} [11]. The interaction between the electric fields and therefore the coupling of the particle resonances will drastically increase at small values of d. Additionally particle coupling focuses the near field between two proximal particles. The incoming light is essentially squeezed into the gap, due to the increase in the field density as d becomes smaller. The high intensity of the local field in these gaps results in an intense environmental sensitivity. This enables sensing applications with single molecule sensitivities [19].

The polarisation of light also has a strong influence on the coupled resonant frequency. With the E field parallel to the dimer axis, the opposing charges across the gap between particles induces a restoring force that acts upon its partner. This mediates the resonant condition and causes a red shift to the coupled resonance (figure 2.7b). With a perpendicular field, the charges of each particle are aligned parallel the dimer axis, increasing the polarisability

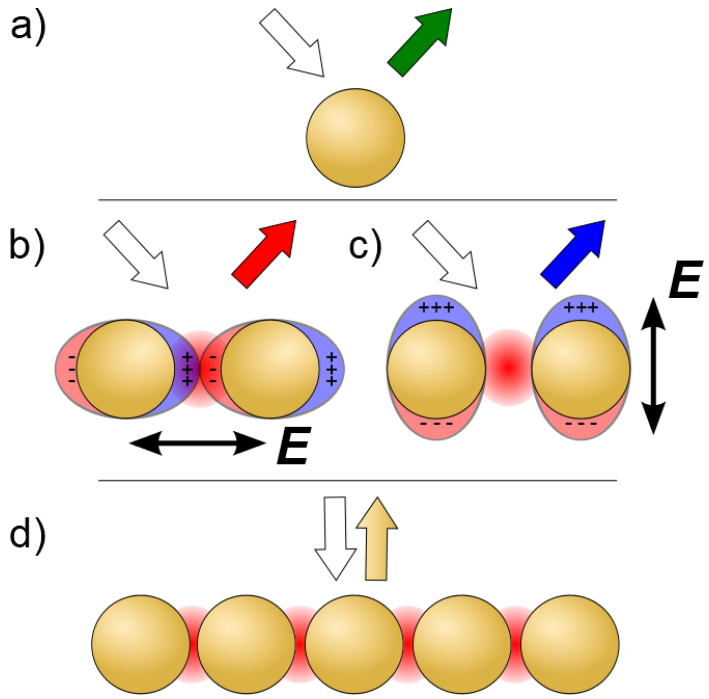

Fig. 2.7 The optical appearance of nanoparticles changes due to interaction between them. a) An isolated nanoparticle of gold will scatter green light. For a dimer resonance, shifts occur due to the field interactions between the particles. b) With the electric field along the dimer axis, a shift to a lower energy occurs and the appearance is redshifted. c) With the electric field perpendicular to the dimer axis, the restoring force on the electrons is increased, resulting in an increase in the resonant frequency and a blue shift in the scattered light. d) The interactions between large numbers of nanoparticles result in broadened resonances over a large wavelength range.

of the dimer and resulting in a blue shift of the coupled resonance (figure 2.7c) [20]. This behaviour holds true for long chains of nanoparticles, with the resonant frequency strongly dependent on how the electric field is aligned along the chain axis [9].

The optical resonance of a grouping of nanoparticles is further influenced by particles other than its nearest neighbour. With increasingly complicated systems, it becomes difficult to mathematically describe these interactions (figure 2.7d). Complete models of nanoparticle-light interactions are specific to the geometry and positioning of selected clusters and are often limited to small numbers of particles [21–23]. Therefore field components of larger structures are usually calculated using numerical calculations such as the boundary element [24] and finite-difference time-domain (FDTD) methods [25]. These methods compute field components over set volumes within structures in order to give accurate theoretical predictions of behaviour. These methods are discussed in Chapter 4.

FDTD calculations of a 60nm diameter nanoparticle chain for increasing chain lengths and the electric field polarised perpendicular to the chain axis are shown in figure 2.8. As the chain length increases the resonance peak redshifts by $\Delta\lambda_{chain}$ and the scattering cross section increases. The magnitude of these shifts is increased with smaller gap separations between particles. Furthermore the diameter of the particles is a key factor in the position of the chain resonance. In figure 2.8d the chain resonance position for 20, 40, and 60nm diameter particles is shown. As particle radius increases, the initial resonance position of the chain and the magnitude of the shift both increase. For example, when a chain of particles with separation $d = 1$nm increases in length, N, from 2 to 6 particles, the resonance shift when $D = 20$nm is $\Delta\lambda_{chain} = 40$nm, whilst when $D = 60$nm, $\Delta\lambda_{chain} = 180$nm.

The asymptotic behaviour of λ_{chain}, seen in figure 2.8d, shows that there is a saturation point beyond which further shifting no longer occurs. For close separations, where $d \ll D$, the asymptotic value is approached in chains with lengths as little as $N = 5$ [26] or $N = 10$ [27] particles, completely reaching the asymptote when $N \approx 18$ [28]. The asymptotic behaviour of a plasmon resonance has also been observed in nanoparticle clusters, with additional particles resulting in a broadening of the resonance rather than further shifting [29].

By using lithographic methods to fabricate chains of nanoparticles with set interparticle distances, the accuracy of these models can be tested. Using e-beam lithography, Maier et al. fabricated long chains ($N = 80$) of $D = 50$nm gold nanoparticles with spacings varying between $d = 25$ and 75nm to experimentally verify the plasmonic properties of nanoparticle chains [9]. The polarisation dependence of λ_{chain} described above is observed, with a

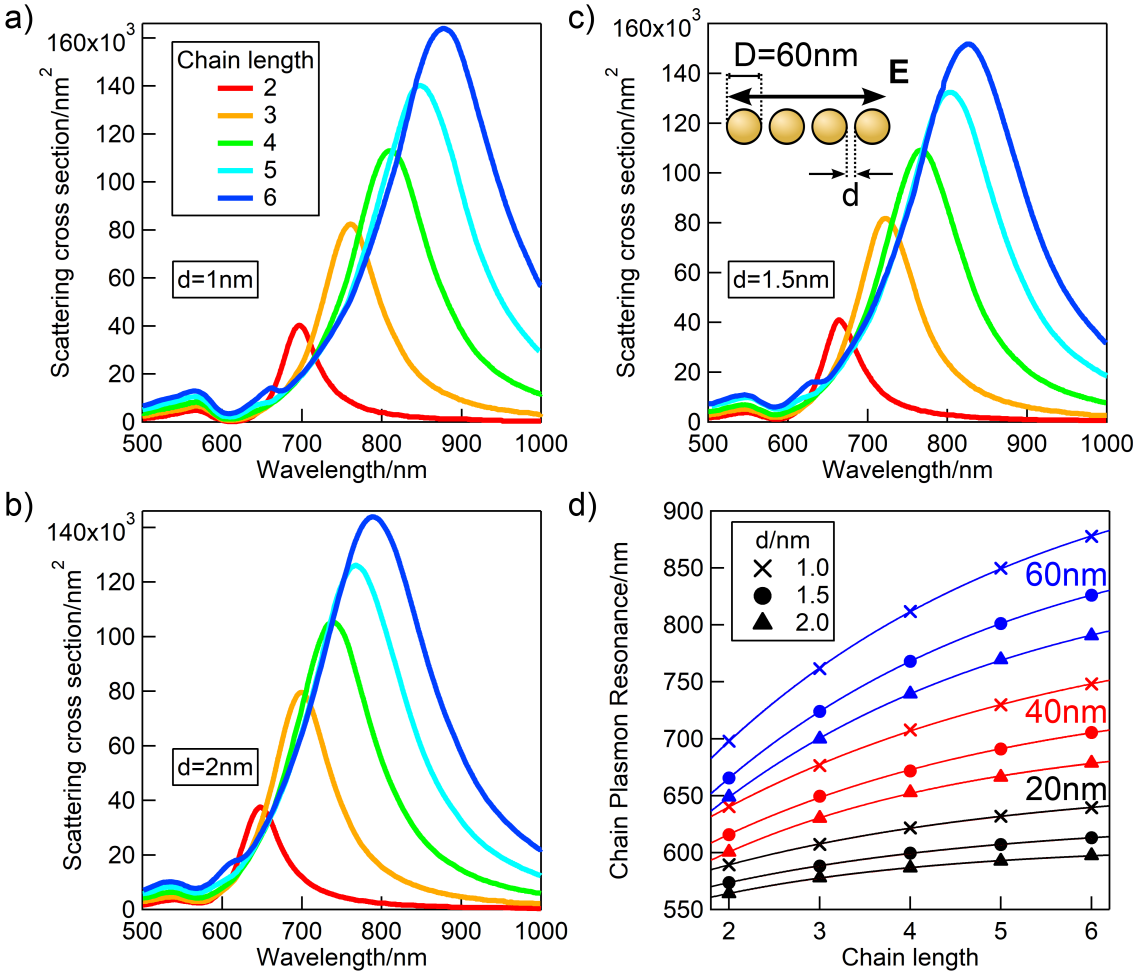

Fig. 2.8 FDTD calculations of the scattering cross section for increasing chain lengths, composed of 60nm gold nanoparticles with interparticle separations of a) 1nm b)1.5nm and c)2nm. As the chain length increases from 2 (red) to 6 (blue) particles, the chain resonance redshifts and the scattering cross section increases. d) The position of the chain plasmon resonance mode against chain length for $D = 20$nm (black), 40nm (red) and 60nm (blue). The wavelength position and the magnitude of the shift both increase with particle diameter and chain length.

red shifting of the plasmon resonance observed when the E-field is aligned along the chain axis and a blue shift observed with the E-field perpendicular to the chain axis (figure 2.9a). With unpolarised light, both resonances can be discerned in the resulting spectra. However, although calculated models of nanoparticle chain behaviour can be verified using this methodolgy, the resolution of lithographic fabrication methods cause complications testing closer spacings of particles ($d < 20$nm), whereas other fabrication methods allow for more flexibility in the testing of interparticle spacings on the order of a few nanometers.

Alternatively, self-assembly methods can be used to fabricate nanoparticle groups and arrays on a larger scale. This allows for a faster, though less directed method, for fabricating closely packed nanostructures ($d < 5$nm). For example, it is possible to fabricate dimers by drying down a diluted solution of nanoparticles onto a substrate. Nanoparticle pairs can be found and, using a dark field objective, the scattered light from them can be collected to observe the coupled optical behaviour [31]. Importantly, this work used a polymer substrate that can deform under an applied strain, actively changing the particle separation and hence the resonance. The concept and potential of tunable plasmonic materials is explored below.

Work has been been done on the effect that disorder has on the plasmonic properties of nanoparticle aggregates, where chain orientation deviates away from a singular axis. The work by Esteban et al. theoretically studied the effect that ordering has on the optical properties of a 1D chain of closely linked nanoparticles [30]. It was found that by introducing disorder to a nanoparticle chain, where the nearest-neighbour particle positions diverge from a straight chain axis, only small changes are observed in the optical response (figure 2.9b). Particles still behave as coupled despite this imperfect ordering. Only when disorder reaches a point where the chain is orientated perpendicular to the incident polarisation and is folded back on itself does the primary resonance shift significantly (over 40nm) away from the straight chain case. With unpolarised light the shift in resonance becomes even less, as the disorder of the chains no longer prevents coupling between them. The resilience of λ_{chain} to deviations from the chain axis is due to the fact that the interaction length of a coupled particle is only on the order of 2 particle diameters [27], leading to a strong spatially confined coupling between nearest-neighbour particles.

The study of nanoparticle chains can be extended into large fractal aggregates of nanoparticles. These can be fabricated using molecular linkers, molecules with a minimum of two binding sites that can connect two particles together. One such molecule, cucurbituril (CB), has a length of 0.9nm, enabling the long range fabrication of nanoparticle aggregates with sub-nanometre separations. During the assembly process of aggregation, the nanoparticles

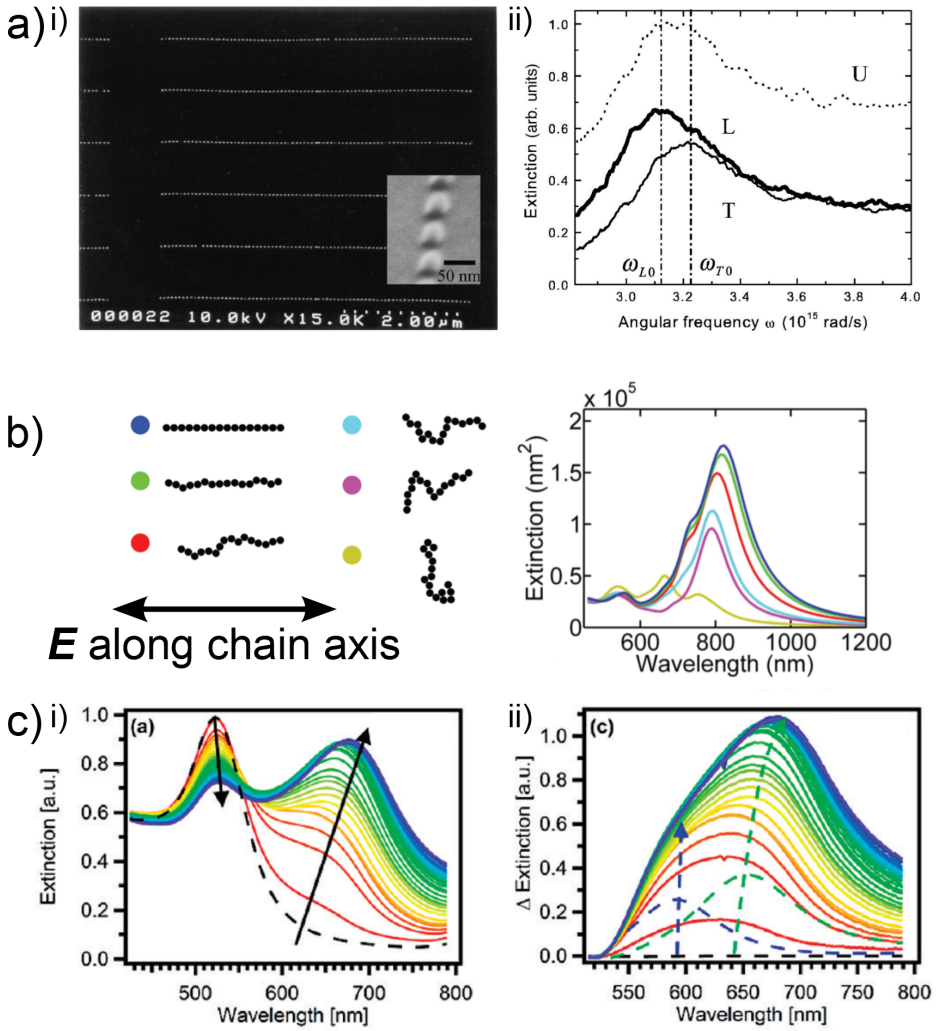

Fig. 2.9 Literature of examples of experimental and theoretical nanoparticle chains. a) i) Nanoparticle chains made of $N = 80$ particles with $D = 50$nm and $d = 25$nm made using e-beam lithography. ii) Extinction spectra from these chains, with light polarised along the chain axis (L) and across it (T) as well as spectra from unpolarised light (U). Along the axis the resonance redshifts to a lower frequency, whilst the transverse mode blueshifts to higher frequencies. The unpolarised spectra exhibits peaks from both these resonances. Adapted with permission from reference [9]. Copyright 2002 by the American Physical Society. b) Extinction spectra for nanoparticle chains with increasing levels of disorder, colour coordinated to the diagrams on the left, with the E-field polarised along the primary chain axis. Chain disorder results in minimal resonance shifts in the extinction spectra until the chain axis sits perpendicular to the incident polarisation. Adapted with permission from reference [30]. Copyright 2012 American Chemical Society. c) The i) extinction and ii) difference in extinction for nanoparticle aggregates formed using a linker molecule, in this case cucurbituril. i) As nanoparticles aggregate a chain mode forms and redshifts as the chain length increases. ii) The difference in extinction is made up of the dimer mode (blue dashed line) and the chain mode (green dashed line). Adapted with permission from reference [28]. Copyright 2011 American Chemical Society.

form dimers and then longer chains. The extinction spectra is seen to redshift due to the gradual retardation of the plasmon resonance as the chain length increases (figure 2.9c). A combination of single, dimer and chain resonances are observed, due to different length chains being present across the aggregate [28, 30]. This assembly process is covered in further detail in Chapter 3.

One dimensional nanoparticle chains allow the study of nanoparticle coupling in the simplest way by confining the aggregate geometry to one dimension. However additional behaviour arises in aggregates that uniformly cover larger areas. The optical behaviour of these will now be discussed.

2.2.2 Coupling between nanoparticles: close-packed nanoparticle arrays

As noble metal nanoparticle aggregates enter the macroscopic domain they begin to appear similar to a metallic bulk, showing a characteristic metallic sheen [2]. Despite this appearance the particles are not sintered together; the components maintain their individuality and appear spectrally different to bulk metallic films.

The origin of this behaviour is explained through the work by Ewald [32] and Oseen [33], studying the optical behaviour of clusters of atomic dipoles. Later work established the same principles work for densely-packed nanoparticle arrays [34–37]. These works determined that this apparent return of specular reflection from densely-packed nanoparticle arrays is a result of interference effects between the scattered light beams from the particles. Specifically, the scattered light from nanoparticles from within closely-packed arrays work constructively along regular geometric optical beam paths and destructively away from these beam paths [16]. Therefore the geometric reflection of a densely packed nanoparticle array is the zero-order diffraction peak of the scattered light beams, with higher angle scattering cancelled out due to interference. Higher order diffraction peaks only appear when interparticle spacings approach sizes on the order of λ.

Oseen found that the intensity of reflected light from a cluster of dipoles could be estimated using a volume fill factor, the volume taken up by the clusters compared to the total volume of the sample, $f = V_{cluster}/V_{sample}$. The reflective intensity is proportional to f^2. As the coverage of scattering dipoles increases so does the reflective intensity. Comparatively the scattering intensity, S, is influenced by defects or fluctuations in the cluster, so that $S \sim (|f_{loc} - f|^2)$. Therefore, S is minimised in a homogeneous isotropic array of dipoles [16].

Due to the dipolar behaviour of noble metal nanoparticles at optical wavelengths, these principles apply to nanoparticle arrays and explain the geometric reflection observed. As f increases, the angular profile of light reflected from the array narrows, leading to specular reflection (figure 2.10a).

The shift from individual scatterers towards the coherent scattering from larger clusters is known as the Oseen transition. Importantly the optical behaviour observed is not caused

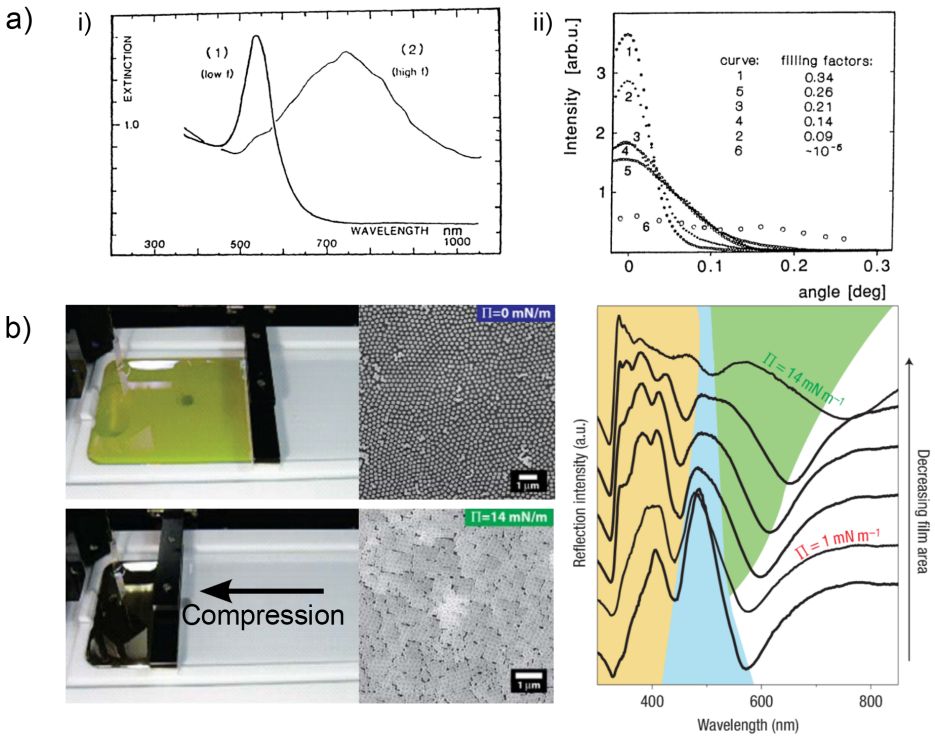

Fig. 2.10 Literature examples of the optical behaviour of nanoparticle arrays. a)i) The extinction from a nanoparticles arrays for (1) low and (2) high density nanoparticle arrays. As the density increases the resonance position redshifts and broadens. ii) The angular distribution of reflection from a densely packed gold nanoparticle array, D= 20nm, for increasing f. As the density of the mat increases, the angular distribution of the scattered light narrows as the array goes through an Oseen transition towards specular reflective behaviour. Adapted with permission from reference [16]. Copyright 1995 Springer Nature. b) Compression of silver nanocrystals D= 200nm on the surface of a Langmuir-Blodgett trough. At low surface pressure ($\Pi - 0$mN/m) the surface of the film shows a vivid colouration, but no metallic behaviour. As the surface pressure increases this changes until a metallic sheen appears. The reflection spectra changes as the surface pressure is increased, decreasing the film area and hence particle separation. Highlighted are the quadrupolar modes (blue), higher order modes (yellow) and a coupled broadening resonance (green). Adapted with permission from reference [35]. Copyright Springer Nature 2007.

by the sintering of the constituent particles into coherent thin film but is still defined by the coupled localised plasmon resonance of the nanoparticles in the cluster. Dusemund et al. verified this for varying density nanoparticle films, finding that as the fill factor increases, scattering intensity decreases significantly and reflection intensity increases [34]. Simultaneously, a redshift and broadening of the plasmon resonance peak is observed (figure 2.10a). This scattering profile observed is equivalent to that from an evaporated gold film, whilst the particles remain cohesive [16].

In Dusemund's work, interparticle spacings are fixed at roughly 3nm, with gelatine used as the spacer molecule. The varying fill fraction is achieved by grouping clusters of nanoparticles, rather than uniformly changing particle spacings. A more complex assembly method is required to enable a more even spread of particles.

A more dynamic way to explore the optics of large-scale nanoparticle arrays is to use a Langmuir-Blodgett trough to slowly decrease the interparticle spacings between particles. Nanoparticles are floated on a liquid surface and laterally compressed, decreasing the surface tension of the film therefore decreasing particle separation. Tao et al. compressed 200nm diameter polyhedral nanoparticles in this manner and observed a transition from the diffuse behaviour of individual nanoparticles to a reflective mirror [35]. Due to their size and morphology, the plasmonic behaviour of these arrays is complicated by the presence of quadrupolar resonances however the stereotypical redshift and broadening of peaks is observed (figure 2.10b). This transition proved to be irreversible, with the particles remaining in their close-packed structure after the surface pressure was lowered.

For smaller particles ($D < 30$nm, as seen in figure 2.10a), the broadened resonance is similar to that of the chain resonance (figure 2.8), and so can be modelled this way. However, as particle size increases, the broadening of the resonance increases, and the chain model can no longer be applied. In this instance FDTD calculations must be made to accurately model the optical properties of the nanoparticle array. Figure 2.11 shows calculated reflection spectra for an array of $D = 60$nm nanoparticles with varying interparticle spacings and refractive index values of the gap. As the gap distance decreases, the spectra redshift. With increasing refractive index, redshifting also occurs, as well as a splitting of the resonance into two distinct peaks. This is attributed to a single and array resonance; this behaviour, both experimental and theoretical, is discussed in detail in Chapter 7.

The sensitivity of the coupled plasmon resonance to proximity and environment allows for the development of structures sensitive to both these factors. By fabricating a dynamic

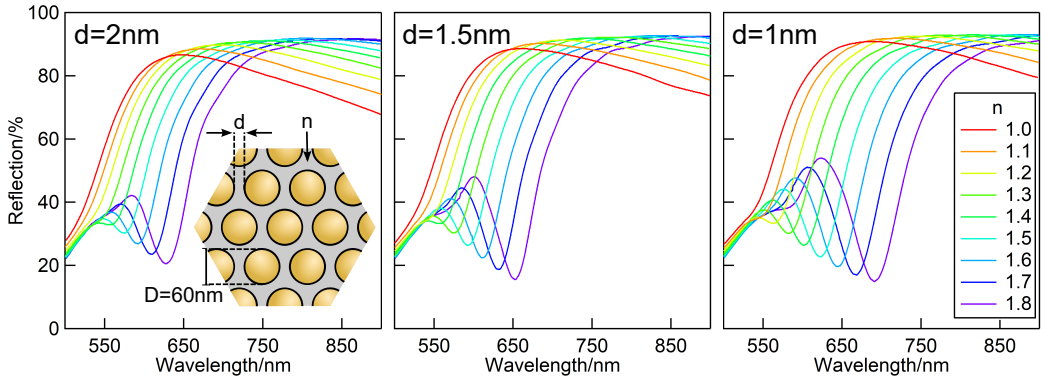

Fig. 2.11 Calculated FDTD spectra of an infinite close packed array of $D = 60$nm gold nanoparticles with varying interparticle separation, d, and gap refractive index, n. As the refractive index increases, the significant features of the spectra redshift, with the magnitude of this shift greater at smaller values of d. As the refractive index of the gap increases, the spectra redshift and the resonance peak splits. This attributed to the single particle plasmon resonance and the array resonance (see Chapter 7).

system where the separation of close packed nanoparticle arrays can be actively changed, this sensitivity can be actively probed and exploited.

2.2.3 Stretch tunable plasmonic structures

The sensitivity of plasmon resonances to nanoparticle proximity can be manipulated by fabricating systems with dynamic interparticle separations. Using elastomers as substrates enables active plasmonic materials with tuneable nanoparticle spacings. In this way a dynamic exploration of coupled plasmons is achieved.

For example, the interactions between small numbers of particles with varying separations have been studied by lithographically fabricating multiple different sets of a given structure with differing characteristic length scales [38]. Using an elastic substrate, the same experiment can be performed using only one of these structures, with the particle separation changed via applied strain. This technique has been used to observe the varying resonances of large (R$>$ 100nm) nanoparticles [31]. As the nanoparticles are separated, the dipole resonance observed shows a blueshift with the E-field polarised along the stretch axis, and a redshift with the E-field polarised perpendicular to the applied strain (figure 2.12a). The experiment has multiple advantages over similar ones using lithographic techniques to make repeating structures of different particle separations. The fabrication process is trivial, since particles are drop cast onto the elastic substrate and a dimer is then selectively found to fit the desired geometry for the experiment. Subsequently a wide range of experimental data

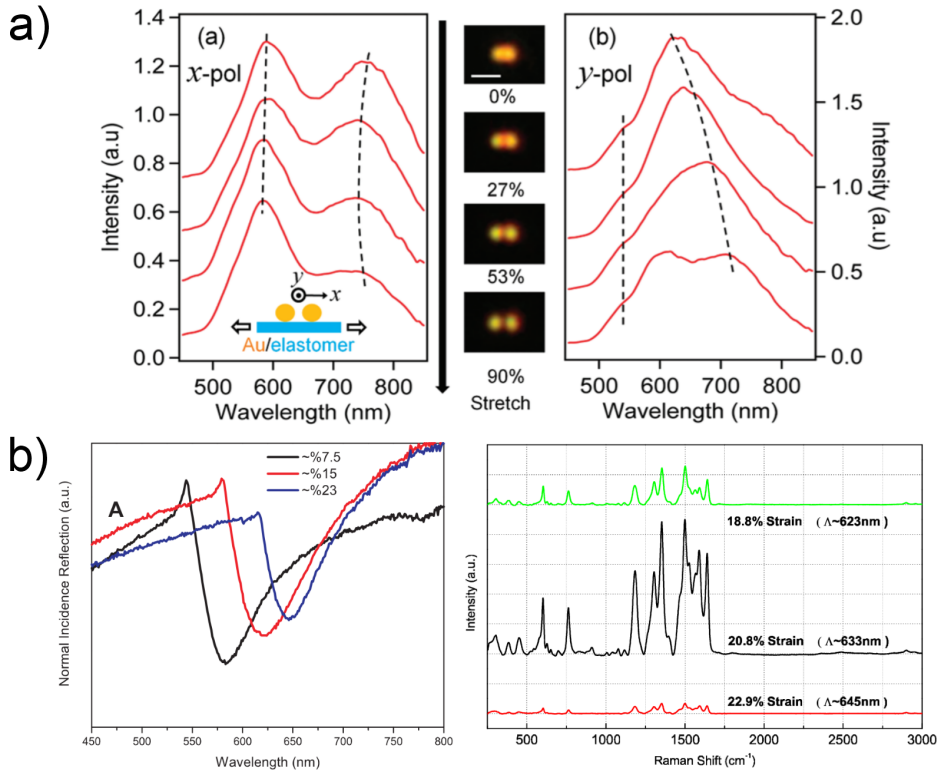

Fig. 2.12 Examples of stretch tuneable plasmons in literature. a) The sensitivity of gap separations for a dimer of R= 125nm gold nanoparticles drop cast onto elastic tape. By straining the substrate the particle distances are altered, allowing the observation of dynamic shifts in the scattering spectra. Reprinted with permission from reference [31]. Copyright 2010 American Chemical Society. b) Reflection spectra from a periodic silver grating on a stretchable PDMS substrate. Under uniaxial strain the grating period increases, resulting in a shift in the reflection spectra. The Raman spectra of R6G solution on this grating shows maximum enhancement when strained to a grating period, Λ, equivalent to the incident laser wavelength. Adapted with permission from reference [39]. Copyright 2009 Optical Society of America.

can be observed from this single dimer due to the tunability of the system.

This example demonstrates how mechanical deformation can be used to examine complicated plasmonic behaviour. More elaborate plasmonic structures that have been incorporated into elastomeric materials include gratings [39, 40] and arrays of nano-antennas [41]. In the instance of a grating, the one dimensional periodicity shows tuning of the grating period, Λ, on the application of uniaxial strain (figure 2.12b). As the film is stretched, Λ increases resulting in the resonance shifting. The resonance shift can then be used in order to tune the Raman enhancement of the materials (Raman spectroscopy is further discussed below). As the film is stretched, the intensity of the Raman spectra increases until the grat-

ing period is equivalent to the incident wavelength, before falling beyond this point. This demonstrates the utility of stretch tuneable devices through their adaptability, in contrast to structures with fixed length scales, as resonance positions can be adjusted via the application of strain. These properties can be used for optical sensing applications, where signal intensities can be maximised via mechanical tuning. However due to the length scales of this structure it does not make use of the increased sensitivity possible with separations on nanometre length scales.

Structures with periodicity in more dimensions have been fabricated either into or onto elastic substrates, shown in figure 2.13. An array of nanovoids (D= 900nm) is imbedded in polydimethylsiloxane (PDMS), an elastomer, by etching away a polystyrene particle array and evaporating a 100nm thick gold film onto the PDMS surface [42]. Upon strain the voids anisotropically deform and the resonance position changes (figure 2.13a). However, this voidal structure is limited by the continuous nature of the gold film on its surface. Due to the defects developing in the gold only a maximum of 5% strain is possible before cracks in the the film result in a loss of reflective intensity and a loss of the resonance of the voids.

Structures can be fabricated using discrete components in order to mitigate destructive cracking during stretch procedures. Zhu et al. [43] used polystyrene (PS) spheres (D= 600nm) on a PDMS substrate as a base for a 40nm evaporated silver film (figure 2.13b). Upon stretching, the silver capped PS spheres reversibly deform, resulting in a redshift as strain is increased. The modularity of the structure enables the observed reversibility as the components respond individually to the applied strain, avoiding the damage observed through cracking in continuous gold structures [42]. Further work on this type of structure, with PS spheres of D=1500nm, shows a polarisation dependent response. The degree of shift observed is sensitive to the orientation of the electric field of incident light [45]. Under uniaxial strain, the transmission dips from plasmon absorption redshifts by 9THz with the electric field aligned to the stretch axis, but only 2THz if aligned perpendicularly. This is caused by anisotropy introduced by the one-dimensional strain applied. Due to the size of these structures, this effect was observed at terahertz frequencies, however the same principle will apply in the visible waveband for structures made on suitable length scales. The polarisation dependence of stretch tuneable plasmonic structures is explored in this thesis.

This approach to design can be applied for structures with smaller components and spacings. Chiang et al. [44] used D= 10nm gold nanoparticles as building blocks to make two-dimensional arrays with interparticle spacings on the order of $1-2$nm (figure 2.13c). These were assembled onto PDMS and stretched, with the reflective intensities observed

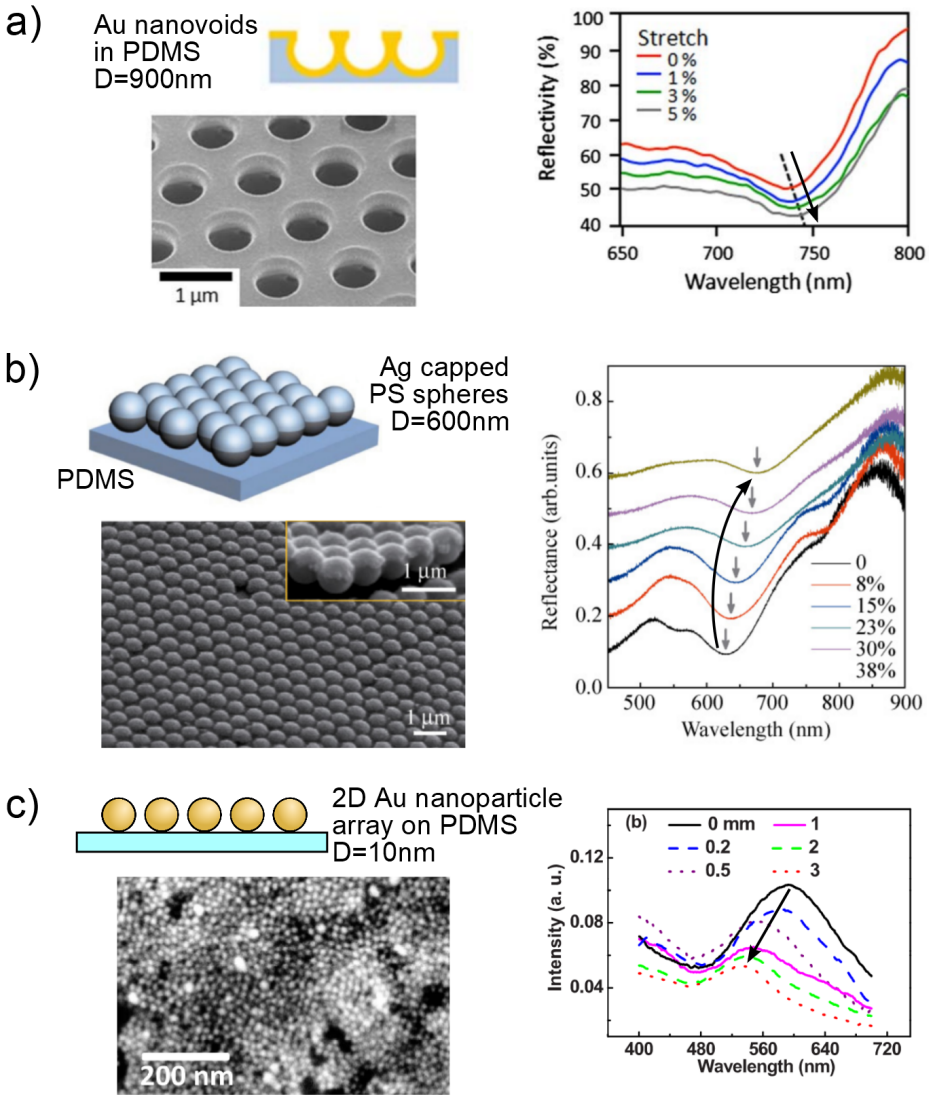

Fig. 2.13 Further examples of stretch tuneable plasmonic nanostructures from the literature, with a design schematic, SEM image and reflection spectra under strain. a) Nanovoids embedded in PDMS show a redshift in the plasmon resonance of 15nm at 5% strain. Reprinted from reference [42], with the permission of AIP Publishing. b) Polystyrene spheres on a PDMS substrate with an evaporated film of silver on their upper surface. Under strain, the PS deforms, resulting in a resonance redshift of 50nm for 38% strain. Adapted from reference [43], copyright Tsinghua University Press and Springer-Verlag Berlin Heidelberg 2010. c) A 2D array of D= 10nm nanoparticles on a PDMS substrate. Under strain, the absorption spectra is observed to blue shift by up to 70nm for 60% strain. Reprinted from reference [44], with permission from AIP Publishing.

to blueshift with increasing strain due to increasing interparticle separations. However this work does not explore in detail the nature of these shifts or comprehensively explain their behaviour theoretically. Additionally, the small particle diameter limits the magnitude of the resonance position shifts, resulting in a lower potential wavelength shift per unit strain of the plasmon resonance than would be possible for larger diameter nanoparticles. As such this work can be greatly expanded upon.

The interactions between localised plasmons are dependent on their environment and their relative proximities. By altering either of these two factors the observed optical behaviours change. This results in sensitivity to the surrounding refractive index (as seen in equation 2.12) and to mechanical strain altering component spacings. Controlling these variables enables the manipulation of the far field response of the system leading to potential sensing applications. On top of these effects is the focusing of the near-field into the nanoscale gaps of these plasmonic structures. The origin and potential application of these effects will now be explored.

2.3 Surface Enhanced Raman Scattering

Arguably the most prolific manner in which plasmonic resonances have been exploited for practical applications is as an amplifier for molecular sensing. By fabricating structures that make use of the field enhancement effects between nanoscopic plasmonic nanoparticles the number of photons interacting with selectively positioned molecules can be dramatically increased. Extremely sensitive measurements of these analytes can be made, increasing scattered intensity by many orders of magnitude, sometimes reported as up to 10^{14} times the original signal strength, though more reasonably cited at 10^{10} to 10^{11} [46], as well as allowing resolution on the scale of individual molecules [19, 47].

Raman scattering occurs when the molecular vibrations of a molecule, that fits to specific selection rules [48, 49], interact with an incident photon, resulting in an exchange in energy between them. The incident photon excites either vibrational or rotational modes in the molecule (figure 2.14a). Depending on the molecule's current energy state the interaction will shift the energy of the photon by the amount required to excite these modes. A lower energy photon is then re-emitted. This process is known as Stokes scattering (figure 2.14b). Alternatively, for a molecule that is in an excited state, the photon can gain energy by dropping the molecule into a lower energy state. This is known as anti-Stokes scattering.

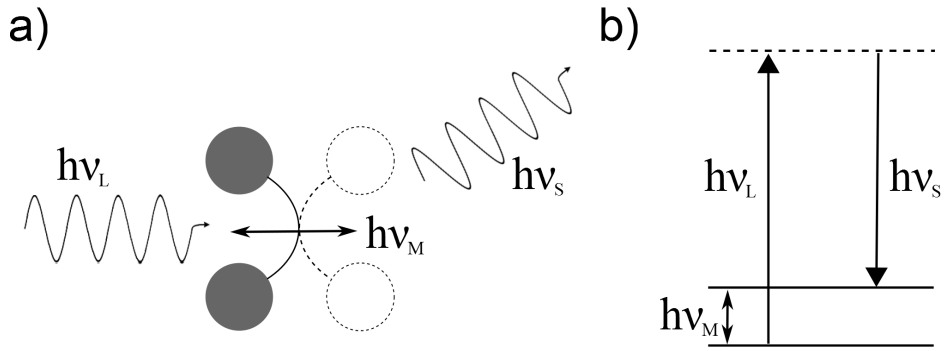

Fig. 2.14 a) An incident photon, ν_L interacts with a molecular bond exciting a vibrational mode, ν_M. An energy exchange between the two results in the re-emission of a different energy photon, ν_S. b) For Stokes scattering the excitation of the molecular bond results in the re-emission of a lower energy photon as it relaxes to a lower energy state.

By its nature, this interaction is quantised. For any given vibrational mode the resultant scattered photon will be of a specific frequency. For Stokes scattering;

$$\nu_S = \nu_L - \nu_M \tag{2.16}$$

where ν_S and ν_L are the frequencies of scattered and incident photons and ν_M is the frequency of the vibrational mode. This means that all photons emitted in this manner will be characteristic of the molecular bonds excited. An entire Raman spectrum is therefore the sum of the multitude of different vibrational modes of any given molecule that are allowed by the Raman selection rules. By collecting the scattered light from a molecule and by filtering out the frequency of the original incident photon, a spectral signature specific to the molecule can be collected. This process is very weak due to the tiny number of photon interactions that occur; only 1 in ten million will scatter this way. This is due to the tiny cross section of these interactions, typically 10^{-31}cm/molecule [11]. However, it is possible to greatly increase the signal strength of these interactions by increasing the local field strength around the molecule, which can be achieved using plasmonic structures.

2.3.1 Enhancing Raman scattering

Surface enhancement of the Raman signal was first observed by Fleischmann et al in 1974 [50]. In this instance an enhancement of the molecule pyridine was observed from the surface of a silver electrode. However, the authors did not realise the origin of this enhancement [51], instead attributing the increase in the Raman signal to changes in the chemical environment

of the molecule. Indeed, a charge transfer effect between a surface and a molecule can generate additional scattering events [52]. However this effect only increases the enhancement by two orders of magnitude and therefore does not explain the enhancements seen.

Any metallic object that has surface features on the nanoscale can, through the excitement of plasmons, enhance the local field around itself. This subsequently magnifies the resultant Raman scattering in the volumes around the surface. In this manner it is possible to achieve resolutions below the diffraction limit, so volumes that cannot typically be resolved by visible light can be probed.

In conventional Raman scattering, the power of the Raman signal, $P_{RS}(\nu_s)$, is given as

$$P_{RS}(\nu_s) = N\sigma_R I(\nu_L) \tag{2.17}$$

where $I(\nu_L)$ is the intensity of the illumination source, σ_R is the Raman cross section of the molecule, and N is the number of molecules in the illumination area. This power changes with surface enhanced Raman scattering to

$$P^{SERS}(\nu_s) = N\sigma^{SERS}|A(\nu_L)|^2|A(\nu_S)|^2 I(\nu_L) \tag{2.18}$$

as the power is increased by the enhancement factors $|A(\nu_L)|$ and $|A(\nu_S)|$ for the illuminating and scattered light respectively. These two enhancement factors are expressed as;

$$|A(\nu_L)| = |E_{loc}(\nu_L)|/|E_0| \tag{2.19}$$

$$|A(\nu_S)| = |E_{loc}(\nu_S)|/|E_0| \tag{2.20}$$

where E_{loc} is the local field from either the incoming light or the scattered light. The difference between ν_L and ν_S is typically negligible, as the vibration frequency of the molecule, ν_M, is much smaller than the frequency of the incident light. This approximation can be used to simplify equation 2.16 to $\nu_L \approx \nu_S$ and therefore $A(\nu_L) = A(\nu_S)$. Using this relation in equation 2.18 gives an enhancement of the SERS intensity proportional to E_{loc}^4.

The coupling of plasmonic materials results in high local electric field intensities between

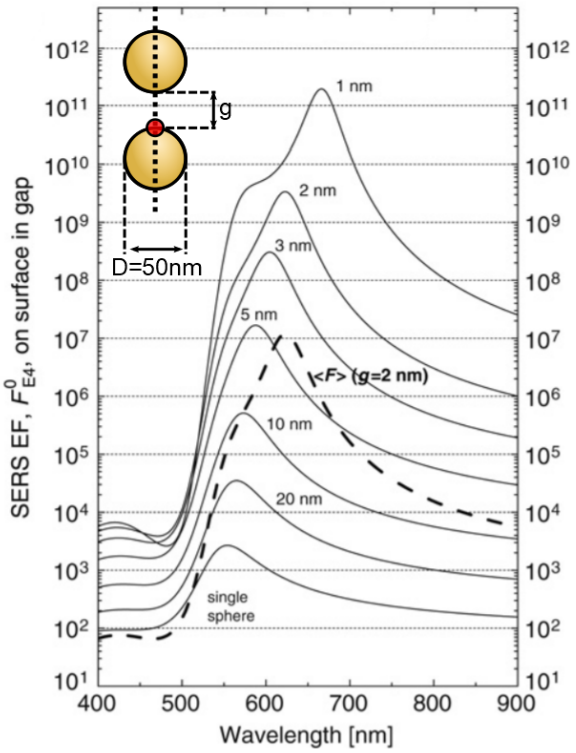

Fig. 2.15 Calculated SERS enhancement factor for different separations distances for a 50nm gold nanoparticle dimer, as found on the nanoparticle surface at the dimer axis (the red spot on the schematic, inset). As the dimer separation decreases the enhancement factor increases and the position of the maximum redshifts. The average value for the whole nanoparticle surface for a gap of 2nm is shown in the dashed black line. Adapted with permission from reference [53] with permission from Elsevier.

them, resulting in a hot spot for SERS enhancement. Le Ru et al. calculated the enhancement on the surface of a gold nanoparticle dimer ($D = 50$nm) with varying gap distance [53]. The enhancement is shown in figure 2.15, with gap distances from $1 - 20$nm, in addition to the enhancement from a single gold nanoparticle. As the gap distance decreases the maximum SERS enhancement factor increases, from 10^4 to 10^{11} times. These results are calculated on the surface of the particles on the dimer axis. The average enhancement factor across the surface for a gap of 2nm is shown in the dashed line. Whilst reduced from the maximum enhancement factor, this average is still 10^7 times greater then the unenhanced Raman spectra. Below approximately 0.6nm quantum tunnelling effects between nanoparticles can reduce the enhancement factor further as electron transport becomes possible between particles [54].

SERS enhancements enable observations of Raman scattering from molecules orders of

magnitude above baseline values. These enhancements are wavelength dependent, and to maximise the SERS intensity the plasmon resonances of a structure must align with those of illumination sources. Many different methods for generating SERS enhancements have been previously explored, these will now be discussed.

2.3.2 SERS structures and their tunability.

From the initial observation of SERS from a rough metal film [50], many different structures have been utilised to produce Raman enhancements. All make use of metallic structures, usually with features on the nanoscale, to produce the local field enhancements required for SERS measurements. For example, the SERS activity of metallic nanoparticles was first looked at in colloidal solutions [55, 56]. However, the increased signals produced through plasmonic coupling are lost when using this method. To counter this, nanoparticles can be aggregated in solution to improve their SERS intensities (figure 2.16b) [56, 57], or alternatively planar metallic nanostructures can be used as a substrate for SERS analytes with surface features that act as hot spots for detection (figure 2.16a). This type of structure provides a base on which analytes can be added for detection, with their designs tailored towards specific applications and resonances.

As an alternative to methods using surface patterning, hotspots can be selectively established by bringing sharpened tips into proximity of either metal films or each other (figure 2.16c) [58]. This method, known as tip enhanced Raman spectroscopy (TERS), is commonly used for selective scanning across large areas of substrate and has demonstrated success with single molecule detection [59].

Many different approaches have been used for planar SERS structures. For example, nanovoids

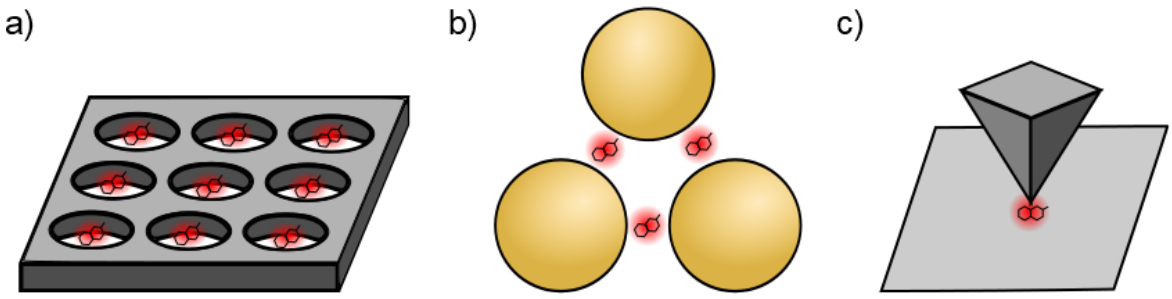

Fig. 2.16 Examples of structures commonly used to produce enhanced Raman scattering, such as a) Voids in metal films [57], b) particle aggregates [60] and c) metallic tips to surfaces [58].

can be embedded within metallic films to create many SERS detection sites, all with the same resonance (figure 2.16a). A commercially available SERS substrate designed in this way, Klarite, has a plasmon resonance of 785nm allowing for maximum enhancement to be seen by illuminating the sample using a near-IR laser. The nature of the substrate, a periodic array of inverted pyramids etched into silicon and coated in a gold layer, allows for reproducible SERS measurements [57]. Similarly, voids made by etching out a self-assembled array of polystyrene spheres allow for a self-assembled approach to fabricating spherical voids embedded within a gold film (figure 2.13a) [42]. This example is notable as the fabrication can be done on an elastic substrate, allowing for a mechanically tunable plasmon resonance, a useful technique that is further discussed below.

Initially experiments to generate SERS enhancements using nanoparticles came from unaggregated solutions [55]. However, aggregates of nanoparticles can produce enhancements beyond what is capable from individual nanoparticles due to the coupling between them [47, 56]. Because of this, large areas of nanoparticles deposited onto substrates have been explored as SERS substrates [60]. Glass has been functionalised to absorb gold nanoparticles on its surface, with an enhancement of 10^4 recorded. Crucially, the linker molecules used, organic silanes, do not show a strong Raman signal and therefore do not interfere with the detection of the analyte. This is attributed to both their low Raman cross section and their position away from the hot spot between the particles. However, this assembly method only produces lower density arrays, with distances between particles of up to 50nm, and therefore this structure does not make the best use of nanoparticle coupling to produce high Raman intensities.

Greatly improved nanoparticle based SERS structures have been demonstrated by using small ($N< 5$) nanoparticle aggregates to detect single molecules, with potential enhancement factors calculated at over 10^{14} times (based on equivalent signals from non SERS measurements) [65, 66]. This is due to the increasing near-field intensity with decreasing particle separation. As the number of particles used in nanoparticle aggregates varies, the magnitude of the SERS enhancement changes (figure 2.17a) [61]. As the cluster size increases to $N> 20$, the intensity of the SERS enhancement falls to as low as 10^6 or 10^7 [61, 67]. Therefore large area nanoparticle assemblies do not have the same degree of enhancement as small clusters. However, they still have utility as large scale substrates with many different hotspots that can be assembled rapidly using bottom-up assembly techniques. Additionally, the broadening of the plasmon resonance within long range nanoparticle structures allows for enhancements over a greater range of wavelengths, allowing the same structure to be

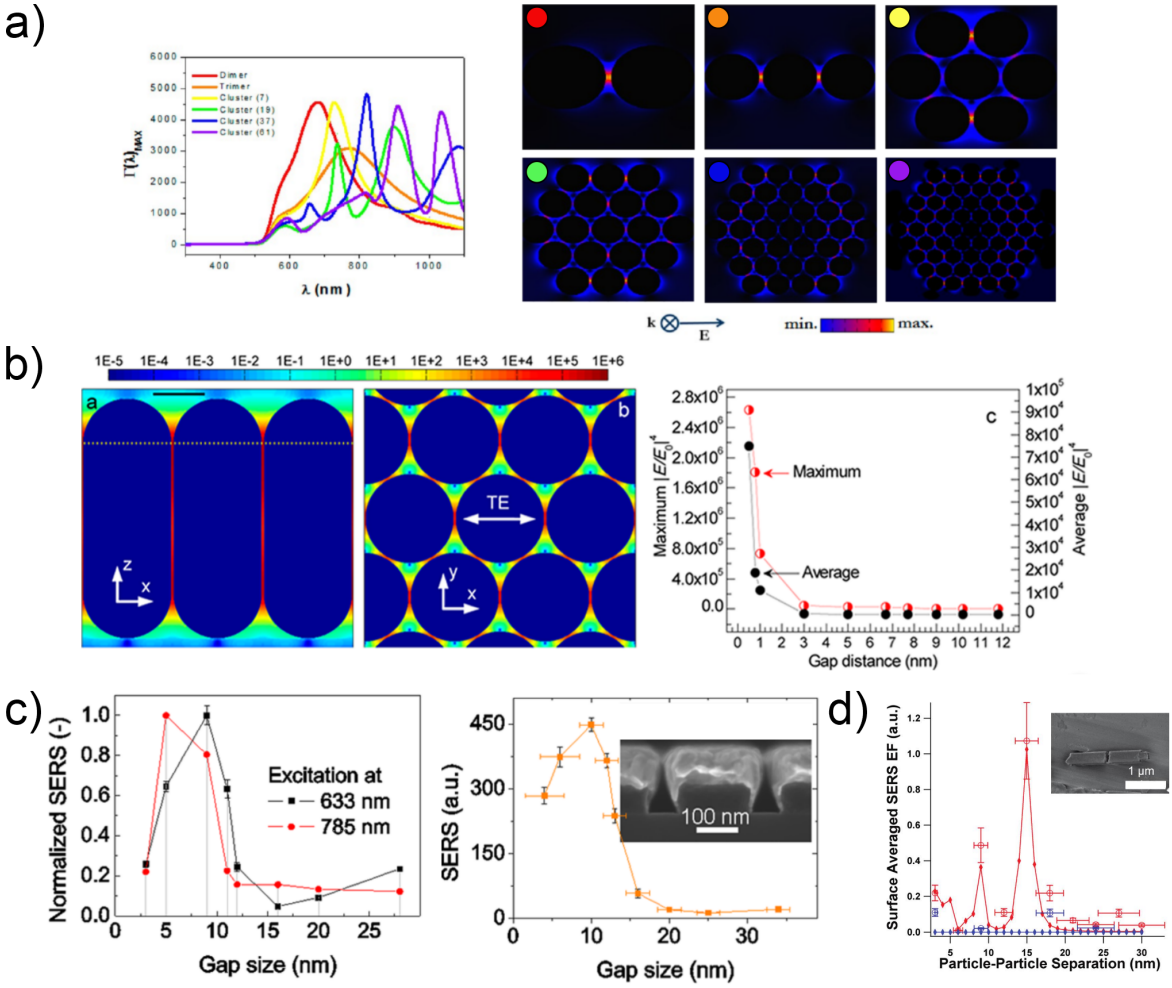

Fig. 2.17 Examples of SERS structures from the literature. a) Simulated near-field enhancement spectrum ($\Gamma(\lambda)_{MAX} = |E(\lambda)/E_0(\lambda)|^2$) for different size clusters of spherical silver nanoparticles with separation of 5nm. Adapted with permission from [61]. Copyright 2013 American Chemical Society. b) A simulation of the local electric field response of an array of gold nanorods with 0.8nm gap separations, and the maximum and average enhancement factor as a function of the gap separation. As the separation decreases towards 1nm the enhancement factor dramatically increases. Reprinted with permission from [62]. Copyright 2013 American Chemical Society. c) The SERS count and normalised SERS intensity of a single peak of the SERS spectrum of benzene-ethane-thiol for varying gap distances from a one-dimensional grating (SEM inset) with varying gap sizes. The maximum SERS count is found at different gap lengths for different excitation wavelengths, 8nm for 633 nanometer illumination and 6nm for 785nm. Adapted with permission from [63]. Copyright 2013 American Chemical Society. d) Stretch tunable separation of a nanorod dimer, with the averaged SERS enhancement factor varying with gap separation. Adapted with permission from [64]. Copyright 2010 American Chemical Society.

probed with different excitation wavelengths.

Similar structures of large arrays of nanoparticles [68], nanorods (figure 2.17b) [62, 69] and nanowires [70] produce similar levels of enhancement. Alternatively other structures can be used as three dimensional substrates. Multilayered nanoparticle films where the analyte is either allowed to infuse or is sandwiched between the layers allows for a greater number of hotspots in any given collection area [71]. The sandwiching technique, where molecules are deposited between layers, shows a slightly stronger signal than if just left to infuse although both types show enhancement on the order of 10^7 times. Large scale 3D woodpile structures of gold nanoparticles show enhancement factors of 10^6 to 10^8 [72]. These spongelike structures allow for numerous potential hotspots in the structural voids. Similarly nanoparticles have been aggregated to form spongelike structures with many different cavities that can act as voidal hotspots [73]. Like large-scale nanoparticle arrays, these structures allow for a large number of SERS dectection spots in a typical microscope collection spot. However, the fabrication processes for these three-dimensional structures are more complex then the simple self-assembly steps for nanoparticle arrays; self-assembly techniques offer a simpler and more rapid approach for the assembly of large area SERS substrates.

One significant disadvantage of the self assembled structures detailed above is that the interparticle spacing is not entirely controllable. Interactions between ligands on the nanoparticle surface and the particles are not always clear, and many possible factors in assembly, such as nanoparticle charge and size variations, affect the interparticle separation. An alternative to these methods is the use of very rigid glue molecules, such as cucurbituril (CB). The well defined length of the CB molecule fixes particles together with a known separation [28]. Other fabrication techniques can also be used to attain nanoscale separations between components. By evaporating gold at an angle onto a grating pattern made using photo-lithography, gaps of below 10nm can be made(figure 2.17c) [63]. This angled assembly allows for fabrication of a controllable and tuneable gap size and film thickness, in order to optimise the SERS signal to a maximum enhancement factor of 10^6.

As an alternative to the fabrication of nanostructures on specific length scales, stretch tuneable substrates can be used to actively change separations of plasmonic components, tuning the coupled resonance of the system and thus optimising the SERS signal. This has been demonstrated by Alexander et al. using a self-assembled nanorod dimer on a silicone rubber substrate [64]. The separation of the dimer is tuned from between 3 and 30nm. As the gap distance changes, the relative observed SERS enhancement factor changes, with a maximum value at a gap distance of 15nm matching closely with calculated values (fig-

ure 2.17d). In this way, the substrate can be manipulated to maximise the SERS intensities from the substrate. Importantly, this signal is polarisation dependent, with the enhancements only observed with the electric field polarised along the dimer axis. This means that, to get the best enhancements from this system, the dimer must be aligned with both the incident electric field and the stretch axis of the apparatus in order to actively tune the separation between them. The low density of dimers on the substrate will make this selection slow, as the dimers of the correct orientation have to be located before illumination. As an alternative, large scale substrates can be used, such as stretch tunable gold gratings on PDMS where tuneable SERS intensities have also been observed (figure 2.12b) [39]. Large scale structures such as this have the advantage of their whole area being usable for SERS sensing, instead of a selective region, enabling faster sample processing for large scale testing. Therefore, by stretch tuning plasmonic components, SERS intensities can be maximised, minimising the need to control gap size in the fabrication process.

Nanoparticle based SERS substrates offer a wide variety of structures that generate large enhancements in the Raman signals from molecules. Fabrication routes can thus be selected on whether it is more important to give strongly enhanced signals over wide range of excitation wavelengths, such as achieved by large scale nanoparticle arrays, or the greatest possible enhancements achieved from just a few particles via separations close to a single nanometre. Either method offers significant opportunities for molecular sensing.

2.4 Summary

From first principles, the origin of the plasmon within metals has been explored. By constricting electron displacement to subwavelength-scale volumes, a specific resonance arises that is sensitive to the geometry of the structure. The frequency of these resonances are dependant on the shape, size, distribution and the surrounding environment of these particles. By bringing them close together the coupling between them can focus light into volumes much smaller than the diffraction limit. These sensitivities allow for groupings of plasmonic nanoparticles to be sensitive to both mechanical strain and local refractive index, whilst strong E-fields between them allow for enhanced Raman scattering that enables such structures to act as molecular sensors.

In order to make full use of these properties, nanoparticles need to be organised into specific structures. The means and methods of creating such assemblies is now explored.

Chapter 3

Nanoparticle Self-Assembly

This chapter will review the different approaches to bottom-up self-assembly that can be used to construct plasmonic nanostructures and the advantages to using them over lithographic methods. Self-assembly methods will be discussed starting with the stabilisation of nanoparticles and how, by adjusting different parameters, this stability can be constructively disrupted in order to fabricate large-scale structures. By fine-tuning these techniques the formation of these structures can be optimised, enabling controlled assembly.

3.1 Nanoparticles as building blocks

Self-assembly allows for the construction of complex structures by taking individual components and placing them in an environment where, by means of manipulating the energetics and kinetics of the system, they will form into a desired pattern. Methodology varies depending on the size of these assemblies, with self-assembled structures ranging from biological structures on molecular length-scales to astronomical formations such as solar systems and galaxies [74]. This work is concerned with those on the lower end of this scale, specifically with the assembly of structures on nano length-scales.

In comparison to lithographic methods, self-assembly is fast and requires minimal manual input. By understanding the variables in any given fabrication method, a large degree of control can be exercised over the resulting structure. For example, large arrays of pillars, sized on the order of tens of nanometers and fabricated into poly(methyl methacrylate), can be deformed and pulled together simply by wetting the structure (figure 3.1a). This is due to the capillary forces that form between the pillars whilst the solvent evaporates.

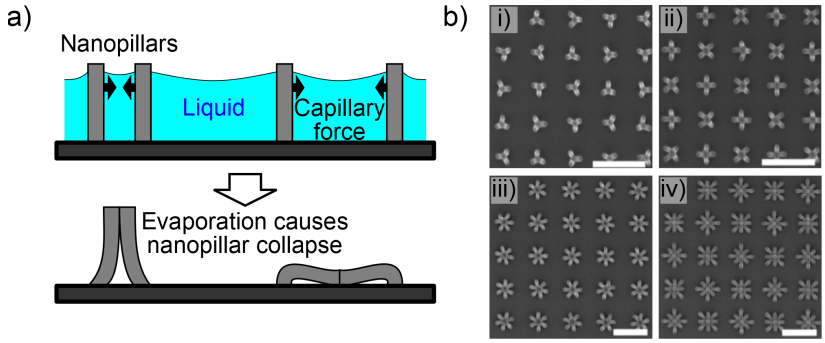

Fig. 3.1 An example of capillary induced self-assembly on a repeating pillar structure fabricated in a polymer. a) The capillary force brings pre-fabricated pillars together. b) By tuning the pillar and array parameters different structures can be formed such as i) a 3 pillar assembly with 3 different rotational positions, ii) 4 pillars, iii) 6 pillars and iv) 9 pillars. Adapted with permission from [75]. Copyright 2010 American Chemical Society.

Different patterns can be made by tuning the length, thickness or area density of these pillars [75, 76], demonstrating the versatility of self-assembly methods in fabricating a large variety of structures (figure 3.1b).

Nanoparticles are ideal building blocks for constructing large nanostructures due to their high adaptability and tuneability. As nanoparticles can be fabricated in various shapes, sizes and with different functionalisations (figure 3.2), structures made from them show a wide range of different topographies. Techniques and scales vary from simple aggregation, where chemical functionalisation induces formation [28], to large scale templated structures, where prefabricated masks are used to direct nanoparticles into the desired complex patterns [78]. Nanoparticles therefore perform a role akin to lego bricks, their versatility allowing for a

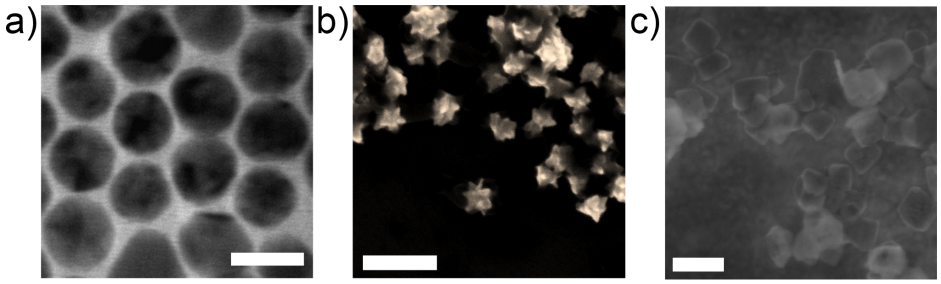

Fig. 3.2 Nanoparticles come in many different morphologies: a) Spherical nanoparticles are approximately spheres, although in actuality are many-faceted crystals (20nm gold nanoparticles, scale bar 20nm). b) Gold nanostars are similar to their spherical counterparts but have spiked facets. In order to stabilize this shape, they are covered in a protective polymer layer (scale bar 200nm). c) LiFePO nanoplatelets are irregularly sized thin ($\approx$ 10nm) sheets that can be fabricated to various different lengths [77] (scale bar 200nm).

wide range of structures to be built up and altered as desired. In order to understand their aggregation, it is first necessary to discuss how they maintain stability within solution, to best find ways to constructively disrupt it.

3.1.1 Nanoparticles in solution

Colloidal nanoparticles use stabilising agents on their surface to prevent agglomeration of the particles into a single mass. Van der Waals forces produce strong attractions between colloidal particles, therefore an opposing force is required to counter this. The behaviour of colloidal systems in this scenario can be illustrated by DVLO theory, as first described by Derjaguin and Landau [79] and later Verwey and Overbeek [80][1]. In this instance, the interaction potential, V_τ, between two surfaces is considered as the sum of the Van der Waals potential, V_{VdW}, and an opposing electrostatic potential, V_{elec}, that arises from a particle's surface charge [82].

$$V_\tau = V_{vdW} + V_{elec} \tag{3.1}$$

This model of nanoparticle interactions can be extended by adding various different attractive and repulsive potentials [83]. Such extended DVLO models can take into account such factors as magnetic attraction between particles and osmotic repulsion caused by the ions between particles. Relevant to this text is elastic-steric repulsion, arising from surfactant molecules on particle surfaces, that acts as a physical barrier to coagulation. Long chain organic molecules are regularly used to stabilise nanoparticles [84], especially in non-polar solvents where charge stabilisation is less energetically favourable [85]. In addition to this, particle shape and size also affect the interaction between particles, as does the chemical composition of the nanoparticle solution. In order to build a simple model of particle interactions only the two basic forces suggested by DVLO theory will be considered now, before a discussion of the implications of steric repulsion.

The electric potential of a nanoparticle in solution can be set by means of a charged surfactant molecule. Coating nanoparticles in this surfactant prevents aggregation by establishing an electrical double layer (EDL) of charged ions around the particle. The surfactant attracts oppositely charged diffuse ions from the solution that then coat the surface (figure 3.3). In the case of gold nanoparticles, negatively charged citrate molecules are often added during

[1] Both pairs were working independently; Verwey and Overbeek initially received credit for the theory and retrospectively referenced Derjaguin and Landau 7 years after publishing [81].

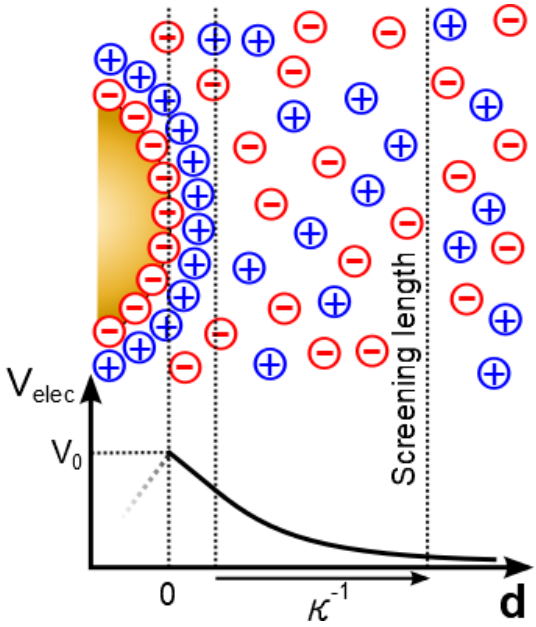

Fig. 3.3 A schematic of the electrical double layer at the surface of a colloid and the resultant electric potential V_{elec} as a function of distance from the nanoparticle surface, d. In this case the negative surfactant molecules coat the nanoparticle, attracting positive ions in the liquid to the surroundings of the particle. The electrical potential is highest at the surface and decays into the liquid as the EDL charge becomes evenly distributed at the Debye screening length, $\kappa^{-}1$, where the free ions of the solution screen the potential. A high electrostatic potential at small values of d prevents aggregation.

nanoparticle synthesis. The number of citrate molecules added defines the size of the particles; a larger concentration of citrate will result in smaller diameter nanoparticles. This is due to the surfactant binding to a greater surface area with the same volume of gold.

The ions that make up the EDL are free to move throughout the nanoparticle solution. Beyond a certain distance, the particle's charge is screened out by these ions, limiting the range of V_{elec} in the solution. This distance is known as the screening length, κ^{-1}, (typically between 1 and 5nm) and is calculated as;

$$\kappa = \left(\frac{e^2 \Sigma n_i(\infty) z_i^2}{\varepsilon_0 \varepsilon K_B T}\right)^{\frac{1}{2}} \tag{3.2}$$

where e is the elementary charge, n_i is ion concentration, z_i is each ion's valance number, ε is the permittivity of the solution, k_B is the Boltzmann constant, and T is the temperature of the solution in kelvin. This can be used to model the electrostatic potential between two metal colloids in solution when the distance between them, d, is less than the screening

length, κ^{-1}, allowing equation 3.1 to be rewritten, along with a calculated van der Waals potential, to give a value for V_τ [86];

$$V_\tau = -\frac{AR}{12d} + 4\pi\varepsilon_0\varepsilon R V_0^2 \frac{d}{d+2R} ln(1+\frac{R}{R+d}e^{-\kappa d}) \tag{3.3}$$

The first term of equation 3.3 defines the van der Waals interaction, where A is the Hamaker constant, which defines the strength of the van der Waals force of materials, R is the particle radius, and d is the separation between the two spheres. The second term defines the electrostatic potential between the two spheres, where V_0 is the surface potential of the particles. The result of the sum of these potentials can be seen in figure 3.4. Depending on the strength of the potential, the electrostatic force may result in a barrier greater than the value of k_BT in the system. If this is not the case, the van der Waals attraction may lead to the particles aggregating [87]. In the example in figure 3.4, V_τ is greater than the value of k_BT at room temperature and so the colloid is stable. Therefore, surface charge is critical in maintaining the stability of the colloidal solution as it acts as the principle barrier to aggregation.

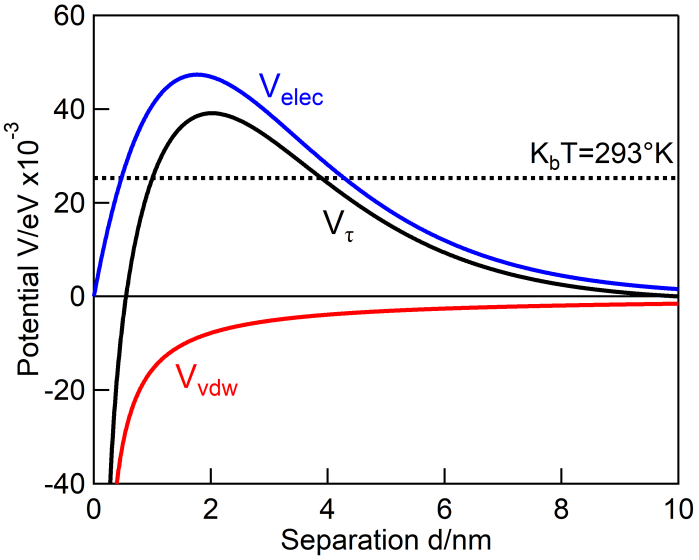

Fig. 3.4 The interaction potential, V_τ, (black) calculated using equation 3.3 between two 60nm gold nanoparticles as a function of their separation. d is calculated as the sum of the repulsive electrostatic potential (blue) arising from the charged nanoparticle surface and the attractive Van der Waals potential (red). Chemically tuning these two potentials can either force prevent aggregation through an overwhelming repulsive force, or encourage it due to a dominant attractive force. The value of k_BT at room temperature is shown as the dashed line. These potentials are calculated with A$= 10 \times 10^{-20}$J [88], $\varepsilon = 78$, $V_0 = -60$mV and $\kappa = 0.6$nm$^{-}1$ [86].

In addition to the two potentials detailed above, further repulsive potentials arise from the interactions between molecular coatings on the nanoparticle surface. For example. repulsive potentials can come from polymer layers encapsulating the particles [89] or long chain organic molecules that form a self-assembled monolayer on the particle surface [90]. The interaction between surfactant layers is close range, with the maximum possible interaction length limited at twice the length of the ligand molecules, a specific case for when ligands are organised, with high densities, perpendicular to the particle surface; this interaction length can be smaller if lower density ligand coatings allow interdigitation between the shells surrounding particles, or if molecular conformations on the particle surface have a dihedral angle of less than 90° .

Using a simple case for an example, for dense coatings of depth L on each particle's surface (for example either polymer shells or densely packed ligand monolayers), when $d > 2L$ there is no extra repulsive potential (figure 3.5a). However, assuming that due to the high coverage density there is negligable interdigitation between the two opposing shells, when $d < 2L$ two additional terms to equation 3.1 are created [91]. The first arises from osmotic pressure caused by the absence of solvent molecules in the gap between particles at this distance. The solvent molecules move into the gaps where they exist at lower concentrations resulting in a repulsive potential on the particles (figure 3.5b). Another repulsive potential can arise due to compression of the ligand molecules reducing the entropy of the system, resulting in elastic-steric repulsion V_{steric} (figure 3.5c).

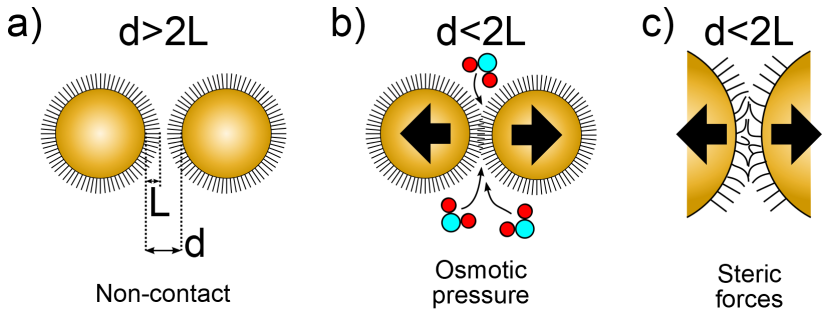

Fig. 3.5 Additional repulsive forces that result in further potentials that extend DVLO models arise from coating nanoparticle surfaces in ligands. a) When the separation distance d is greater than the combined length of the ligand shell around the particle, $2L$, there is no contact between them and therefore no interaction. b) When $d < 2L$, a concentration gradient forms resulting in osmotic pressure from the solvent molecules moving into the interparticle gap. c) Deformation of the ligand shell results in a steric repulsion due to the ligand molecules preferring a lower energy configuration on the particle surface.

Quantifying these potentials can be rather complex. They are not solely additive onto equation 3.1, as the introduction of a self-assembled monolayer (SAM) of a molecule onto the surface of the particle will substantially effect the EDL, reducing the electrostatic potential. Additionally they can also be dependant on assumptions such as non-distortion of the ligand until a certain separation, such as $d < L$, presuming interdigitation and ignoring factors such as solvent-ligand miscibility . By coating the nanoparticles with a steric ligand it is possible to stabilise them on nanometer length scales, whilst reducing the repulsive V_{elec}.

3.1.2 Examples of nanoparticle aggregation

To induce aggregation, it is necessary to reduce the repulsive potentials of the nanoparticles. The simplest way to do this is to increase salt concentration, resulting in a screening of the electrostatic interactions between the particles and reducing the repulsive potential. Alternatively, adding a molecule to the system that interferes with the EDL can also act to reduce V_{elec}. The introduction of ethanol into aqueous gold nanoparticle solutions is enough to induce aggregation. This is due to the lowered polarity of the solution reducing V_{elec} [92]. Minimising V_{elec} can also be achieved by displacing the charged surfactant with an alternate capping agent.However, these approaches can result in uncontrolled aggregation, leading to large, clumped aggregates, so care is needed to regulate the reaction.

A good example of this method of nanoparticle aggregation is seen in the aggregates formed by cucurbiturils [CBs]. As CB molecules displace citrate and bind to nanoparticle surfaces, adding the linker molcule to a nanoparticle solution can result in large scale aggregates, and the concentration of CB added defines the behaviour of aggregation. At low concentrations,

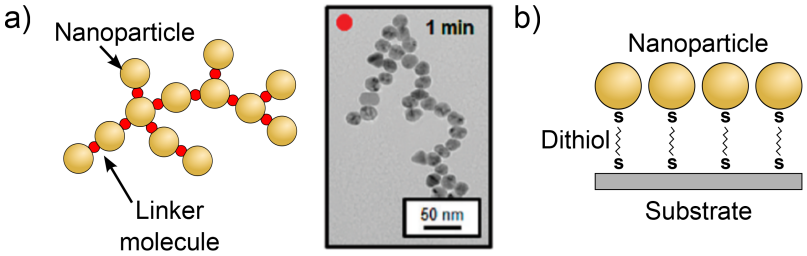

Fig. 3.6 Sketch of self assembly of nanoparticles using linker molecules. a) Binding molecules such as cucurbiturils and dithiols can be used to form large scale fractal aggregates of nanoparticles [28], with SEM of a fractal aggregate made from CB linker molecules. SEM image adapted with permission from reference [28]. Copyright 2011 American Chemical Society. b) Nanoparticles can be adhered to a substrate using a linker molecule, such as a dithiol [93].

the chance of particles successfully binding is lower, limited by particle diffusion through the solution. In this case, particles form dimers that then connect together to form larger fractal chains of particles (figure 3.6a). This is known as diffusion limited colloidal growth. Increasing the concentration of linker molecules raises the rate that particle encounters successfully bind resulting in denser, closely packed three-dimensional aggregates. Furthermore, when enough CB molecules are added, the result is a saturation of the particle surface with little to no aggregation due to the complete coating of the particles [28].

In a similar manner, dithiols can also be used to induce assembly between negatively charged nanoparticles. In a dithiol ligand, positive sulphur bonds are found at either end of a long carbon chain. These can adhere the particles to either each other or alternatively another surface, such as an evaporated gold film (figure 3.6b) [93]. Particles can also be coated with a mixture of polymers that coil up or relax depending upon the surrounding solvent, resulting in pH-tunable interparticle separations [94]. Alternatively, ligands that bind to an intermediary linker molecule can be used to create tunable 2D and 3D networks of nanoparticles [95].

Instead of linker molecules, particles can be coated by a ligand with only 1 binding site [84, 96–99]. In this manner particles are sterically protected. However, by manipulating the chemical interaction between these molecules and their environment, it is possible to induce aggregation. The polarity of the surfactant molecules defines their solubility in different solvents, with hydrophobic and hydrophilic molecules being soluble in non-polar and polar solvents respectively. Particles coated in hydrophobic molecules will aggregate when in polar solvents. This is due to the system minimising the solvation free energy between hydrophobic surfaces and hence reducing the enthalpy of the solution [100]. This dynamic can be taken advantage of for self-assembly. Importantly, as long as the reduction in enthalpy is larger than the drop in entropy of the system, the assembly is spontaneous and therefore produces complex structures [101].

In the instance of Rycenga et al. [102], silver nanocubes of diameter 100nm are selectively coated in different self-assembled monolayers (SAMs) of polymer molecules. Before surface treatment, the particles are freely suspended in solution with a steric protective layer. After drying the nanocubes to a silicon substrate, the particles can be either submersed in a ligand solution, coating five sides simultaneously, or covered by a polymer substrate before submersion, coating four sides. The silicon and polymer substrates act as protective barriers against SAM formation on those faces, allowing for one, two or four faces to be selectively functionalised hydrophobically. When the nanocubes are redispersed in water, the parti-

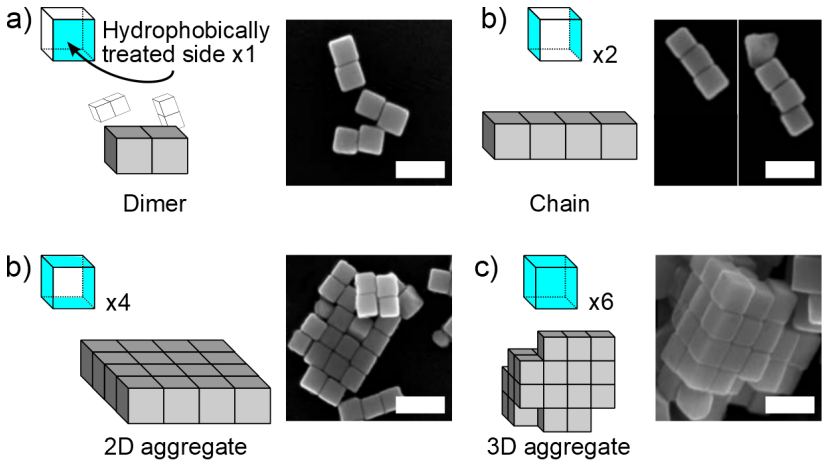

Fig. 3.7 Selectively coating the sides of $D = 100$nm nanocubes with a hydrophobic molecule before suspension in water can induce aggregate formation through the reduction of the interfacial energy between surfaces, resulting in a) dimers with one side coated, b) small (length < 5 particles) chains with two opposing sides coated, c) flat plates with 4 opposing sides coated or d) 3D aggregates with 4 sides coated [102]. Scale bar 200nm. SEM images adapted with permission from [102]. Copyright WILEY-VCH Verlag GmbH & co. KGaA, Weinheim.

cles will self assemble in order to reduce the free energy of the system, with the structures formed reliant on the number of faces coated hydrophobically (figure 3.7). For example, coating one face results in dimers, coating two opposing faces results in small length chains and coating all sides of the cube results in large three dimensional aggregates (figure 3.7d).

To accurately direct the fabrication of dimers, trimers, and more complicated nanoparticle geometries, DNA strands can be used that specifically bind together different particles [103, 104]. By functionalising different nanoparticle batches with different DNA strands that only bind to a specific partner molecule, long-range assemblies of multiple particles can be fabricated (figure 3.8a) [103], as well as smaller ordered aggregates (figure 3.8b) [103, 105]. Similarly single strands of DNA linking two nanoparticles can be folded together by adding in extra stapling sections of RNA, decreasing the interparticle separation in a dimer [106]. This so called DNA origami allows for control over the formation of small aggregates of nanoparticles, the rigid structure originating from the folded DNA chain, defining particle separation of $3-5$nm.

The chemical based methods above are ideal for self-assembling short range nanostructures made up of small numbers of nanoparticles. Controllable separations and geometries are achieved via functionalisation of different surfaces with different molecules. However these

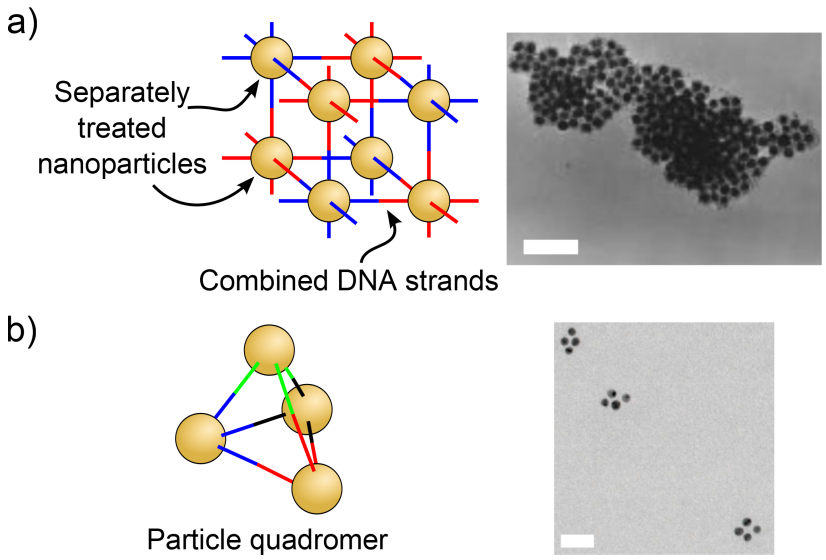

Fig. 3.8 Coating particles with different polymers that selectively bind to each other, such as DNA, can form organised structures such as a) long range particle structures (scale bar 160nm, SEM image adapted with permission from [105], copyright 2009 American Chemical Society) and b) pyramidal quadromers (scale bar 20nm, SEM image adpated with permission from [103], copyright 1998 American Chemical Society).

techniques alone are not always enough make large scale macroscopic structures. For example, in the nanocube chain formation detailed previously, long chains are not observed as forming freely in solution, with most observed being below 4 particles in length. This is attributable to the strength of the force binding the particles being unable to overcome other forces resulting from particle movement in solution. In the case of linker molecule growth, collisions result from the diffusion of particles through the solution, enabling particle binding. This demonstrates the importance of kinetic effects in any self-assembly process.

Kinetic forces have been used to great success in making large-scale self-assembled structures. The typical example is the formation of 3D photonic crystals from latex colloids [107]. Here drying techniques are used to encourage the movement of the particles into a large three dimensional structure. Convective currents and capillary forces direct particles to the same spacial position, where the interactions between them can happen with greater efficiency. The problem with this technique is that it is often reliant on long time scales and becomes less effective as particle size decreases [108]. Nevertheless, the manipulation of kinetic effects is an effective way of driving assembly. One such method, where a kinetic trap is used to spatially restrict particle movement, will now be detailed.

3.2 Interfacial self-assembly

It has been known for over 100 years that colloids are able to stabilize the interface between two immiscible liquids, such as water and an organic non-polar oil [109]. So called Pickering emulsions use the surface tension at the interface to trap objects, reducing the interfacial energy between the two liquids. This kinetic trap enables the formation of large-scale two-dimensional arrays of nanoparticles in time scales of minutes, comparatively fast next to evaporative methods used in the fabrication of both two and three-dimensional colloidal crystal structures. By fabricating these arrays of noble metal nanoparticles, the optical properties due to plasmonic coupling can be studied.

A particle at the interface between two immiscible fluids is subject to a number of different forces. Consider a colloidal sphere trapped at the interface between two liquids (shown in figure 3.9). The interfacial tensions between the particle and the liquids are described by the Young equation [110];

$$\gamma_{po} - \gamma_{pw} = \gamma_{ow} cos\theta_{ow} \tag{3.4}$$

This relates the surface tensions of the particle to water, γ_{pw}, particle to oil, γ_{po}, oil to water, γ_{ow}, and the contact angle between the oil and water, θ_{ow}. Using this equation, the Helmholtz free energy of the system can be calculated [111, 112];

$$\Delta E = -\pi R^2 [\gamma_{ow} - (\gamma_{pw} - \gamma_{po})]^2 / \gamma_{ow} < 0 \tag{3.5}$$

Here ΔE is the free energy change from the particle submerssed in water to being positioned at the interface. The interface acts as a potential well when particles are trapped, due to the reduction of the free energy of the system . As a result it is possible to encourage and control the trapping of particles at an interface by manipulating the respective surface energies of the particle to the solvents. In this manner large 2D arrays of nanoparticles can be made.

Small radii particles are harder to trap at the interface due to the free energy dependence on the square of the radius (equation 3.5). The difficulty in trapping smaller particles can be taken advantage of to facilitate a phase transfer of particles between two different immiscible liquids. Martin et al. demonstrated that small gold nanoparticles of size $\approx$ 4nm can be transferred from water to hexane by changing the functionalisation of the particle surface.

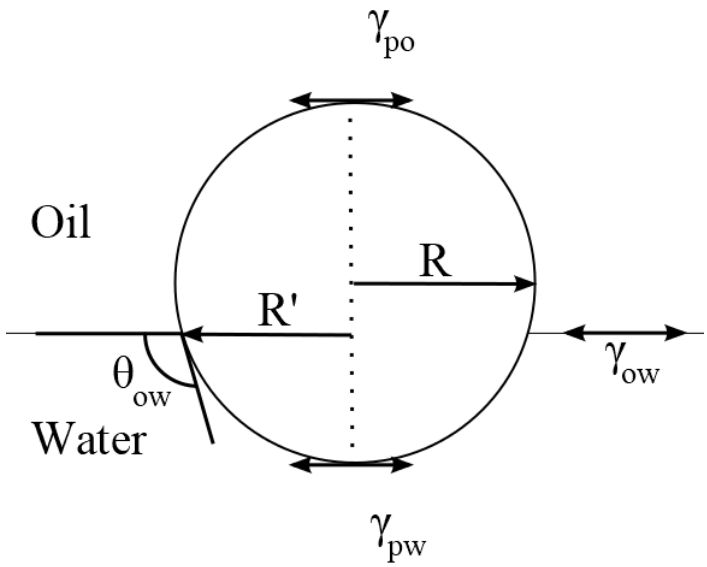

Fig. 3.9 A particle trapped at the interface between two different immiscible liquids. The interfacial tensions of the three surfaces, oil-water, γ_{ow}, particle-oil, γ_{po}, and particle-water, γ_{pw}, are shown along with the contact angle between the oil and water θ_{ow}. The particle radius is R and the effective radius at the interface is R'.

The transfer can be induced simply by shaking the liquids together [84]. A similar method using larger particles of size $>$ 10nm results in them being trapped at the interface [113]. With larger particles on μm length scales, the adhesion to the interface is so large as to be irreversible. This is purely due to the larger particle radius and altering the surface chemistry is not required in order to stabilise the system [114].

The reason for this discrepancy is that the reduction in the Helmholtz free energy is much smaller for small radius nanoparticles and therefore the particles at the interface are much less stable. For example Kutuzov et al. calculated ΔE for CdSe particles at a water/toluene interface as $-3.3k_bT$ and $-13.1k_BT$ for 1 and 3nm radius particles respectively [115]. Because of this radial dependence, particles at this size are much more likely to be displaced from the interface. However, the reduction in ΔE increases as a function of R^2, so by the time the radius is 10nm, $\Delta E = -250k_BT$. Calculated values for this example are shown in figure 3.10 and illustrate the dramatic increase in values of ΔE to many thousand times k_BT for particles where $R >>$ 10nm.

Although the particles can be kinetically trapped at this oil-water interface, they will not in-

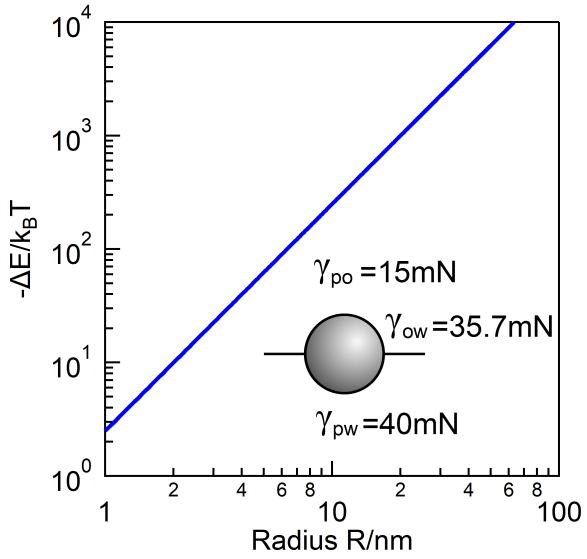

Fig. 3.10 The Helmholtz free energy of a CdSe particle at the interface between water and toluene for increasing particle radius. As the radius increases, the energy reduction increases exponentially until it is many times the value of k_BT at room temperature. The values for the interfacial tension from all surfaces are shown inset and sourced from reference [115].

stantaneously position there. In order to facilitate trapping at the interface, an inducer chemical is used to adjust the values of the particle-liquid surface tensions. This inducer can be a solvent with a lower polarity than the host solution that lowers the surface charge density of the nanoparticle [113]. This effect can be observed in the reduction of the ζ-potential of a nanoparticle solution mixed with such a solvent [112]. The ζ-potential is a measure of the electrical potential of the colloid's EDL, usually observed by measuring the scattering from a solution of particles moving under an alternating potential difference across the solution. Matsui et al. demonstrated this reduction for carbon nanotubes in water with increasing concentrations of ethanol [116]. With decreasing charge density, the particles become soluble in the non-polar solvent and the potential contact angle of particles at the interface increases to 90°[2] (figure 3.11b). With spherical or near spherical nanoparticles, this maximizes the effective radius at the interface, minimising the interfacial energy between the two liquids, trapping the particle [118]. Reinke et al. have observed this effect by altering the pH of an aqueous gold nanoparticle solution underneath a layer of heptane [90]. By reducing the pH from an initial value of 9 to a value of 2 through the addition of HCl the negatively charged stabilising surfactant of the nanoparticles is protonated and this lowering of surface charge again induces assembly at the interface. Importantly, with small diameter particles

[2]This increase in contact angle was observed by Reincke et al. by looking at the contact angle of a water ethanol droplet on a gold film in a solution of heptane [117].

(2 <d< 10), when the pH is raised back to 9 the particles redisperse themselves in the water layer, whilst larger 16nm diameter nanoparticles do not. This again demonstrates the importance of particle size to stability at the interface.

Although the addition of an inducer spontaneously allows nanoparticles to be kinetically arrested at the interface, the resulting structure can be sparsely organised and loosely packed with many holes in the arrays. This arises from remaining charge stabilisation on the particle surfaces preventing close-packing. The introduction of small quantities of the inducer is not enough to aggregate the colloid in the water phase showing that charge stabilization remains effective even though the nanoparticles are trapped at the interface [117]. In order to reduce this repulsion and increase the packing of charged nanoparticles at the interface, an additional molecule can be added to reduce the surface charge of the particles, therefore lowering V_{elec} (figure 3.11c). Alkanethiol chains perform this function well, bonding via a sulphur atom to the surface of gold nanoparticles, displacing the charged surfactant, and

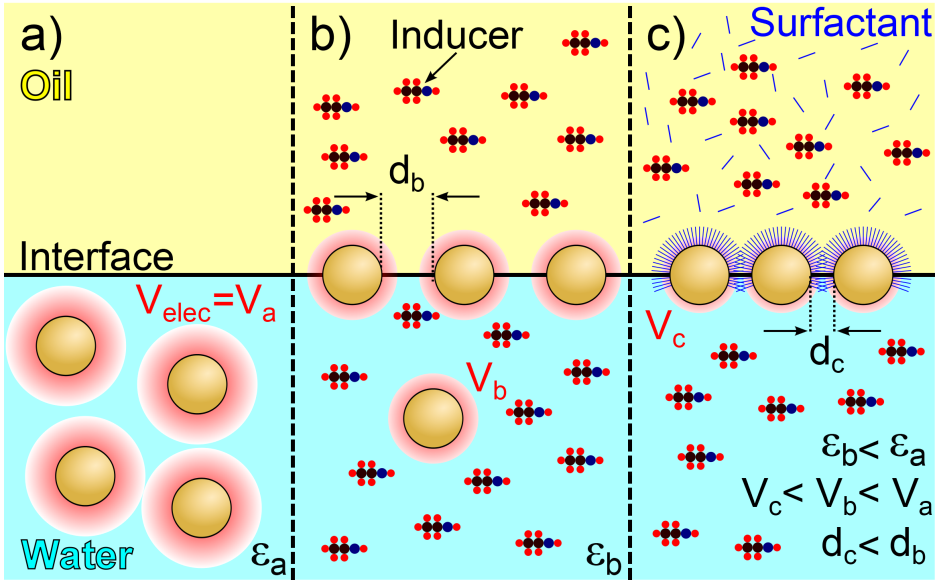

Fig. 3.11 A schematic of the stabilisation and assembly of nanoparticle monolayers at a liquid-liquid interface, based on water and oil. a) Initially two immiscible liquids, one containing nanoparticles that have an electrostatic potential V_a, and a relative permittivity value of ε_a. b) After the addition of an inducer chemical such as ethanol, the relative permittivity of the nanoparticle solution decreases so that $\varepsilon_b < \varepsilon_a$. This lowers the value of V_{elec} to V_b, changing the contact angle between the water, oil and particle closer to 90°, enabling the particle to become trapped at the interface [117]. c) A surfactant ligand, for example an alkanethiol, added to the oil reduces the surface charge of the nanoparticle upon binding, further reducing V_{elec} and decreasing the separation distance, d, between particles [119].

therefore reducing the residual surface charge density allowing aggregation.

The amount of thiol added has a significant effect on the nanoparticle arrays formed. By using different length thiols, interparticle separations can be tuned, though the size of these separations can be affected by different environmental factors. Longer chain thiols have been found to be more rigid, resisting surface pressure to compress assembled arrays in Langmuir-Blodgett monolayers [120]. Chen et al. demonstrated separation distances from 2.2 to 3.4nm using thiols with 12 to 16 carbon links [99]. Interestingly, this distance is around 60% of what would be expected from from two fully solid shells of thiol around the nanoparticle. To explain the discrepancy in the observed particle separation distance, it has been suggested that the thiols interdigitate allowing for closer proximity between particles than would be expected between ligands touching end to end [99, 113] . However Pei et al. point out that the affinity of the thiols to the solvent may result in different behaviour [121]. Arrays of thiolated nanoparticles from two different solvents, toluene and hexane, were found to show different degrees of ordering due to the interaction of the thiol ligands with the solvent. In hexane, the thiol chains deform to reduce contact with the solvent resulting in less ordered nanoparticle arrays. This would also allow for a reduction in the minimum distance between particles.

Ligand functionalisation can define not only how the particles assemble at the interface but also their interactions with each other. Park and Park found that as alkanethiol concentration is increased, multilayered gold nanoparticle films, rather than monolayers, begin to form at the interface [113].

The above factors detailed in this section give a working model to control and manipulate the assembly of 2D particle arrays at liquid-liquid interfaces [122]. It is worth noting that there are many other potential factors that can influence particle absorption to an interface. On a microscopic level, thermal effects, capillary forces, nearest neighbour particle interactions and the depletion of solvent molecules near the interface can reduce the amount of energy needed to release the particle from an interfacial trap [123]. The most significant of these will now be explored, specifically how capillary forces can aid assembly.

3.3 Surface and evaporative techniques

An alternative to inducing assembly at a liquid-liquid interface is to deposit small volumes of nanoparticle solutions onto a surface, either liquid or solid, and allow the solvent to evap-

orate. The forces covered in the previous section still play a role in particle interactions on this surface but additional factors such as lateral pressure and capillary forces can help particles assemble into densely packed arrays. The approach of using a liquid surface to group microscopic objects is hardly new; Irvine Langmuir and Katherine Blodgett developed the technique to fabricate molecular monolayers in the 1930's [124–126]. Originally this approach was used to study oils on a liquid surface and developed into an effective way of fabricating layers of molecules and, more recently, nanoparticles. An advantage of a Langmuir-Blodgett trough is that a lateral compression of the surface can be applied by means of a movable bar that reduces the available surface area. This physically condenses the molecular or particulate layer, increasing the film density and reducing separation distances (figure 3.12).

From original work with very small ($\approx$ 5nm) hydrophobic nanoparticles, the Langmuir-Blodgett approach has been used to try and control the separation and ordering of 2D nanoparticle arrays [127]. As the nanoparticle's solvent evaporates, particles begin to group into small islands. The size of these islands is dependant upon the particle density of the solution. The same hydrophobic forces that drive assembly at liquid-liquid interfaces mentioned above aid in this process, as well as movement in the fluid caused by the solvent evaporating [128]. These islands are then drawn into long range arrays on centimetre length scales. Optical and electrical changes have been observed under this compression as the particles become irreversibly compacted and sinter together [35, 127].

As an alternative to surface compression achieved with a solid bar, it is possible to use a separate liquid added to the surface to reduce the area available to the particles. By careful selection of ligands and solvents to take advantage of particle miscibility, it is possible to compress nanoparticles on a surface using only this method (figure 3.12) [129]. As discussed previously, controlling surface tension can help to induce nanoparticle self-assembly at an interface. These same forces are applied here to allow for the movement and compression of nanoparticles trapped between a three phase system consisting of two immiscable liquids and air. A gradient in the surface tension between the fluids forces the nanoparticles together, being surrounded on the first liquid surface by the second fluid.

It is worth noting at this point that even before a compressive force is added, nanoparticles begin to show filament-like structures at the interface. Sashuk et al. noted this, viewing that upon induced compression from adding tetrahydrofuran (THF), the separation between these closely grouped nanoparticles (measured via X-ray scattering patterns) does not significantly change. In this case, the packing of nanoparticles is increased, resulting in a

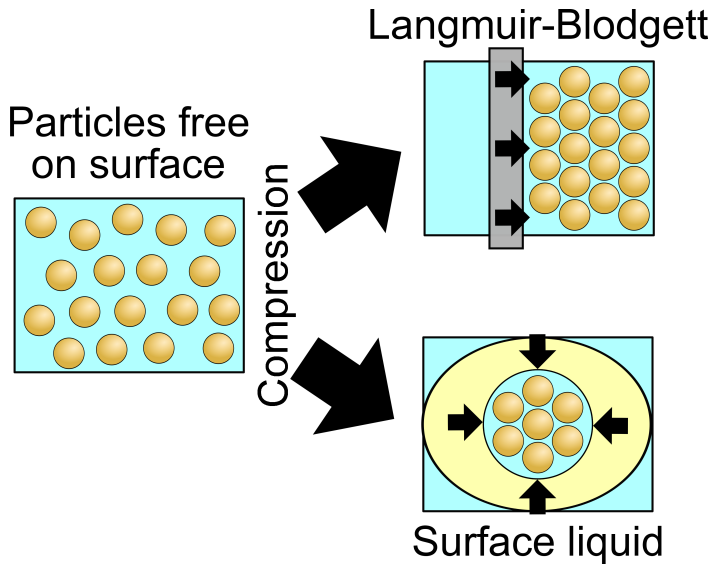

Fig. 3.12 Nanoparticles can be compacted together on a liquid surface in order to instigate large-area formation of particle monolayers. This can be achieved using a moving bar to reduce the available surface area to the particles, such as in a Langmuir-Blodgett trough, or alternatively by adding an immiscible liquid as a supernatant to surround and compress the particles.

densely packed array forming, rather than particle separations decreasing. Reversibility was also observed, with nanoparticles separating back to smaller clusters upon the removal of the THF [129]. This demonstrates the advantage of using long chain ligands on the nanoparticle surface to prevent irreversible aggregation.

The spontaneous aggregation of particles on liquid surfaces discussed above is caused by convective flows within the solution. The movement of particles within drying liquids can be utilised as a driving force for self-assembly. This method is widely used with larger, micro-sized particles, such as polystyrene [130] and latex [131] as well as with smaller nano-sized particles [132]. As solvents evaporate into an atmosphere, movement of molecules in the fluid develops, pulling particles to the solvent surface. Particles at this surface become trapped and, if they encounter any other particles, attractive forces between them will allow for aggregation (figure 3.13a).

This aggregation is aided as the solvent layer's thickness decreases to equal the diameter of a particle. At this point capillary forces can begin to act in the interparticle gaps and surface tension can drag particles together (figure 3.13b). This movement is independent of whether the evaporating solvent is sitting on a solid or liquid surface [128]. However, the magnitude of these capillary forces is significantly different depending upon the surface.

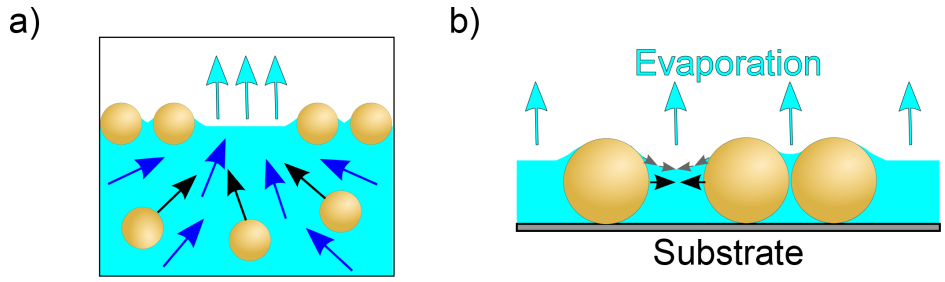

Fig. 3.13 a) Particles are drawn to a liquid surface via convective flow. As the solvent evaporates (light blue arrows) the solution will move to surface (dark blue) and draw particles with them. Particles then get trapped due to the surface tension at the liquid surface. b) As the solvent evaporates between adjacent particles, the meniscus that forms between them causes an attractive force that pulls particles together.

For latex particles on liquid surfaces with diameters $< 10\mu$m, the energy produced from capillary forces is less than k_BT so DVLO forces will dominate their interactions. On a solid surface, these forces remain orders of magnitude above k_BT even for particles with sizes on the order of 10's of nanometers.

The greater significance of capillary forces on particles resting on a solid surface comes from the constant contact angle made between the particle and the liquid. When particles are resting on a solid substrate, the deformation of the liquid surface due to the constant particle-liquid contact angle produces a significant attractive lateral capillary force that can drag particles together [131]. Conversely, particles at a liquid surface will produce minimal distortion to the interface, as particles will float with the particle-liquid contact angle aligned along the interface, unless the particle is acted on by an external force (such as gravity).

Combining the above techniques enables multiple avenues for the control of the formation of nanoparticle arrays. Santhanam et al. used a teflon ring to contain a solution of gold nanoparticles dispersed in a 50/50 mixture of hexane and dichloromethane [133]. The shape of the water interface is controlled by adjusting the water level within the hexane ring, allowing the capillary forces at the interface to be tuned. A slightly convex shape was found to encourage the aggregation of the particles. Upon evaporation of the solvent, the array can be picked up from the surface (see next section). An alternative to this method is to place droplets of nanoparticle solutions onto droplets of other solvents and let them both evaporate. Martin et al. demonstrated that by placing a droplet of nanoparticles dispersed in hexane onto a droplet of toluene, large area particle arrays form. The smaller quantity of hexane evaporates faster than the toluene leaving the array of nanoparticles on the surface of the toluene droplet. As the toluene evaporates the film is deposited onto the solid substrate

underneath [84].

A final assembly method to consider is direct assembly onto a substrate. Instead of assembling in solution, or at a liquid/liquid or liquid/air interface, drying down solutions of nanoparticles on a substrate results in their deposition. Particles are drawn via convective movement towards the drying line of the droplet, and are packed closer together resulting in array deposition at the moving interface as the solvent evaporates [131]. These structures exhibit varying nanoparticle densities due to deposition at different concentrations, resulting in so-called coffee ring structures (figure 3.14) [134–136]. The density and formation of these coffee rings can be tuned by adding additional solvents to the mix to change the viscosity and evaporation rate [137]. Additionally, repeat depositions of particle solution can result in extra layers of particles assembling on top of pre-existing layers [138].

Inside these rings small clusters of nanoparticles form. By reducing the concentration of the initial solution, the density of particles drawn to the drying line can be reduced, resulting in localised cluster formation that can be selectively observed in order to study the behaviour of small numbers of nanoparticles, such as dimers or trimers [31, 139]. Additionally, drying particle solutions onto prefabricated patterned templates, such as arrays of nanorod dimers [140] or discs [141], can force large scale regular arrays of a desired structure, albeit with an added lithographic step.

By manipulating the drying of solvents, nanoparticle arrays can be assembled on both liquid and solid surfaces. These methods display a wide range of versatility in fabricating diverse

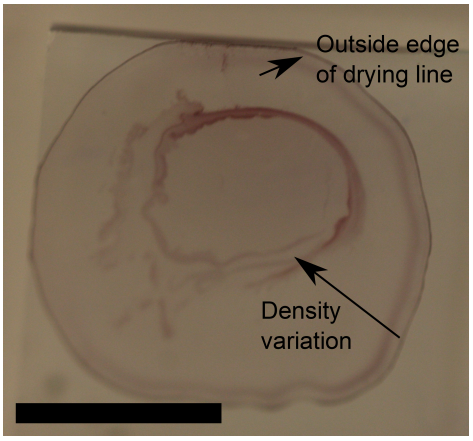

Fig. 3.14 An image of a coffee ring structure made by drying down a solution of 20nm Au nanoparticles on a hydrophobic polymer substrate. From the outside of the deposit a varying particle density is seen across the substrate to a second drying line. Scale bar approx 100mm.

structures. One advantage of these methods, as opposed to fabrication at liquid-liquid surfaces, is that these drying methods often directly assemble structures onto substrates. In the case where arrays are made on a liquid surface it becomes necessary to transfer them onto a substrate in order to investigate their properties.

3.4 Transferring assemblies to substrates

The capillary and convection forces that aid in evaporative deposition can also help to self-assemble nanoparticles directly onto vertical substrates. This technique has long been used in Langmuir-Blodgett troughs to form molecular monolayers on substrates. A hydrophilically functionalised substrate creates capillary forces that generate a convective flow similar to the movement of liquid to the contact point on a horizontal substrate (figure 3.15a). Again particles are drawn to this line and deposited. Unlike drop casting solutions onto horizontal substrates, which cause coffee ring patterns, it is easier to deposit a large area of evenly packed nanoparticles as the substrate can be withdrawn gradually, typically at a rate on the order of 10's of mm per minute [142, 143], to ensure close packing and an even distribution of particles. Additionally this method can be repeated to make multilayer nanoparticle films [142].

Alternatively, self-assembled nanoparticle arrays at liquid interfaces can be removed directly

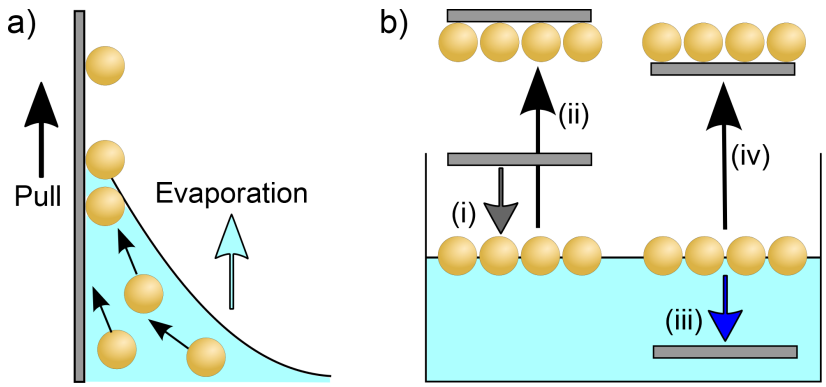

Fig. 3.15 Different methods for transferring particles onto substrates. a) As a nanoparticle solution evaporates, the meniscus of the solvent on a vertical substrate can, via convection, move the particles towards the interface where they are deposited [143]. b) Particle arrays can be directly picked up from a liquid surface either by (i) contact printing from above, touching the surface and (ii) lifting the array, (iii) removing the liquid from the solution until the mat makes contact with a sub-surface substrate or (iv) lifting the substrate from below the surface [113].

from the surface. Depending upon the functionalisation on both the nanoparticles and the substrate, arrays can be lifted up from the surface using horizontally orientated substrates (the Langmuir-Schaefer technique, figure 3.15b) [143]. Typically, hydrophobic substrates enable particle removal from water surfaces, allowing adhesion to the nanoparticle assembly whilst repelling the solvent.

Arrays of nanoparticles can also be picked up from below the surface by raising a substrate to the interface or lowering the surface to a substrate by pumping out the solution [113]. Horizontal substrates brought to the surface allow for a direct pick up of the array, potentially removing any disruption due to capillary forces found for vertically orientated substrates. It is possible to add additional patterning to a film picked up in this way by using a patterned substrate. By imprinting a grating structure onto an elastomeric substrate, a grating structure can be directed onto a nanoparticle array [78].

3.5 Summary

There are many different techniques to enable and control the self-assembly of differing density nanoparticle films. Of particular relevance to this thesis is the advantage of manipulating enthalpy to minimise the interfacial energy between two different liquids, creating a potential trap for nanoparticles which subsequently forces them together, enabling large scale arrays of particles to be fabricated. Also important is the reliance on nanoparticle size in these processes. The reduction of the interfacial energy due to interfacial particle trapping scales as R^2, therefore larger particles reduce the interfacial energy by a much greater degree than smaller particles. Other factors, such as convective flow and capillary forces can also be used in order to self-assemble large scale materials made of nanoscopic components. Using these techniques, large scale plasmonic nanoparticle arrays can be assembled and their optical properties analysed. In the following chapter, different experimental apparatus to explore these optical properties will be detailed.

Chapter 4

Apparatus and Experimental Methods

This chapter will review the apparatus used for the following experimental work. The bulk of experimentation is carried out on modified Olympus BX51 microscopes that are set up to allow for bright field reflection, dark field scattering and transmission measurements. Stretch measurements were performed on specially modified stretch rigs that allow for applied uniaxial and biaxial strain. The Renishaw Raman microscope system is detailed, covering how Raman measurements were taken. Finally, the methods used for the theoretical calculations carried out to compliment the experimental results will be reviewed.

4.1 Microscopy

The primary tool used for the categorisation of the self-assembled nanostructures featured in this thesis is a modular Olympus BX51 confocal microscope. The design of the BX51 enables multiple ports to be added to the microscope for different inputs and outputs, as well as the addition of more complicated optical components such as liquid crystal filters or a Bertrand lens. An optical diagram of the set up is shown in figure 4.1, and a detailed schematic of the objective lenses for bright and dark field measurements are shown in figure 4.2. The light source used was a standard halogen Olympus microscope bulb with a broad emission spectrum from visible light into the infrared.

Alternative light sources, specifically LED lamps, were explored, but were dismissed due to a narrower emission spectrum. However, these LED lamps [1] were used to align the focal

[1] Two different LED light sources were used, one from ocean optics and one custom designed in house by the technician Anthony Bartlett

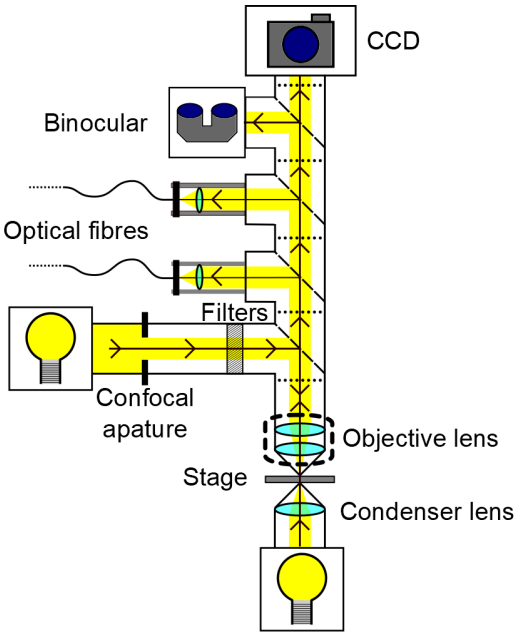

Fig. 4.1 A schematic of the BX51 microscope used for taking reflection, scattering and transmission measurements. For reflection and scattering, light from the light source is collimated through the apature stop before encountering a beam splitter (diagonal dashed lines), sending it into the objective lens and then returns from the sample to the fibre ports, camera and view port. For transmission measurements, the light source from the bottom of the microscope passes through a condenser lens onto the sample, before following the same path as before. The filter port is used to place polarisers into the beam path. The dotted lines show the modular breaks in the microscope system, allowing for components to be removed or added as desired.

point for the spectrometers by shining them through a 50μm optical fibre to a silver mirror on the microscope stage. Alignment was carried out to maximise the signal and prevent chromatic aberration. All of these outputs run through beam splitters in modules on the microscope stack, with switches that allow for active port selection, preventing unnecessary losses in light intensity through the microscope. Optical images were taken using a Luminara Infinity 2 CCD camera mounted onto the top of the stack. The beam splitters in the stack make it possible to take optical images and record spectra simultaneously. A motorised and computer controlled stage, a Prior H101A, was used to move the samples with sub μm accuracy.

The versatility of the microscope comes from the switchable objective lenses (figure 4.2) that can be selected for specific measurements. Olympus objectives ranging from 5x to 100x magnification were used. These objectives have a high numeric aperture of 0.8, therefore a large collection angle, enabling a dark field block to be placed in front of the objective

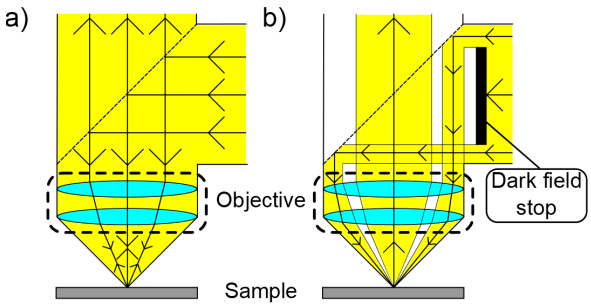

Fig. 4.2 The configuration of the objective lens can alter how light is collected and therefore the optical measurement. a) In the regular configuration the objective collects light returning from the sample. b) With the dark field stop over the centre of the light source only the edge of the objective is used. This results in the incident light reaching the sample at a high angle of incidence. In this manner scattered light is collected.

to prevent light at low incident angles from illuminating the film, allowing the collection of high-angle scattered light from the sample (figure 4.2b). Without the dark field block, the objective functions as a traditional microscope lens and collects reflected light. For transmission measurements, a second halogen bulb illuminates the sample from below. A condenser lens is used to match the numerical aperture of the objective in order to keep the illumination of the sample consistent across both reflection and transmission measurements.

The two fibre ports on the microscope allow for simultaneous measurement of the spectrum by two different spectrometers of different wavelength ranges. Alternatively, the secondary port can act as a second input for an alternative light source or laser. In this work, the primary spectrometer used was an Ocean Optics QE65000. For IR measurements, an Ocean Optics Red Tide IR spectrometer was used.

Light is collected via the couping of the spectrometers to different optical fibres that are cage mounted onto the microscope, typically a 50μm diameter core fibre. Cage mounting this fibre to the microscope enables the fibre apature to be easily translated to the focal position of a lens within the cage mount, enabling the maximum light intensity to be collected for analysis. The light into the fibre corresponds to a circular collection spot on the sample, with the collimated beam path travelling through the microscope optics from the sample to the fibre. The size of this collection spot varies depending upon both the fibre diameter and the magnification of the objective lens used for the experiments, from a 6μm diameter for a 20x objective, to a 1μm diameter for 100x for a 50μm diameter fibre. The integration times used to collect light can be varied, and required times are heavily dependant on the magnification of the microscope objectives. For smaller magnifications, such as 20x, integration times can

be close to their minimum value of 3ms, but for dark field measurements it is necessary to use times on the order of seconds, to get a signal intensity sufficiently above the background noise.

To normalise optical measurements, spectra from the light source were measured before every experiment. A Thor Labs PO1 silver mirror was used as the reflection normal standard, whilst an opaque diffuser disc, with an even and broad scattering spectrum, was used to define a maximum scattering values to normalise scattering measurements. Transmission measurements were normalised by shining light through either an area of the substrate that is clear of any of our self-assembled structures, or from a similar clean substrate. Measurements were collected and processed using in-house software that runs in Wavemetrics Igor Pro.

The BX51 microscope is a versatile tool for optical investigation. It enables the probing of many different aspects of an optically interesting material in one piece of equipment. In addition to the customisation offered by the microscope stack, it is possible to mount additional equipment onto the stage to enable different manipulations of the sample being investigated. Modifications for dynamic strain-sensitive measurements will now be detailed.

4.2 Stretch rigs

The Prior stage on the BX51 microscope can be used as a mount for other equipment. In order to stretch the elastic materials in this work, multiple different stretch rigs were designed, built and fitted on the Prior stage to manipulate the samples at the collection plane of the microscope. Depending on the desired manipulation of the elastomer, it was necessary to use different mechanisms.

To create a biaxial strain of elastomeric films, it is important to hold each side of the substrate and stretch it apart equally. Manipulating the film in this manner keeps the centre of the film in the same location, enabling the examination of a central spot with minimal repositioning of the film required to ensure the area under investigation remains in the microscope collection spot. There are two ways of ensuring this even application of strain; a square elastic substrate can be held on each side and be pulled apart equally from all directions, or the substrate can be clamped down and manipulated by either a downwards or upwards force. In the former method, a clamp can be used to hold the film on each side [144, 145]. The latter can be performed by placing the film over a chamber that uses changes of air

pressure to manipulate an elastic film [146].

In the following experiments, both of the above approaches were used to stretch elastomer films. Initially, a biaxial strain was achieved using a mechanism to lower a substrate down onto a hemispherical lens. This uniformly deforms the substrate to allow even stretching in every direction (figure 4.3a). Lubrication on the surface of the lens was achieved by placing an index matching oil, matched to the refractive index of the lens, on the lens' surface. This system allowed for biaxial strain even with thick (<1mm) films. However the equipment was bulky, and the mechanism used to lower the clamped film required careful management to ensure that all sides were equally lowered.

A second stretch rig, illustrated in figure 4.3b, was constructed to be lighter and easier to use from four-jaw geared scroll chuck. This mechanism allowed for the film to be stretched whilst keeping the film flat, minimising reflective losses seen in the lens method due to the curved surface of the lens.

The downside to the chuck method is that the strain does not stay even across the film, with only the central region of the substrate strained in a biaxial fashion. When stretching films in this way, extra care must be taken prevent the elastomer from tearing under the applied strain. In the following experiments, square films were fixed at their corners, instead of at the centre of their sides, to minimise the issues caused by enhanced strain at the corners of the clamps exceeding the possible strain of the material.

In comparison to biaxial strain, one-dimensional strain is trivial to accomplish (figure 4.3c). Clamping two opposing sides into two movable jaws allows for a uniaxial strain to be applied to the film. Uniaxial strain was applied using either two opposing clamps in the four-

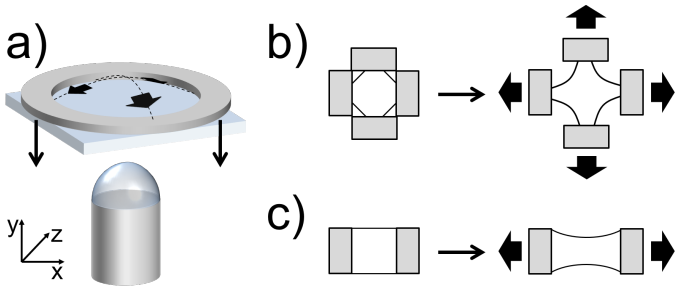

Fig. 4.3 Biaxial strain can be applied to elastic films by a) lowering a film onto a hemispherical lens to stretch the surface along the x and z axes by applying pressure to the y axis or b) by clamping each edge and stretching evenly perpendicular directions. c) Uniaxial strain is achieved by clamping to opposite sides and stretching

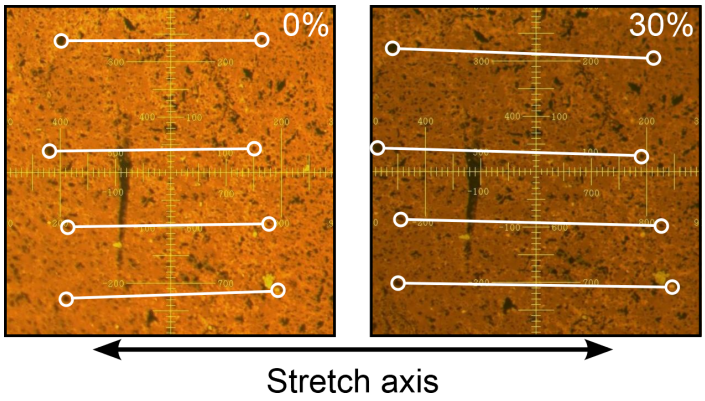

Fig. 4.4 By tracking the movements of defects, it is possible to measure the local strain applied to a material. In this 1D example, the amount of strain is observed from 0% to 30% by measuring the increase in the distance between these defects.

jaw chuck rig, or alternatively a motorised stage with the same configuration that could stretch the film via computer control within Igor Pro.

An issue observed during stretch measurements was the gradual slipping of the film from the clamps as strain increased. This was attributed to a thinning of the film due to Poisson contraction. In order to counter this issue, the clamps were tightened as strain was applied, ensuring a continuous clamping force on the film. A torque driver was used to precisely adjust the screws whilst maintaining an even force across the clamps.

Applied strain was calculated by tracking the movement of defects on the films under strain (figure 4.4). By using optical images to measure the distance between multiple defects, an average value of the local strain of the film was calculated [144]. These measurements were found to be within a few percent of the macroscopic Cauchy strain values. The lack of divergence is attributed to measurements being taken at the centre of the material. However, in order to give the most accurate value for the strain applied for any given measurement in this work, local defect calculated strain values were used.

By fitting compact stretch rigs onto the Prior stage of a BX51 microscope, strain can be applied to samples alongside simultaneous optical measurements. These stretch rigs were designed to fit on other microscope stages, so strain measurements could be made on other pieces of equipment. One such set-up is detailed in the next section: the Raman microscope used to take SERS spectra.

4.3 Raman microscopy

Raman spectra of our samples were taken using a Renishaw InVia microscope dedicated to Raman spectroscopy. The microscope is connected to three different lasers with emission wavelengths 532nm, 633nm and 785nm, allowing for probing samples at different excitation wavelengths. The system is automated and self contained, allowing for experimentation to be run primarily using computer control.

A schematic of the Raman microscope is illustrated in figure 4.5. The selected laser enters the main body of the microscope and passes through a neutral density filter that selectively attenuates incident laser power. The beam is then directed to the sample through a 50x objective before returning to the microscope. An optical filter removes the laser light from the beam path, and the remaining scattered light is split using a diffraction grating and directed to a CCD, where it is collected for analysis. A separate white light source is used to illuminate the sample, and a CCD camera is also fitted to take photographic images of a sample.

Through automation, the microscope is capable of self-alignment to maximise the scattering signals received by the microscope. Time-resolved spectra can be taken to monitor spectral changes over time. Numerous stops are also automated and closed to protect the eyepiece and camera from incident laser light.

The Renishaw Raman InVia is an easy to use and versatile microscope that enables the

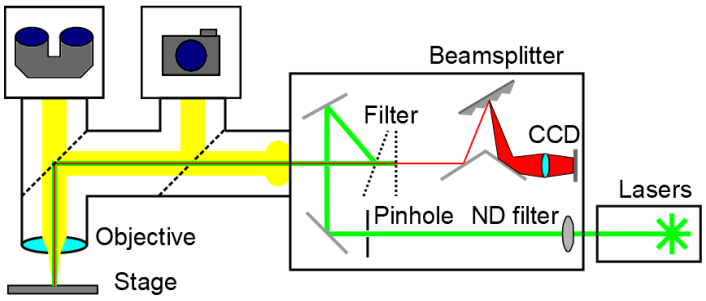

Fig. 4.5 A simplified schematic of a Renishaw Raman InVia microscope. The selected laser is directed into the device where it passes through a neutral density filter and a pinhole before being being reflected onto the sample. The inelastically scattered Raman photons and the reflected laser light are passed back through the system, where a filter removed the laser light and a diffraction grating splits up the Raman photons to be incident on a CCD for collection. A binocular viewport and a CCD camera are attached for viewing the sample, with illumination from a white light source.

taking of Raman spectra. As the stretch rigs used above can be mounted onto the microscope in the same manner as the BX51 microscope, stretch measurements can be carried out. This allowed us to investigate the stretch tunable Raman response from nanoparticle arrays.

4.4 Numerical calculations

In order to accurately model the plasmonic behaviour of the systems in this work, it was necessary to use numerical calculations that could compute the spectral changes of the system over time. Numerical methods were employed to model the systems studied and allow comparisons with experimentally observed behaviour.

Two different programme suites were used in this course of this work. The first was BEMAX, which carries out boundary element method (BEM) calculations for nanoparticle chains, developed and extensively tested by collaborators from the the theory of nanophotonics group at the Donista International Physics Center. The boundary element method is a frequency domain approach that returns solutions to Maxwell's equations across any structure at specific boundaries, rather than calculate solutions across its bulk volume. Specifically, a mesh is constructed over the modelled structure that acts as the boundary at which different boundary conditions can be fitted to solve integral forms of Maxwell's equations, without calculating values across the entirety of the structure. This treatment can give an approximate model of the optical behaviour of a structure.

BEMAX was used to model chains of nanoparticles, rather than large scale arrays, to simplify the required calculations. Although the optical response of 2D arrays of nanoparticles is much more complicated than that of a chain, previous theoretical work on nanoparticle aggregates formed using the CB glue suggest that a chain model is a good approximation [30]. It is important to note that beyond a certain length the chain mode no longer red shifts. This limit is observed for 20nm Au particles to be $N = 18$. This saturation leads to simplification of the model - calculations need only be performed on a saturated chain of particles. The author thanks Dr Fumin Huang who carried out these calculations with myself.

The second program utilised in this work is the Lumerical calculation suite. Lumerical performs finite difference time domain (FDTD) calculations of the strength and direction of the electric and magnetic fields at discrete points, set by a three-dimensional grid across a structure. In this manner the electromagnetic behaviour over the entirety of the structure can be calculated for any given frequency and point in time. The advantage of FDTD compared

to the BEMAX simulations is that it allows for more complex and complete structures to be modelled, with the sacrifice of requiring much more computing power. The author thanks Dr Lars Herrmann for aiding with these calculations.

These methods of simulation allow for the calculation of spectra to complement the experimental work detailed below. They are used to contextualise the experimental results, allowing an understanding of the behaviours observed.

4.5 Summary

Microscopy is the primary tool for the investigation of the different plasmonic materials fabricated in this work. Bright and dark field microscopy techniques enable the fast optical analysis of many samples. The modularity of the BX51 microscope allows for the customisation of measurement techniques used, such as simultaneous detection from multiple spectrometers or the fitting of a stretch rig to enable strain measurements, seen in Chapters 6 and 7. The Renishaw InVia microscope enables the use of Raman spectroscopy to study SERS spectra from self-assembled nanoparticle mats to see how applied strain affects the observed signal strength. These measurements are detailed in Chapter 8.

With the detailing of these tools and experimental methods complete, the review of the experimental work can begin.

Chapter 5

Self-Assembly of Closely-Packed Nanoparticle Arrays

In this chapter the self-assembly of closely-packed plasmonic nanoparticle arrays will be discussed. First, the synthesis of gold nanoparticles using a citrate reduction method will be explained. From here methodologies for the fabrication of closely-packed nanoparticle arrays will be detailed, with particular focus on interfacial assembly methods to fabricate gold nanoparticle mats at liquid-liquid interfaces.

5.1 Gold Nanoparticle Synthesis

The nanoparticles used in this work came from two different sources. Primarily used were commercially sourced particles, synthesised by British Biocell International. To complement these, lab synthesised particles were used. Both sets have different advantages. Commercial particles are well characterised and documented with small size variations. However, due to their unknown fabrication methodology, the particle solutions contain chemicals, such as additional stabilizing agents, that introduce random factors in any assembly process. Particles made in the lab may not exhibit as monodisperse a size distribution as the commercial ones but give the benefit of full knowledge of their chemical make-up. In practise, little difference has been observed in mat assembly when using either set of particles. This is likely due to any extra surfactants in industrial solutions not interfering with the assembly methods used.

Gold nanoparticles were synthesised using a citrate growth method, based upon the standard

method described by Turkevich et al. [147]. Many variations of this method exist across literature sources but the basic principle behind the fabrication of particles remains the same. Initially, 2ml of a 10mM solution of chloroauric acid (HAuCl4) was added to deionised water. This was then heated in a round bottomed flask within an oil bath at 130°C and mixed using a magnetic stirrer bar. These measures acted to mix the solution, as well as ensured a consistent environment for the formation of particles throughout the solution. When the solution was boiling vigorously, an amount of sodium citrate was added to the solution via pipette. The solution instantly changed colour from pale yellow to black. After continued stirring for 10 minutes, the solution became a deep red colour and was left to cool and sit for a day before the particles were ready for experimentation.

The added sodium citrate acts as a reducing agent, donating an electron to the gold atoms and allowing crystals to form. The important factor in size control is the ratio of sodium citrate to chloroauric acid. Citrate molecules coat the nanoparticle after its formation, preventing aggregation of nanoparticles due to their negative charge and the subsequent formation of an electrical double layer. A higher concentration of sodium citrate in the solution results in smaller nanoparticles, while lower citrate concentrations result in larger nanoparticles. The weight to weight ratio of gold acid to sodium citrate relates linearly to nanoparticle diameter, due to volume and surface area being directly correlated to the number of gold atoms and citrate molecules respectively (figure 5.1).

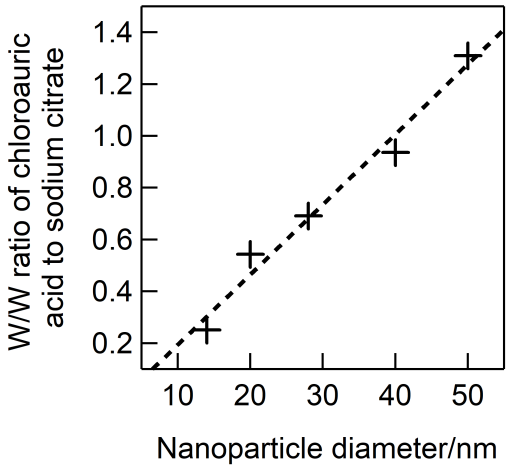

Fig. 5.1 Weight to weight ratio of chloroauric acid to sodium citrate for the formation of increasing diameter spherical nanoparticles. A linear fit is shown due to the correspondence between the number of gold atoms making up the volume of the particle and the number of citrate molecules coating the surface.

Particle sizes of the 20nm gold particles were measured using a scanning electron microscope (SEM) and were found to be within a few nanometers of expected values with a size variation of $\pm$3nm.

5.2 Interfacial assembly of closely-packed nanoparticle monolayers

As detailed in Chapter 3, closely-packed monolayers of nanoparticles with separations on the order of nanometers can be fabricated by trapping nanoparticles at the interface of two liquids. This section will overview such an assembly process, detailing how different variables affect fabrication, before ending with specific assembly instructions with exact quantities of materials used to enable replication.

Initial fabrication of nanoparticle monolayers was guided by the work of Martin et al. [84]. In Martin's method a citrate coated gold nanoparticle-water solution is mixed with acetone in a glass vial. A suspension of dodecanethiol (DDT) in hexane is added and sits above the water phase. The vial is then shaken, forcing the two liquids to mix and allowing the DDT to bind to the particle surface.

This method was used initially to move small ($<$ 5nm) gold nanoparticles from the aqueous solution into the organic hexane. However, when replicated using larger nanoparticles the transfer failed. This is due to the size dependence of the reduction of interfacial energy at the liquid-liquid interface. For nanoparticles with diameters $>$ 10nm, this reduction of the interfacial energy resulted in particles becoming trapped and subsequently rafting together at

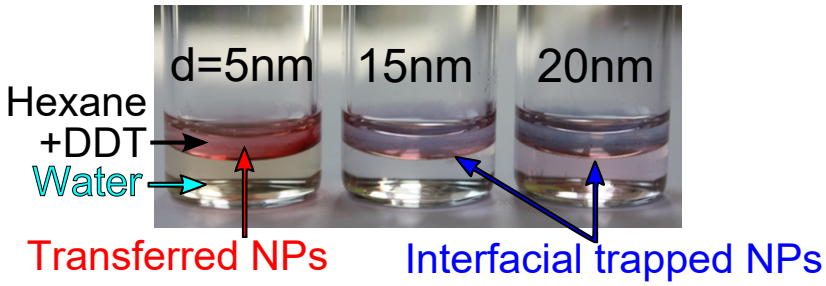

Fig. 5.2 Photo showing the size dependent transfer of gold nanoparticles from aqueous to organic solvents. The smaller 5nm diameter nanoparticles are completely transferred from water into hexane, indicated by the red colouration of the upper liquid. As diameter size increases particles get trapped at the interface forming large arrays of particles, shown by the slight golden sheen and blue transmission around the interface when d= 15 and 20nm.

the liquid-liquid interface. This effect is shown photographically in figure 5.2, with smaller 5nm particles clearly transferred into the hexane layer, as seen by the distinct red colouring of the upper liquid. The 15 and 20nm diameter particles did not transfer to the hexane, instead showing a distinct blue colouring at the interface due to transmitted light passing through the aggregated nanoparticles.

Initially, a transfer method modelled on the one used by Martin was used to remove these nanoparticle arrays and deposit them on substrates for analysis. For smaller 5nm particles, a volume of transferred particles was taken via a pipette and deposited onto a droplet of toluene (figure 5.3), with a volume ratio of toluene to hexane-nanoparticle solution of 3 : 1. As hexane is more volatile and the extracted volume has a smaller volume than the toluene droplet, it evaporates rapidly, depositing particles onto the surface of the toluene droplet. The drying of both the hexane and toluene acts to compress the nanoparticles into a dense mat before they are deposited onto the polyethylene terephthalate (PET) substrate. The process results in a dense area of particles as well as a notable coffee ring pattern towards the edge of the original toluene droplet (figure 5.3e). This is attributed to particles deposited from the hexane solution directly onto the substrate instead of the toluene.

As the larger diameter particles do not transfer fully to the hexane, they have to be withdrawn from the water-hexane interface. This results in the withdrawal of a volume of water as well as hexane (figure 5.4a)[148]. After withdrawal and deposition onto the toluene the

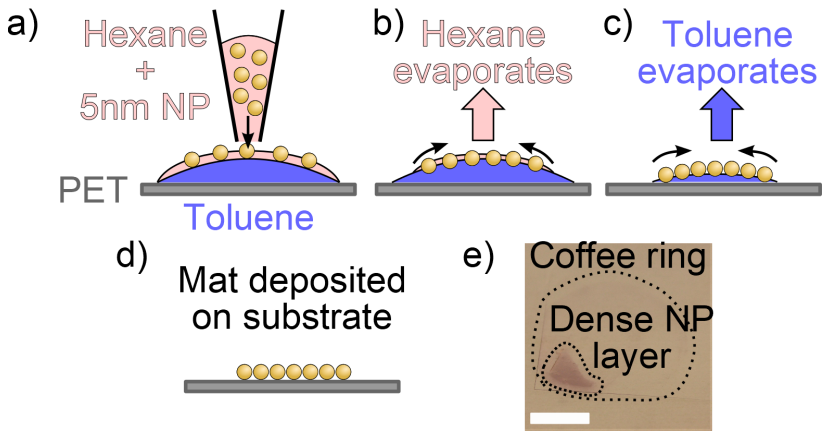

Fig. 5.3 The assembly of 5nm gold nanoparticles on an evaporating droplet. a) Nanoparticles transferred from water to hexane by a thiol coating are deposited dropwise onto a droplet of toluene. b) As the hexane solvent evaporates the particles are packed together and left on the toluene surface which then c) evaporates, until d) the condensed particle mat is deposited onto the PET substrate. e) A photograph of a deposited 5nm mat showing a faint coffee ring pattern and a dense compact layer of particles. Scale bar $\approx$ 5mm.

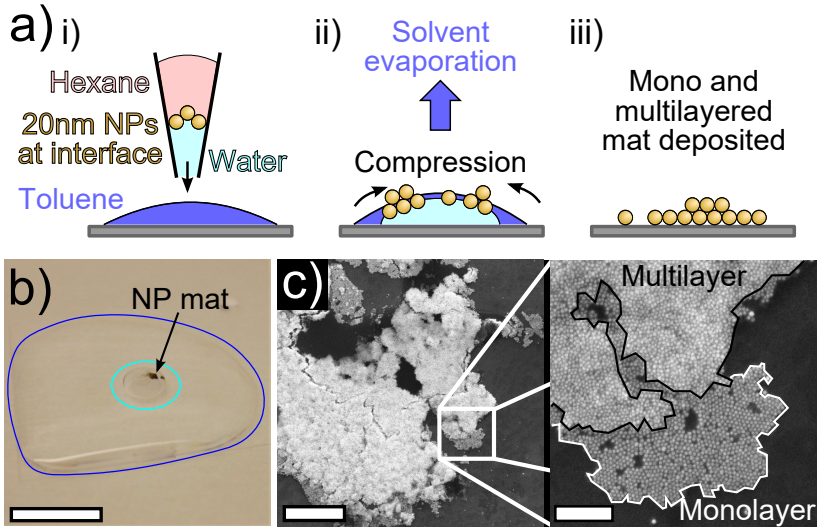

Fig. 5.4 a) The assembly of $>$ 15nm diameter nanoparticles using the droplet assembly method. i) The nanoparticles are withdrawn from the water-hexane interface, along with a quantity of both solvents, via pipette. This solution is then deposited onto a droplet of toluene. ii) The aggregates at the interface further aggregate into larger areas, due to the convection formed by the evaporating solvents until iii) they are deposited onto the substrate. b) A photograph of the mat assembly. The dark blue line highlights the toluene layer and the light blue the water droplet. The nanoparticle mat is forming on the water droplet. Scale bar $\approx$ 5mm. c) SEM images of multilayered nanoparticle mats made using the droplet assembly method. In the second image, the black line borders multilayered nanoparticles and the white indicates a monolayered area. Scale bars are 2μm and 300nm respectively.

nanoparticles remain at the water interface. Large chunks with gold colouring are observed moving on the droplet surface, suggesting that aggregates formed at the water-hexane interface have retained some structural coherence during the transfer process. This is shown in figure 5.4b, where the nanoparticle mat can be clearly seen on the water droplet. In order to investigate the structure of these aggregates the assembly process was performed on highly ordered pyrolitic graphite (HOPG) as a conductive substrate for SEM imaging. The nanoparticle arrays observed were multilayered and porous (figure 5.4c); this structuring was attributed to the particle aggregates settling on top of one another during the aggressive processes of extraction from the interface. This flaw prevents the fabrication of large scale uniform nanoparticle monolayers using this assembly process.

5.2.1 Direct assembly at a water-hexane interface

In order to avoid multilayered mats, alternative methods of transfer were explored, where the particles were picked up directly from the interface. Similar to microcontact printing and

the Langmuir-Scheaffer technique, a hydrophobic substrate was lowered onto the surface after the evaporation of the upper solvent [113]. Once in contact with the particles, the hydrophobic thiol ligands were attracted to the substrate and adhered to its surface. The substrate was then removed, rinsed with ethanol, and inspected (figure 5.5). This process was found to be robust enough for transfer to be achieved by hand.

Polydimethylsiloxane (PDMS), a common elastomer, was used as the substrate. A PDMS film was lowered to the surface on a clean piece of silicon wafer attached to an optical post with silicon tape. PDMS is as ideal substrate for the transfer from the interface, as it can be fabricated easily and can be used to transfer the nanoparticle mat to other surfaces via microcontact printing, for example to a silicon substrate for SEM imaging. The elastomeric properties of PDMS allowed the transferred mats to be stretched directly from fabrication, allowing for experimentation to be performed without additional sample preparation. Additionally, as long as the film was sufficiently thin it could be considered optically transparent.

To optimise this process, the quantities of acetone and thiol were varied and the experimental

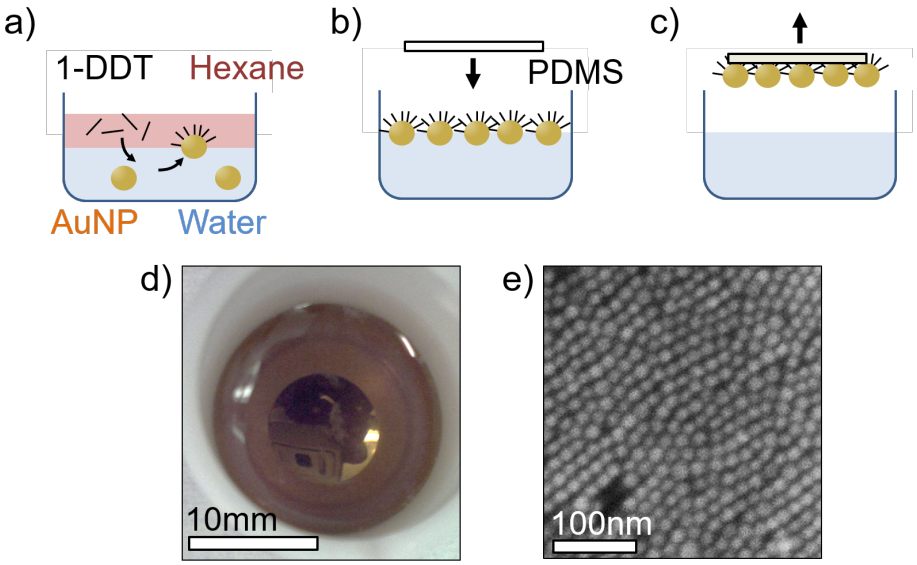

Fig. 5.5 Interfacial assembly method of gold nanoparticle mat at water-hexane interface. a) DDT is added to the hexane phase and the solutions are mixed via vigorous shaking. After leaving to settle, the particles are spontaneously trapped at the interface between the two liquids. b) The particles subsequently form a large scale mat at the interface. c) Upon evaporation of the hexane layer, the mat can be picked up by bringing a PDMS substrate down into contact with the surface and removing it. d) A photo of the mat at the water-hexane interface. e) An SEM micrograph of the assembled mat after transfer to a silicon wafer.

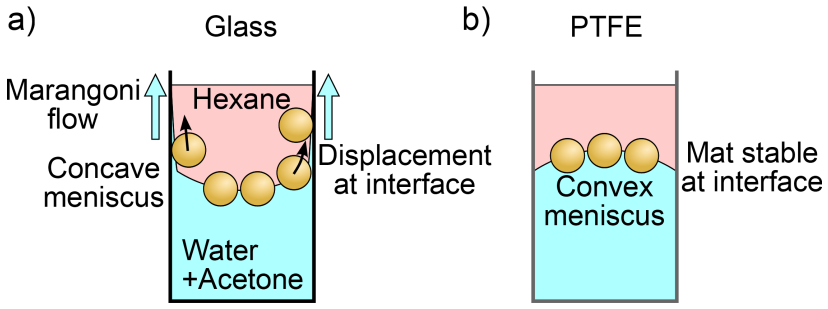

Fig. 5.6 A cross section of the interface meniscus between hexane and a water and acetone mix where nanoparticle mats have been assembled in a) a glass vial and b) a PTFE beaker. In the glass vial capillary effects produce a Marangoni effect that disrupts mat formation and results in particle aggregates being displaced up the surface of the vial. With a hydrophobic PTFE beaker this effect is removed enabling stable mat formation at the interface.

environment was adjusted. Initial experiments exhibited Marangoni flow, where capillary action resulted in a water-acetone layer moving up the sides of the vial (figure 5.6a). This disrupted the formation of the mats as particles were displaced along with the fluid. Moving the solution to a hydrophobic polytetrafluoroethylene (PTFE) beaker was found to remove this problem, as the water solution no longer shared the same affinity to the beaker walls as before, resulting in a convex meniscus and no observed flow (figure 5.6b).

Qualitative experiments were performed in order to confirm the roles of each component in the assembly process. With less acetone in the solution, the water phase retained a reddish tinge due to the presence of nanoparticles that were not transferred to the interface. This is attributed to the lower polarity acetone being required to reduce DVLO repulsion, reducing the surface charge density on the particle surface. Without the reduction in the DVLO repulsion, nanoparticle adsorption to the interface is hindered [149].

The quantity of the thiol added was also observed to have an effect on the transfer of particles to the interface, with smaller volumes of thiol resulting in a failed assembly, with little to no particles transferred. This is attributed to how the addition of a thiol to the nanoparticle surface affects the particles miscibility in different polarity solvents, thereby altering the particle-interface contact angle towards the optimal 90° required for trapping and increasing the attractive hydrophobic potential of the particle to the interface. Additionally, the binding of thiol to the particle surface reduces the repulsive potential between particles that allows closer packing of particles at the interface [113].

For larger diameter particles, higher concentrations of both acetone and DDT were required in order to successfully complete the particle transfer. For a diameter increase from 20nm to

60nm, twice the acetone and ten times the thiol were found to be necessary for monolayer assembly. The increase in thiol concentration agrees with previous work by Park and Park, who noted that as the particle diameter increases, a greater surface coverage of thiol ligands to surface area is required in order to stabilize the particles at a water-hexane interface [113]. The higher volume of thiol required for assembly is attributed to the increase in the surface area of the particles local to the interface and therefore an increase in local surface charge. With higher thiol concentrations, the chance of thiol molecules binding to the particle surface is increased and therefore more of the particle is coated with thiol, resulting in a greater reduction of surface charge. This explanation accounts for the excess of thiol compared to the available binding site on the particles observed in previous works [113]. The increase in the acetone required is attributed to reducing the electrostatic repulsion between particles, as well as increasing the level of solvent flux at the interface allowing the particles to be more easily adsorbed [149]

Experiments with different length thiols showed that fabrication still occurs when the thiol chain length is varied. 60nm gold nanoparticle mats were fabricated using 1-butanethiol (BT), 1-nonanethiol (NT) and 1-dodecanethiol (DDT) with equal quantities of solvents, in particular the same quantity of acetone across each assembly. It was observed that with shorter length thiols, the assembled mats showed less coverage after transfer than DDT-based mats, with average coverage of 50% for BT and 60% for NT. These values of coverage were calculated using microscope images of 0.24mm^2 and compare with coverage of 85% and up for the same equivalent areas of DDT coated nanoparticle mats.

It is possible that steric forces or increased hydrophobic attraction were responsible for the denser mats observed with longer thiols, however as full parameter optimisation was not carried out for thiols other than DDT this result should be viewed as a guide for future experimentation. It should be noted that previous literature indicates that higher density mats with shorter length thiols are possible with more controls applied [99, 120]. Regardless, this fabrication method resulted in the formation of monolayers of nanoparticles on the order of hundreds of microns, length scales large enough for optical experimentation.

5.2.2 Detailed assembly method

The dense nanoparticle mats fabricated in this work used both 20nm and 60nm gold nanoparticles. For 20nm gold nanoparticles, 500 μL of the nanoparticle solution was added to a teflon beaker and mixed with 330 μL of acetone. Then 380 μL of 15 mM DDT in hexane

was deposited on top of this solution, producing an immiscible organic/water interface (figure 5.5a). The beaker was then covered and shaken vigorously in a vortex mixer for one minute before being left to settle until the hexane evaporated (figure 5.5b). The assembled mat was then picked up from the surface (figure 5.5c). A densely packed array of nanoparticles was formed, with interparticle separations of between 1-2nm, depending on the length of thiol used ((figure 5.5d and e). These variations in interparticle separation are explored further in Chapter 7.

For 60nm gold nanoparticles, twice the volume of acetone was used and the concentration of the dodecanethiol was increased by a factor of 10. This enabled the complete transfer of the nanoparticles and resulted in good quality areas of mat on the order of many mm^2 to optically probe. The drastic increase in the volume of dodecanethiol was required in order to assemble a closely-packed nanoparticle mat. This agreed with similar literature fabrication methods where it was found that proportionally greater amounts of thiol are required for larger diameter nanoparticles than the associated increase in surface area would suggest [113].

The above fabrication method can be adapted for different sized nanoparticles. In order to optimise the packing and coverage of the fabricated mats, the volumes of acetone and thiol can be tuned. The trend of increasing volumes of thiol and acetone relative to increasing diameter is attributed to the associated increase of surface area with larger nanoparticles. This results in a greater charge density on or around the liquid-liquid interface and hence a greater potential barrier to overcome to assemble closely-packed arrays. By picking up these nanoparticle mats directly onto flexible substrates, their stretch reponsive optics could be explored. The optical properties of closely-packed nanoparticle mats are examined in Chapters 6 and 7 of this thesis.

5.2.3 Other attempts at closely-packed nanoparticle mat assembly

In addition to the method used above, less successful attempts were made to fabricate closely-packed nanoparticle monolayers. The first of these was the method adapted from Martin's work, detailed above [84]. In this method, nanoparticles were attempted to be withdrawn directly from the interface of a water-hexane layer and deposited onto a toluene droplet, where they were left to evaporate. As mentioned in the earlier discussuion of the Martin method, this resulted in large areas of muiltilayered nanoparticle arrays being deposited onto the substrate (see figure 5.4). This was caused by the attractive forces between

particles maintaining the structuring of at least some of the monolayer formed at the interface throughout the transfer process, with the subsequent disruption during the evaporation process resulting in aggregates sitting on top of one another.

As an alternative to forming monolayers directly at the interface between two liquid layers, Langmuir-Blodgett troughs were also used for mat fabrication. Techniques employing Langmuir-Blodgett (LB) troughs are widely employed in order to fabricate nanoparticle monolayers of different sizes and morphologies [35, 121, 128, 150]. In an attempt to replicate these, a method of transferring citrate capped nanoparticles to organic solvents was adopted [128] (figure 5.7a). Initially, multiple 5ml batches of 20nm nanoparticles were centrifuged at 11000 x g for 30 minutes, after which 4.5ml of supernatant water was removed. The remaining nanoparticle solution was mixed with ethanol and the centrifugation process was repeated and again the supernatant was removed, resulting in the particles precipitating out of solution. This step removed the remaining water from the solution. Then a 10mM solution of DDT in ethanol was added, and the solution was sonicated to redisperse the particles before being left for a day. Finally, the solution was again centrifuged and the ethanol removed, before adding 5ml of chloroform and sonicating to redisperse the particles in the solution.

Deposition of the transferred NP solution was performed using a syringe pump depositing at rates as low as 5μl/min and as high as 60μl/min. Slower deposition speeds gave the most reliable particle depositions, however all of the deposited films resulted in aggregates of varying densities on the surface of the trough (seen in figure 5.7b). Picking up these mats onto conductive substrates via the Langmuir-Schaefer method revealed films made up of both mono and multilayers with structuring apparently defined by the droplet deposition, as they showed circular patterns akin to coffee ring structures from drying droplets (figure 5.7c). Closing the area of the trough seemed to result in little packing, attributed to the asymmetric coverage of the particles over the surface caused by the particle aggregation.

In an attempt to increase the particle packing and get better coverage over the surface area of the liquid, transferred solutions were instead deposited using the syringe pump onto a water surface within a conical funnel. The water level in the funnel was then lowered from the bottom reducing the available surface area and packing the particles together. This method produced the same flaws as observed in the LB trough, with multilayered mats produced. Further experiments were also performed without added DDT (step iii in figure 5.7a) in an attempt to fabricate monolayers without a thiol coating, to reduce the interparticle spacings of the mat. However, the use of these unthiolated particles was found to produce large

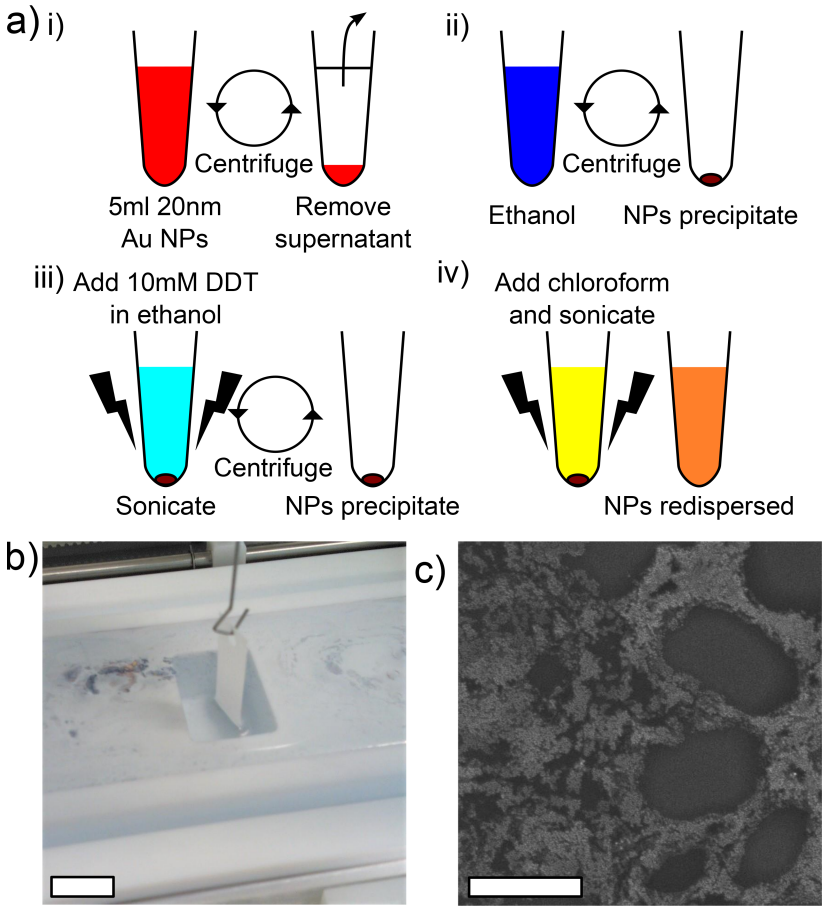

Fig. 5.7 a) The transfer process of water based citrate capped nanoparticles to an organic solvent in preparation for deposition onto a Langmuir-Blodgett trough. i) 5ml of citrate capped Au NPs are centrifuged at 11000 x g for 30 minutes. The 4.5ml of supernatant is removed and ii) replaced with ethanol, centrifuged under the same conditions, resulting in the precipitation of the particles. iii) Next a 10mM solution of DDT in ethanol is added and sonicated to redisperse the particles and then centrifuged again, precipitating out the particles and allowing for the removal of ethanol. iv) 5ml of chloroform is then added and the solution sonicated to redisperse the particles. b) After deposition, the particles aggregate on the surface of the LB trough. Scale bar equal to 20mm. c) SEM showing varied density and thickness of the particle layers formed on the trough surface as well as patterning akin to that seen from drying droplets (the "coffee ring" effect). Scale bar equal to 1μm.

aggregates with no discernible monolayer areas.

Both these fabrication methods showed considerable downsides in comparison to the liquid-liquid interface method performed. The fabrication time was many times longer, relying on extremely long deposition times to produce inferior coverage onto LB troughs. Due to the rate of deposition of, at most, tens of microlitres per minute, the fabrication process could take hours to complete. In comparison, the liquid-liquid interface method takes only a matter of minutes to perform. The monolayers made using the liquid-liquid interface method were seen to be larger and more uniform, with fewer defects and multilayered areas. Additionally, the transfer method was observed to leave many particles deposited in the centrifuge tubes used during transfer, despite long periods of sonication in an attempt to redisperse them. This irreversible deposition resulted in a lower concentration of transferred particles than for an equivalent volume of citrate capped particles. Due to these flaws, the nanoparticle structures produced have not been optically explored.

In addition to the above methods, some alternative methods were examined for densely packed nanoparticle assembly. These included;

- A nanoparticle embedded polymer was briefly explored. However, the resulting polymer was largely transparent, and optical measurements taken suggest little to no plasmonic interaction was occurring between particles. The nature of the polymer linkers automatically increased particle separation, making this assembly ill-suited to fabricating sensitive plasmonic materials with particle separations on the order of a few nanometers.

- Gas synthesised nanoparticles [151] were collected on solid substrates. This method was promising as it allowed for uncoated nanoparticles to be brought into proximity. However the number of particles produced in this way was too small to give practical coverage of a substrate, with long deposition times of many hours required for even low densities of particles.

- A second liquid-liquid interface method was explored, where nanoparticles were floated onto a layer of dichloroethane, after which they spontaneously formed an array at the interface [152]. The array was then withdrawn carefully from the interface and deposited onto a substrate where the particles were dried down. The mats produced using this method are comparable in speed of fabrication and interparticle spacing from the liquid-liquid interface method, with the advantage of being uncoated in any stabilising ligand. However, the removal of the mats from the interface and subsequent

drying does destabilise the mats, resulting in smaller area mats. The optical response from mats fabricated using the dichloroethane method are optically compared to mats fabricated using the liquid-liquid interface method in Chapter 7.

Of all the methods of fabrication explored during the course of this work, the thiolated liquid-liquid interface method produced the smallest interparticle separations. Additionally, the liquid-liquid interface method required minimal processing time, enabling the rapid fabrication of experimental samples.

5.3 Summary

In this chapter, differing self-assembly techniques for the fabrication of closely-packed nanoparticle monolayers have been detailed. Closely-packed nanoparticle monolayers can be made by trapping nanoparticles at liquid-liquid interfaces, and can be transferred to substrates in order to explore their optical properties. This technique is repeatable, scalable and has been used to make nanoparticle monolayers at centimeter length-scales. An examination of the optical properties from interfacially assembled closely-packed nanoparticle monolayers will be detailed in the subsequent 3 chapters, beginning with a study of optical response of 20nm nanoparticle mats under strain.

Chapter 6

Stretch tunable nanoparticle mats

By controlling the separation distances between the components of a plasmonically active nanostructure, it is possible to tune the structure's optical response. In this chapter, the effect of mechanical strain applied to elastomeric plasmonic materials will be explored. Initially, the behaviour of a stretched evaporated gold film is detailed, showing the optical behaviour of a structure without nanostructuring under strain. Then, the optical responses of densely packed arrays of 20nm nanoparticles, assembled onto elastic polymer substrates, are comprehensively explored using biaxial and uniaxial strain as well as different polarisation states of incident light. This behaviour is modelled by comparison to a nanoparticle chain. Finally, the optics of a silver nanoparticle monolayer under strain is observed, and the difference in the optical response to gold nanoparticle mats explained.

6.1 Stretching an evaporated gold film

Before examining the behaviour of a closely packed gold nanoparticle array under strain, it is interesting to first briefly examine the optical behaviour of an evaporated gold film when stretched (figure 6.1a). Due to the lack of nanostructuring in a continuous gold film, its optical behaviour is defined by the fracturing of the material, resulting in a loss of reflective intensity. However, due to the film fragmenting on length scales much greater than a nanometer, there should be no change in the spectral lineshape and therefore the intensity loss is the only significant optical variation before and after the application of strain. This result contrasts significantly with nanoparticle arrays, as the gaps in the lattice can act as fault lines for separation, resulting in potentially uniform nanoscopic variations in nanoparticle

separation and therefore spectral shifts. By examining the continuous film case, expected intensity losses can be studied and the plasmonic shifts of stretched gold nanoparticle arrays can be contextualised.

Biaxial strain was applied to an ≈ 15nm thick gold film by lowing the film onto a hemispherical lens. Under strain, the reflective intensity of the film decreased by half at 22% strain (figure 6.1b). Throughout the drop in reflective intensity, the lineshape remains consistent, though there is a ±3.5% difference in the percentage change across the wavelength range of the spectra, with lower wavelengths experiencing a smaller percentage intensity change than longer ones. Upon release, the film's reflection returned to 94% of its previous value.

The drastic reduction in the reflective intensity of the gold film is caused by fractures in the metal film, that form as a result of the increasing lateral size of the substrate [153]. This cracking results in islands of gold on the order of tens and hundreds of microns in width. As these islands are far above the wavelength of the incident light, they are too large to develop localised plasmonic responses, and therefore show the same characteristic optics of a gold film, with the exception of the reduced reflective intensity.

The expected reduction in reflective intensity is shown by the solid black line in figure 6.1b.

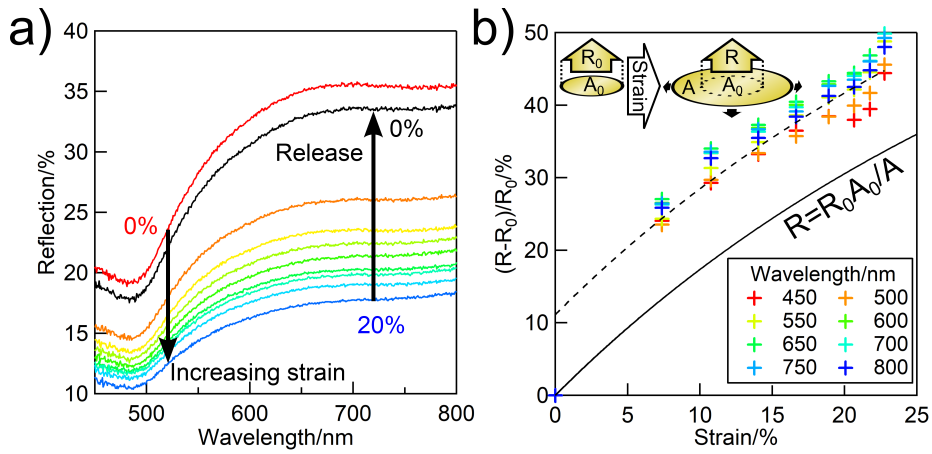

Fig. 6.1 a) Reflective intensity of a ≈ 15nm evaporated gold film under biaxial strain from 0% (red) to 20% (blue). Upon relaxation the film does not return to its previous value of reflection (black). b) Percentage difference of reflective intensity, R, from the initial value, R_0, collected from the area in the correction spot area, A_0. The solid black line is from a model of the reflective intensity of a gold film under strain, calculated as the initial intensity measured from the collection spot, R_0, times by area fraction from the initial area measured, A_0, to the area after strain is applied, A. The dashed line is a fit to this model, suggesting that a small value of strain has been applied to the film before measurement.

This simple model is calculated by assuming the reflectivity, R, of a given area is directly proportional to the material in the collection spot, and hence the inverse of the fractional increase in area of the film under an applied strain. Light is collected from a specific area, A_0, giving an initial reflectivity, R_0, so that as the area is increased to A the resultant reflectivity R is modelled $R = R_0 \frac{A_0}{A}$ (inset figure 6.1b). The resultant change in intensity in the experimental data is observed to be greater than the model predicts, though still fits the general trend after a lateral shift. This difference may arise from a deformation of the film by the clamp, pre-stretching the film for the R_0 measurement. Alternatively, this additional reduction may be due to the film being stretched over a curved surface, resulting in some angular reflection out of the light cone of the objective. This effect would be more pronounced the larger the collection spot and hence lower magnifications.

Upon the relaxation of the film, these fractures result in surface defects in the film, such as lifting from the surface and folding, that explain the observed reduction in reflective intensity after stretching [154]. It is possible to maintain a films' continuity by texturing the substrates surface to minimise this cracking [155]. Without these prevention measures, a thin gold film will crack under the application of strain, reducing the reflective intensity while still optically behaving as bulk gold.

6.2 Stretch tuneable plasmonic monolayers

Unlike a solid gold film, a plasmonic material made of nanoscopic building blocks is not a continuous structure. As a nanoparticle mat is made up of individual particle components, applied strain can increase the separation of the existing gaps between the constituent parts of the structure. This will induce a shift in the plasmonic resonances exhibited by the array. Therefore it is possible to fabricate dynamic optical materials that respond to changes in applied strain.

A mat of 20nm gold nanoparticles was assembled using the liquid-liquid interface assembly method detailed in Chapter 5 and lifted from a water surface using a small square ($5mm^2$) of PDMS. This substrate was then covered in a second layer of liquid PDMS that was subsequently cured, encapsulating the monolayer within the polymer. This increases the size of the film, enabling it to be stretched. This was primarily done to increase the substrate size, making the strain measurements easier to perform, although the encapsulation also ensured that the particle array remained fixed within the substrate allowing strain to be applied evenly across the mat.

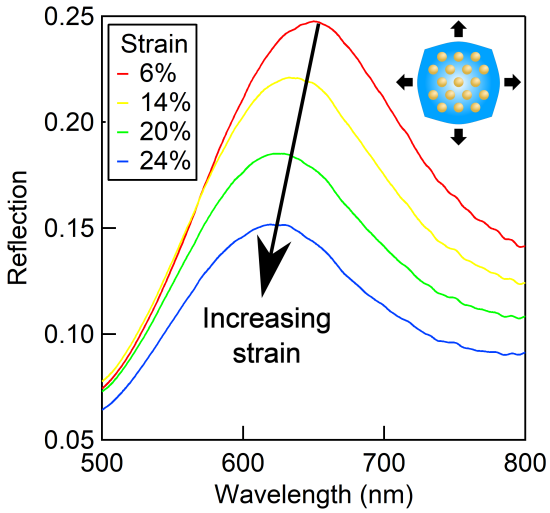

Fig. 6.2 Reflection spectra from a 20nm gold nanoparticle mat stretched biaxially over a hemispherical lens. As the strain is applied the peak in the reflection spectra is seen to blueshift by up to 50nm indicating an increasing interparticle separation of the nanoparticles.

Biaxial strain was applied using the hemispherical lens stretch rig. The reflection spectra from the mat was seen to change, with the peak in the spectra shifting towards the blue by around 50nm at 25% strain, indicating that the nanoparticle separations were increasing (figure 6.2). As the strain increases, the intensity of the reflection decreases, reducing by 40% at 25% strain, within a few percentage points of the expected value from the decreasing fill-fraction of particles. This is due to a decrease in the number of particles in the collection spot as strain is applied. Additionally, the scattering cross section of the nanoparticles will also decrease as the gaps between particles increases, which also contributes to the observed decrease in the reflective intensity. The application of further strain was limited by the thickness of the film, with tearing of the substrate observed at higher strains.

The initial rate of blueshift change, calculated via the shift in wavelength of the reflection divided by the strain ($\Delta\lambda/\Delta\varepsilon$) is 70nm per unit strain. This rate of change slows as further strain is applied (green dashed line in figure 6.4). The relationship between the wavelength change $\Delta\lambda$ and nanoparticle separation d has been found to fit to a power law dependence, where $\Delta\lambda \propto d^x$. This has been observed in plasmonic systems with increasing separation distances between components, such as particles suspended above films [156] and voids [157] as well as in particle chains [158]. This power law dependence is again observed here (dashed green line in figure 6.4), suggesting that the increase in nanoparticle separation d is directly proportional to the strain increase. This indicates that with applied

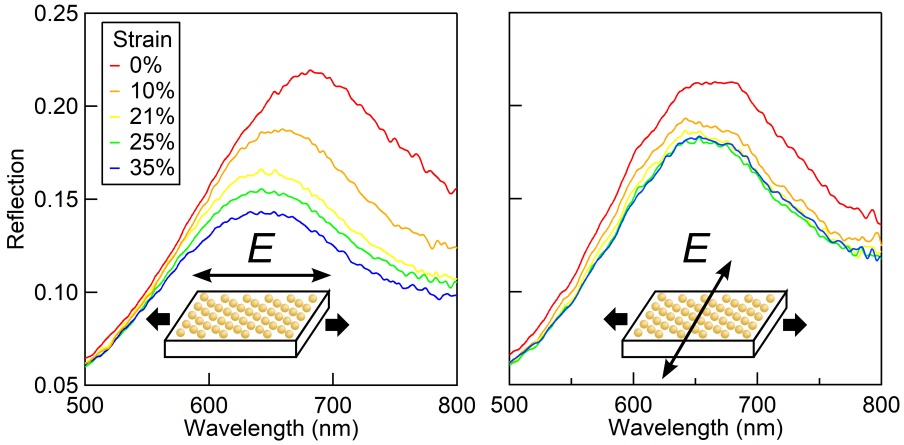

Fig. 6.3 Reflection spectra of a 20nm gold nanoparticle mat under uniaxial strain using polarised light. With the E field polarised along the axis of strain (left) the reflection peak blueshifts as the nanoparticles are separated. With the E field polarised perpendicular to the strain more complex behaviour is seen, with an initial blueshift of the peak followed by a redshift.

strain the nanoparticles are separating uniformly across the observed area.

The advantage of a two dimensional biaxial strain is that the nanoparticles should move apart from each other equally in all directions. This can be seen by an independence of the optical response in relation to the polarization of the incident light. Strain applied uniaxially affects the optical behaviour of the mat in a more complex manner due to anisotropy in the direction of nanoparticle movement.

For one-dimensional strain measures, a motorised stretch rig was used. Upon the application of strain, a shifting of the reflection spectra was again observed, however the optical shifts were seen to have a clear polarisation dependence (figure 6.3). When the electric field is polarized parallel to the direction of applied strain, the spectrum blueshifts as expected. However, this shift is only 40nm for 35% strain, noticeably less than the biaxial strain. When the polarization is perpendicular to the stretch direction, the measured reflection spectra show more complex behaviour; initially blueshifting, before redshifting above 10% strain. Unpolarised spectra of the mat under uniaxial strain show spectral shifts that fall between these two opposing polarisations. This stretching process was shown to be reversible; when the stretched PDMS is relaxed, the spectrum redshifts back as the interparticle spacing decreases.

The observed shifts seen with the application of both uniaxial and biaxial strains are shown

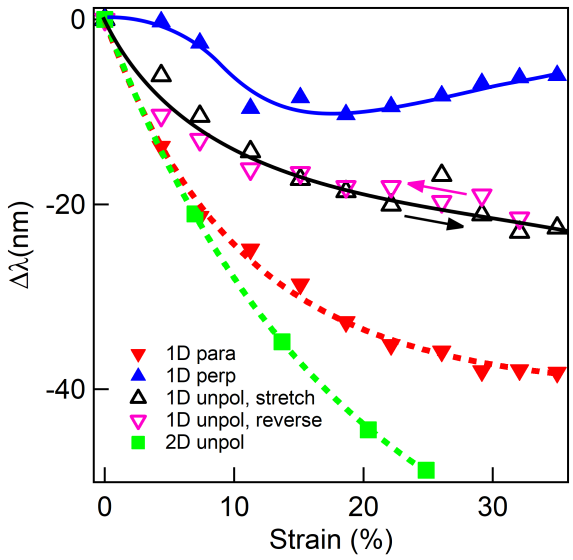

Fig. 6.4 Peak shift in reflection spectra against strain from a 20nm gold nanoparticle mat for biaxial (■) and uniaxial (△ extension and ▽ contraction) strains, with uniaxial polarisation measures ∥ (▼) and ⊥ (▲) to the strain axis. Power law fits shown as dotted lines.

in figure 6.4. At low strains, biaxial stretching (shown in green) produces a faster initial rate of blueshift in comparison uniaxial strain (black), 70nm/unit strain to 40nm/unit strain respectively. At higher strains, the shifts for uniaxial stretching in the unpolarised and perpendicularly polarised cases has a non power law dependence. In comparison, biaxial strains show a power law dependence and no saturation despite a gradually reducing shift per unit strain rate. The parallel polarised uniaxial stretch measures also show a power law dependence on strain, despite the lower value of $\Delta\lambda/\Delta\varepsilon$ at high strains, saturating at 30% strain.

Previously it has been observed that the coupling of plasmons in nanoparticle chains is minimally influenced by orientational disorder of the chain along the plane of polarisation [30]. However, when nearest neighbour particles are angularly displaced away from the stretch axis the change in separation caused by the induced strain is affected. This is due to only a component of the separation distance increasing along the direction of applied strain. This explains the reduction of $\Delta\lambda/\Delta\varepsilon$ in the uniaxial parallel polarised measurements in comparison to the observed biaxial shifts; due to disorder in the lattice, the increase in d is less than the biaxial case where strain is applied evenly across the film. Additionally, particle orientation has effects on the perpendicularly polarised measurements that are explored quantitatively below.

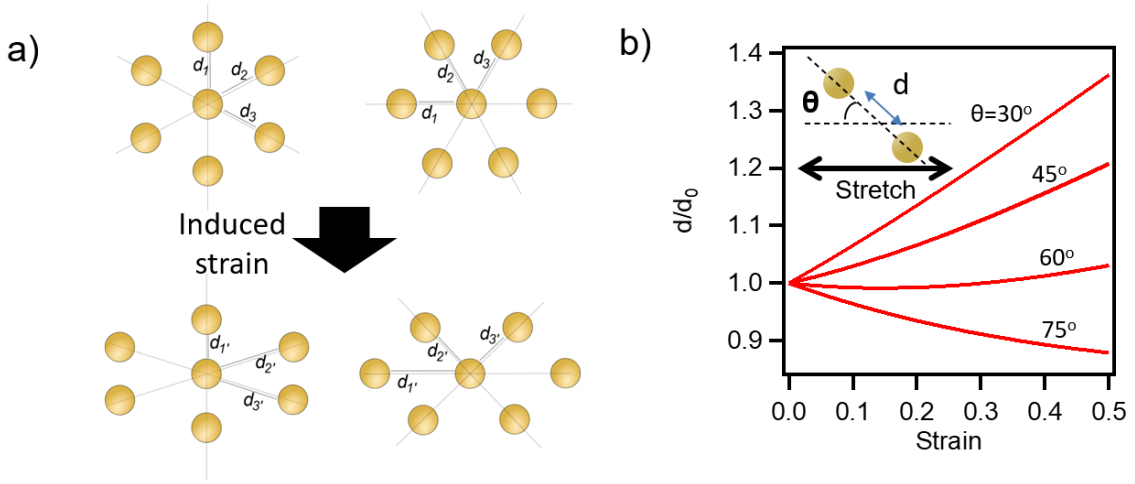

Fig. 6.5 a) Each particle has three potential chain axes, with separations labelled as d_1, d_2, and d_3. Under uniaxial strain, the change in these separations is dependent upon the chain axes orientation to the plane of strain. b) The dependence of particle separation in a nanoparticle dimer on the orientation to a stretch axis.

The blueshift in the perpendicularly polarised uniaxial strain measures can be partially explained by contraction of the PDMS substrate perpendicular to the applied strain. The Poisson ratio of PDMS is usually given $\nu = 0.5$ [159], therefore a film will contract perpendicular to the stretch axis half the length extension. However, this contraction does not explain the initial redshift observed. This can be explained qualitatively by considering a small grouping of nanoparticles arranged in a hexagonal array (figure 6.5). In comparison to a one dimensional nanoparticle chain, where there is only one gap orientation and at most two neighbouring particles along either direction of the chain axis, a hexagonally-packed nanoparticle array contains multiple nanoparticle chains of various orientations. In this case each particle has 6 nearest neighbours. Therefore each particle has three different chain axes, each running through two neighbouring particles.

The deformation that a hexagonally packed array of nanoparticles experiences under uniaxial strain is therefore dependent upon the angle of each nanoparticle chain to the stretch axis. Chains orientated along or $<60^\circ$ to the stretch axis move further apart and hence exhibit a spectral blueshift under incident light when the E-field is polarised along the strain axis. Due to converse contraction experienced perpendicular to the strain axis with unixial strain, chains perpendicular or at $>60^\circ$ to the stretch direction move closer together. In this case, with the E-field polarised across the strain axis, the spectra will redshift.

This behaviour can be illustrated using a simple dimer model, with the interparticle separation under strain of the two particles changing as a function of angle to the stretch axis (fig. 6.5b). The increase in separation, d/d_0, decreases as the angle between the stretch axis and the dimer axis increases. At 60°, the increase is minimal, and at angles greater than this, the length contracts.

In the perpendicularly polarised case, the initial blueshift occurs due to the PDMS substrate stretching twice as much along the stretch direction as it contracts in the perpendicular direction, resulting in an initial increase in interparticle separation. At higher strains the contraction perpendicular to the stretch axis becomes dominant and results in closer particles and stronger coupling, with the associated blueshift to a higher energy resonance. With the E-field polarised along the stretch axis, plasmonic coupling strength between particles drops significantly as they move apart faster than they are brought together. Therefore the polarisation of the incident light allows for selective detection of particle movement for different particle orientations with applied uniaxial strain. In comparison, biaxial strain displays a more typical blueshift as all nanoparticle spacings increase independent of orientation.

6.3 Modelling nanoparticle mats as one-dimensional chains

Comparing the optical spectra from a mat of densely packed nanoparticles with those of a single nanoparticle and a gold film demonstrates the optical differences between these different morphologies. The 20nm gold nanoparticle mat shows a broad resonance akin to that of a chain resonance from a group of nanoparticles (red line, figure 6.6). It contrasts sharply with the scattering peak of a single 20nm gold nanoparticle (blue line, figure 6.6) in that it shows a significant shift in the peak wavelength towards the red and has a much greater FWHM. Also interesting to note is the significant change from a calculated 20nm thick gold film (black line, figure 6.6). The spectra seen from the mat shows a significantly lower reflective intensity. Of course, a nanoparticle mat has less material by volume than an equivalent thickness of gold film. The volume fill fraction of the mat in comparison to a gold film is around 55%. The spectra of the nanoparticle mats were observed in the bright field configuration of the microscope, measuring reflective intensity. Dark field measurements of scattering from the mats, that would typically be used with nanoparticle aggregates, show minimal intensities with bright spots only appearing at the edges of the mat or at localised defects. This shows that light is predominantly directed back towards the source rather than scattered away as is typical of nanoparticle-light interactions. This agrees with previous lit-

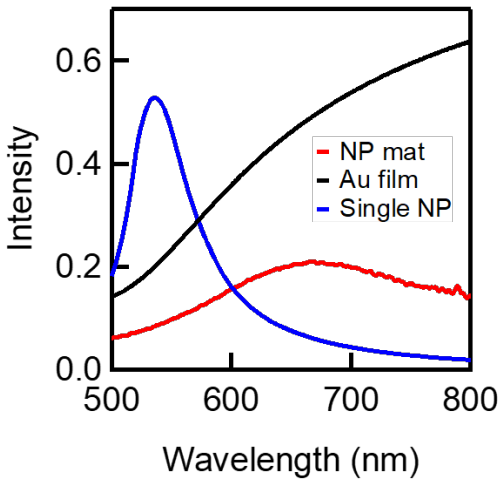

Fig. 6.6 A spectral comparison between the scattering of a 20nm gold nanoparticle (blue), a 20nm gold nanoparticle mat (red) and a 20nm gold film (black). The nanoparticle mat exhibits a reduced intensity from the film and shows a red shift from the single scattering spectra due to the coupled plasmons between the particles.

erature sources that saw a transition from scattering to reflective behaviour from particulate films due to interference effects [34].

In order to theoretically describe the behaviour of these densely-packed nanoparticle arrays, complicated finite-difference time-domain techniques can be employed to accurately model the electromagnetic behaviour of the mats. This is computationally very intensive. However, as the observed optics and spectral shifts of these mats are similar to those observed previously from nanoparticle dimers [31] and many-particle three dimensional chain aggregates [28], a simpler 1D linear chain of gold nanoparticles was simulated in order to provide a quantitative estimate of the system and model the change in plasmonic coupling between particles (figure 6.7).

Simulations of $N = 19$ spheres of size 20nm were calculated using a boundary element method. N is chosen at 19 particles as it falls beyond a saturation point found at $N \geq 18$ spheres (similar to results seen in literature sources [9, 28]). The surrounding media was set using the refractive index of PDMS, n= 1.4, based on the polymer fully encapsulating the particle array. The scattering spectra were then calculated for a variety of different particle separations to model the varying gap distance in a stretch tunable nanoparticle mat.

As expected, a blueshift in the peak position of the calculated scattering spectra was observed in calculations with the E-field along the stretch axis, agreeing with the experimental

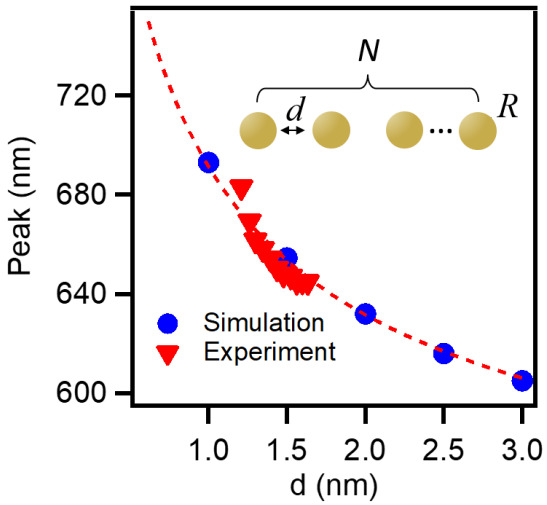

Fig. 6.7 A simulated nanoparticle chain with the E-field polarized along the chain axis. The uniaxial parallel polarised experimental data is fitted against the simulated resonance positions in order to extract the particle separation d. Inset: a schematic of the chain modelled where N= 19, R= 10nm and a local refractive index n= 1.4 for the chain embedded within PDMS.

results. Conversely, the observed shifts from the polarisation perpendicular to the stretch were minimal. Therefore, a nanoparticle mat can be theoretically modelled as a sheet of linear chains in the case of of polarisation along the stretch axis. This is due to the dominance of coupling in this orientation, over the minimal coupling perpendicular to the axis of polarisation. It is worth noting that when modelling particles with a significantly larger diameter, this simplification may not be possible due to additional coupling perpendicular to the polarisation axis [31].

The peak positions of the 1D nanoparticle chains modelled follow a power-law dependency on the interparticle separation with a observed relation of $\lambda \propto d^{-0.6}$. By comparing this relationship with the experimental shifts of the 1D uniaxial parallel polarised strain measurements, a theoretical fit for the initial interparticle separation can be made. An initial interparticle separation of 1.2 ± 0.1nm was found by this fit, with a final separation of 1.6 ± 0.1nm, representing a length extension of 33%, within two percent of the measured applied strain. The initial separation is a similar value as the measured thickness of a single self-assembled monolayer (SAM) of DDT at 1.7nm [160, 161]. The discrepancy in these two values is potentially due to changes in the conformation of the ligand on the surface of the molecule, as the organisation of thiol ligands on a gold surface is known to be sensitive to its surroundings, particularly in the presence of toluene[121]. Therefore either a

compression of the thiol molecules affects their orientation on the surface or, alternatively, interdigitation of the ligands enables this close proximity of the particles.

The modelling of the nanoparticle mat as a one-dimensional nanoparticle chain allows for a theoretical basis for the observed behaviour and gives calculated values for the interparticle separations. This modelling fits well with the experimental results for biaxial strain.

6.4 Silver nanoparticle monolayers

Silver nanoparticles display similar optical properties to their gold counterparts, with the exception that their initial resonance is blueshifted. As a comparison to the gold nanoparticle mats, a monolayer of 20nm silver nanoparticles was assembled using the liquid-liquid interface assembly method and transferred to a PDMS substrate. Initial investigations showed that both the scattering and reflection spectra display a similar resonance peak to the 20nm gold nanoparticle mat (figure 6.8). Importantly, this resonance peak is located at the same wavelength in both the bright and dark fields, with the spectra showing broadly similar lineshapes apart from at the the lower and upper bounds of the measurements, such as towards 450nm in the scattering spectra where additional factors such as artefacts from increased noise result become more significant.

The similarity of the bright and dark field reflection and scattering spectra demonstrates that

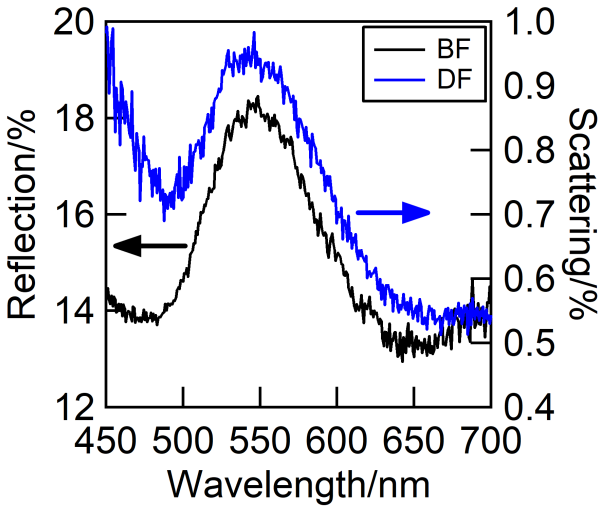

Fig. 6.8 Reflection (black, left axis) and scattering (blue, right axis) spectra indicating the plasmon resonance peak from a closely packed array of 20nm silver nanoparticles.

the reflective optical response from plasmonic nanoparticle monolayers is dominated by the coupled plasmon resonance, with a normalised intensity over twenty times greater than that of the normalised scattering. This further proves that as the size of a nanoparticle aggregate increases, there is a transition where scattered intensity diminishes in favour of increasing specular reflection, due to destructive interference away from the geometric optical paths (as discussed in section 2.2.2 and reference [34]). However, although scattering is strongly diminished, it is not removed entirely due to defects across the array preventing total destructive interference. This effect is most obvious at voids and edges of the array, which show high intensity scattering under dark field illumination at their edges.

Upon the application of uniaxial strain, there was an observed polarised blue shift in the reflection spectra (figure 6.9a). However, the shift is minimal, with only a 5nm blueshift observed with 60% strain (figure 6.9b). In comparison to a gold nanoparticle film, this is a small change in the resonance peak despite a 12% drop in the intensity of the reflected light.

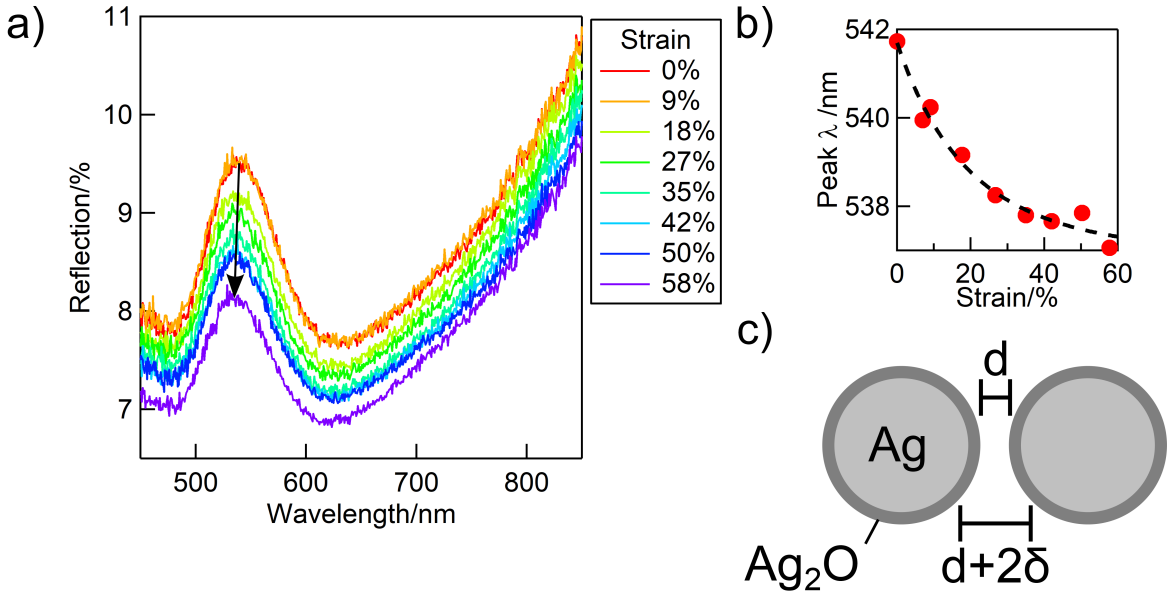

Fig. 6.9 a) Strain induced shift in the plasmon resonance of 20nm silver nanoparticles with the E-field polarised along the strain axis. b) Peak positions with respect to strain showing a 5nm shift over 60% strain, fitted by a power law (dashed line). c) Schematic of particles with interparticle separation d and oxide layers with thickness δ, artificially increasing the effective distance between the plasmonically active silver core to $d+2\delta$.

The reduction in stretch tuneability of the silver nanoparticle mat was unexpected, as the optical response should be similar to that of the gold nanoparticle mat. Due to the identical assembly process, it was expected that the initial interparticle separations would fall

between $1 < d < 2$nm. As this is significantly less than the nanoparticle diameter the mat should show strong coupling between particles and therefore exhibit a high sensitivity to interparticle separation. The proximity of the particles can also be inferred by the similarity of the reflection and scattering spectra. The change in peak position under strain, though slight at 5nm for 60% strain, displays a power law dependence on strain, and therefore particle separation. The explanation for the difference lies in the nature of silver, specifically its oxidisation. The silver nanoparticles are likely developing a layer of silver oxide, thickness δ, on their surface either as the particle mat sits exposed on the substrate or via the introduction of air to the solution during the mixing step of mat assembly [162]. This layer, a few nanometers ($1 < \delta < 10$, [163, 164]) in depth, changes the effective particle separation from the interparticle separation, d, to the core separation, d+2δ, reducing the coupling strength between the particles (figure 6.9c). A side effect of this oxide layer is that strain is no longer representative of the increase between particles, as it only acts on the interparticle distance and does not affect the oxide layer. These factors contribute to the reduced effectiveness of strain as a method to tune the plasmon resonance.

The oxidisation of silver nanoparticles acts to decrease the effectiveness of a silver nanoparticle mat as an active plasmonic material. Although some dynamic plasmonic behaviour is observed, silver nanoparticle mats display significantly less sensitivity to strain than their gold counterparts.

6.5 Summary

Self-assembled monolayers of metal nanoparticles can be fabricated at the interface of two immiscible liquids. As these nanoparticle mats are made up of discrete components, it is possible to manipulate their structure via the application of strain. This in turn induces changes to their optical response which are observed to be reversible and anisotropic. The changes are dependant upon the manner of the applied strain and the polarisation state of the incident light.

The anisotropic response observed in the plasmon resonance under uniaxial strain arises from symmetry breaking in the nanoparticle array ordering. This is induced by the perpendicular contraction of the elastomeric substrate upon the application of strain. The behaviour from a biaxial strain is comparatively simple, as the deformation of the substrate results in the uniform separation of nanoparticles, removing the complexities introduced by uniaxial strain.

The optical behaviour of these mats under polarised light can be modelled as a one-dimensional chain of particles with chain like resonances dominating the optical response. Silver nanoparticles are seen to be less effective than gold in their stretch tunability due to their oxidisation in air.

Due to the size dependence of particle trapping at interfaces, increasing diameter nanoparticles become easier to assemble into large scale arrays. Additionally, strength of the coupled field between particles increases with diameter. The optical behaviours of these larger sized nanoparticle mats are examined over the next chapter.

Chapter 7

Optical investigation of larger diameter nanoparticle monolayers

As nanoparticle diameter rises, the polarisabilty of the particles increases due to the cubic dependence on nanoparticle radius. Therefore, the magnitude of the scattered light intensity and the local field intensity around a particle also dramatically increases, changing the strength of particle coupling. In this chapter, arrays of larger diameter nanoparticles are explored, in order to study the effect this increase has on the optical response of a nanoparticle monolayer. The changes to the local refractive index and thiol surfactant on this optical response are also studied, as well as the behaviour of these larger diameter particle mats under strain.

7.1 Optics of larger diameter closely packed nanoparticle monolayers

As the diameter of nanoparticles increases, the interfacial assembly method for monolayer fabrication becomes easier due to thel dependence on particle radius of the interfacial energy reduction. Commercial 60nm gold nanoparticles were self-assembled into large scale arrays using the liquid-liquid interface method detailed in Chapter 5. The increase in radius is alone not enough to trap the particles at the interface, so larger volumes of acetone and DDT were required to assemble a large area mat. However, once formed the larger diameter mats were observed to be more stable and easier to pick up than those made from smaller diameter nanoparticles. This extra stability was attributed to the increase in particle size.

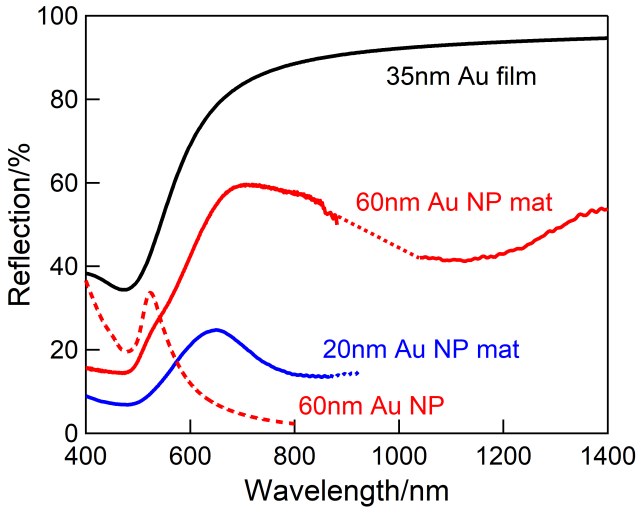

Fig. 7.1 Reflection spectra of 60nm gold nanoparticle mat (red). For comparison, the calculated reflection spectra of both a 35nm thick gold film (black), a 20nm gold nanoparticle mat (blue) and a Mie calculated scattering spectra of a single 60nm gold nanoparticle are displayed.

In comparison to smaller size nanoparticle mats, the reflection spectra of a 60nm diameter close-packed gold nanoparticle monolayer shows distinct differences. Whilst the 20nm particle mat shows a very clear peak in reflection spectra (blue line, figure 7.1) that corresponds to the scattering from the chain plasmon mode of the nanoparticle mat, the 60nm particle's reflection spectra shows a much broader response (red line, figure 7.1). The lineshape has very similar characteristics to that of a gold film, growing in intensity from around 470nm and flattening out, with a small gradient of decreasing intensity after 710nm. This gradient leads to a significant dip in intensity in the infrared around 1120nm. Another significant deviation is that of a small shoulder in the increasing gradient of the scattering spectra around 560nm.

As seen in Chapter 2, the optical behaviour of a nanoparticle mat with particles of diameter $>$ 30nm is more complex than the chain model can describe. Because of this discrepancy, a finite-difference time-domain (FDTD) simulation was used to calculate the optical response of an infinite nanoparticle mat from a repeating unit cell of the array. In this manner the optical behaviour of the system was modelled with more precision.

FDTD calculations were carried out using the Lumerical software and are seen in figure 7.2. The calculated behaviour was similar to the experimental observations with a steep gradient rising from 500nm to anywhere from 600 to 700nm, followed by a gradual decrease in

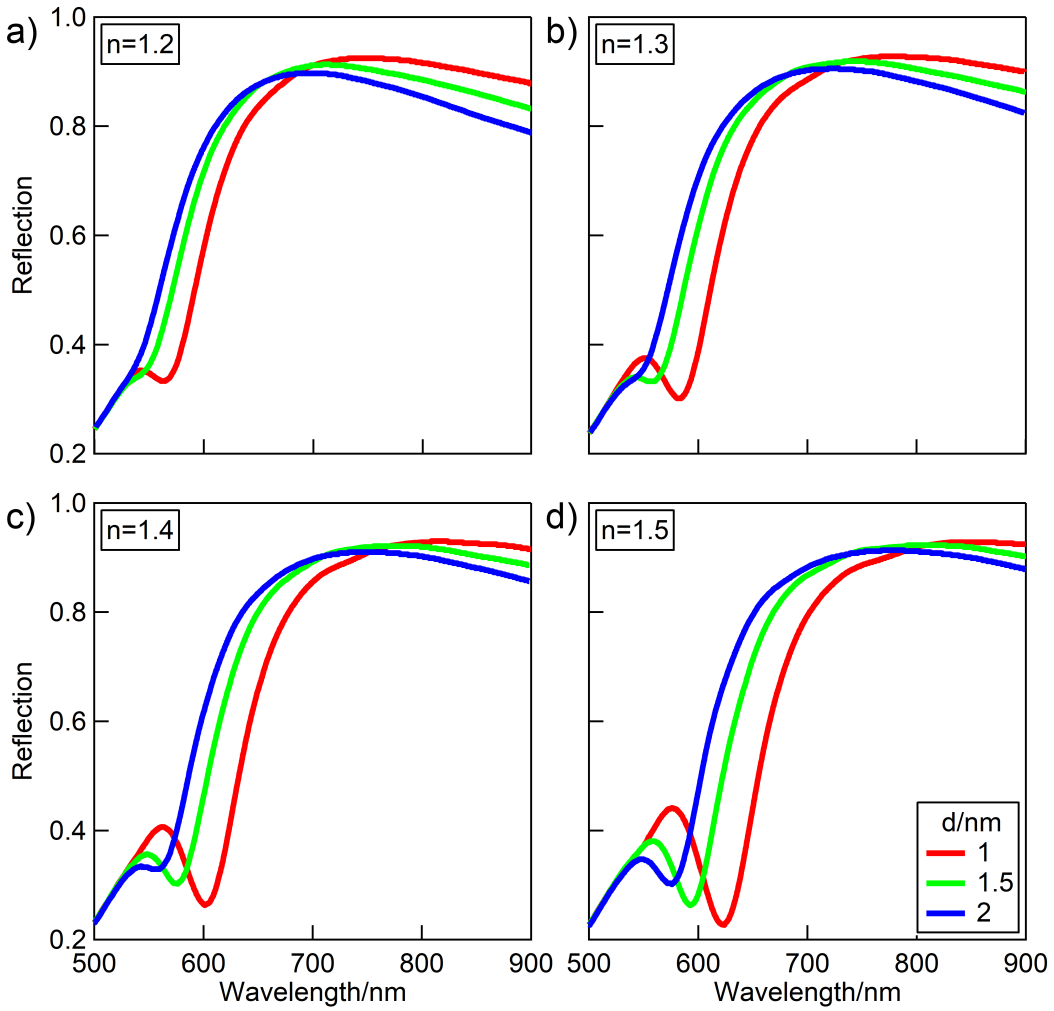

Fig. 7.2 FDTD calculations carried out for 60nm nanoparticle mats with separations d of 1nm (red), 1.5nm (green) and 2nm (blue). Different values of the refractive index have been calculated to account for varying gap materials with a) $n_{gap} = 1.2$, b) $n_{gap} = 1.3$, c) $n_{gap} = 1.4$ and d) $n_{gap} = 1.5$.

intensity. Additionally, a dip in the reflective intensity was observed, redshifting with decreasing interparticle separation or increasing refractive index of the interparticle medium, indicating a relation between coupling strength and the position of the intensity dip.

Using these FDTD calculations, the reflectance dips in the experimental data were fitted to give a value range for the interparticle separation between 0.9 and 1.3nm, and the refractive index of the gap between 1.1 and 1.3. It is important to note that the range of refractive index values is less than that of the thiol surfactant of the particle, which has a value of 1.4. This indicates that surfactant surrounding the particle does not entirely define the interpar-

ticle gap refractive index. As the outstretched thiol length is around 1.7nm, this suggests a deformation of the thiol close to the particle surface. This is supported by literature sources indicating that thiol molecules deform due to the presence of hexane [121]. The lower than expected value of n would therefore be explained by the presence of other substances, such as air, water or PDMS, influencing the effective refractive index of the gap. Other potential causes of this lower refractive index value could be from interdigitation of low coverage density of thiols lying along the particle surface, although this can be considered less likely due to the high concentration of thiols within the hexane, or from thiols lying more closely to the particle surface, rather than arrayed across the gap.

As seen in the previous chapter, the optical response of nanoparticle mats can be further explored by manipulating the interparticle spacing. In addition to this manipulation, the plasmon resonance can be altered by changing the contents of the gap. To complement stretch measurements, it is possible to alter these properties by changing the particle surfactant. Additionally the above result suggests that the gap is not saturated by thiol molecules and therefore other molecules can be introduced into the gap to change the refractive index of the particle surroundings.

7.2 Changing gap refractive index

In order to study the optical changes caused by differing refractive index materials on the dense nanoparticle mats, different fluids were drop cast onto 60nm gold nanoparticle mats. Index matching oils and water were chosen as the liquids, with the matching oils ranging from 1.4 to 1.7 refractive index units (RIU) with increasing increments of 0.1 RIU (sourced from Cargille). These index matching oils are made up of combinations of different molecules in order to gain the specific refractive index required.

The liquids were deposited onto the mats in situ under a microscope objective, allowing for reflection and transmission spectra to be taken immediately after deposition. Subsequently, the oils were rinsed off with water and ethanol, allowing scattering spectra to be observed. The resultant spectra are shown in figure 7.3. The significant features in the reflection and transmission spectra show no shifting with refractive index oils up to n=1.6. With the n=1.6 index matching oil, there is a subtle blueshift of around 10nm in the minimum value of transmission. The corresponding scattering spectra shows a peak value blueshift of 45nm. This opposite to the expected response to an increase in the refractive index of the medium surrounding the particles.

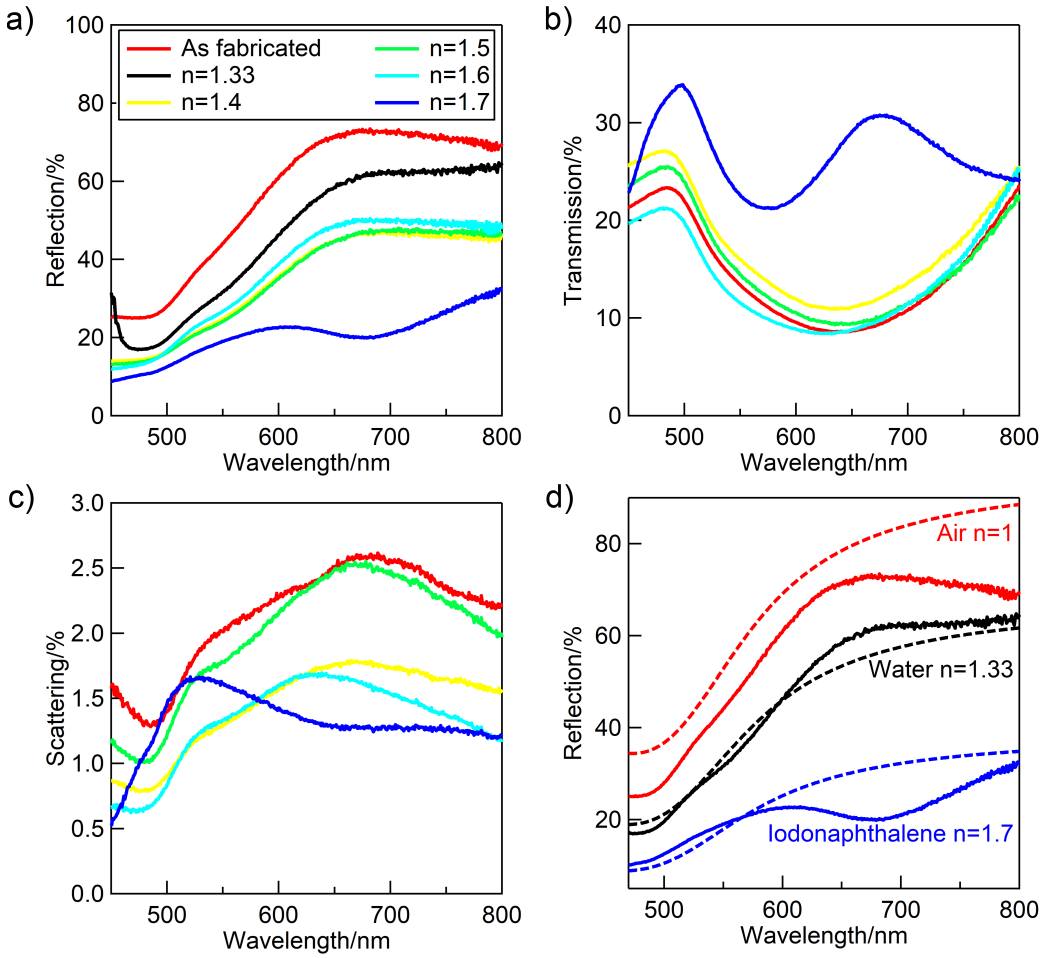

Fig. 7.3 a) Reflection, b) transmission and c) scattering spectra from 60nm gold nanoparticle mats with different refractive index oils drop cast on their surface. Minimal spectral changes are observed beyond varying intensity with the exception of the n=1.7 refractive index oil (iodonaphthalene), which shows a significant spectral shift. d) Calculated reflection spectra of a 35nm gold film with different refractive index top layers, matching air (red), water (black) and iodonaphthalene (blue).

The minimal change in the optical response of the mats shows that these oils are not permeating into the interparticle spacings, and are instead sitting above the mats. This can be explained by considering the interaction between the thiol surfactant on the nanoparticle surface and the different molecules in the oil. The penetration of the molecules into the gap will rely on their affinity. In this instance, it is clear that water will not permeate into the thiol layer at all due to their immiscability. Additionally, it is possible that the reaction between the molecules may result in the rearrangement of the thiol molecules on the nanoparticle surface, resulting in a reduction of the the local refractive index in the mat gaps and exhibited in the minor blueshifts observed [121].

These minimal changes in the above spectra are sharply contrasted with the results from the n=1.7 refractive index oil, which is pure iodonaphthalene (figure 7.3, blue line). Upon the introduction of the iodonaphthalene, a sharp change in the spectra was observed, showing considerable redshift, a broadening of the peaks and an intensity dip.

The difference in intensity from the spectra of the mats in air to the spectra of the mats in the different media can be attributed to changes in reflection from the surface of the different fluids. This can be demonstrated by comparing the reflection spectra of these fluids to a simulated 35nm gold film submerged in different fluids (figure 7.3d). A 35nm thickness is modelled, as it matches the averaged thickness of a close packed array of 60nm gold spheres.

The experimental mat and calculated continuous film reflective intensities behave similarly for each index value modelled, with reflective intensity decreasing due to the increased refractive index, because of phase changes at the interface as per the Fresnel coefficient for planar incidence, $R = (\frac{n_1 - n_2}{n_1 + n_2})^2$. There is a $\approx 20\%$ difference between the original mat and the theoretical film, but only a few percent difference between the subsequent submerged films, indicating the reflectance value drops are due to the surrounding medium refractive index changes.

However, the lineshapes of the experimental mat spectra and the modelled continuous film spectra differ significantly. There is a noticeable extra dip in the reflection spectra of the mats which is located around 550nm for air and water and around 680nm for the high index iodonaphthalene, which is also seen in the scattering spectra. The second difference is the decrease in the reflective intensity going into the infrared. Extended spectra taken into the infrared show this decrease in intensity at longer wavelengths (figure 7.4). This is in stark contrast to a theoretical gold film which maintains its intensity out into the IR. These differences arise from the optical response of the mat being caused by a coupling of localised plasmons rather than collective movements of the free electrons in a gold film. In addition to the spectral shift a sharp dip appears in the spectra at around 1250nm. This is attributed to absorption from the iodonaphthalene.

The movement of iodonaphthalene into the interparticle gaps of the nanoparticle mats is the source of the observed optical changes. The infusion into the gaps is not instantaneous and therefore the movement of the oil into the gaps can be observed optically by taking spectra over time. An initial reflection spectra of the sample was taken before a droplet of iodonaphthalene was drop cast onto the mat. The microscope was refocused through the

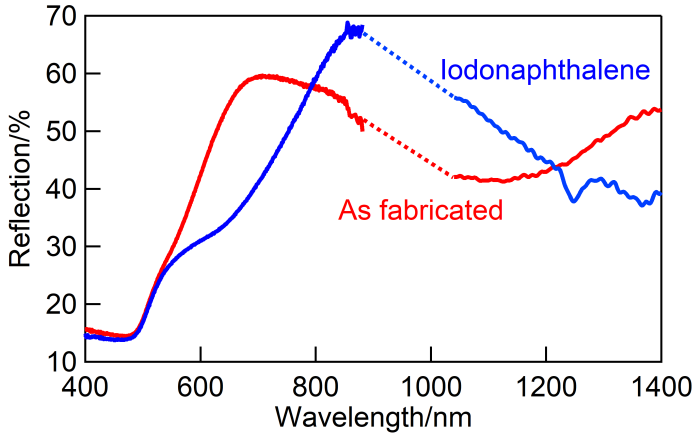

Fig. 7.4 Reflection spectra from 60nm gold nanoparticle mats as-fabricated (red) and infused with n=1.7 refractive index oil (iodonaphthalene) (blue) ranging from the visible to near-IR. The reflection from the nanoparticle mats shows a significant decrease after reaching a peak value, in contrast to the continuous gold film.

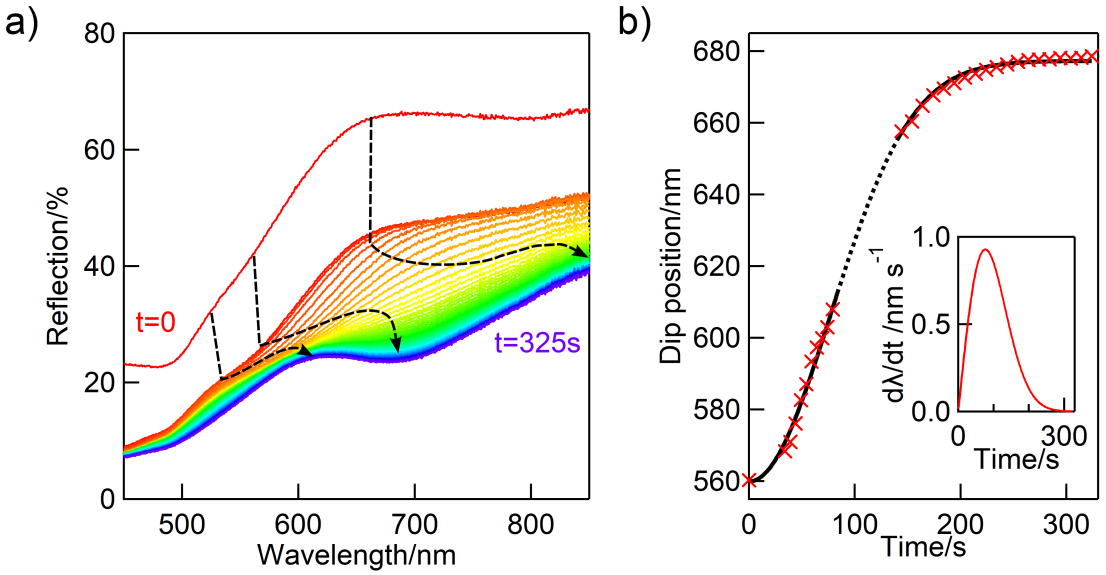

Fig. 7.5 a) The infusion of iodonaphthalene into a 60nm nanoparticle mat over time from initial infusion over a period of 325s (from red to blue). The spectra changes gradually as the iodonaphthalene infuses into the gaps between the particles with the significant features of the spectra redshifting as the population of iodonaphthalene molecules in the gap increases (highlighted using dashed lines). b) The shift of the dip over time showing a slow initial diffusion before a constant rate of change and finally reaching a saturated value. The gap in data arises from an obscuration of the dip in the reflection spectra (dashed line). Inset shows the rate of change of the dip position against time showing a rapid initial shifting before peaking after 75s then dropping until the gaps are saturated.

droplet, and reflection spectra were taken every second for 5 minutes. The tracked infusion is shown in figure 7.5a. The spectra begins to change immediately after the introduction of the iodonaphthalene and continued to shift for over 5 minutes. The optical change was measured by tracking the position of the dip in the reflection spectra, enabling the analysis of the rate of change of the optical response and hence the movement of distinctive features in the spectra (figure 7.5b). Initially, the rate of change in the dip position is rapid, with a rate of change of dip position reaching a maximum of 0.93nm/s 75 seconds after deposition. After this time, the rate of change decreases until it falls below 0.2nm/s after 250s, before stopping entirely after 330s (figure 7.5b, inset).

The rate of spectral dip movement was fit to a cumulative distribution function based upon the rate of change of the dip position over time, indicative of diffusive behaviour where a limited total of iodonaphthalene molecules move into the mat until reaching a saturated value. During the period of rapid shifting (between 90 and 140s) the reflection dip becomes less visible in the spectra making it difficult to fit its position. However, the fit to the distribution function suggests that the rate of shifting remains consistent within this region, and therefore that the dip is merely obscured or flattened due to other moving features in the spectra, rather than the dip being two separate features with differing origins.

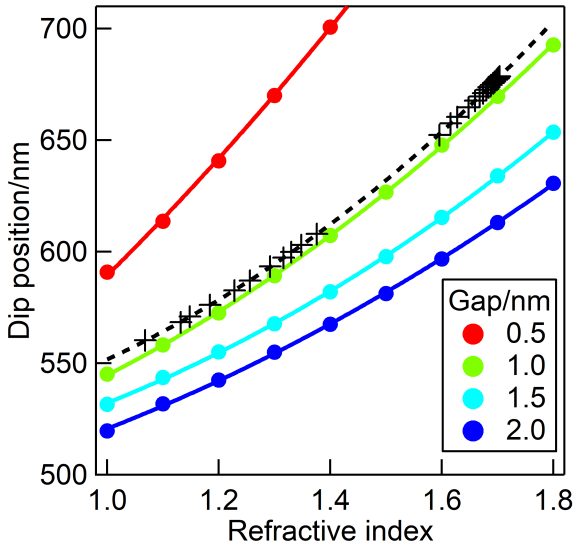

Fig. 7.6 The shift in the dip position fitted to theoretical calculations of the dip positions for different interparticle gaps and refractive index values of the interparticle media. The data is fitted assuming that the maximum value of refractive index is that of iodonaphthalene, with a value of 1.7, and fitted backwards giving an interparticle separation of 0.95 ± 0.1nm and a starting value of the gap refractive index $n_{gap} = 1.1$.

The particle separation of the 60nm nanoparticle mats can be found through fitting the moving spectral dip to calculated FDTD reflection spectra with differing interparticle spacings and refractive index values. The fitting was done by assuming that the maximum refractive index value of the gaps was $n_{gap} = 1.7$, arising from a saturation of iodonaphthalene with no contribution from the thiol present. The result is an initial index value of $n_{gap} = 1.1$ and an interparticle separation of 0.95 ± 0.1nm (figure 7.6). This separation is significantly less than the gap distance extracted for the 20nm mats from the previous chapter, despite the same particle surfactant. This discrepancy can be attributed to a larger van der Waals attractive force between the particles pulling the particles together for a closer equilibrium state [165].

The diffusion of iodonaphthalene into nanoscale gaps has been measured optically. Due to the restricted volume of the gaps, only a limited number of iodonaphthalene molecules can transfer into the interparticle spaces. The observed optical shift originates from the changing dielectric properties in the interparticle gaps, showing a slow diffusion on the order of minutes. This change in refractive index enables the estimation of particle separation through comparison to simulated FDTD calculations.

7.3 Changing spacing via varying surfactant length

As a contrast to increasing gap separations in nanoparticle monolayers via the application of strain, it is possible to alter the spacing between particles by changing the surfactant on the nanoparticle surface [99, 120, 166]. By changing the thiols used as particle surfactant and replacing them with alternative ligands, a different number of carbon links in the thiol chain, the interparticle separations can be altered.

During the liquid-liquid interface assembly method, the 1-dodecanethiol (12 carbon atoms, DDT) was switched out a selection of different thiols, detailed in table 7.1 below. In this manner small flakes ($1mm^2$) of 60nm gold nanoparticle mats with different surface functionalisations were made. The small areas formed were due to no optimisation used for the

Thiol	Chain length
1-dodecanethiol	12
1-nonanethiol	9
1-butanethiol	4

Table 7.1 A list of thiols and their associated carbon chain lengths used for experimentation.

assembly process, but were large enough areas for experimentation.

Additionally, an alternative fabrication method developed by Dr Vladimir Turek was utilised for a further comparative measure. This method assembles monolayers of nanoparticles without a thiol capping layer [152, 167], and again uses a liquid interface as a potential well to trap particles at a liquid-liquid interface. However, in this instance the surface tension is higher than in the primary method of liquid-liquid assembly detailed in this thesis. The higher surface tension was achieved by using a different solvent, dichloroethelene, enabling the assembly without the thiol surfactant. The self-assembled arrays were removed from the interface via pipette, and placed on a substrate to dry. The lack of thiol coating alters the interactions between the particles, removing the steric repulsion present from the thiol ligands and instead relying on electrostatic repulsion to prevent nanoparticle agglomeration.

The reflection and scattering spectra from each of these nanoparticle mats are shown in figure 7.7. Each spectra is normalised to its highest value in the wavelength range to aid comparison between them. As before, the reflection and scattering spectra show the same peak positions, indicating the homogeniety of the two, with the exception of the dichloroethelene method assembled nanoparticle mat, which displays a sharp drop in scattering intensity after a second peak at 700nm.

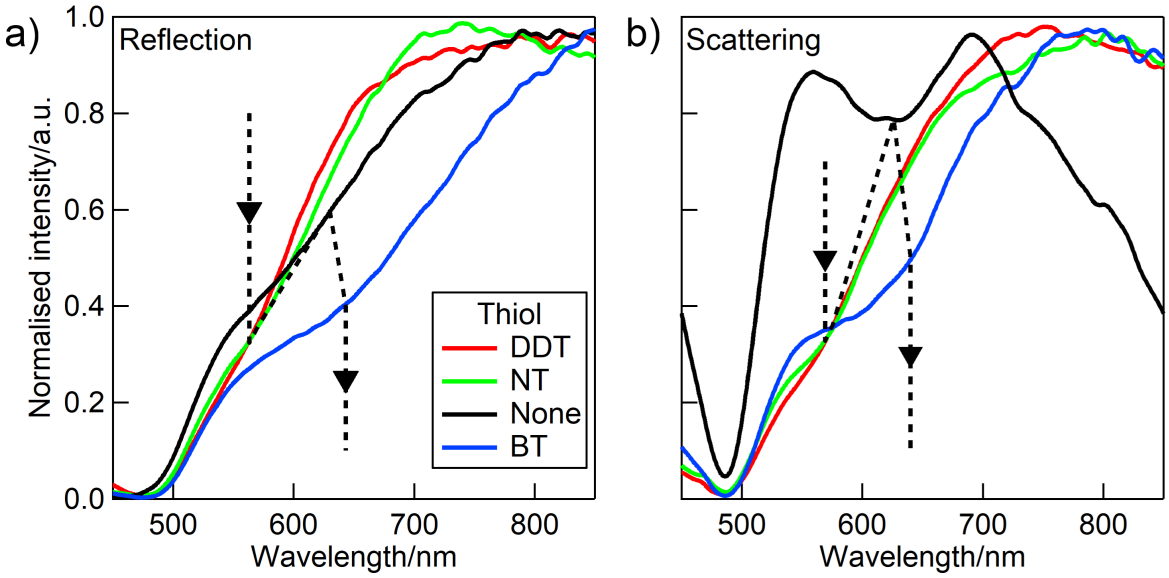

Fig. 7.7 a) Reflection and b) scattering spectra normalised to their maximum values from nanoparticle mats assembled using different length thiols (red, green and blue) or, alternatively, with no thiol surfactant (black). The dashed black line follows the dips in the reflection and scatterings data, showing a redshift of 75nm as the thiol length is decreased.

As the thiol length decreases (from 12 carbon links to 4), there is a distinct redshift in the spectral features with a magnitude of 75nm. This indicates that the coupling between particles is increasing in strength, due to a decreasing particle separation. In order to give a value of this interparticle separation, the refractive index of the interparticle medium was estimated using the initial value found from the infusion data above, specifically $n_{gap} = 1.1$. We can therefore assume that either the refractive index is constant and independent of the thiol length, or alternatively the refractive index value of the gap is variable depending on the conformation and density of the thiols coating the nanoparticles.

These two behavioural extremes are plotted onto the theoretical plots of dip position against interparticle separation for different refractive index values ranging from n= 1.0 to n= 1.5 in figure 7.8. The theoretical values of the dip positions for gap distances of 0.5, 1, 1.5 and 2 nm are plotted and fitted using a power law dependence. Using the above starting point of n= 1.1 for DDT, with constant value for n, the interparticle separation for BT is 0.4nm, a reduction of 55% from the separation in the DDT coated mats. Alternatively increasing the refractive index could also explain the shift in the dip position. A second fit is also performed, with the BT positioned at the refractive index value of BT, n=1.44. In

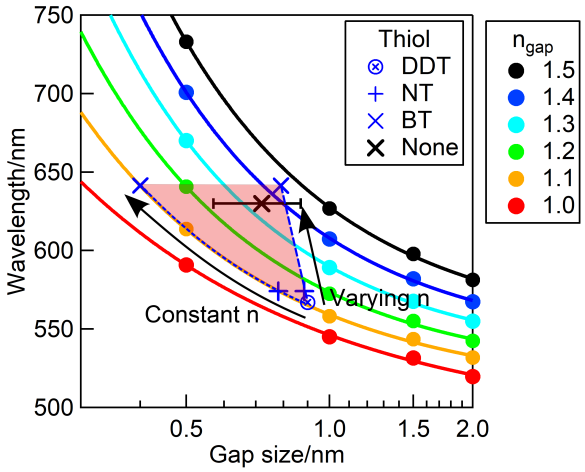

Fig. 7.8 Spectral dip positions from nanoparticle mats fabricated using dodecanethiol (DDT, 12 carbon chains), nonanethiol (NT, 9 chains), butanethiol (BT, 4 chains) and without thiolation, compared to theoretical values of the reflective intensity dip, for mats with varying size spacings and refractive index values of the gap. Two alternative fits are suggested, with constant value refractive index of the gap (short dashed line) and varying refractive index (long dashed line) with the area of potential values of d between them highlighted in red. The unthiolated mat is fitted to an approximate value of n based on the refractive index of water.

this instance, the change in interparticle separation is 0.1nm, a drop of 11%.

With the refractive index of the gap kept constant, the interparticle separation for the BT ligand, at 0.4nm, is far less than might reasonably be assumed, as at this point the calculated spectra are likely to be less accurate due to potential quantum effects and charge transfer between particles beginning to affect the plasmonic response [24, 168]. Such effects would also likely result in significant changes to the spectra and can be discounted. Therefore, we can conclude that the refractive index value of the gap increases with different thiols. This can be explained by changes in the orientation and organisation of thiols on the nanoparticle surface. For example, such refractive index increases could be caused by an increase in density of thiols in the gap, where the SAMs forming on the particle surface are either arrayed along the particle surface, or interdigitated together. In the extreme case of increasing refractive index, the interparticle separation reduces only 0.1nm, which suggests that electrostatic repulsion is playing a significant role in defining the interparticle separation, rather than steric repulsion from the thiol ligands. It is expected that the actual value of separation lies between these two extremes, shown as the red shaded area on figure 7.8, with both the molecular orientation and interdigitation of the SAMs, as well as closer interparticle separations due to the reduced chain lengths of the SAMs.

The interparticle separations indicated by these fits are up to 50% smaller than have been observed elsewhere [99, 120]. This is attributed to forces during the fabrication of the mat affecting the molecular organisation of the SAM. As reported by Pei et al. [121], the organisation of thiol molecules on the particle surface can be affected by the solvents used in the fabrication process. Hexane molecules are unable to penetrate the thiol layer, resulting in a twisted and deformed SAM that allows for closer interparticle separations than would be allowed for by a rigid thiol layer. This change in molecular orientation is expected to have a considerable impact on both the minimum particle separation distance allowed by steric repulsion, as well as molecular densities that could impact refractive index values. At these single nanometer length scales, it is unclear how the different potential factors such as the interdigitation of thiols, the conformation of thiol on the particle surface and deformation of thiols in response to both interparticle attractive forces and interactions to solvents, affect the refractive index of the gap. More work, both in theoretical modelling and experimentation using simpler controllable systems, such as movable ball tips to manually manipulate interparticle separations [168], are suggested to further define these parameters.

SEM images of the mat made using DDT are used to try and confirm the optical measurements of interparticle separation. Nanoparticles are found to be 58 ± 6nm in diameter. Using

this diameter, the average gap distance is found to be 0.7nm but the wide size distribution of the nanoparticles results in an error significantly greater than this distance, resulting in a potentially inaccurate measurement. However, as this value is within the same order of magnitude as calculated above, this suggests that the gap length is indeed between 0.6 and 1.2nm.

The dichloroethelene fabricated mat without any thiols present, is positioned with a refractive index of $n_{gap} = 1.33 \pm 0.1$, based upon the refractive index of water, n= 1.33[168]. The subsequent placement sets it within error of the fit line for increasing refractive index, with an approximate interparticle separation of 0.7 ± 0.2nm. The potential error here is large due to the uncertainty in the refractive index value of the gap. However, this value is also very similar to those of the thiolated particle mats suggesting that minimal particle separations are defined by charge separation rather than due to steric repulsion from ligand coatings.

7.4 Interpreting the optical response of larger diameter nanoparticle mats

The optical behaviour of small nanoparticle aggregates is dominated by scattering with minimal reflective intensities. The frequency of this scattering is determined by the coupling between these particles, with coupled particles showing a redshifted resonance compared to that of a single particle. For example, dimer and trimer modes are the result of coupling between two or three particles respectively. Aggregates made up of greater numbers of particles display a more complex optical response that is defined as combinations of different resonant conditions occurring within the structure. Large aggregates of nanoparticles, formed using a linking molecule, have an optical response that can be estimated as the sum of the single, double and chain resonances within the particle aggregate[28]. Further theoretical studies of these chain aggregates showed that more potential resonances arising from different length chains can also be found within the optical response[30].

A study on 2D metallic nanoshell arrays displayed a similar composite optical response. The observed extinction from the array showed a sharp peak from the quadrupolar optical response of the individual particles and a broadened resonance extending out into the infrared due to the coupling of the dipolar response across the array. This lead to large field enhancements across the gaps over wide ranging wavelengths[29]. Calculated spectra of these arrays showed that this broadening is amplified by anisotropy in the arrays, with de-

fects and imperfections in the fabricated arrays resulting in broader coupling and greater intensity local field enhancements.

In order to further interpret the behaviour of our nanoparticle mats, the transmission spectra gained from the 60nm nanoparticle mats is used to calculate the optical extinction. This is shown in figure 7.9. As expected, the peaks in the reflection spectra roughly align with those of the extinction spectra, indicating that the reflective intensity of a mat is an acceptable measure of the plasmon resonance. Interestingly, in figure 7.9a, there is a significant drop off in the intensity of the extinction in comparison to that of the reflection from the mat. The high intensity reflection arises from interference effects cancelling out high-angle scattering of light, resulting in a coherent backscattering from the film [34].

In order to fit the extinction spectra, a similar method to that used by Taylor et al. [28] is taken, simultaneously fitting both resonances. Due to the broadening of the resonances arising from the defects in the particle array, Gaussian functions were used, as opposed to the sharper Lorentzian functions that correspond to sharper plasmon resonances from structures with a greater degree of homogeneity, such as those found in rigidly spaced nanoparticle chains.

The extinction curves show the presence of two peaks in the lineshape. The as-fabricated mat shows a distinct peak around 540nm before reaching a maximum extinction at 640nm. This two peak structure results in the dip in reflective intensity observed above. The infusion of the iodonaphthalene (7.9b) redshifts the two peaks by 30 and 190nm respectively. These peaks are attributed to those of the single particle transverse resonance, and an array resonance, with the particles across the mat coupling together. The dip in the spectra that is present in both the reflection and extinction spectra is therefore a result of the reduced interaction of incident light and the mat at these wavelengths.

An alternative explanation for the reflectivity dip is the presence of a Fano type resonance. These have been observed for small clusters of hexagonally close packed nanoparticle clusters [169] where the Fano resonance arises from the superposition of two separate resonances [170]. However, the presence of a Fano resonance is discounted due to the gradual broadening of the dip after the introduction of the higher index oil, and literature detailing larger clusters of nanoparticles without such resonances [29, 171]. Additionally, Fano resonances typically arise as a result of the supposition of higher order modes, such as a quadrupolar mode.

The fitted values for these two resonances for all refractive index fluid tests are shown in fig-

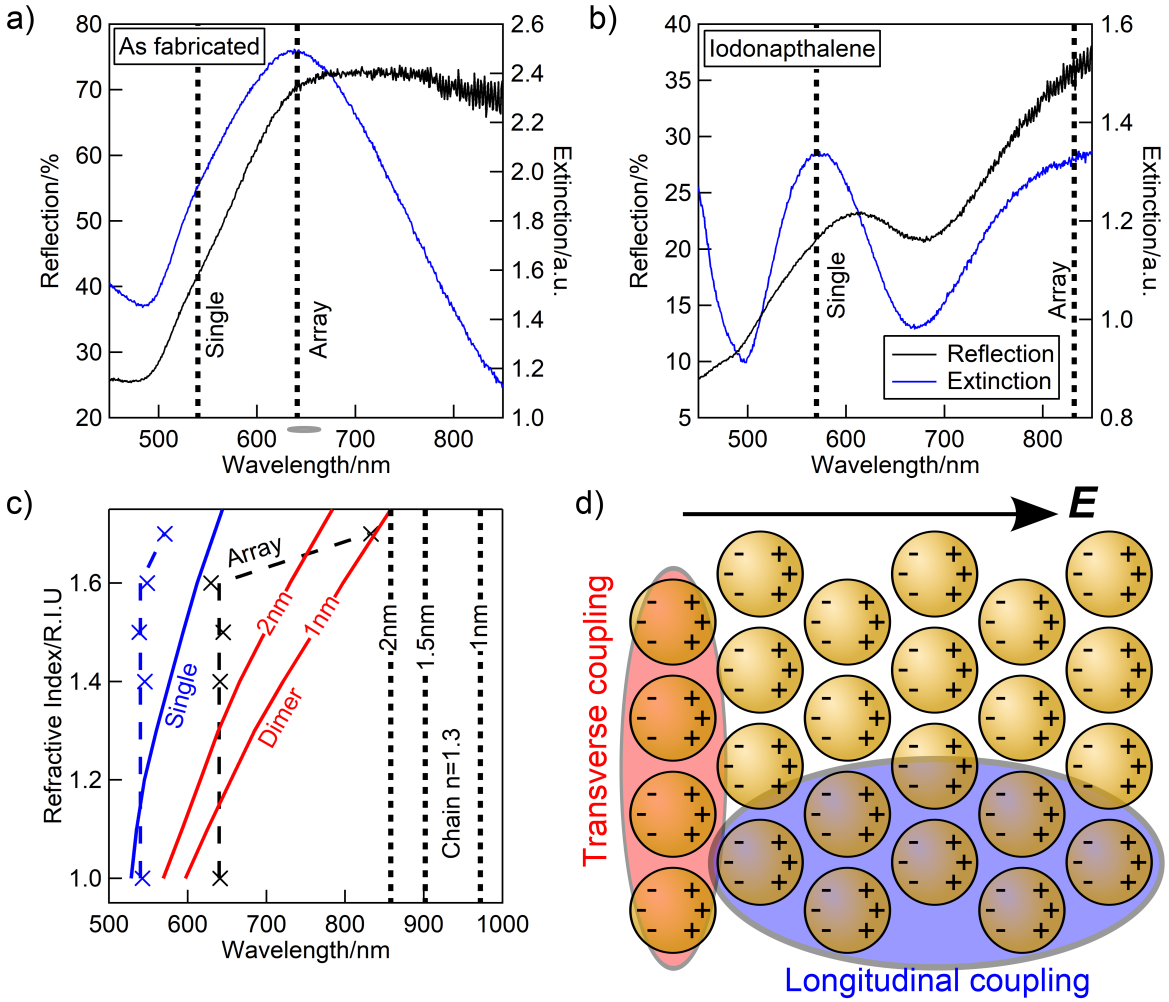

Fig. 7.9 The reflection spectra (black) and extinction spectra (blue) from a 60nm nanoparticle mat both a) before and b) after the infusion of iodonaphthalene into the interparticle medium. Fitted values for the single particle and array plasmon resonances are shown as dotted lines. c) Fitted resonances from the extinction spectra for varying refractive index fluids. Calculated single particle, dimer, and chain resonances are also illustrated in blue, red, and black respectively. The array resonance is shown to be closer in value to the dimer resonance than the values of an equivalent chain resonance. d) The lower than expected values for the array resonance are attributed to the simultaneous transverse (red oval) and longitudinal (blue oval) coupling of the particles across the array, resulting in a broadened higher frequency resonance than that of a lone chain.

ure 7.9c. These again show that the resonance positions are not observed to change by more than 10nm with respect to the initial value. This confirms that there is no local refractive index change in between particles until the introduction of the n=1.7 iodonaphthalene results in significant redshifting. The array resonance is shorter than would be expected from the previous results with smaller nanoparticle arrays as seen in Chapter 6. In this instance the resonance values are 200nm less than the calculated chain resonances. This is attributed to the larger particles having a more influential interaction transverse to the incident E-field resulting in resonances that are both broader and of lower wavelength. The chain model for plasmonic interactions of an array of particles falls down in the region 20 $<$d$<$ 60nm meaning that only more complicated FDTD modelling can be used to explain particle interactions for larger particle arrays.

The broadening observed in these resonances both here and elsewhere[29, 30] results in high intensity near-field coupling over a wide range of wavelengths. There are variations in the intensity of the field introduced due to imperfections in the nanoparticle lattice as well as differences in nanoparticle morphology, such as flattened particle surfaces deviating from the spherical particle ideal. The effects of this on local field enhancement are explored in the next chapter. The long range coupling of particles is shown in the far-field by an array plasmon that is shown to redshift as the local refractive index of the particle changes. These resonances are seen in the extinction spectra, but also define the reflection spectra due to the backscattering of light from the nanoparticle mat [34].

7.5 Stretching larger nanoparticle monolayers

Uniaxial strain was applied to self-assembled 60nm gold nanoparticle mats both with and without high index oil. Unlike the mats fabricated using smaller diameter nanoparticles, no obvious shifting of the reflection spectra was observed, particularly with the unpolarised (figures 7.10a and 7.11a) and parallel polarised (figures 7.10b and 7.11b) data sets.

For as-fabricated mats, without index oil, very minimal shifting is seen in the fitted resonance positions. For an applied strain of 39%, the array resonance shifts to the red by 9 and 7nm for the unpolarised and parallel polarised spectra respectively. This occurs simultaneously with a 30% decrease in the observed reflective intensity. This minor redshift is suggestive of a slight decrease in the interparticle separation, which is counter to the increase that would be expected. This is attributed to a minor reorientation of the particles, similar to sheer-induced ordering [172] whereby strain variations over a given area induce

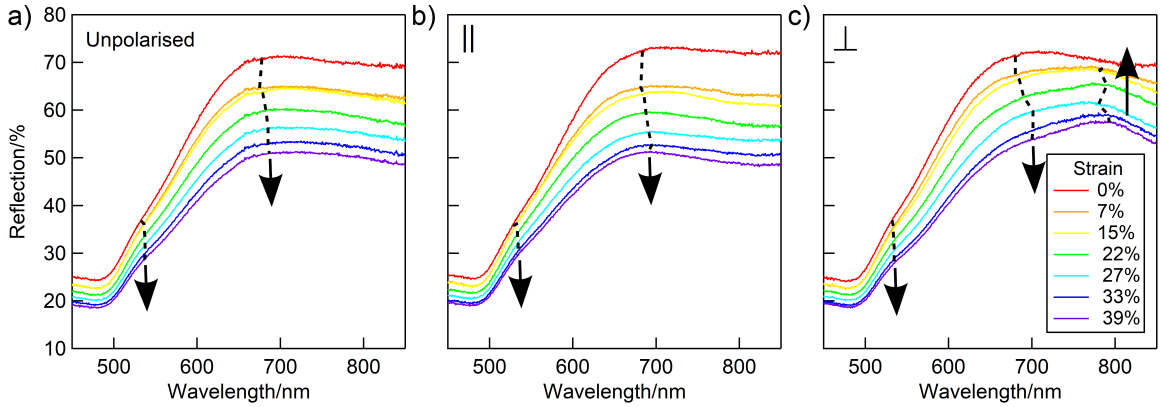

Fig. 7.10 Stretch measures of an as-fabricated mat (without iodonaphthalene) using a) unpolarised, b) parallel polarised and c) perpendicular polarised light. Peak positions are shown with dashed black lines.

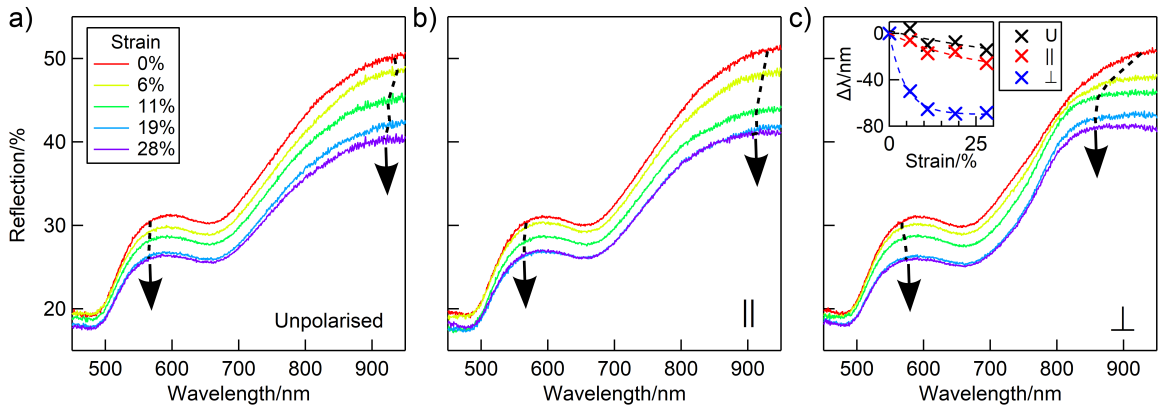

Fig. 7.11 Stretch measures of a 60nm gold nanoparticle mat after infusion of iodonaphthalene (n= 1.7) using a) unpolarised, b) parallel polarised and c) perpendicular polarised light. Peak positions are shown with dashed black lines. Inset in c): The peak shifts of the array resonance for the oil infused mats (unpolarised in black, parallel in red, perpendicular in blue).

changes in particle orientation. With light polarised perpendicular to the stretch axis, more complex behaviour is observed. The array resonance is seen to redshift by 20nm, and a new peak in the data, which shows no clear shifting behaviour, is seen to appear at 790nm.

After the introduction of the high refractive index oil, changes in the array resonance are more typical of what is expected, with blueshifts of 15nm and 25nm for unpolarised and parallel polarised light respectively for 28% strain (figure 7.11c inset). The perpendicular data set also shows a blueshift, indicating the separation of particles. However, this blueshift is observed to be much greater than the other polarisation, with a 70nm shift of the array res-

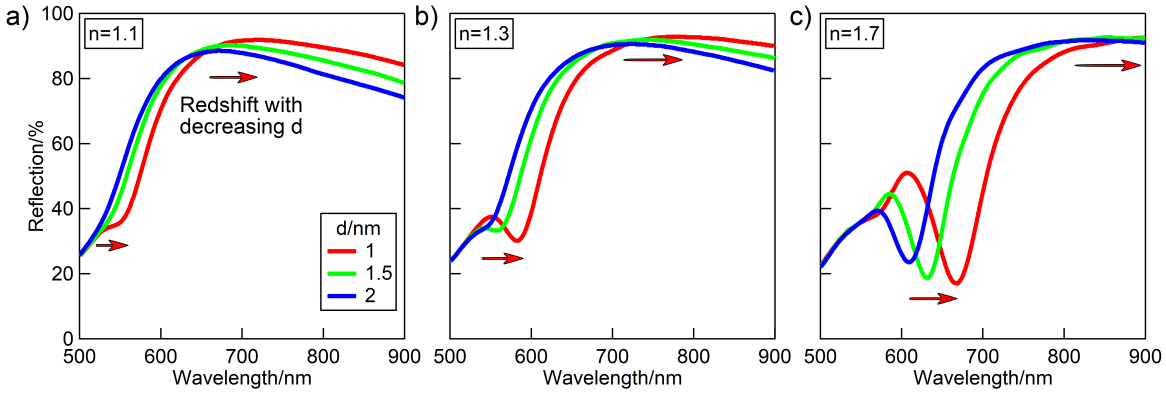

Fig. 7.12 FDTD calculations for 60nm gold nanoparticle mats in different refractive index media, a) $n_{gap} = 1.0$, b) $n_{gap} = 1.3$ and c) $n_{gap} = 1.7$. The changes of the spectra shown are due to decreasing interparticle separation from 2nm (blue), 1.5nm (green) and 1nm (red).

onance. Small blueshifts are also observed with the single nanoparticle resonance, though only on the order of a few nanometers. The rate resonance position change in the perpendicularly polarised case is significantly more than previously observed in mats made using 20nm nanoparticles. A power-law fit shows $\delta\lambda \propto d^{-22}$, significantly larger than the value of $d^{-0.6}$ previously observed in the smaller diameter mats. This drastic shift corresponds with a gradient change in the spectra, resulting in a local relative increase in the reflective intensity with respect to the rest of the mat. Elsewhere, a maximum decrease of reflective intensity of 20% of the initial value is observed. Therefore, whilst this shifting broadly matches the expected behaviour of a mat of nanoparticles with increasing gap separations, the asymmetry of the result across polarisations, as well as the small blueshifts of the unpolarised and parallel polarised data sets, suggests that the movement of these nanoparticles is different than previously observed with smaller diameter particles.

FDTD calculations for reflection from these mats were performed in order to compare theoretical values with experimental data. These show distinct changes dependent upon interparticle spacing and the refractive index of the surroundings (figure 7.12). As the nanoparticle separation decreases, the resonances are seen to significantly blueshift, up to 70nm in the case of n=1.7, from 1 to 2nm separation. As the stretch spectra do not show this uniform blueshift, this further indicates that the particles are not uniformly separating, and that some other mechanism is driving the changing optics.

Investigation of the sample during stretching under 100 times magnification showed that, instead of each particle evenly separating with applied strain, clusters of particles are moving (figure 7.13). The width of these aggregates falls between 0.5 and 1.5μm, with each

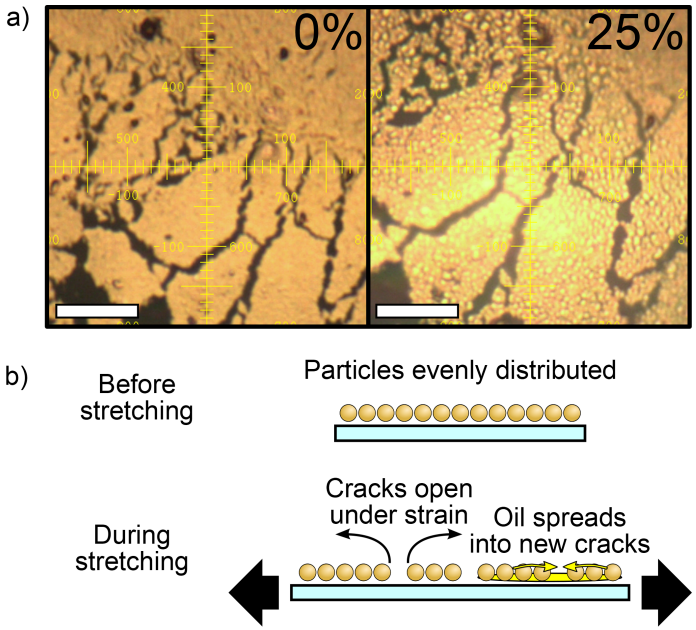

Fig. 7.13 a) 100x microscope images of 60nm gold nanoparticle mats at 0% (left) and 25% (right) strain. After applied strain, mats are observed to break up into small islands of d$\approx 1\mu$m. Scale bar 10μm. b) Sketch of crack formation under strain. After stretching, small aggregates stick together, resulting in the emergence of cracks in the mat. Any unbound oil can then move freely into these cracks, changing the refractive index of the gap.

aggregate made up of a small number of particles, $50 < N_{particles} < 200$. As has been previously reported, chain resonances saturate at a certain length, usually $N_{particles} > 18$ particles [26, 28, 173]. Beyond this size, resonances no longer shift, as particles beyond a set distance no longer influence each other. Similar effects have been observed in clusters where greater numbers of particles added to clusters beyond a certain size resulted in broadening of the resonance rather than shifting [29].

The behaviour observed in our spectra can therefore be explained by the separation of nanoparticle clusters without a change in their spacing. The rising peak observed in the as-fabricated mats for light polarised perpendicular to the stretch axis (figure 7.10b) can be attributed to some contraction along this axis. The clearer blueshifting observed with higher index oils can, instead of being attributed to particles moving, be attributed to the movement of iodonaphthalene. As the high index oil is not bound to the particles under strain, the oil can move into the cracks around the mat, resulting in a thinning of the oil coating and therefore a refractive index decrease (figure 7.13b). This could also explain the relative lack of movement for the single particle resonance, as this would display less sensitivity to this change than the array plasmon. Alternatively, the shift could potentially arise as a result

of clusters with widths of $N_{particles} < N_{saturation}$, resulting in the chain length shortening as a grouping of particles is separated into two smaller groupings. This effect could explain the larger resonance change perpendicular to the stretch axis in figure 7.11c as the applied strain may result in clusters where $N_{\parallel} > N_{\perp}$, resulting in asymmetric clusters with greater length along the stretch axis. Finally, as observed previously, the intensity change is caused by the movement of clusters from out of the spectral collection spot, resulting in less material to reflect back light with respect to the initial value, in a similar manner observed when stretching an evaporated gold film (shown in section 6.1).

As the polarisabilty exhibited by nanoparticles increases as a function of diameter, this can predict a simultaneous increase in attractive forces between particles [174]. An increase in binding can be inferred from the strength of the field enhancement between the particles [165]. As the van der Waals force scales $\propto r$, larger diameter particles have a greater attractive force binding them together; the 60nm particles have 3 times the attractive force of the 20nm mats. Additionally, these mats have not been encapsulated, and indeed attempts to encapsulate failed. It is suspected that excess DDT left over from the fabrication process prevents the curing of the PDMS layer added on top of the mat. Due to this the lack of encapsulation, the stretch force is only applied on the lower side of the mat in contact with the substrate, instead of on both sides, reducing the application of strain on the particles.

With increasing particle diameter, the stretch tunability of a nanoparticle mat is limited. The attractive forces between particles result in the formation of nanoparticle clusters upon stretching, instead of uniform particle movement. However, the interactions between these particle clusters will be different in the near-field.

7.6 Summary

Larger diameter nanoparticle mats are optically different to those of sub-30nm diameters. The subsequent arrays no longer display an optical response that can be accurately modelled as a nanoparticle chain. Instead, the transverse coupling between particles interacts with longitudinal coupling, resulting in an array resonance that can only be accurately modelled by more complex simulations of the entire system. This coupling results in a broadened resonance that enables the interaction with light over long wavelengths into the infrared.

Upon the application of strain to these nanoparticle mats, only small wavelength shifts are observed, especially in comparison to mats made with smaller diameter nanoparticles. This

is due to the greater degree of attractive forces between the particles, resulting in the movement of nanoparticle clusters instead of individual particles. As these clusters couple to each other, the plasmonic interaction between them, in addition to the already broad wavelength coupling of these large diameter mats, result in ideal substrates for near-field sensing applications and it is these that are explored in the next chapter.

Chapter 8

Strain induced SERS enhancements in nanoparticle mats

The scattering of photons from the molecular bonds of molecules gives a fingerprint of the molecule itself, enabling molecular sensing. The intensity of light scattered in this way can be increased by using plasmonic structures, such as nanoparticle arrays, as a substrate. The focusing of the electric field between components of plasmonic nanostructures enables a dramatic increase in the interaction between incident light and the gap contents, a technique known as surface enhanced Raman spectroscopy (SERS). In this chapter, the potential of stretch tunable nanoparticle mats as SERS devices will be explored. The enhancement to the near-field is used to increase the intensity of Stokes scattering to identify molecules placed on and around the nanoparticle surface.

8.1 Strain enhanced SERS of dodecanethiol within nanoparticle mats

SERS signals were obtained from liquid-liquid interface assembled monolayers of 60nm diameter gold nanoparticles. Larger sized particles were used due to the relative ease of monolayer assembly and broadened resonance over a wide range of wavelengths. DDT was used as the initial analyte for detection. A self assembled monolayer is formed on the particle surfaces during mat fabrication. Initial experiments with a 50x objective and an $\approx 1\mu$m spot size showed that a 785nm laser obtained the cleanest spectra for detecting the thiol. The signal strength here was a benefit of the broad resonance observed in the mats

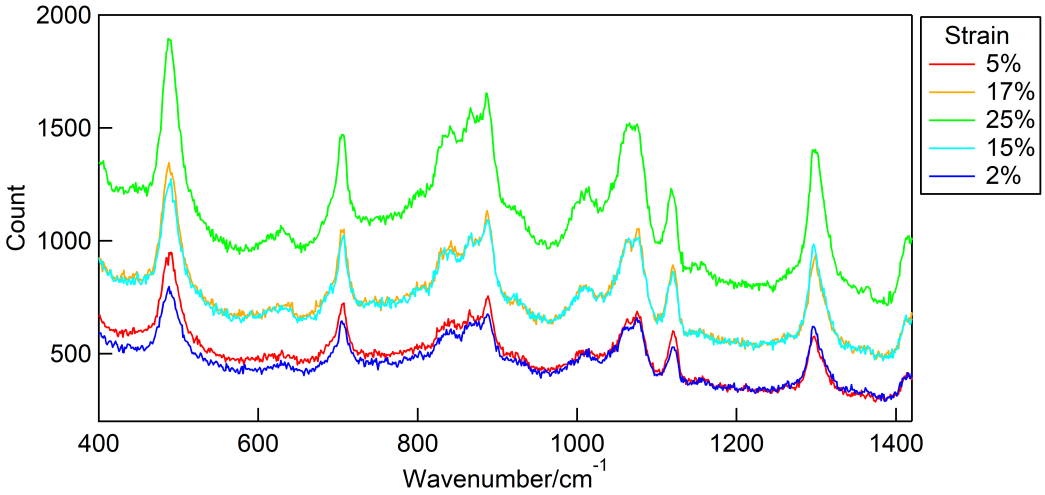

Fig. 8.1 Strain amplified SERS spectra of a 60nm gold nanoparticle mat on PDMS. As the strain is increased, both peak amplitudes and the background intensity rise (red to green). With a decrease in strain back to zero, the spectra returns to the original intensity (blue).

despite the maximum enhancement occurring around 650nm.

Observed SERS spectra show a match to literature sources [175]. Stretching was carried out with nanoparticles mats on PDMS and polyurethane (PU). PU allows for higher values of strain than PDMS films, although is irreversibly deformed after stretch measurements. PU also has rougher surface than PDMS.

Upon the application of strain, the signals of both the Raman modes and the background increase (figure 8.1). By using PDMS as the substrate, reversibility can be tested. It was found that upon relaxation after stretches of up to 25%, almost identical signals to initial values were returned. Both the background signal and the peak amplitudes behave in this manner. Similar behaviour is observed from the PU stretch, with signals increasing on most of the Raman peaks up to 75% strain (figure 8.2). The positions of the vibrational modes matches well to previously measured self-assembled 1-DDT monolayers (table. 8.1) therefore it is assumed that the molecules were predominantly bound to the nanoparticle surface, with no unbound thiols being evident in the SERS spectra.

The total signal count of the vibrational modes minus the background signal was observed to increase up to four times after strain is applied (figure 8.3). This enhancement is not even across all vibrational modes, varying from a maximum amplification of three to four times at 75% strain. The average enhancement is shown via a dotted line on both figures. Upon relaxation of the PDMS film, the enhancement values closely follow those of the

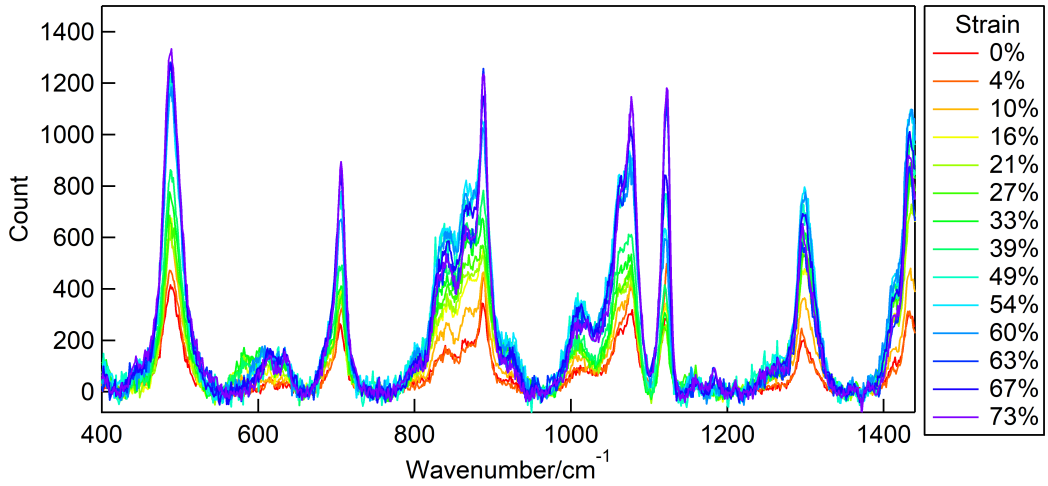

Fig. 8.2 SERS spectra of DDT from a 60nm gold nanoparticle mat as-fabricated (without iodonaphthalene) on polyurethane. The background has been removed to show the increase of the different vibrational modes as the strain increases.

Vibrational mode	Bulk liquid	SAM	L/L interface	Measured
$\nu(C-S)$, G	654	636	608-14	610-632
$\rho(CH_2)$	707			
$\nu(C-S)$, T	735	707	659-709	704
$\rho(CH_2)$		789	788	798
$\rho(CH_2)$	850		849	836
	870	869		867
$\rho(CH_3)$, T	889	892		888
	925	933	900-925	920-925
$\rho(CH_3)$, T	960			
$\nu(C-C)$, T	1064	1064		1061
$\nu(C-C)$, G	1081	1081	1080	1074-1078
$\nu(C-C)$, T	1120	1097		
$\nu(C-C)$, T		1126	1118-1126	1119-1122
		1189		
		1215		
$\omega(CH_2)$	1301	1300	1295-1298	1296-1301
		1329		
$\delta(CH_2)$		1430-1450		1435-1450

Table 8.1 SERS spectral positions (cm^{-1}) of dodecanethiol from the bulk liquid, a self-assembled monolayer, a liquid-liquid interface and as experimentally measured. Data and assignments sourced from [175, 176]. Key to terms: ν, stretch modes (G, gauche and T, trans conformations); ρ, rocking modes; ω, wagging modes; δ, bending modes.

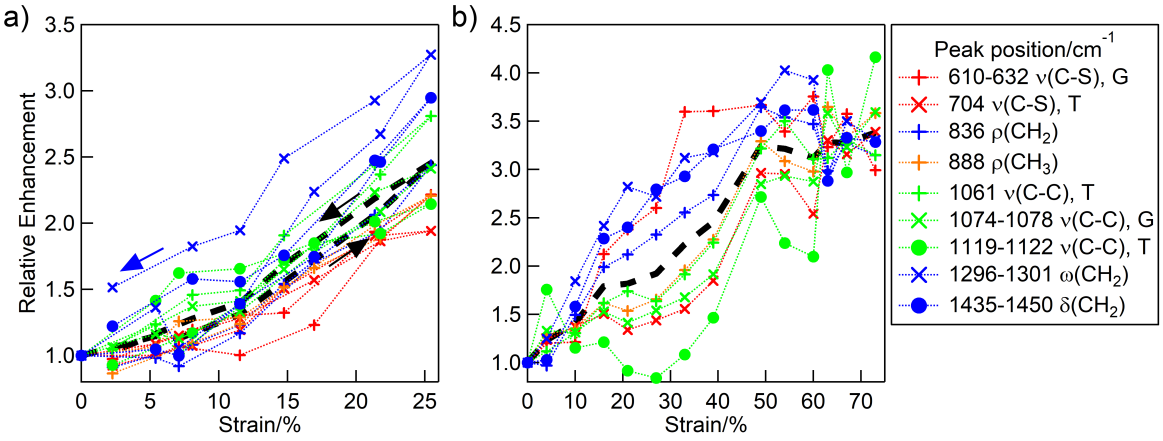

Fig. 8.3 The relative enhancement in intensity of the different vibrational modes of 1-DDT increasing against strain on a) PDMS and b) PU substrates. The overall enhancement varies depending on the different modes, shown with the various markers. The average enhancement is shown in the dashed black line, with direction of strain for the PDMS strain shown with arrows. Key to terms: ν, stretch modes (G, gauche and T, trans confromations); ρ, rocking modes; ω, wagging modes; δ, bending modes.

outward strain. The average enhancement is almost identical upon relaxation, indicating good repeatability of the enhancement with strain.

The behaviour of the average enhancement differs between the two substrates. For the PDMS substrate, the rate of enhancement increases with strain. However, for the PU substrate, a linear behaviour is observed until a saturation point. The enhancement behaviour for the individual modes in the PU strain show a wider distribution than those of the PDMS case. In particular, with the PU substrate, the relative enhancements of the gauche and trans modes for the C-S stretch mode (figure 8.4a) show a divergence after 15% strain before returning to similar values of enhancement after 50% strain. This indicates orientational changes of the surfactant on the particle surface with applied strain, with the DDT transitioning from transverse to gauche conformations (figure 8.4b). Additionally, the gauche C-S stretch mode appears to shift significantly between $610-632\text{cm}^{-1}$, further indicating this reorientation. Previously, it has been inferred that thiol ligands can be compressed and deformed around nanoparticle arrays due to interactions with solvents used during assembly processes, this result indicates a similar effect is happening here [121]. The average enhancement observed in the PU substrate caps at a value of 3.3 ± 0.2 times the initial signal strength beyond 50% strain, with only minor changes observed beyond this strain value, as well as tightening in the distribution of enhancement values.

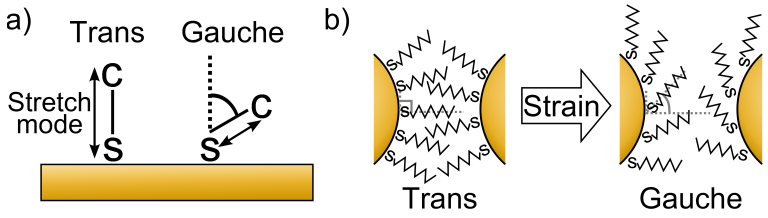

Fig. 8.4 a) A schematic of the trans and gauche conformations of a C-S bond to a gold surface. The direction of vibrational stretch mode is illustrated by the arrows. b) A sketch illustrating a change in conformation from trans to gauche of the C-S bond as strain is applied. As higher ($> 15\%$) strains are applied, a greater relative enhancement in the gauche conformation with respect to trans suggests a reorientation of thiols on the gold surface from trans to gauche conformations.

As the position of the vibrational modes matches well to previously measured assembled 1-DDT monolayers (figure 8.1), it can be assumed that the measured thiols are bound to nanoparticle surfaces, rather than freely suspended in the particle gaps. Therefore, the observed enhancement comes despite a decrease in the number of analyte molecules in the collection spot. Under a 75% biaxial strain, the volume of analyte material in the collection spot will have been reduced to as little as 33% of the orginal amount, meaning the actual enhancement could be as much as 10 times more than before strain is applied.

The application of strain has been observed to increase the overall count of the Raman signal, and therefore offers a potential way to actively tune a plasmonic response in order to maximise returned signals for Raman sensing. The variation of the enhancements observed is attributed to changes in molecular orientation as strain is applied. Adding additional analytes into the system will act to change the system as a whole, such as altering the local refractive index, which affects both the near-field and the plasmon resonance positions. Such changes will now be discussed.

8.2 High refractive index oil SERS

Iodonaphthalene (IDNT) was introduced to the nanoparticle mats to simultaneously change the refractive index of the interparticle medium as well as add a second analyte to be studied. Because of this change, the behaviour of the enhancement is modified, whilst maintaining the existing proximity of the particles.

SERS spectra of the absorbed IDNT matched Raman spectra taken from the bulk oil, and agree with assignments from literature sources (table 8.2, [177] and [178]).

Vibrational mode	Raman	Measured
δ(CCC)	510	511
δ(CCC)	524	524
ν(C-C)	642	642
δ(CCC)	788	789
δ(C-H)	796	797
δ(CCC)	924	
δ(C-H)	945	940-944
δ(C-H)	1021	1022
δ(C-H)	1055	1057
		1130
δ(C-H)	1143	1150
δ(C-H)	1160	1161
ν(C-C)	1320	1335
		1357
δ(C-H)	1365	1366
ν(C-C)	1431	1432
δ(C-H)	1452	1452
		1497-1500

Table 8.2 SERS spectral positions (cm^{-1}) of iodonaphthalene from the bulk liquid and as measured after infusion into gold nanoparticle mats. Key to terms: τ, twisting modes; δ, bend modes; ν, stretch modes. Assignments taken from [177, 178].

As with the previously observed enhancement of DDT, the IDNT lines exhibited a relative enhancement for a majority of the molecular resonances, with the enhancement slowly increasing up to 2 times the initial count after 12% strain (figure 8.6). At higher strains, this value begins to decrease again. Two peaks, the 1022cm^{-1} C-H bending mode, and the 1432cm^{-1} C-C stretch mode, show a significantly higher maximum enhancement than this average, increasing 4.2 and 5.3 times respectively at 12% strain. However, these peaks do follow the trend of the average enhancement, displaying an increase to a peak value at 12% strain and the subsequent reduction of relative enhancement.

There were some lines that showed a marked decrease from their initial values. The 1130cm^{-1} mode and the 1150cm^{-1} C-H bending mode dropped from their initial values after the application of strain, before rising slightly at 17% strain, though still at lower enhancement values than their initial intensities. The 1161cm^{-1} and 1452cm^{-1} C-H bending modes do show an initial decrease in intensity up to 5% strain, but subsequently show the rise and fall of the other peaks.

The variation in the relative enhancements is attributed to movements of the IDNT molecule

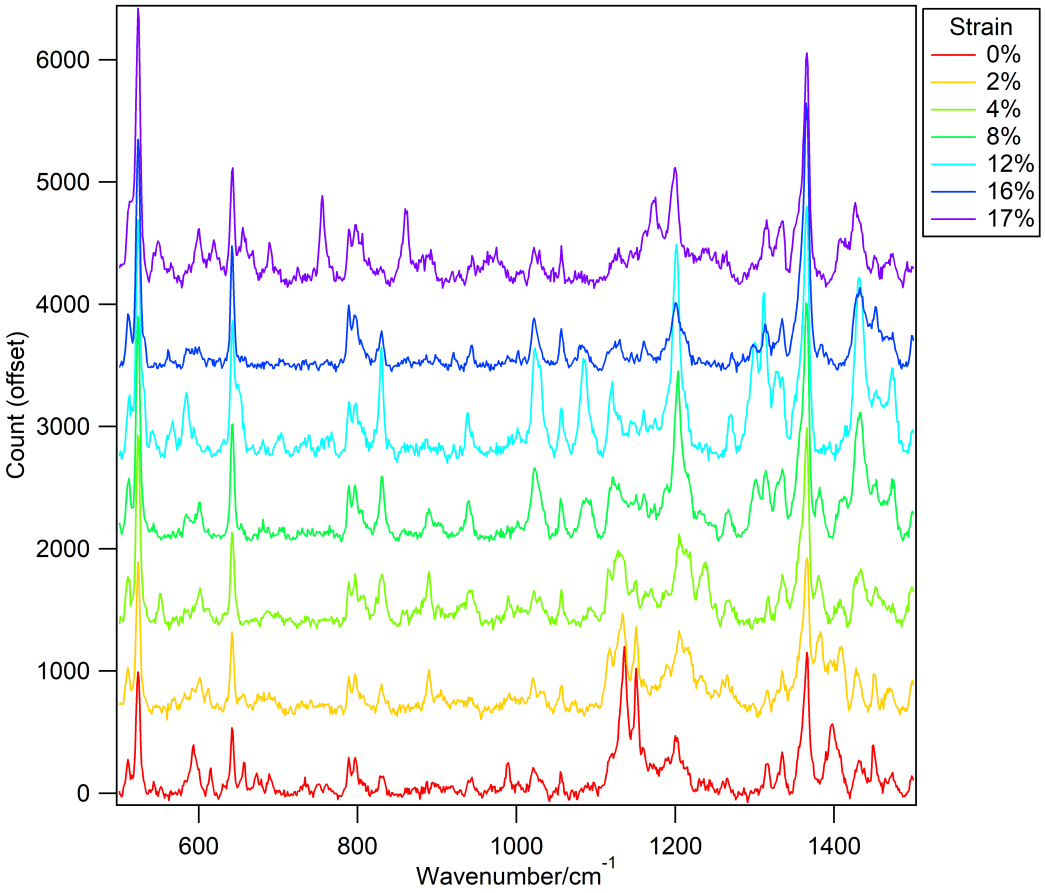

Fig. 8.5 SERS spectra from Iodonaphthalene absorbed into a 60nm gold nanoparticle mat under applied strain from 0% to 17% (red to blue).

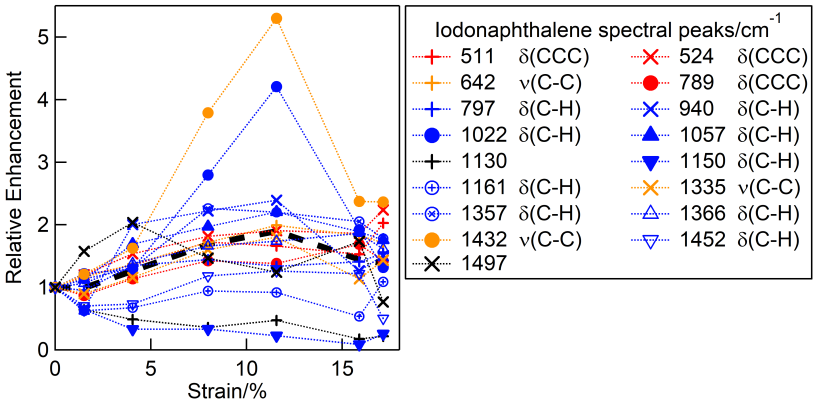

Fig. 8.6 Relative enhancement of the SERS spectra of iodonaphthalene vs strain with respect to the initial intensity. Key to terms: τ, twisting modes; δ, bending modes; ν, stretch modes.

within the interparticle space. Movements under strain could allow for changes in the photonic interactions with the molecular bonds due to molecular movement and reorientation as well as changes in bond conformation. In particular, the changes of strength of the nine different C-H bending modes observed (blue points in figure 8.6) suggest a selection of the vibrational modes happening, indicating either conformational changes to these bonds, or a dependence on the molecular orientation to the relative enhancement. Additionally, a relative enhancement is observed up to a peak point of strain before decreasing, suggesting that the particle clusters move into and out of a resonance position spot for the 785nm laser.

In addition to the peaks observed from the IDNT, spectral peaks are also observed from the DDT bound to the particle surfaces. There is no clear increase in the signal count after the addition of the higher index oil, with many of the Raman peaks at the same order of magnitude as the previous stretch measures without oil. The exact value is complicated by the variations in individual peak intensities under strain. In the case of the C-S gauche stretching vibration of the DDT molecule, the signal intensity reaches a maximum of 10 times that seen in the SERS measurement from mats before the IDNT is added. This might be attributable to the molecule being forced into this conformation due to steric effects from the IDNT. The opposing trans conformation is 10% less than the as-fabricated mats' signal. Other dodecanethiol peaks show a reduction in signal count by as much as 50% after the introduction of the iodonaphthalene, however it is unclear if this is due to a reduction in the field enhancement in the gap or if this arises due to a reduced interaction of incident light with the thiol.

The relative enhancements of the DDT peaks observed under strain show a greater distribution than those from the IDNT, although a peak in enhancement again occurs at 12% strain, up to 6 times the original signal count (figure 8.7). Despite this variation, the average trend (dashed black line in figure 8.7) follows the same behaviour of the IDNT average enhancement. The largest enhancements of the CH_2 rocking and wagging modes at 830 and 1300cm^{-1} respectively show a dramatic increase, far above the average enhancement, with the 1300cm^{-1} CH_2 wagging mode peaking at 25 times the initial value at 12% strain. The value of this enhancement is due to the dramatic emergence of the peak, initially being barely distinguishable above the noise.

The appearance of the 1300cm^{-1} CH_2 wagging mode is potentially attributable to changes in the position of the collection spot, which was attempted to be kept consistent across measurements, though some minor movements on the order of microns are observed. The count of SERS measurements across a mat do show some variation in peak intensity. Therefore,

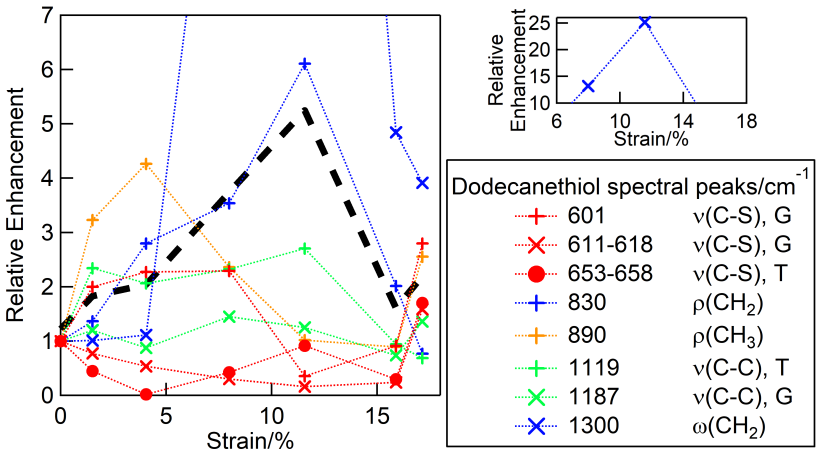

Fig. 8.7 Enhancement of the SERS spectra of dodecanethiol vs strain after the introduction of high index iodonaphthalene with respect to the initial intensity for various Raman peaks, shown with different markers. The maximum relative enhancement of the CH_2 wagging mode is shown in the offset graph. Key to terms: ν, stretch modes (G, gauche and T, trans conformations); ρ, rocking modes; ω, wagging modes; δ, bending modes.

the relatively large enhancement of this peak may be attributable to local variations in the Raman signal, though this is exhibited in intensity values of existing peaks rather than the emergence of new ones. It is also possible that at 0% strain this mode is quenched by the presence of the IDNT between thiol ligands. Steric forces from the introduced IDNT into the gap could result in a physical prevention of the bond vibration or an alternative bond conformation. As strain is applied, space is created for the molecules in the gap, resulting in its emergence.

The 1300cm^{-1} CH_2 wagging mode is not the only peak that appears and then vanishes in the Raman spectra, with unallocated modes seen at 755, 860, 1175, 1271 and 1311cm^{-1}. These peaks appear with varying intensities in multiple spectra, with most having a particularly strong presence in the 17% strain measure. Additionally, the DDT 890cm^{-1} CH_3 rocking mode peaks by 5% strain, then diminishes until it is indistingishable from the noise, before again reappearing at 17% strain.

The IDNT 1130cm^{-1} mode and 1150cm^{-1} C-H bending mode show a significant decrease in their initial intensity that remains low as the film is stretched. This behaviour potentially indicates molecular conformational changes as the mat is strained, resulting in molecular vibrations with different wavenumber values. Further investigation is needed to study the effect of strain on the Raman response of densely packed molecules under strain, to determine if this is indeed the case.

The behaviour of the C-S stretching mode is of particular interest, as it tells us about the orientation of the thiols on the particle surface. Vibrations come from the gauche (G) and trans (T) conformations of the bond (figure 8.4c). Before the introduction of the IDNT, the two different conformations are clearly visible in the spectra, the gauche stretch mode appearing as a broadened peak centred between 610 and 632cm^{-1}, and the trans conformation at 704cm^{-1} (figure 8.8a). The gauche peak is broad and initially of very low intensity before strain-induced enhancement. In contrast, the trans mode is very sharp and defined, suggesting that the trans conformation is dominant on the particle surface over the the gauche conformation. After the introduction of IDNT, the gauche and trans modes have similar count values 8.8b). The wavenumber values are significantly shifted in comparison to before, with gauche modes attributed to the lines at 601 and $611-618$cm^{-1} and the trans located at $653-658$cm^{-1}. These are within a few cm^{-1} to the values previously observed in the literature at a liquid-liquid interface of water and cyclohexane, another cyclic compound [175].

Previously, it has been observed that when the intensity of the trans conformation dominates the gauche conformation, the DDT molecules are in a highly ordered state akin to that of solid packing [175]. Before the introduction of the IDNT, the intensity of the trans conformation is on average 5 times greater than the equivalent gauche vibration, indicating strong ordering of the molecule on the particle surfaces. After the IDNT is added to the mats, this ratio changes, with the vibration associated with the gauche conformation having an increased relative intensity to be approximately equal with the trans conformation (figure 8.8c). In addition to this change, the intensity of the diffferent vibrations is mirrored with rises and falls occurring in tandem, with the exception of at 16% strain. This shows that the introduction of the oil causes significant disordering of the thiol at the nanoparticle surface, indicating a steric interaction on a molecular level between the two molecules, affecting their conformations and therefore their Raman response.

In addition to the modes found at 601, $611-618$cm^{-1} and $653-658$cm^{-1} in the IDNT infused mats, other peaks around these values may be due to the same vibrational mode. The peaks around 588 and 593cm^{-1} may be linked to the gauche conformation, and peaks at 672 and 688 may be related to the trans conformation. These peaks are not consistently evident in the spectra as strain is applied, and in particular the strength of the 588cm^{-1} peak seems tied to that of the $611-618$cm^{-1} gauche stretch mode, rising in intensity as the gauche stretch mode disappears. This behaviour, along with the subtle wavenumber shifting of the $611-618$cm^{-1} gauche stretching mode and the $653-658$cm^{-1} trans stretching mode,

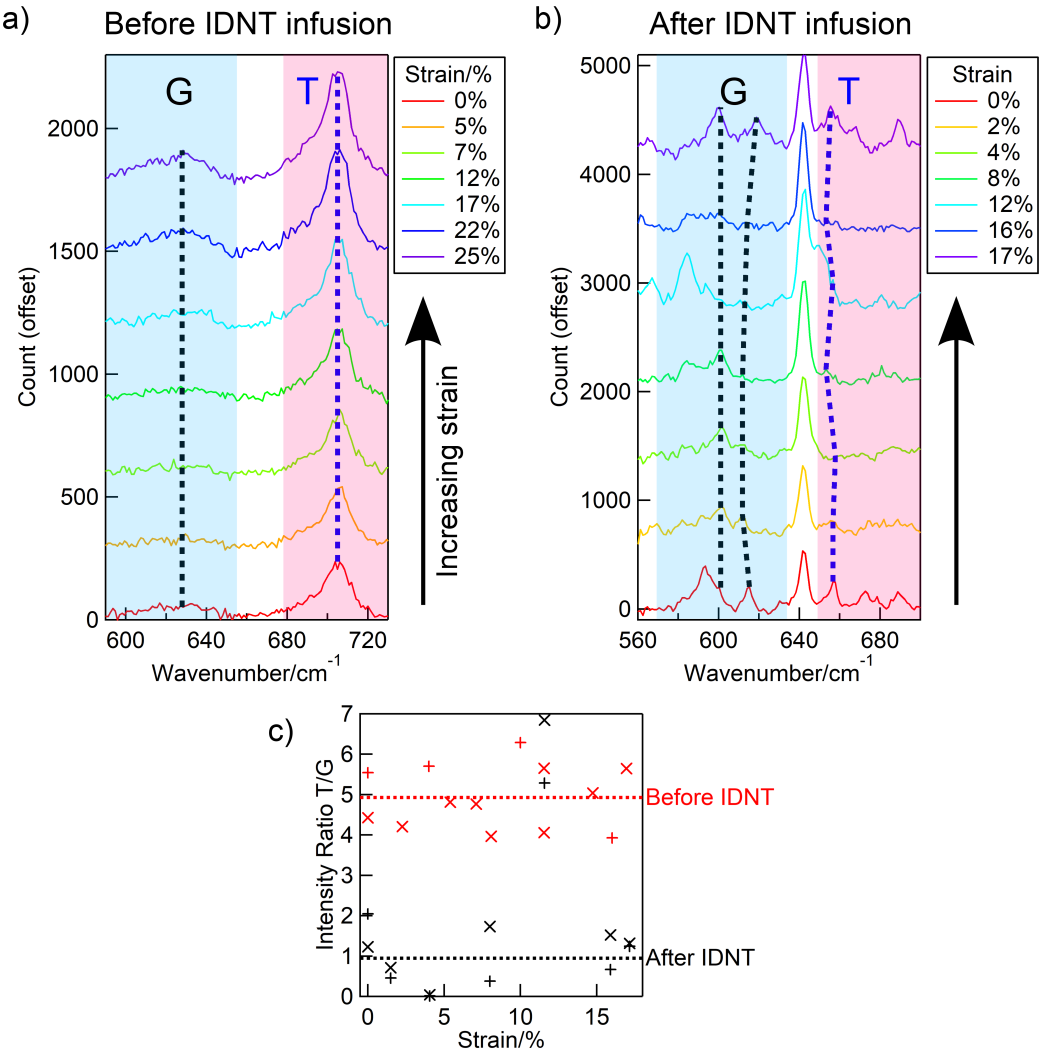

Fig. 8.8 SERS spectra of the $\nu(C-S)$ gauche (blue highlight) and $\nu(C-S)$ trans (red highlight) stretching modes against increasing strain for a self-assembled nanoparticle mat both a) before and b) after the addition of iodonaphthalene. Dash lines show the progression of the gauche (black) and trans (blue) conformations respectively. c) Ratio of the trans to gauche vibrations for both the as-fabricated mats (red, PDMS $\times$ and PU $+$) and the oil-infused mats (black, 590cm^{-1} $\times$, 615cm^{-1} $+$) under strain. The decrease of this ratio when the oil is added is attributed to the iodonaphthalene molecules disrupting the ordering of the DDT monolayer on the nanoparticle surface.

further indicates that applied strain has an effect on the molecular bonds of the analytes.

The changes to these vibrational modes are attributed to the IDNT molecules producing steric forces on the DDT. As strain is applied these pressures would change resulting in the differences that are seen during the stretch procedure (figure 8.8a and b). This effect is also present, although to a lesser degree, in the as-fabricated mats; the C-S gauche mode moves around between 610 and 632cm^{-1}, although the C-S trans mode remains at 704cm^{-1}. This variation is also seen in literature specifically with thiols bound to a nanoparticle surface indicating that the crystal faceting of the nanoparticle surface also affects the ordering of the thiol monolayer [175].

Introducing additional molecules to the mat causes a distinct observable change in the ordering of molecules in the relative intensity of the C-S bond of the thiol to the nanoparticle surface. However, the failure to infuse other refractive index oils into the gaps between molecules shows an inherent difficulty in introducing molecules into already populated $<$ 2nm gaps. Infusion is resisted either chemically or sterically by the ligands on the nanoparticle surface. In contrast to the literature [179, 180], an attempt to plasma clean a nanoparticle mat failed to change this. This is likely due to the topography of the sample protecting the thiols within the gap.

After the introduction of IDNT, 60nm gold nanoparticle mats were stretched and an enhancement relative to the initial peak intensity was observed. This enhancement reaches a maximum at 12% strain before decreasing. As previously seen, the individual peaks respond differently upon the application of strain. This is attributed to the mechanical deformation and reorientation of the molecules with different conformations of molecular bonds being forced upon the system by the proximity of other molecules. The behaviour of the field enhancement in this scenario will now be explored, to see how interparticle spacing can change the potential for SERS enhancement in the interparticle gaps.

8.3 Nanoparticle morphology and field enhancement in the gaps

The intensity of the electric field in close proximity to the particles can be modelled using FDTD software. Using this method, the near-field enhancement of the nanoparticle mats was analysed. 60nm gold nanoparticle mats were modelled within media of set refractive indices set to 1.5 and 1.7 (figure 8.9). The field enhancement from the higher refractive

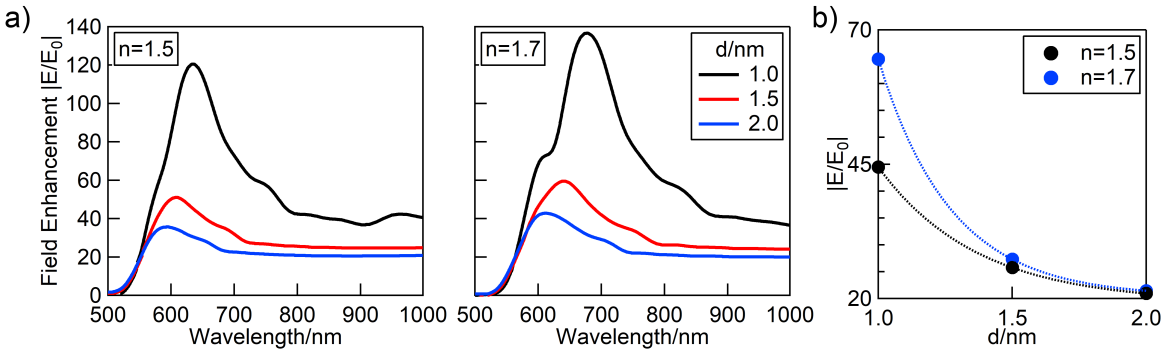

Fig. 8.9 a) Near-field enhancement within a 60nm gold nanoparticle mat embedded in a medium of refractive index values 1.5 and 1.7 RIU for varying interparticle separations. b) The field enhancement from the two different values of n at 785nm with respect to particle separation.

.

index material generated a 13% greater maximum value of the field enhancement. This enhancement is redshifted by 40nm, as would be expected by an increase of the refractive index. However, the modelled enhancement at 785nm, the wavelength of the laser used during experimentation, results in a 50% increase in the field enhancement between 1 and 1.5nm particle separations, our expected particle separation (figure 8.9b). These results suggest that the near-field intensity should decrease as the particles are separated.

The increase of Raman signals upon the application of strain is therefore contradictory to the calculated decreases in the near-field intensity. In order to explain this result, the effect of particle geometry on the near-field intensity is modelled. Initially, the nanoparticle mats were specified as spherical particles with set spacings. Calculations were made with smaller steps in particle separation (figure 8.10a). At 785nm, the enhancement decreases constantly with increasing interparticle separation. Between 1 and 2 nm separations, the SERS enhancement is predicted to decrease by a factor of 100 (figure 8.10b).

In practice, nanoparticles are not truly spherical and are in fact multi-faceted crystals. By changing the modelled particle geometry, the overall behaviour of the enhancement changes [181]. Particles were subsequently modelled as truncated spheres, with flattened neighbouring faces (figure 8.11c). Although the near-field enhancement does not reach the same magnitude as previously modelled, the behaviour beyond 700nm is considerably more complicated, with further peaks in enhancement beyond those around 600nm (figure 8.11a). Importantly, the field enhancement as a function of separation actually increases by a factor of 10 between 0.7 and 1.1nm separations (figure 8.11b). This shows that, contrary to expec-

tations, small changes to the geometry of the nanoparticle mat can lead to increases in the local field enhancement for given wavelengths with increasing interparticle separation.

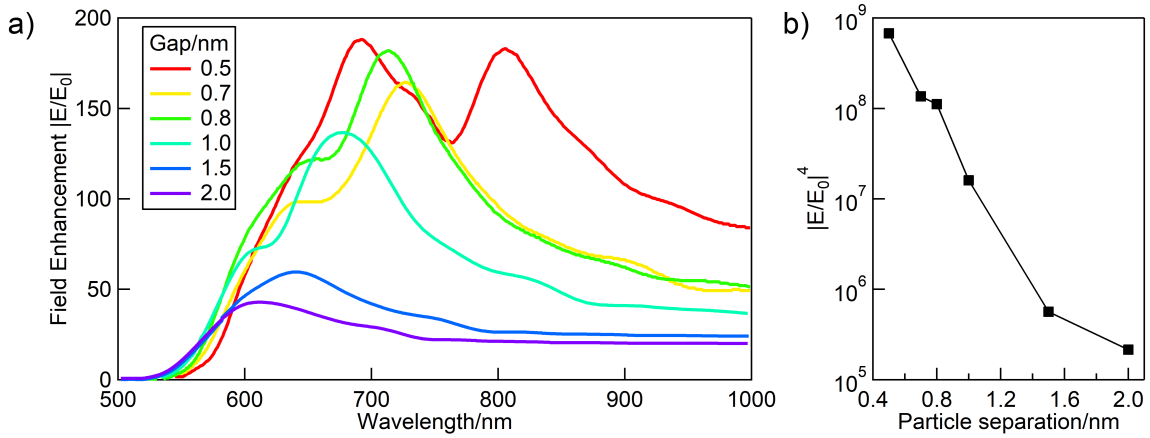

Fig. 8.10 a) Field enhancement values of a spherical 60nm gold nanoparticle mat for increasing nanoparticle separations where n= 1.7. b) The field enhancement to the fourth power at 785nm. Between 0.5 and 1.5nm, the local field enhancement is predicted to decrease by a factor of 10^3.

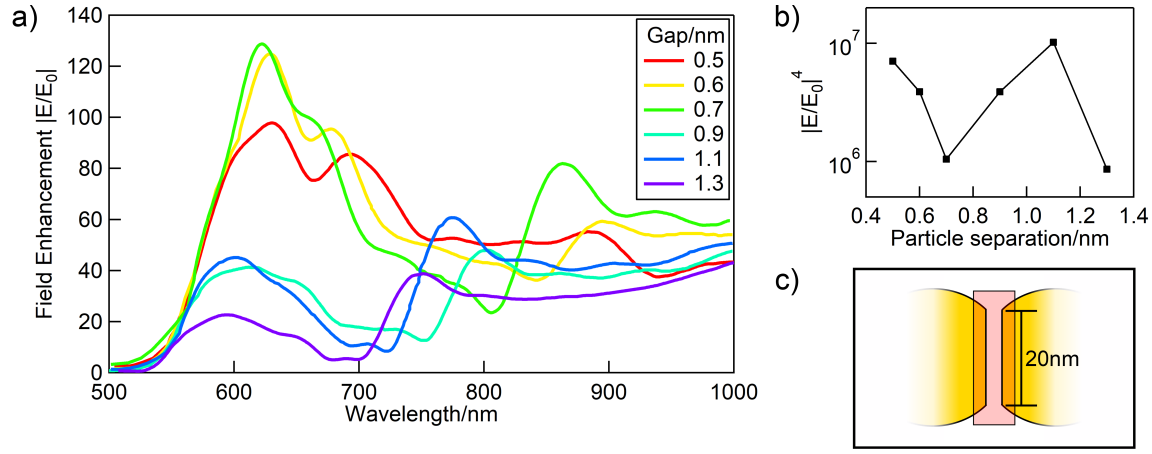

Fig. 8.11 a) Field enhancement values of a truncated 60nm gold nanoparticle mat for increasing nanoparticle separations where n= 1.7. b) The field enhancement to the fourth power at 785nm. c) Schematic of the modelled particles. At closest proximity to neighbouring particles, surfaces are truncated into circles with a 20nm diameter.

8.4 Comparing the optical strain behaviour and stretch SERS measurements

Due to the reversible nature of the SERS enhancement shown under strain, and the closely distributed and consistent nature of the enhancements observed, the observed behaviour is attributed to changes in the plasmonic coupling of the mat due to changes in particle separation. However, as discussed within chapter 7, optical spectra of 60nm Au nanoparticle mats under strain show inconsistant interparticle spacing changes, resulting in the fracturing of the arrays into irregular clusters. There is an obvious discrepancy between these two findings, with the stretch SERS results suggesting that particles are moving more than the optical spectra show.

There are multiple explainations for the disparity between the optical and SERS spectra. The first, and most obvious, is that although the under strain nanoparticles are not evenly separated, there are still significant changes on macroscopic length scales, specifically the breaking up of the mat into irregular clusters, as imaged in chapter 7. This would result in near-field changes at the cluster boundaries, resulting in SERS enhancements. It is possible that such cracking is present, albiet at a smaller scale, throughout the clusters themselves, resulting in a anisotropic changes in nanoparticle separations across the mat. Such variations in interparticle separation would change the plasmonic coupling between particles across the mat, and may therefore be the root cause of the SERS enhancements observed.

A more complex explaination considers how strain is applied within the clusters themselves, and specifically how the applied strain influences the molecular conformation and organisation on and around the particle surface. It is possible that applied strain does not influence particle separations but instead does effect the potentially interdigitated thiol layer around each nanoparticle. Such molecular changes could result in changes to SERS enhancements independent of nanoparticle movements. However, this explaination does not explain the reversibility of the SERS enhancement values.

A further alternative explanation for the observed enhancement is the introduction of surface defects and cracking on the substrate itself under strain. However, this is unlikely, as any surface cracking would remain on the surface upon relaxation of the polymer. Additionally, this would not affect the SERS within the particle clusters, and the peaking of the enhancement at a maximum value before falling suggests that the mechanism of enhancement has at least some origin in plasmonic behaviour.

To determine the exact origin of the observed behaviours, more experimentation and theoretical modelling is required. Further FDTD modelling of the observed system, specifically separating nanoparticle clusters, would enable a greater understanding of the near-field changes at cluster boundaries and which may alone explain the SERS enhancements observed. Whilst computationally intensive, this would give a more complete picture of near-field changes due to the breaking up of a naoparticle mat into clusters.

Additionally, by breaking down the system into a simplest possible representation would enable the measurement of strain induced changes to particle separation of closely spaced nanoparticles. Fabricating either a thiolated nanoparticle dimer or, preferably, chain on an elastic substrate would enable more direct measurements of nanoparticle separations when stretch, enabling closer studies of how applied strain affects particle spacings. This would be particualrly useful within a chain, as variations in interparticle distances across multiple particles could be observed. Studies on these structures would also enable more direct measurements of conformational and organisational changes to molecular layers on the particle surface.

In practise, assembling thiolated dimer or chain structures is challenging, in particular fabricting these structures with interparticle spacings of around a nanometer. However, a microfluidics approach may enable the thiolation and capture on single nanoparticles onto water droplet surfaces, with subsequent droplet amalgamation enabling the interfacial close packing on nanoparticle dimers. From these starting building blocks it may be possible to fabricate long range linear chains of particles.

Such further experiments would give a deeper understanding of the mechanics and optics of closely-packed nanoparticles under strain, and therefore determine the exact physical origin of these stretch SERS enhancements.

8.5 Summary

Stretch tunable nanoparticle arrays can be used to tune the SERS enhancements of analyte molecules. Theoretical calculations predict a high degree of sensitivity to strain with potential increases and decreases in the degree of enhancement dependent upon the proximity of particles, local refractive index and individual particle morphology. In practice, stretch-tuneable nanoparticle arrays demonstrate a strain sensitive enhancement of Raman signals with increasing and peaking signal counts with applied strain. After infusing a sec-

ond molecule into the interparticle medium, changes in molecular orientation are observed, allowing insight into the interactions between molecules in nanometric volumes.

Chapter 9

The Self-Assembly and Optical Properites of Mid to Low Density Nanoparticle Monolayers

In contrast to the preceding experimental work, this chapter concerns the fabrication and optical properties of lower density nanoparticle monolayers. As the density of nanoparticle arrays decreases, plasmonic coupling between particles becomes less dominant, until only isolated particle scattering remains. However, the sensitivity of plasmonic nanoparticles to their environment, and their ability to scatter relatively large intensities of light despite being sized below the diffraction limit, means that many interesting optical effects can be seen across all array densities. Within this chapter, the fabrication and optical behaviour of less dense nanoparticle arrays is discussed, starting with a study of how array density impacts refractive index sensitivity, before exploring the potential of a high scattering intensity low-density plasmonic nanoparticle monolayer as a backscattering layer within an optical device.

9.1 Isolated nanoparticle monolayers for refractive index sensing

Sparsely packed nanoparticle monolayers can be deposited onto a vertically aligned substrate at the air-water interface of a drying nanoparticle solution. The convective flow through the solution can direct the particles to the interface where they are deposited [142].

Importantly, as the particle concentration of the solution increase during evaporation, the concentration of particles being deposited onto a film increases over time. This offers the opportunity to explore the influence of particle density on the refractive index sensitivity of a nanoparticle monolayer.

9.1.1 Evaporative assembly onto a functionalised substrate

By selectively functionalising a substrate, particles can be fixed to the surface. This can be achieved using a silanization process, where a molecular monolayer of a silane is assembled on the substrate which, in addition to providing a binding site for the particles, also increases the surface hydrophobicity, establishing a distinct contact line between the water and the substrate. Amino-propyltriethoxysilane (APTES) was diluted into toluene, 1 part APTES to 100 parts toluene. This solution was then heated to 70 °C. Silicon substrates sonicated in both organic and inorganic solvents were then submerged in this solution and left for one hour before removal. Finally, the substrates were rinsed in toluene and water and then dried using nitrogen.

These substrates were then placed in solutions of commercial nanoparticles and left at a constant temperature of 40 °C for a period of days, until the solution had evaporated. During this time, the capillary forces packed the nanoparticles onto the substrate as convective flow moved them to the contact line (figure 9.1a). A useful side effect of this process is that the nanoparticle solution gets more concentrated as the liquid evaporates. This results in the salt concentration of the nanoparticle solution increasing, which affects the electrical double layer of the nanoparticles. The electrostatic repulsion caused by the electrical double layer is reduced by this salt increase, resulting in the increased packing of the nanoparticles as the water level decreases.

Surface coverage increases as a function of distance down the substrate, reaching a maximum surface coverage of 70% (figure 9.1b). This is attributed to topological factors: at this density the nanoparticles are packed tight enough that it becomes difficult to fit another nanoparticle in the gaps between them. Nanoparticle packing, whilst dense, is random, and the interparticle separations vary significantly. However the film's optical properties are observed to be locally consistent, depending upon regional particle density.

In comparison to the spun deposition of low density nanoparticle arrays, the density of particles in this method is seen to be much higher and more consistent across the entire substrate. This is due to the nature of the fabrication. The functionalisation of the surface allows for

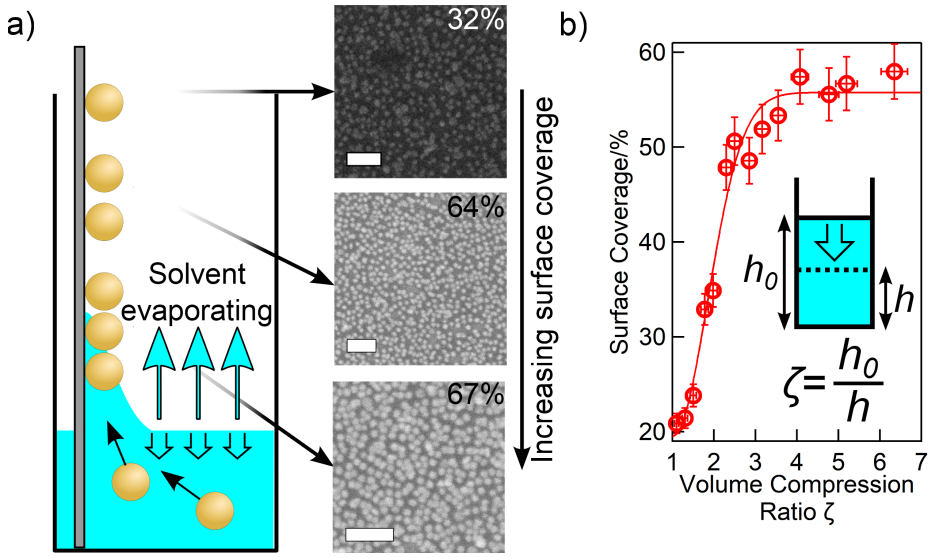

Fig. 9.1 a) Evaporative assembly method where nanoparticles are deposited onto a silane coated silicon substrate via convective flow. As the solvent evaporates, the salt concentration in the remaining solvent increases and the particle surface coverage increases. The SEM images to the right show differing concentrations of 80nm gold nanoparticles as the solvent evaporates, with surface coverage values of 32%, 64% and 67% and scale bars equal to 200nm. b) The surface coverage as a function of a volume compression ratio, ζ, of the nanoparticle solution. ζ is a ratio of the height reduction of the fluid through evaporation; $\zeta = h_0/h$ (shown inset). After an initial rapid period of increase, the maximum surface coverage plateaus around 60%, at which point the interparticle spacings become close enough to prevent additional packing of particles. As the volume ratio increases, further increases in salt concentration result in more screening of the particle's electrostatic potential, causing increased packing until a maximum surface coverage of 70% is reached.

chemically aided nanoparticle to surface binding over the entire substrate. This is not possible for the spinning fabrication method due to the requirement of substrate preparation.

With the spinning method, much of the variation in surface coverage of particles is due to remaining particle solution on the substrate after the spinning procedure. As these droplets dry, convective flow moves particles to the edge of the solution, leading to coffee ring structures with denser particle distributions. With the vertical deposition method, the density variations from the localisation of particles within a droplet are removed, due to the substrate being submersed into large volumes of nanoparticle solution. As a result, nanoparticle density on the substrate increases only as a function of depth into the evaporating liquid, due to changes in the particle concentration and salinity of the solution.

Another advantage of vertical deposition is that it is applicable to all nanoparticle diam-

eters, without changing any component of the procedure. Any variation to the nanoparticle solution, such as the stabilizing salt concentration, will manifest itself in a relative increase or decrease in the initial density of deposited nanoparticles, and as the solvent evaporates this density will increase. A similar though contrasting method is a Langmuir-Blodgett technique, where a substrate is withdrawn from a solution at a consistent rate. For Langmuir-Blodgett films, the density can be varied by changing the rate of withdrawal. However, withdrawing a substrate in this manner adds complication; the simplicity of vertical substrate fabrication is a significant advantage in making varying density nanoparticle monolayers.

9.1.2 Refractive index sensitivity of varying density nanoparticle monolayers

Varying density nanoparticle arrays are ideal platforms for sensing due to their lack of extra chemical functionalisation and their sensitivity to their surroundings. The sensitivity of the plasmon resonance to the local refractive index particularly makes them an ideal refractive index sensor. The varying density of nanoparticle coverage enables the measurement of the maximum possible shift of the plasmon resonance to a refractive index unit (RIU).

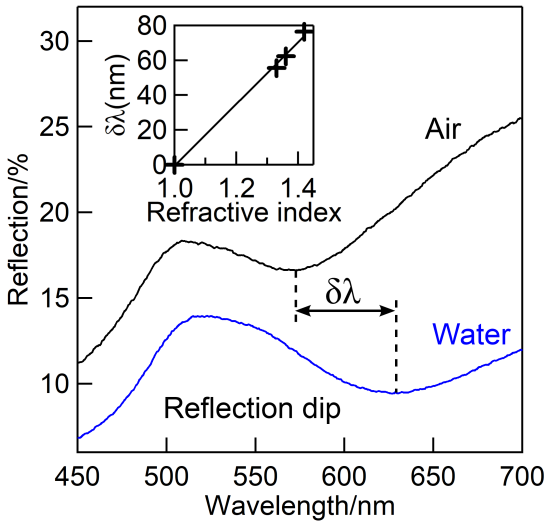

Fig. 9.2 The change in reflection of an 80nm gold nanoparticle monolayer with 35% surface coverage. The spectral features redshift with increasing refractive index, with the wavelength shift in the position of the reflection dip measured as $\delta\lambda$. Inset: $\delta\lambda$ plotted against refractive index to determine the sensitivity, nm/RIU, of this surface coverage.

By submersing the films in different fluids, the effects of refractive index changes can be studied. Figure 9.2 illustrates the change in reflectance from air to water of a film of 80nm gold nanoparticles with surface coverage of 35%. The significant features of the spectra show the expected redshift after the increase in refractive index. The dip in reflectance was studied, as it displays a greater wavelength shift than the peak in reflectance. The wavelength change of this reflectance dip, $\delta\lambda$, was measured for different fluids, allowing the dip to be fit against refractive index unit change. This relation was found to be linearly proportional (9.2, inset).

By systematically measuring $\delta\lambda$ for different surface coverages of particles, the effect that surface coverage has on refractive index sensitivity can be measured (figure 9.3, red). The maximum sensitivity of 180nm/RIU was seen at a coverage of 35% for $D = 80$nm gold nanoparticles, which corresponds to an average spacing of around 1.6 times the particle diameter. After this point, refractive index sensitivity decreases with increasing surface

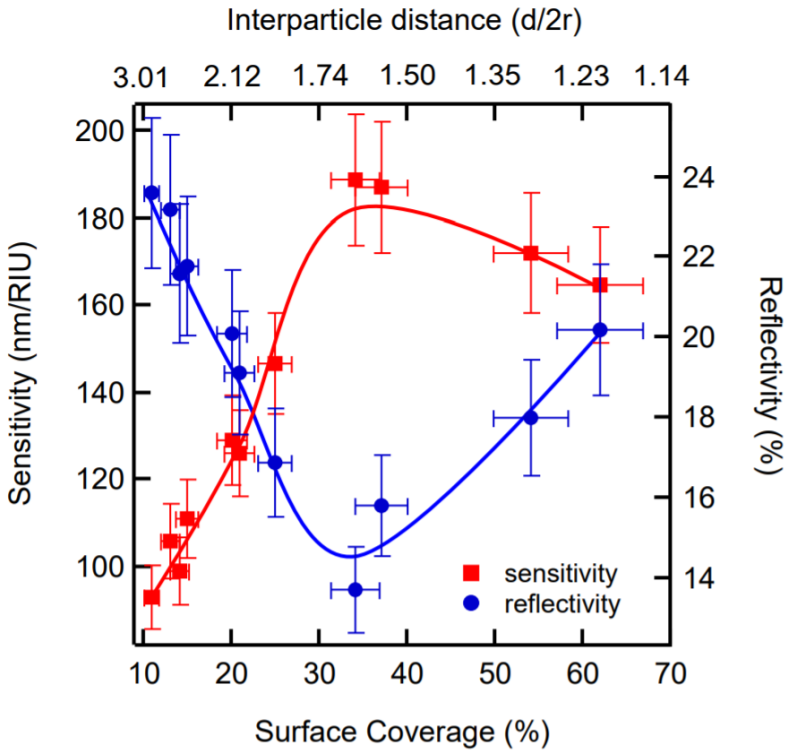

Fig. 9.3 The refractive index sensitivity in nm/RIU for different surface coverages of nanoparticles and interparticle distances (blue). The reflectivity of the films at the reflection minima is also plotted (red) and seen to behave conversely to the sensitivity. The average interparticle distance in terms of $d/2r$ is calculated using the surface coverage.

coverage. The peak in sensitivity is matched by the minima in the reflectivity of the films (figure 9.3, blue). This is paired with the maximum observed scattering of the films. The origin of this behaviour can be intuitively explained as scattering and absorption are minimal at lower surface coverages, with high reflective intensities from the silicon substrate. As particle coverage rises, the scattering from the films increases until it reaches a maximum. Beyond this point, the scattering cross-sections of the particles begin to overlap, resulting in the increased reflection and broadening of the resonance. This result shows that in order to maximise the sensitivity of a nanoparticle film to changes in the refractive index, it is necessary to ensure a density of particles below that where the scattering cross-section of particles overlap.

In addition to the refractive index sensing capabilities of these films, their reflection minimising capabilities display potential as antireflection coatings. The reflection from the silicon substrate reduces from 24% to 14% at the minima of reflectivity. With other sized particles, this reflective intensity can be reduced towards 0%. This work will not be covered in detail in this thesis and I refer the reader towards the publication written by my collaborator, Dr Fumin Huang, for a thorough analysis of the reflection minimising properties of these nanoparticle monolayers, as well as theoretical models using Maxwell-Garnett theory to quantitatively explain the optical responses of these films and further analysis of refractive index sensitivity [17].

The evaporative assembly of nanoparticle monolayers is an effective, though slow, method of assembling varying density nanoparticle mats. These have been used to show how particle density affects sensitivity to refractive index changes. Additionally, the reduction of reflective intensities observed suggests that mid-density ($20-40\%$) packing of nanoparticle mats may be an effective method to make antireflection coatings with minimal thickness. However, the length of the assembly process is such that prevents the scaling up required for industrial fabrication and therefore other methods of assembling such densities of nanoparticle surface coverage are required.

9.2 Isolated nanoparticle monolayers to increase scattering within OLEDs

An interesting problem for self-assembly fabrication methods lies in not bringing nanoparticles into close proximity with each other but in having them regularly positioned across

a substrate. Unlike lithographic methods where component position can be set specifically, bottom up assembly often results in closely-packed groupings of particles due to the induced disruption in particle stability during fabrication. In the case of drying methods, particle densities often vary hugely across substrates.

A low density nanoparticle film is of interest due to the scattering properties of nanoparticles. Due to their high scattering cross-sections, plasmonic nanoparticles deposited onto a surface will encourage the backscattering of light from a substrate even with low area-density surface coverage and a minimum of surface roughness, therefore not introducing the extensive deformations that are typically seen in high-intensity scattering surfaces. By using self-assembly techniques, a scattering layer can be produced in a fast and scalable way. This method can then be applied to place an integrated scattering layer into an existing optical device with minimal disruption to the established assembly process.

For example, organic LEDs are made using a layer-by-layer method. Light is produced by an emissive layer that shines light omnidirectionally. Typically light can only be emitted from one side of the device, leading to intensity losses and lower efficiencies. Any patterning or reflective layers introduced to the device can interfere with the functioning of the OLED, by removing the functionality of the device. However it is possible to sparsely coat an area behind the emissive layer with nanoparticles in order to backscatter the emitted light and therefore increase the overall efficiency of the device.

Different methods may be used to achieve this, such as drying down solutions of nanoparticles onto a substrate. However, as mentioned in Chapter 4, this can result in coffee ring type structures created by the convective flow of particles to the edge of the liquid. Even with low concentrations of nanoparticles, aggregates may form through convective flow, resulting in a lower scattering intensity than smaller groupings of particles over a larger area. Additionally, these processes are defined by their reliance on long evaporation periods which are not ideal for manufacturing devices. In this section, different methods of producing large scale low density nanoparticle films are explored, in an effort to maximise the recorded scattering intensities, with the aim of using them in OLEDs to increase their efficiency.

9.2.1 Spinning sparse nanoparticle monolayers

Spin coating nanoparticle solutions is a viable method for depositing sparse nanoparticle arrays in a manner that fits into the existing manufacturing procedures for OLEDs. The procedure allows for fast deposition of particles and is scalable to large areas. Multiple

depositions can also be used for an easy method to increase the density of the particles. Control parameters for assembly include spin speed as well as the volume and concentration of the nanoparticle solutions used [182, 183].

Silver nanoparticles were selected for these procedures due to their initial scattering in the blue end of the spectrum. In contrast to gold nanoparticles, which scatter light from around 530nm in the green area of the spectrum, coupling between silver nanoparticles will result in a broadened resonance over the entirety of the optical spectrum. This broadened resonance allows for a relatively higher integrated scattering intensity over the entirety of the visible spectrum.

Initial experiments using commercial 80nm Ag nanoparticles followed methods from literature sources, using spin speeds from of 3000 rpm for 1 minute on a substrate consisting of a thin film polymer layer on silica[1]. These were unsuccessful, showing little to no deposition on the film. At this speed the droplets were observed to be flung off the substrate. Subsequent experiments at reduced spin speeds of 1000, 750 and 500 rpm were then performed. At slower speeds, even with longer spin cycles, small volumes of solution are left over and, on drying, left a coffee ring of particles. Longer spin times were found to mitigate this effect although a density variation of particles across the surface remained.

A multi step process was used to increase the density of particles deposited with multiple spins using a commercial 80nm Ag particle solution at 750rpm . The highest scatterer coverage density achieved was 4% surface area coverage, calculated via optical microscopy (highlighted in blue in figure 9.4). However this was limited to certain areas of the substrate and indicative of dried down solution left over from the spinning process. Away from these areas, the particle density was significantly less. The multi spin process is seen to increase the particle density, though not uniformly across the sample.

In order to record the scattering over a large area, a large core optical fibre (600μm) was used in conjunction with the 100x dark field objective. This enabled the viewing of many particles within the collection spot. The scattering intensity showed a broadband increase with increasing particle density (seen in figure 9.4). In order to quantify the increasing scattering intensity, the spectra was integrated between 430 and 800nm, then normalised to the equivalent calculation from a Lambertian diffuser. This integrated scattering intensity value is seen to increase with surface coverage density, calculated as a percentage of the surface

[1]The substrate this work was carried out on was a polymeric electron transport layer (ETL) supplied by Cambridge Display Technology Limited.

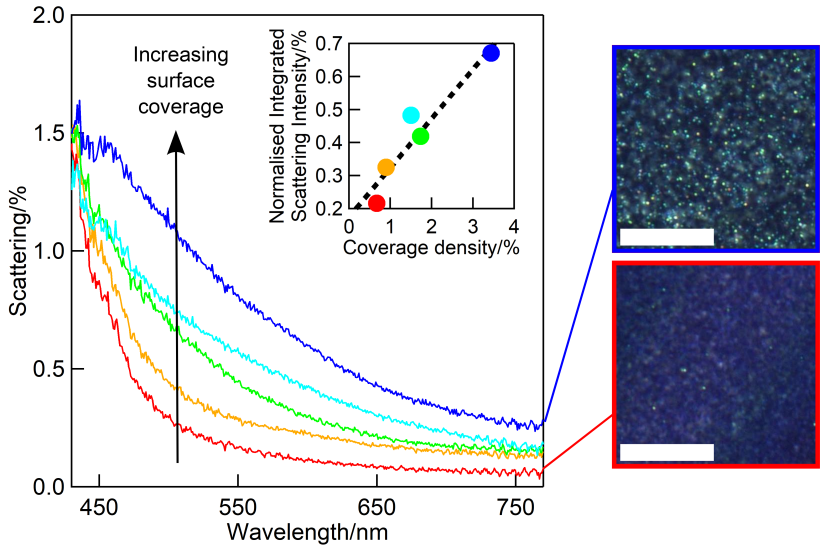

Fig. 9.4 With increasing particle density, the broadband scattering intensity from a sparse array of 60nm Ag nanoparticles is seen to increase. Inset: the relation between integrated scattering intensity, from 430 to 800nm, against particle density, normalised to the integrated scattering from a white Lambertian diffuser. Increased density of scattering points resulted in higher values for the integral. Right: Microscope images of coverage densities 0.7% (red) and 3.4% (blue). Scale bar 5μm.

covered by scattering points on the microscope image and correlated to the real coverage area of the particles (inset, figure 9.4). The scattering intensity does not follow an expected λ^{-4} dependence as expected from Mie scatterers, which is attributed to additional contributions from the substrate. However the magnitude of the integrated scattering intensity is seen to increase linearly as a function of the surface coverage on the substrate, as expected, with no particle interactions.

9.2.2 Nanoparticle aggregate deposition

In order to increase the intensity of the scattered light, an additional step is added to the fabrication method. Cucurbituril (CB) molecules, specifically CB[7], were added to the solution to aggregate the nanoparticles into small clusters. After only a couple of minutes, a coupled chain mode appeared in the spectra indicating the aggregation of the colloids. As N aggregated nanoparticles have significantly larger scattering cross sections, $\propto N^2$, they should act as significantly brighter scattering points than individual nanoparticles. The broad optical response produced by these aggregates was observed using absorption spectroscopy, recording the light absorbed from a Ag nanoparticle solution over time after the introduction of

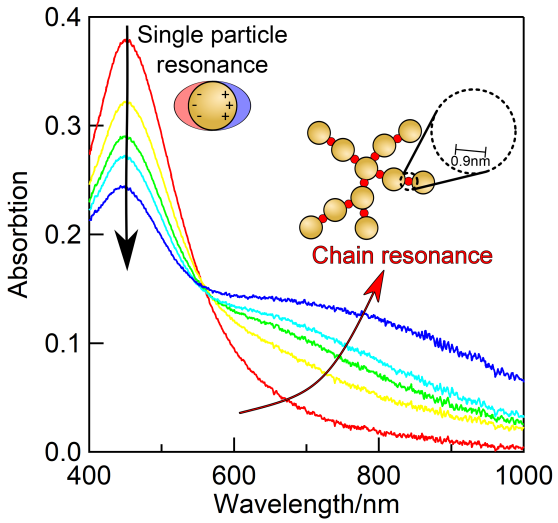

Fig. 9.5 The change in absorbance over time of 80nm Ag nanoparticles after introduction of CB. Over time, the inital peak, which is the plasmon resonance of a single Ag nanoparticle, reduces in intensity (black arrow) as the particles form fractal aggregates (shown schematically), with interparticle separations of 0.9nm. At higher wavelengths, the chain plasmon mode from these aggregates appears and red shifts (red arrow). The first four spectra (red to light blue) are taken every 50 seconds from insertion of the CB, with the dark blue spectra taken 15mins after insertion.

the CB molecule (figure 9.5). After a couple of minutes a coupled chain mode appears in the spectra indicating the aggregation of the colloids.

Before the nanoparticle solution was spun onto the substrate, 100μl of a CB[7] solution (7mg of CB[7] in 15ml deionised water) was added to 500μl of commercial 80nm Ag nanoparticle solution and left for 5 minutes. 100μl of this mix was then spun under the same procedure as performed with unaggregated nanoparticles. The delay between depositions allows for different chain length aggregates to be deposited, resulting in a broader scattering profile with different size aggregates from different stages of aggregation. The subsequent spectra shows more complex behaviour than that of the unaggregated particle solution, with greater intensities observed at higher wavelengths, indicative of long nanoparticle chain resonances (figure 9.6).

In comparison with the spectra of the unaggregated nanoparticle depositions, the coverage density of particles is significantly higher, with coverage of as much as 9% for a normalised integrated scattering intensity value of 0.75%. This is over twice the 4% coverage observed for the same procedure using unaggregated nanoparticles. However, direct comparison between the multiple scans reveals a slower increase of the integrated scattering density in the

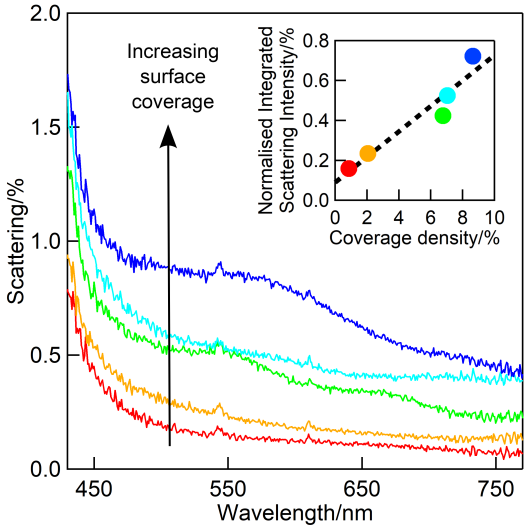

Fig. 9.6 Multiple spins of CB aggregates show a greater intensity of scattering across the spectrum than multiple spins of unaggregated nanoparticles. This is still highly dependant on the position of particles. In high density areas there is a greater intensity of light with peaks suggesting scattering from aggregates between 500 and 700nm.

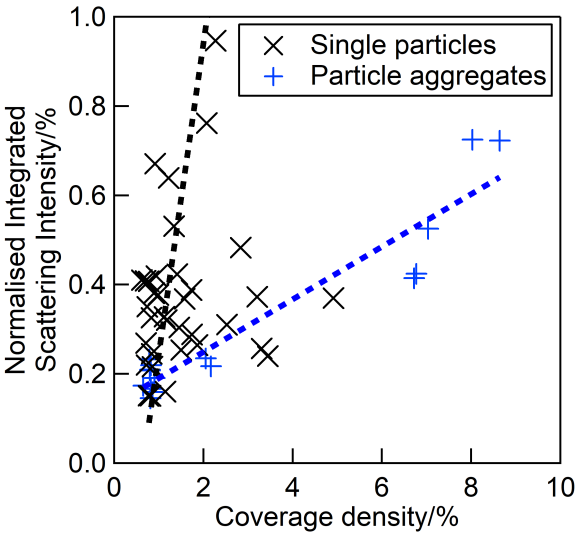

Fig. 9.7 Integrated scattering intensity from spun nanoparticle and nanoparticle aggregate films with different coverage densities. The rate of increase of integrated scattering intensity is much greater than spun individual nanoparticle films, with spun aggregates having a higher surface coverage for the same maximum integrated scattering intensity.

spun CB aggregates than that of the individual particles with respect to the coverage density on the substrate (figure 9.7).

This result goes against the expectation that the scattering intensity from the CB aggregates would be superior to that of the individual spun particle substrates. It is worth noting that the increased scattering in the single nanoparticle depositions arises from denser groupings of nanoparticles, whilst the aggregated particle solution was deposited after being left to aggregate in solution for up to 20 minutes. The scattering from the CB aggregates is therefore dominated by larger aggregates formed from depositions made later in the aggregation period. It is probable that the strong coupling due to the very small separations of aggregates was bright enough to saturate the optical image used to categorise the coverage density. However, as the magnitude of integrated scattering intensity is similar in both cases, this result indicates that it is better to have a greater number of dimmer scattering points with better distribution than larger, brighter scatterers.

As with the isolated nanoparticle depositions, the density of particles was far from uniform over the sample with distinct density variations across the width of the substrate. To illustrate this density variation, spectra are taken every 100μm across the substrate, with the integrated scattering intensity calculated at each point. Figure 9.8 shows the distribution of

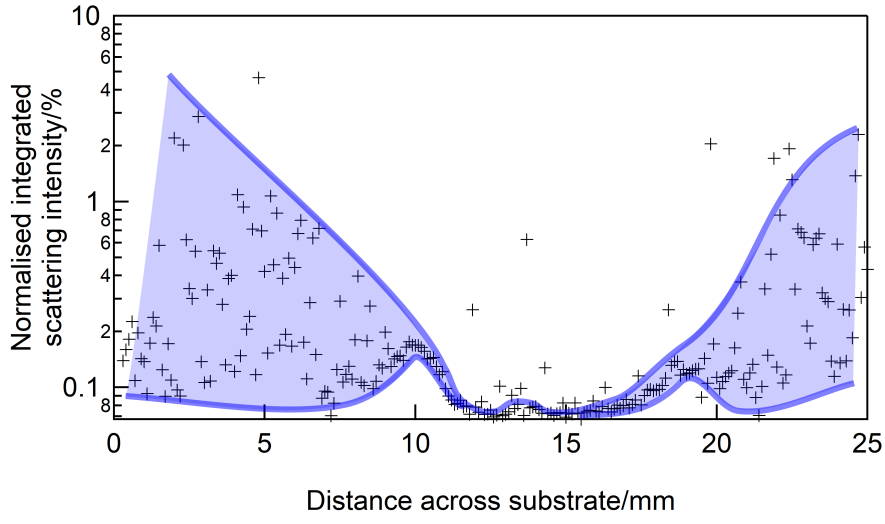

Fig. 9.8 A cross section over the centre of a substrate spun four times with CB aggregated nanoparticles. The variation in the integrated scattering intensity arises from the distribution of particle aggregates across the substrate. Highlighted in blue are areas reminiscent of a coffee ring structure suggesting that the drying of the solution concentrated particles towards the edge of the sample.

scattering points across the substrate. The centre had consistently minimal values due to an absence in nanoparticles, except for a small rise at around $14,000\mu$m where a droplet of solution may have dried. At the extremes of the sample, there was a huge random distribution of intensities that increase as much as 100x the minimum value.

This distribution is explained by the nanoparticle aggregates moving to the outside of the substrate during the spin process. The increase in intensity at the edges of the sample, highlighted in blue in figure 9.8, shows that a drying process was occuring, where nanoparticle density gradually increases from the central distribution leading to a structure akin to that of the "coffee ring". Initially, the rise in intensity is very narrowly distributed, as the nanoparticle packing becomes more dense, before many-particle aggregates deposited across the edges of the substrate result in large variation in the integrated scattering intensity.

The uneven distribution of scatterers across the substrate is problematic. The resultant coffee ring structures suggest that the spinning procedure prevents the deposition of a consistent distribution of particles across the substrate. To counter this, more involved multi-step fabrication methods may be required. It is possible to alter the nanoparticle distribution by using a masking method in order to selectively position nanoparticles across the substrate. A self-assembled mask could be applied in a manner that still allows fast fabrication of the substrate, enabling a process that can fit into the existing fabrication methodology of the OLEDs.

9.2.3 Increasing deposition order using a polystyrene sphere monolayer mask

Spinning a solution of polystyrene (PS) spheres onto a substrate results in the formation of a large scale self-assembled removable masking layer. By drying a nanoparticle solution on top of this layer, the gaps of the mask will selectively allow nanoparticle placement onto the substrate. The PS layer can then be removed resulting in a uniform distribution of particles across the substrate.

A solution of 460nm PS spheres was mixed in a 4 : 1 solution with ethanol and then 50μl of this solution was placed onto a substrate and spun at 500 rpm for 5 minutes. The added ethanol acted to reduce the viscosity of the solution for the spin coating process. This produced arrays of PS spheres that were inconsistent and occasionally multilayered, but with large area monolayers on the mm scale. Mono and multilayers could be discerned both spectrally and by eye (figure 9.9).

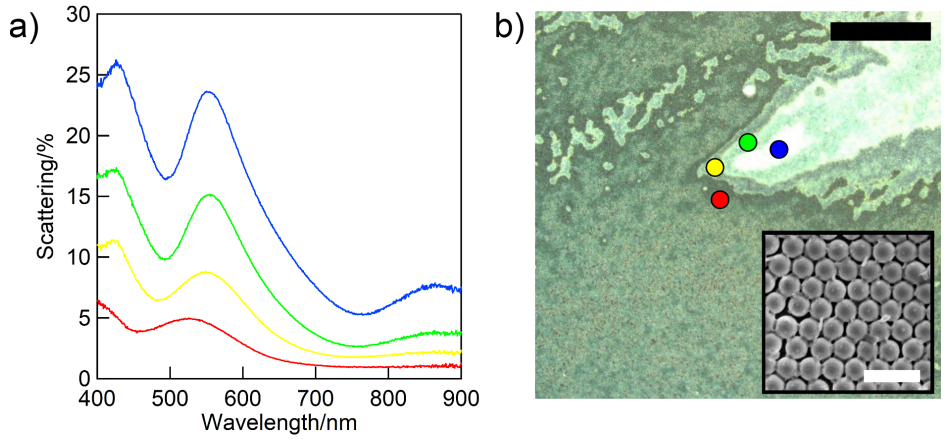

Fig. 9.9 a) Scattering spectra of increasing thicknesses of polystyrene monolayers. b) Microscope image of PS sphere mono and multilayers with coloured circles corresponding to equivalent spectra in a). Scale bar= 100μm. Inset: SEM image of a PS sphere monolayer, courtesy of Dr Lindsey Ibbotson. Scale bar= 1μm

An alternative fabrication method was also used, where the PS particle solution was deposited onto a water surface where they spontaneously form monolayers [184]. The PS spheres can be compacted by adding a detergent, specifically sodium dodecyl sulphate, to the water surface, which encloses the particle mat and forces it into a highly ordered structure. These monolayers could then be lifted off the surface from below by the desired substrate.

Nanoparticle deposition was carried out in two ways. Firstly, the spinning procedure from above was performed. Secondly, a drying method was used, where 100μl of nanoparticle solution was placed onto a masked substrate and heated on a hot plate at 50°C. Nanoparticle densities achieved by the spinning methods showed similar variations of values to the samples fabricated without a mask, while drying samples showed more consistent high densities of particles. The drying method was studied in more detail in order to test the distribution pattern in these masked samples.

After particle deposition, the PS spheres were etched away in a solvent wash, using either dichloromethane or toluene. It was observed that the etching process left a pattern on the polymer layer upon the substrate. This imprinting was not visible via visible microscopy, only showing up under SEM and atomic force microscopy (AFM). AFM scans showed that the polystyrene spheres left a distinct imprint onto the surface polymer layer (figure 9.10). This indicates that either the PS spheres were not fully etched away, or the polymer layer underneath was patterned by the spheres. The dips fall sharply up to depths of 40nm, sig-

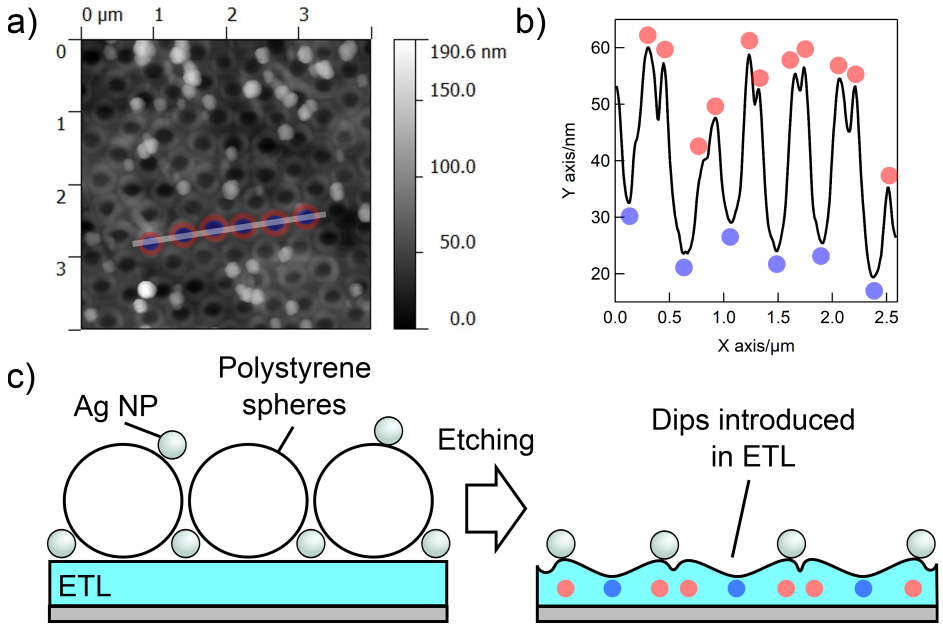

Fig. 9.10 a) AFM scan of etched substrate after nanoparticle deposition and PS sphere etching. The ring structures illustrate the position of the PS spheres prior to etching and the bright white spots are deposited nanoparticles. b) A scan across a section of the substrate seen in image a) by the white line. The troughs in the scan (marked by the blue circles) correspond to the centres of the etched PS spheres (marked by blue circles in the AFM scan). The peaks (marked by red circles) are the edges of the etched PS spheres (marked red in a). c) Schematic of the patterning introduced by the etching procedure. Before etching, NPs sit on the ETL and on the polystyrene. After etching there are dips where the PS spheres are centred, and the particles sit predominantly on the edges. Peaks and troughs are highlighted in red and blue respectively.

nificantly smaller than the diameter of the PS spheres, and the spherical nature of the dips suggest that they are more likely to be imprints in the polymer layer underneath than left over polymer remnants.

The patterning made by the PS spheres on the substrate fortuitously allows for direct observation of nanoparticle positioning on the substrate relative to the PS sphere pattern. It is found that $85 \pm 1\%$ of the particles are outside the circular imprints made by the polystyrene spheres indicating that the PS monolayer mask does encourage nanoparticle deposition in a more spread out fashion. It is unclear whether all particles are deposited between the gaps in the mask, or if anything deposited on top of the PS spheres is washed away in the etching process.

As seen before, the increasing density of particles is matched by a rise in the scattering

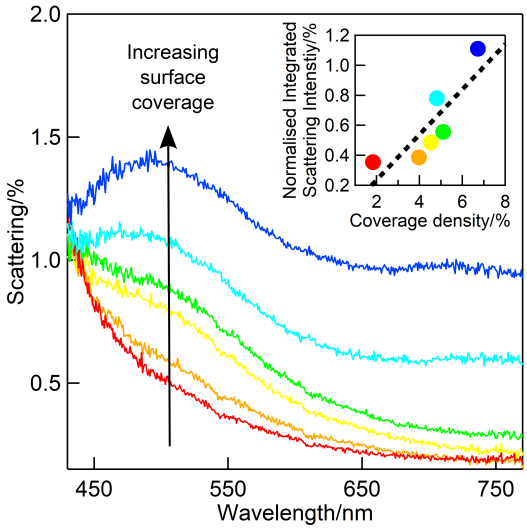

Fig. 9.11 Scattering spectra from silver nanoparticles dried on a PS sphere mask. The scattering increases over time and the rise of scattering peaks at 500nm and 720nm indicates plasmonic coupling. The integrated scattering intensity (inset) increases as a function of nanoparticle coverage density.

intensity and thereby the integrated scattering intensity. The maximum coverage density reached was 7%, and there were distinct peaks at 500nm and 720nm suggesting the presence of a coupled nanoparticle resonance (figure 9.11). It is important to observe that the values for the integrated scattering intensity are slightly greater for similar coverage densities than those observed for deposited CB aggregates, whilst still showing evidence of nanoparticle coupling. This is attributed to the mask forcing nanoparticles into proximal positions as they are deposited, whilst simultaneously limiting the number of nanoparticles deposited due to surface area restrictions. In this manner, smaller nanoparticle aggregates are formed and distributed simultaneously over the substrate.

The use of the PS sphere mask allows for the selective deposition of nanoparticles. However, this distribution is still not uniform over the entire substrate. The highest ratio of integrated scattering intensity to coverage density was attained using this method, however this was achieved using a drying process that does not fit to the prescribed aim of inserting the scattering layer into OLED fabrication methodology. Nevertheless, PS sphere masking procedures show great promise in allowing the distribution of nanoparticles over a large area, particularly by encouraging the formation of small aggregates without linker molecules.

Overall the steepest increase in the integrated scattering intensity with coverage density of particles comes from spun individual nanoparticles. Although greater intensities in the

scattering were observed with CB induced nanoparticle aggregates, these were paired with very large coverage densities. This is due to the presence of large aggregates with poor distribution over the substrate. The deposition of individual nanoparticles results in a lower percentage coverage of the substrate with similar levels of integrated scattering intensity. Masking methods with a removable array of PS spheres allow for selective nanoparticle deposition, creating a physical trap to encourage the formation of small particle aggregates without need for a linker molecule, enabling a regulated distribution of particles.

Although the maximum scattering intensities produced by these loosely packed nanoparticle monolayers are only around 3-4% of our Lambertian normalisation scattering disc, the combination of these methods show that a large scale loosely organised array of particles may be able to promote a significant level of scattering. Further optimisation of these fabrication methods should result in maximisation of the scattering intensity from such particle monolayers.

9.3 Summary

In this chapter, differing self-assembly techniques for the fabrication of varying densities of nanoparticle monolayers have been detailed. Low density nanoparticle monolayers have been fabricated using evaporative and spin-coating methods. These show varying successes in uniformity, but present interesting optical properties for investigation, such as density dependent refractive index sensitivity and high scattering intensity to surface coverage ratios.

The advantages of these methods, as opposed to lithographic techniques that could be used to fabricate similar structures, are that the speed of fabrication can be significantly faster and the techniques used can be scaled up to much larger areas for effective manufacturing. However, the downside to self-assembly techniques is a lack of direct control, although this flaw can be compensated for by using techniques such masking methods to help position nanoparticle formation. Further experimental work must be performed to optimise and characterise these structures, to enable the practical use in optical devices or sensors.

Chapter 10

Conclusions, future work and outlook

In this final chapter, the findings of this work will be summarised. Further potential avenues of investigation for these nanoparticle assemblies will also be described. After these points the text will finish with my thoughts on the possible applications and the general future of plasmonics.

10.1 Experimental summary

By manipulating fundamental physical forces that exist in chemical solutions, large scale structures can be self-assembled from nanoscopic components. Noble metal nanoparticles have been used as the fundamental building blocks to fabricate large scale monolayer arrays. This two-dimensional material is interesting due to plasmonic nanoparticle sensitivity to light below the diffraction limit, a result of the interactions between the incident electric field and the particle's internal electrons. The dipoles produced within the nanoparticles couple together, and are sensitive to the proximity of other particles, as well as their local environment.

Closely packed nanoparticle mats have been fabricated at the interface of two immiscible fluids. With an increase in nanoparticle diameter, more action is required to counter electrostatic repulsion in the system, with higher volumes of thiol and inducing agent required in order to form stable long range arrays. Close packed arrays of nanoparticles showed resistance to the infusion of chemicals into interparticle spacings, which is attributable to chemical and steric effects from the thiol ligand present at the particle surface. When a molecule can permeate into these gaps, the coupled plasmonic resonance frequency of the

system changes, indicated by a redshift in the optical spectra. Interparticle separations can be controlled by changing the length of the thiol surfactants on the particle surface. These changes can be observed optically.

By assembling close-packed nanoparticle arrays onto an elastomeric substrate the stretch tunability of these particle mats can be observed. For particles of diameter < 30nm, encapsulated into a polymer substrate, the particles uniformly separate under the application of biaxial strain. This is shown by a blueshift in the plasmonic response of the mat. After applying uniaxial strain, an anisotropic response is observed. Perpendicular to the strain axis, a redshift is observed in the plasmon resonance. This is caused by the the contraction of the elastomer in this plane [173]. As nanoparticle diameter increases, stretching no longer uniformly separates particles and only small resonance shifts are observed. Instead small clusters of particles are seen to break apart under strain. This is attributed to a greater binding force between particles, arising due to their van der Walls attraction.

Stretch tuneable 60nm gold nanoparticle arrays have been tested as SERS substrates. Increases in the signal with strain have been observed for incident laser light at 785nm. This is counter to the expected result from models with spherical nanoparticles, but can be explained by changes to the near-field from particles with crystalline morphologies. After the addition of a second analyte, changes to molecular conformation of the thiol ligands on the particle surface are observed, indicating molecular length scale changes within the interparticle gaps.

Sparse nanoparticle arrays can be formed via spin coating to spread a particle solution over a substrate. Although density variations were observed, these can be mitigated via a masking procedure using an etchable layer of polystyrene spheres. The intensity of light scattered from these structures was measured by calculating the integrated intensity over set wavelengths, and higher scattering values were found from greater densities of nanoparticles. The scattering intensity was found to have a larger integrated value to coverage ratio when using individual nanoparticles rather than nanoparticle clusters. This is attributed to a lack of control over cluster size.

An alternative method for fabricating sparsely packed nanoparticle arrays has been explored, using the capillary force from an evaporating solvent to deposit particles on a vertially positioned silanized silicon substrate. This process was more effective than spin-coating in producing evenly distributed particles. Particle density was observed to increase down the substrate, due to the increasing salt concentration within the solvent during the evaporation

process. The response of these monolayers to different refractive index fluids is detailed in greater detail elsewhere [17].

10.2 Future work

In this section, further experimentation will be detailed that could be performed to both further explore the structures studied in this thesis and to potentially improve on the observed results. As the fabrication methods detailed here have proved to be repeatable and scalable, additional samples can be produced in large numbers for experimentation.

The behaviour of nanoparticle arrays under strain has been extensively studied in this text. The limitation of nanoparticle adhesion caused in larger diameter particles could potentially be overcome by alternative particle treatments, such as longer length ligands or polymer particle capping [89, 185]. However, this would act to increase particle separation and therefore decrease sensitivity to changes to interparticle distance. Further experimentation should be done to reduce this particle binding whilst maintaining low separation values. Further studies could also be done on the effect of refractive index changes on nanometre length scales. By changing and selecting different particle surfactants, it should be possible to comprehensively study changes of refractive index within the gaps of a closely packed nanoparticle array. Large scale fabrication of these films could enable the development of a stretch tunable substrate for sensing applications.

The results of our stretch tunable SERS measurements suggest that conformational changes of molecules arising from high density films can be detected and measured. Further experiments could be performed to see if dynamic changes to molecular conformations can be induced. Previous work has shown molecular changes of this kind [19]. It is possible that with greater strain applications, changes in molecular conformations could be dynamically changed and observed. If applied to nanoparticle dimers, it may be possible to induce and detect changes to single molecules.

The spun low density nanoparticle monolayers show potential for creating a high intensity scattering surface with minimal modification to the substrate and a low coverage area, fabricating a scattering layer into a device with minimal disruption to the encapsulating layers. Much optimisation is needed to make uniform densities over large surface areas at high speed. Nanoparticle aggregates formed using cucurbituril linkers were seen to be less effective for a low density scattering film than individual nanoparticles. However, it is possible

that by applying more control over the fabrication to limit aggregate size, this could be changed. Alternatively, a multi step process is possible, whereby nanoparticles deposited onto a film could be coated in linker molecules after deposition, then soaked in nanoparticle solution to encourage the rapid formation of dimers. As dimers have a higher scattering cross section than individual particles, this would increase the integrated scattering intensity over the film without dramatically increasing the surface coverage. This hybrid method could be used in conjuction with the masking method, to enable the maximum possible scattering intensities from the minimal surface coverage of particles.

The work in this thesis gives a good exploration of the plasmonic behaviour of nanoparparticle arrays. By building on this work, practical sensing applications could be developed and maybe even fundamental physical behaviour could be probed.

10.3 An outlook: the potential and future applications of plasmonic devices

This thesis has explored the interactions between the plasmonic behaviour of nanoparticle aggregates to incident light, as well as their chemical surroundings. Because of this sensitivity, there is considerable interest in plasmonic sensors to make practical use of these properties [186]. A subset of these investigations focuses on the potential for flexible nanoparticle based sensors [8], where changing interparticle distances can be manipulated to make best use of both near and far-field optical coupling between particles. This concluding section will give a quick review of some select applications for plasmonic and nanoparticulate materials that show promise for commercialisation and widespread use.

The environmental sensitivity of plasmonic structures has been explored in this work mainly via changing the local refractive index values. Clear changes in colouration for different refractive index fluids can result in extremely sensitive measures of refractive index values, and the potential for this application has gathered considerable interest [17, 187, 188]. Optical changes to nanoparticle films induced by changes to their surrounding media can also be used to directly detect molecules present in the film environment, by selectively choosing the ligand coatings of the particles that bind to specific molecules. In this way, tests for specific antibodies have been developed [189]. Similarly changes to the optical response of a nanoparticle film can also be induced by temperature changes by selecting thermally sensitive linking molecules to connect the aggregate [190].

An area that has not been explored in this thesis is the potential for conductive materials to be made out of metal nanoparticle building blocks. Percolation paths can form within large nanoparticle aggregates that allow currents to flow within nanoparticle assemblies. These properties can be aided by using conductive connecting molecules between the metal particles [191, 192]. Embedding these structures within polymers leads to stretchable conductive films that have potential applications within bendable devices [193]. Additionally, due to the composite nature of these films, conductivity is very sensitive to pressure, temperature and strain, enabling their use as touch sensors [194].

The potential for SERS applications is widely known. Nanoparticle based SERS substrates can detect very small quantities of harmful substances, such as heavy metals, caught up within the ligands on the particle surface [195]. More importantly they have been used to detect small concentrations of toxins within complex solutions like orange juice, showing how even in solvents with many different Raman active molecules, it is possible to distinguish particular analytes [62]. Finally, SERS measurements have even been achieved through a mobile telephone's camera by using a surface enhanced substrate to improve Raman intensities [196]. This shows that personal SERS detectors are possible even now, although to make them accurate and durable is still a work in progress.

Although still far from deployment, the capabilities of plasmonic materials has experienced a massive jump over the last two decades due to improvements in fabrication, measurement and modelling techniques. Further study of plasmonic structures will hopefully lead to the commercialisation of many of these potential applications.

Appendix A

Permittivity of non-magnetic materials from Maxwell's equations

The macroscopic forms of Maxwell's equations can be used to describe all the electromagnetic effects on a system as a whole. This allows for a simplified picture of the bulk response, as opposed to the microscopic form which describes the behaviour at an atomic scale. These equations are;

$$\nabla \cdot \mathbf{D} = \rho \tag{A.1}$$

$$\nabla \times \mathbf{E} = -\frac{\partial \mathbf{B}}{\partial t} \tag{A.2}$$

$$\nabla \cdot \mathbf{B} = 0 \tag{A.3}$$

$$\nabla \times \mathbf{H} = \mathbf{J} + \frac{\partial \mathbf{D}}{\partial t} \tag{A.4}$$

Here **E** is the electric field, **D**, the electric displacement, **H**, the magnetic field and **B**, the magnetic induction. In addition to these four fields, the effects of the charge carriers are accounted for in the variables **J**, for the current density, and ρ, for the charge density.

The solutions to these equations are dependent upon the materials that the electromagnetic waves are travelling through. For our purposes we will consider our material to be linear

and isotropic so that the response over its volume is universal and has no local variations. In this case, we can use the following relations to describe the subsequent internal fields;

$$\mathbf{D} = \varepsilon_0 \varepsilon \mathbf{E} \tag{A.5}$$

$$\mathbf{B} = \mu_0 \mu \mathbf{H} \tag{A.6}$$

Here ε_0 is the permittivity of free space, μ_0 the permeability of free space, ε is the relative permittivity (or dielectric constant), and μ is the relative permeability of the material. For non-magnetic materials the relative permeability is equal to 1, and therefore equation A.6 can be simplified. In addition, we can also define $\mathbf{D}$ and $\mathbf{H}$ in terms of the polarisation $\mathbf{P}$ and magnetization $\mathbf{M}$ exhibited by the medium with the following macroscopic relations:

$$\mathbf{D} = \varepsilon_0 \mathbf{E} + \mathbf{P} \tag{A.7}$$

$$\mathbf{H} = \frac{1}{\mu_0} \mathbf{B} + \mathbf{M} \tag{A.8}$$

When modelling for non-magnetic materials we can simplify the above equations by stating that the magnetization $\mathbf{M} = 0$, removing from consideration magnetic effects.

By combining equations A.5 and A.7 an expression for the dielectric constant can be derived in terms of the polarisation of the material;

$$\varepsilon = 1 + \frac{\mathbf{P}}{\varepsilon_0 \mathbf{E}} \tag{A.9}$$

The dielectric constant of this linear, isotropic and non-magnetic material is therefore heavily influenced by the distribution of charge across its bulk. By modelling the movement of charge carriers across the material, we can describe its optical response.

References

[1] I. Freestone, N. Meeks, M. Sax, and C. Higgitt, "The lycurgus cup—a roman nanotechnology," *Gold Bulletin*, vol. 40, no. 4, pp. 270–277, 2007.

[2] M. Faraday, "The bakerian lecture: experimental relations of gold (and other metals) to light," *Philosophical Transactions of the Royal Society of London*, vol. 147, pp. 145–181, 1857.

[3] G. Mie, "Beiträge zur optik trüber medien, speziell kolloidaler metallösungen," *Annalen der physik*, vol. 330, no. 3, pp. 377–445, 1908.

[4] h.-s. Wikipedia Commons.

[5] R. Ritchie, "Plasma losses by fast electrons in thin films," *Physical Review*, vol. 106, no. 5, p. 874, 1957.

[6] I. R. Hooper, T. Preist, and J. R. Sambles, "Making tunnel barriers (including metals) transparent," *Physical Review Letters*, vol. 97, no. 5, p. 053902, 2006.

[7] W. P. Klein, C. N. Schmidt, B. Rapp, S. Takabayashi, W. B. Knowlton, J. Lee, B. Yurke, W. L. Hughes, E. Graugnard, and W. Kuang, "Multiscaffold DNA origami nanoparticle waveguides," *Nano Letters*, vol. 13, no. 8, pp. 3850–3856, 2013.

[8] M. Segev-Bar and H. Haick, "Flexible sensors based on nanoparticles," *ACS Nano*, vol. 7, no. 10, pp. 8366–8378, 2013.

[9] S. A. Maier, M. L. Brongersma, P. G. Kik, and H. A. Atwater, "Observation of near-field coupling in metal nanoparticle chains using far-field polarization spectroscopy," *Physical Review B*, vol. 65, no. 19, p. 193408, 2002.

[10] P. Drude, "Zur elektronentheorie der metalle," *Annalen der Physik*, vol. 306, no. 3, pp. 566–613, 1900.

[11] S. A. Maier, *Plasmonics: fundamentals and applications*. Springer Science & Business Media, 2007.

[12] P. B. Johnson and R.-W. Christy, "Optical constants of the noble metals," *Physical Review B*, vol. 6, no. 12, p. 4370, 1972.

[13] L. Novotony and B. Hecht, *Principles of nano-optics*. Cambridge University Press, 2012.

[14] S. Salvatore, A. Demetriadou, S. Vignolini, S. S. Oh, S. Wuestner, N. A. Yufa, M. Stefik, U. Wiesner, J. J. Baumberg, O. Hess, *et al.*, "Tunable 3D extended self-assembled gold metamaterials with enhanced light transmission," *Advanced Materials*, vol. 25, no. 19, pp. 2713–2716, 2013.

[15] S. Yokogawa, S. P. Burgos, and H. A. Atwater, "Plasmonic color filters for CMOS image sensor applications," *Nano Letters*, vol. 12, no. 8, pp. 4349–4354, 2012.

[16] U. Kreibig and M. Vollmer, *Optical properties of metal clusters*, vol. 25. Springer Science & Business Media, 2013.

[17] F. Huang, S. Drakeley, M. G. Millyard, A. Murphy, R. White, E. Spigone, J. Kivioja, and J. J. Baumberg, "Zero-reflectance metafilms for optimal plasmonic sensing," *Advanced Optical Materials*, vol. 4, no. 2, pp. 328–335, 2016.

[18] A. Blanchard-Dionne, L. Guyot, S. Patskovsky, R. Gordon, and M. Meunier, "Intensity based surface plasmon resonance sensor using a nanohole rectangular array," *Optics Express*, vol. 19, no. 16, pp. 15041–15046, 2011.

[19] F. Benz, M. K. Schmidt, A. Dreismann, R. Chikkaraddy, Y. Zhang, A. Demetriadou, C. Carnegie, H. Ohadi, B. de Nijs, R. Esteban, *et al.*, "Single-molecule optomechanics in "picocavities"," *Science*, vol. 354, no. 6313, pp. 726–729, 2016.

[20] W. Rechberger, A. Hohenau, A. Leitner, J. Krenn, B. Lamprecht, and F. Aussenegg, "Optical properties of two interacting gold nanoparticles," *Optics Communications*, vol. 220, no. 1, pp. 137–141, 2003.

[21] A. Taleb, C. Petit, and M. Pileni, "Optical properties of self-assembled 2D and 3D superlattices of silver nanoparticles," *The Journal of Physical Chemistry B*, vol. 102, no. 12, pp. 2214–2220, 1998.

[22] A. Taleb, V. Russier, A. Courty, and M. Pileni, "Collective optical properties of silver nanoparticles organized in two-dimensional superlattices," *Physical Review B*, vol. 59, no. 20, p. 13350, 1999.

[23] S. Biring, H.-H. Wang, J.-K. Wang, and Y.-L. Wang, "Light scattering from 2D arrays of monodispersed Ag-nanoparticles separated by tunable nano-gaps: spectral evolution and analytical analysis of plasmonic coupling," *Optics Express*, vol. 16, no. 20, pp. 15312–15324, 2008.

[24] I. Romero, J. Aizpurua, G. W. Bryant, and F. J. García De Abajo, "Plasmons in nearly touching metallic nanoparticles: singular response in the limit of touching dimers," *Optics Express*, vol. 14, no. 21, pp. 9988–9999, 2006.

[25] M. Kyung Oh, S. Park, S. K. Kim, and S.-H. Lim, "Finite difference time domain calculation on layer-by-layer assemblies of close-packed gold nanoparticles," *Journal of Computational and Theoretical Nanoscience*, vol. 7, no. 6, pp. 1085–1094, 2010.

[26] S. A. Maier, P. G. Kik, and H. A. Atwater, "Observation of coupled plasmon-polariton modes in Au nanoparticle chain waveguides of different lengths: Estimation of waveguide loss," *Applied Physics Letters*, vol. 81, no. 9, pp. 1714–1716, 2002.

[27] N. Harris, M. D. Arnold, M. G. Blaber, and M. J. Ford, "Plasmonic resonances of closely coupled gold nanosphere chains," *The Journal of Physical Chemistry C*, vol. 113, no. 7, pp. 2784–2791, 2009.

[28] R. W. Taylor, T.-C. Lee, O. A. Scherman, R. Esteban, J. Aizpurua, F. M. Huang, J. J. Baumberg, and S. Mahajan, "Precise subnanometer plasmonic junctions for SERS within gold nanoparticle assemblies using cucurbit [n] uril "glue"," *ACS Nano*, vol. 5, no. 5, pp. 3878–3887, 2011.

[29] F. Le, D. W. Brandl, Y. A. Urzhumov, H. Wang, J. Kundu, N. J. Halas, J. Aizpurua, and P. Nordlander, "Metallic nanoparticle arrays: a common substrate for both surface-enhanced Raman scattering and surface-enhanced infrared absorption," *ACS Nano*, vol. 2, no. 4, pp. 707–718, 2008.

[30] R. Esteban, R. W. Taylor, J. J. Baumberg, and J. Aizpurua, "How chain plasmons govern the optical response in strongly interacting self-assembled metallic clusters of nanoparticles," *Langmuir*, vol. 28, no. 24, pp. 8881–8890, 2012.

[31] F. Huang and J. J. Baumberg, "Actively tuned plasmons on elastomerically driven Au nanoparticle dimers," *Nano Letters*, vol. 10, no. 5, pp. 1787–1792, 2010.

[32] P. P. Ewald, "Die berechnung optischer und elektrostatischer gitterpotentiale," *Annalen der physik*, vol. 369, no. 3, pp. 253–287, 1921.

[33] M. Born, *Optik: ein Lehrbuch der elektromagnetischen Lichttheorie*. Springer-Verlag, 2013.

[34] B. Dusemund, A. Hoffmann, T. Salzmann, U. Kreibig, and G. Schmid, "Cluster matter: the transition of optical elastic scattering to regular reflection," *Zeitschrift für Physik D Atoms, Molecules and Clusters*, vol. 20, no. 1, pp. 305–308, 1991.

[35] A. Tao, P. Sinsermsuksakul, and P. Yang, "Tunable plasmonic lattices of silver nanocrystals," *Nature Nanotechnology*, vol. 2, no. 7, pp. 435–440, 2007.

[36] M. Quinten and U. Kreibig, "Optical properties of aggregates of small metal particles," *Surface Science*, vol. 172, no. 3, pp. 557–577, 1986.

[37] C. Sorensen, "Light scattering by fractal aggregates: a review," *Aerosol Science & Technology*, vol. 35, no. 2, pp. 648–687, 2001.

[38] N. Verellen, Y. Sonnefraud, H. Sobhani, F. Hao, V. V. Moshchalkov, P. V. Dorpe, P. Nordlander, and S. A. Maier, "Fano resonances in individual coherent plasmonic nanocavities," *Nano Letters*, vol. 9, no. 4, pp. 1663–1667, 2009.

[39] S. Olcum, A. Kocabas, G. Ertas, A. Atalar, and A. Aydinli, "Tunable surface plasmon resonance on an elastomeric substrate," *Optics Express*, vol. 17, no. 10, pp. 8542–8547, 2009.

[40] P. Reader-Harris, A. Ricciardi, T. Krauss, and A. Di Falco, "Optical guided mode resonance filter on a flexible substrate," *Optics Express*, vol. 21, no. 1, pp. 1002–1007, 2013.

[41] A. Di Falco, M. Ploschner, and T. F. Krauss, "Flexible metamaterials at visible wavelengths," *New Journal of Physics*, vol. 12, no. 11, p. 113006, 2010.

[42] R. M. Cole, S. Mahajan, and J. J. Baumberg, "Stretchable metal-elastomer nanovoids for tunable plasmons," *Applied Physics Letters*, vol. 95, no. 15, p. 154103, 2009.

[43] X. Zhu, L. Shi, X. Liu, J. Zi, and Z. Wang, "A mechanically tunable plasmonic structure composed of a monolayer array of metal-capped colloidal spheres on an elastomeric substrate," *Nano Research*, vol. 3, no. 11, pp. 807–812, 2010.

[44] Y.-L. Chiang, C.-W. Chen, C.-H. Wang, C.-Y. Hsieh, Y.-T. Chen, H.-Y. Shih, and Y.-F. Chen, "Mechanically tunable surface plasmon resonance based on gold nanoparticles and elastic membrane polydimethylsiloxane composite," *Applied Physics Letters*, vol. 96, no. 4, p. 041904, 2010.

[45] X. Zhu, S. Xiao, L. Shi, X. Liu, J. Zi, O. Hansen, and N. A. Mortensen, "A stretch-tunable plasmonic structure with a polarization-dependent response," *Optics express*, vol. 20, no. 5, pp. 5237–5242, 2012.

[46] E. Le Ru, E. Blackie, M. Meyer, and P. G. Etchegoin, "Surface enhanced Raman scattering enhancement factors: a comprehensive study," *The Journal of Physical Chemistry C*, vol. 111, no. 37, pp. 13794–13803, 2007.

[47] H. Xu, J. Aizpurua, M. Käll, and P. Apell, "Electromagnetic contributions to single-molecule sensitivity in surface-enhanced Raman scattering," *Physical Review E*, vol. 62, no. 3, p. 4318, 2000.

[48] M. Moskovits, "Surface selection rules," *The Journal of Chemical Physics*, vol. 77, no. 9, pp. 4408–4416, 1982.

[49] M. Moskovits and J. Suh, "Surface selection rules for surface-enhanced Raman spectroscopy: calculations and application to the surface-enhanced Raman spectrum of phthalazine on silver," *The Journal of Physical Chemistry*, vol. 88, no. 23, pp. 5526–5530, 1984.

[50] M. Fleischmann, P. J. Hendra, and A. McQuillan, "Raman spectra of pyridine adsorbed at a silver electrode," *Chemical Physics Letters*, vol. 26, no. 2, pp. 163–166, 1974.

[51] B. Sharma, R. R. Frontiera, A.-I. Henry, E. Ringe, and R. P. Van Duyne, "SERS: materials, applications, and the future," *Materials Today*, vol. 15, no. 1, pp. 16–25, 2012.

[52] G. McNay, D. Eustace, W. E. Smith, K. Faulds, and D. Graham, "Surface-enhanced Raman scattering (SERS) and surface-enhanced resonance Raman scattering (SERRS): a review of applications," *Applied Spectroscopy*, vol. 65, no. 8, pp. 825–837, 2011.

[53] E. Le Ru and P. Etchegoin, *Principles of Surface-Enhanced Raman Spectroscopy: and related plasmonic effects*. Elsevier, 2008.

[54] L. Mao, Z. Li, B. Wu, and H. Xu, "Effects of quantum tunneling in metal nanogap on surface-enhanced Raman scattering," *Applied Physics Letters*, vol. 94, no. 24, p. 243102, 2009.

[55] J. Suh, D. DiLella, and M. Moskovits, "Surface-enhanced Raman spectroscopy of colloidal metal systems: a two-dimensional phase equilibrium in p-aminobenzoic acid adsorbed on silver," *The Journal of Physical Chemistry*, vol. 87, no. 9, pp. 1540–1544, 1983.

[56] O. Siiman, L. Bumm, R. Callaghan, C. Blatchford, and M. Kerker, "Surface-enhanced Raman scattering by citrate on colloidal silver," *The Journal of Physical Chemistry*, vol. 87, no. 6, pp. 1014–1023, 1983.

[57] S. Mahajan, T.-C. Lee, F. Biedermann, J. T. Hugall, J. J. Baumberg, and O. A. Scherman, "Raman and SERS spectroscopy of cucurbit [n] urils," *Physical Chemistry Chemical Physics*, vol. 12, no. 35, pp. 10429–10433, 2010.

[58] K. Uetsuki, P. Verma, P. Nordlander, and S. Kawata, "Tunable plasmon resonances in a metallic nanotip–film system," *Nanoscale*, vol. 4, no. 19, pp. 5931–5935, 2012.

[59] R. Zhang, Y. Zhang, Z. Dong, S. Jiang, C. Zhang, L. Chen, L. Zhang, Y. Liao, J. Aizpurua, Y. Luo, and J. Yang, "Chemical mapping of a single molecule by plasmon-enhanced Raman scattering," *Nature*, vol. 498, no. 7452, pp. 82–86, 2013.

[60] K. C. Grabar, R. G. Freeman, M. B. Hommer, and M. J. Natan, "Preparation and characterization of Au colloid monolayers," *Analytical Chemistry*, vol. 67, no. 4, pp. 735–743, 1995.

[61] J. C. Fraire, L. A. Perez, and E. A. Coronado, "Cluster size effects in the surface-enhanced Raman scattering response of Ag and Au nanoparticle aggregates: experimental and theoretical insight," *The Journal of Physical Chemistry C*, vol. 117, no. 44, pp. 23090–23107, 2013.

[62] B. Peng, G. Li, D. Li, S. Dodson, Q. Zhang, J. Zhang, Y. H. Lee, H. V. Demir, X. Yi Ling, and Q. Xiong, "Vertically aligned gold nanorod monolayer on arbitrary substrates: self-assembly and femtomolar detection of food contaminants," *ACS Nano*, vol. 7, no. 7, pp. 5993–6000, 2013.

[63] T. Siegfried, Y. Ekinci, O. J. Martin, and H. Sigg, "Gap plasmons and near-field enhancement in closely packed sub-10 nm gap resonators," *Nano Letters*, vol. 13, no. 11, pp. 5449–5453, 2013.

[64] K. D. Alexander, K. Skinner, S. Zhang, H. Wei, and R. Lopez, "Tunable SERS in gold nanorod dimers through strain control on an elastomeric substrate," *Nano letters*, vol. 10, no. 11, pp. 4488–4493, 2010.

[65] S. Nie and S. R. Emory, "Probing single molecules and single nanoparticles by surface-enhanced Raman scattering," *Science*, vol. 275, no. 5303, pp. 1102–1106, 1997.

[66] K. Kneipp, Y. Wang, H. Kneipp, L. T. Perelman, I. Itzkan, R. R. Dasari, and M. S. Feld, "Single molecule detection using surface-enhanced Raman scattering (SERS)," *Physical Review Letters*, vol. 78, no. 9, p. 1667, 1997.

[67] J. Fontana, J. Livenere, F. J. Bezares, J. D. Caldwell, R. Rendell, and B. R. Ratna, "Large surface-enhanced Raman scattering from self-assembled gold nanosphere monolayers," *Applied Physics Letters*, vol. 102, no. 20, p. 201606, 2013.

[68] S. Zhu, C. Fan, J. Wang, J. He, and E. Liang, "Self-assembled Ag nanoparticles for surface enhanced Raman scattering," *Optical Review*, vol. 20, no. 5, pp. 361–366, 2013.

[69] B. N. Khlebtsov, V. A. Khanadeev, M. Y. Tsvetkov, V. N. Bagratashvili, and N. G. Khlebtsov, "Surface-enhanced Raman scattering substrates based on self-assembled pegylated gold and gold–silver core–shell nanorods," *The Journal of Physical Chemistry C*, vol. 117, no. 44, pp. 23162–23171, 2013.

[70] C. Chen, J. Hao, L. Zhu, Y. Yao, X. Meng, W. Weimer, and Q. K. Wang, "Direct two-phase interfacial self-assembly of aligned silver nanowire films for surface enhanced Raman scattering applications," *Journal of Materials Chemistry A*, vol. 1, no. 43, pp. 13496–13501, 2013.

[71] H. Y. Jung, Y.-K. Park, S. Park, and S. K. Kim, "Surface enhanced Raman scattering from layered assemblies of close-packed gold nanoparticles," *Analytica Chimica Acta*, vol. 602, no. 2, pp. 236–243, 2007.

[72] I. Izquierdo-Lorenzo, S. Jradi, and P.-M. Adam, "Direct laser writing of random Au nanoparticle three-dimensional structures for highly reproducible micro-SERS measurements," *RSC Advances*, vol. 4, no. 8, pp. 4128–4133, 2014.

[73] Z. Yi, J. Luo, X. Li, Y. Yi, X. Xu, P. Wu, X. Jiang, W. Wu, Y. Yi, and Y. Tang, "Plasmonic coupling effect in silver spongelike networks nanoantenna for large increases of surface enhanced Raman scattering," *The Journal of Physical Chemistry C*, vol. 117, no. 49, pp. 26295–26304, 2013.

[74] G. M. Whitesides and B. Grzybowski, "Self-assembly at all scales," *Science*, vol. 295, no. 5564, pp. 2418–2421, 2002.

[75] H. Duan and K. K. Berggren, "Directed self-assembly at the 10 nm scale by using capillary force-induced nanocohesion," *Nano Letters*, vol. 10, no. 9, pp. 3710–3716, 2010.

[76] B. D. Hatton and J. Aizenberg, "Writing on superhydrophobic nanopost arrays: Topographic design for bottom-up assembly," *Nano Letters*, vol. 12, no. 9, pp. 4551–4557, 2012.

[77] S. Furutsuki, S.-C. Chung, S.-i. Nishimura, Y. Kudo, K. Yamashita, and A. Yamada, "Electrochromism of Li x FePO4 induced by intervalence charge transfer transition," *The Journal of Physical Chemistry C*, vol. 116, no. 29, pp. 15259–15264, 2012.

[78] V. Santhanam and R. P. Andres, "Microcontact printing of uniform nanoparticle arrays," *Nano Letters*, vol. 4, no. 1, pp. 41–44, 2004.

[79] B. Derjaguin, L. Landau, *et al.*, "Theory of the stability of strongly charged lyophobic sols and of the adhesion of strongly charged particles in solutions of electrolytes," *Acta Physicochimica URSS*, vol. 14, no. 6, pp. 633–662, 1941.

[80] E. J. W. Verwey and J. T. G. Overbeek, *Theory of the Stability of Lyophobic Colloids*. 1948.

[81] E. J. W. Verwey and J. T. G. Overbeek, "Theory of the stability of lyophobic colloids," *Journal of Colloid Science*, vol. 10, no. 2, pp. 224–225, 1955.

[82] T. Kim, K. Lee, M.-s. Gong, and S.-W. Joo, "Control of gold nanoparticle aggregates by manipulation of interparticle interaction," *Langmuir*, vol. 21, no. 21, pp. 9524–9528, 2005.

[83] E. M. Hotze, T. Phenrat, and G. V. Lowry, "Nanoparticle aggregation: challenges to understanding transport and reactivity in the environment," *Journal of environmental quality*, vol. 39, no. 6, pp. 1909–1924, 2010.

[84] M. N. Martin, J. I. Basham, P. Chando, and S.-K. Eah, "Charged gold nanoparticles in non-polar solvents: 10-min synthesis and 2D self-assembly," *Langmuir*, vol. 26, no. 10, pp. 7410–7417, 2010.

[85] S. K. Sainis, V. Germain, C. O. Mejean, and E. R. Dufresne, "Electrostatic interactions of colloidal particles in nonpolar solvents: Role of surface chemistry and charge control agents," *Langmuir*, vol. 24, no. 4, pp. 1160–1164, 2008.

[86] H. Eckstein and U. Kreibig, "Light induced aggregation of metal clusters," *Zeitschrift für Physik D Atoms, Molecules and Clusters*, vol. 26, no. 1, pp. 239–241, 1993.

[87] J. N. Israelachvili, *Intermolecular and surface forces: revised third edition*. Academic press, 2011.

[88] A. Hallock, P. Redmond, and L. Brus, "Optical forces between metallic particles," *Proceedings of the National Academy of Sciences*, vol. 102, no. 5, pp. 1280–1284, 2005.

[89] T. Ding, V. K. Valev, A. R. Salmon, C. J. Forman, S. K. Smoukov, O. A. Scherman, D. Frenkel, and J. J. Baumberg, "Light-induced actuating nanotransducers," *Proceedings of the National Academy of Sciences*, vol. 113, no. 20, pp. 5503–5507, 2016.

[90] F. Reincke, W. K. Kegel, H. Zhang, M. Nolte, D. Wang, D. Vanmaekelbergh, and H. Möhwald, "Understanding the self-assembly of charged nanoparticles at the water/oil interface," *Physical Chemistry Chemical Physics*, vol. 8, no. 33, pp. 3828–3835, 2006.

[91] G. Fritz, V. Schädler, N. Willenbacher, and N. J. Wagner, "Electrosteric stabilization of colloidal dispersions," *Langmuir*, vol. 18, no. 16, pp. 6381–6390, 2002.

[92] J. Liao, Y. Zhang, W. Yu, L. Xu, C. Ge, J. Liu, and N. Gu, "Linear aggregation of gold nanoparticles in ethanol," *Colloids and Surfaces A: Physicochemical and Engineering Aspects*, vol. 223, no. 1, pp. 177–183, 2003.

[93] S. Wakamatsu, J.-i. Nakada, S. Fujii, U. Akiba, and M. Fujihira, "Self-assembled nanostructure of Au nanoparticles on a self-assembled monolayer," *Ultramicroscopy*, vol. 105, no. 1, pp. 26–31, 2005.

[94] L. Cheng, A. Liu, S. Peng, and H. Duan, "Responsive plasmonic assemblies of amphiphilic nanocrystals at oil- water interfaces," *ACS Nano*, vol. 4, no. 10, pp. 6098–6104, 2010.

[95] M. M. Abul Kashem, D. Patra, J. Perlich, A. Rothkirch, A. Buffet, S. V. Roth, V. M. Rotello, and P. Muller-Buschbaum, "Two-and three-dimensional network of nanoparticles via polymer-mediated self-assembly," *ACS Macro Letters*, vol. 1, no. 3, pp. 396–399, 2012.

[96] M. Brust, M. Walker, D. Bethell, D. J. Schiffrin, and R. Whyman, "Synthesis of thiol-derivatised gold nanoparticles in a two-phase liquid–liquid system," *Journal of the Chemical Society, Chemical Communications*, no. 7, pp. 801–802, 1994.

[97] R. Jin, "Quantum sized, thiolate-protected gold nanoclusters," *Nanoscale*, vol. 2, no. 3, pp. 343–362, 2010.

[98] R. Klajn, K. J. Bishop, M. Fialkowski, M. Paszewski, C. J. Campbell, T. P. Gray, and B. A. Grzybowski, "Plastic and moldable metals by self-assembly of sticky nanoparticle aggregates," *Science*, vol. 316, no. 5822, pp. 261–264, 2007.

[99] C.-F. Chen, S.-D. Tzeng, H.-Y. Chen, K.-J. Lin, and S. Gwo, "Tunable plasmonic response from alkanethiolate-stabilized gold nanoparticle superlattices: evidence of near-field coupling," *Journal of the American Chemical Society*, vol. 130, no. 3, pp. 824–826, 2008.

[100] D. Chandler, "Interfaces and the driving force of hydrophobic assembly," *Nature*, vol. 437, no. 7059, pp. 640–647, 2005.

[101] C. T. O'Mahony, R. A. Farrell, T. Goshal, J. D. Holmes, and M. A. Morris, "The thermodynamics of defect formation in self-assembled systems," in *Thermodynamics-Systems in Equilibrium and Non-Equilibrium*, InTech, 2011.

[102] M. Rycenga, J. M. McLellan, and Y. Xia, "Controlling the assembly of silver nanocubes through selective functionalization of their faces," *Advanced Materials*, vol. 20, no. 12, pp. 2416–2420, 2008.

[103] R. C. Mucic, J. J. Storhoff, C. A. Mirkin, and R. L. Letsinger, "DNA-directed synthesis of binary nanoparticle network materials," *Journal of the American Chemical Society*, vol. 120, no. 48, pp. 12674–12675, 1998.

[104] S. J. Barrow, A. M. Funston, X. Wei, and P. Mulvaney, "DNA-directed self-assembly and optical properties of discrete 1D, 2D and 3D plasmonic structures," *Nano Today*, vol. 8, no. 2, pp. 138–167, 2013.

[105] A. J. Mastroianni, S. A. Claridge, and A. P. Alivisatos, "Pyramidal and chiral groupings of gold nanocrystals assembled using DNA scaffolds," *Journal of the American Chemical Society*, vol. 131, no. 24, pp. 8455–8459, 2009.

[106] V. V. Thacker, L. O. Herrmann, D. O. Sigle, T. Zhang, T. Liedl, J. J. Baumberg, and U. F. Keyser, "DNA origami based assembly of gold nanoparticle dimers for surface-enhanced Raman scattering," *Nature Communications*, vol. 5, 2014.

[107] B. G. Prevo and O. D. Velev, "Controlled, rapid deposition of structured coatings from micro-and nanoparticle suspensions," *Langmuir*, vol. 20, no. 6, pp. 2099–2107, 2004.

[108] J. F. Galisteo-López, M. Ibisate, R. Sapienza, L. S. Froufe-Pérez, Á. Blanco, and C. López, "Self-assembled photonic structures," *Advanced Materials*, vol. 23, no. 1, pp. 30–69, 2011.

[109] S. U. Pickering, "CXCVI.-emulsions," *Journal of the Chemical Society, Transactions*, vol. 91, pp. 2001–2021, 1907.

[110] B. P. Binks and J. H. Clint, "Solid wettability from surface energy components: relevance to pickering emulsions," *Langmuir*, vol. 18, no. 4, pp. 1270–1273, 2002.

[111] Y. Lin, H. Skaff, T. Emrick, A. Dinsmore, and T. Russell, "Nanoparticle assembly and transport at liquid-liquid interfaces," *Science*, vol. 299, no. 5604, pp. 226–229, 2003.

[112] L. Hu, M. Chen, X. Fang, and L. Wu, "Oil–water interfacial self-assembly: a novel strategy for nanofilm and nanodevice fabrication," *Chemical Society Reviews*, vol. 41, no. 3, pp. 1350–1362, 2012.

[113] Y.-K. Park and S. Park, "Directing close-packing of midnanosized gold nanoparticles at a water/hexane interface," *Chemistry of Materials*, vol. 20, no. 6, pp. 2388–2393, 2008.

[114] W. H. Binder, "Supramolecular assembly of nanoparticles at liquid–liquid interfaces," *Angewandte Chemie International Edition*, vol. 44, no. 33, pp. 5172–5175, 2005.

[115] S. Kutuzov, J. He, R. Tangirala, T. Emrick, T. Russell, and A. Böker, "On the kinetics of nanoparticle self-assembly at liquid/liquid interfaces," *Physical Chemistry Chemical Physics*, vol. 9, no. 48, pp. 6351–6358, 2007.

[116] J. Matsui, K. Yamamoto, N. Inokuma, H. Orikasa, T. Kyotani, and T. Miyashita, "Fabrication of densely packed multi-walled carbon nanotube ultrathin films using a liquid–liquid interface," *Journal of Materials Chemistry*, vol. 17, no. 36, pp. 3806–3811, 2007.

[117] F. Reincke, S. G. Hickey, W. K. Kegel, and D. Vanmaekelbergh, "Spontaneous assembly of a monolayer of charged gold nanocrystals at the water/oil interface," *Angewandte Chemie International Edition*, vol. 43, no. 4, pp. 458–462, 2004.

[118] R. Krishnaswamy and A. Sood, "Growth, self-assembly and dynamics of nano-scale films at fluid interfaces," *Journal of Materials Chemistry*, vol. 20, no. 18, pp. 3539–3552, 2010.

[119] G. Yang and D. T. Hallinan, "Gold nanoparticle monolayers from sequential interfacial ligand exchange and migration in a three-phase system," *Scientific reports*, vol. 6, p. 35339, 2016.

[120] K. D. Comeau and M. V. Meli, "Effect of alkanethiol chain length on gold nanoparticle monolayers at the air–water interface," *Langmuir*, vol. 28, no. 1, pp. 377–381, 2011.

[121] L. Pei, K. Mori, and M. Adachi, "Investigation on arrangement and fusion behaviors of gold nanoparticles at the air/water interface," *Colloids and Surfaces A: Physicochemical and Engineering Aspects*, vol. 281, no. 1, pp. 44–50, 2006.

[122] F. Bresme and M. Oettel, "Nanoparticles at fluid interfaces," *Journal of Physics: Condensed Matter*, vol. 19, no. 41, p. 413101, 2007.

[123] D. L. Cheung, "Molecular dynamics study of nanoparticle stability at liquid interfaces: effect of nanoparticle-solvent interaction and capillary waves," *The Journal of Chemical Physics*, vol. 135, no. 5, p. 054704, 2011.

[124] I. Langmuir, "The mechanism of the surface phenomena of flotation," *Transactions of the Faraday Society*, vol. 15, no. June, pp. 62–74, 1920.

[125] K. B. Blodgett, "Monomolecular films of fatty acids on glass," *Journal of the American Chemical Society*, vol. 56, no. 2, pp. 495–495, 1934.

[126] K. B. Blodgett, "Films built by depositing successive monomolecular layers on a solid surface," *Journal of the American Chemical Society*, vol. 57, no. 6, pp. 1007–1022, 1935.

[127] C. Collier, R. Saykally, J. Shiang, S. Henrichs, and J. Heath, "Reversible tuning of silver quantum dot monolayers through the metal-insulator transition," *Science*, vol. 277, no. 5334, pp. 1978–1981, 1997.

[128] S. Huang, G. Tsutsui, H. Sakaue, S. Shingubara, and T. Takahagi, "Formation of a large-scale langmuir–blodgett monolayer of alkanethiol-encapsulated gold particles," *Journal of Vacuum Science & Technology B*, vol. 19, no. 1, pp. 115–120, 2001.

[129] V. Sashuk, K. Winkler, A. Zywocinski, T. Wojciechowski, E. Gorecka, and M. Fiałkowski, "Nanoparticles in a capillary trap: dynamic self-assembly at fluid interfaces," *ACS Nano*, vol. 7, no. 10, pp. 8833–8839, 2013.

[130] P. Pieranski, "Two-dimensional interfacial colloidal crystals," *Physical Review Letters*, vol. 45, no. 7, p. 569, 1980.

[131] N. Denkov, O. Velev, P. Kralchevski, I. Ivanov, H. Yoshimura, and K. Nagayama, "Mechanism of formation of two-dimensional crystals from latex particles on substrates," *Langmuir*, vol. 8, no. 12, pp. 3183–3190, 1992.

[132] M.-H. Wang, J.-W. Hu, Y.-J. Li, and E. S. Yeung, "Au nanoparticle monolayers: preparation, structural conversion and their surface-enhanced Raman scattering effects," *Nanotechnology*, vol. 21, no. 14, p. 145608, 2010.

[133] V. Santhanam, J. Liu, R. Agarwal, and R. P. Andres, "Self-assembly of uniform monolayer arrays of nanoparticles," *Langmuir*, vol. 19, no. 19, pp. 7881–7887, 2003.

[134] M. Maillard, L. Motte, A. Ngo, and M. Pileni, "Rings and hexagons made of nanocrystals: a marangoni effect," *The Journal of Physical Chemistry B*, vol. 104, no. 50, pp. 11871–11877, 2000.

[135] T. Ming, X. Kou, H. Chen, T. Wang, H.-L. Tam, K.-W. Cheah, J.-Y. Chen, and J. Wang, "Ordered gold nanostructure assemblies formed by droplet evaporation," *Angewandte Chemie*, vol. 120, no. 50, pp. 9831–9836, 2008.

[136] A. Crivoi and F. Duan, "Fingering structures inside the coffee-ring pattern," *Colloids and Surfaces A: Physicochemical and Engineering Aspects*, vol. 432, pp. 119–126, 2013.

[137] S. Jeong, L. Hu, H. R. Lee, E. Garnett, J. W. Choi, and Y. Cui, "Fast and scalable printing of large area monolayer nanoparticles for nanotexturing applications," *Nano Letters*, vol. 10, no. 8, pp. 2989–2994, 2010.

[138] L. Motte, F. Billoudet, E. Lacaze, J. Douin, and M. Pileni, "Self-organization into 2D and 3D superlattices of nanosized particles differing by their size," *The Journal of Physical Chemistry B*, vol. 101, no. 2, pp. 138–144, 1997.

[139] J. A. Fan, C. Wu, K. Bao, J. Bao, R. Bardhan, N. J. Halas, V. N. Manoharan, P. Nordlander, G. Shvets, and F. Capasso, "Self-assembled plasmonic nanoparticle clusters," *Science*, vol. 328, no. 5982, pp. 1135–1138, 2010.

[140] K. J. Stebe, E. Lewandowski, and M. Ghosh, "Oriented assembly of metamaterials," *Science*, vol. 325, no. 5937, pp. 159–160, 2009.

[141] V. Liberman, C. Yilmaz, T. Bloomstein, S. Somu, Y. Echegoyen, A. Busnaina, S. Cann, K. Krohn, M. Marchant, and M. Rothschild, "A nanoparticle convective directed assembly process for the fabrication of periodic surface enhanced Raman spectroscopy substrates," *Advanced Materials*, vol. 22, no. 38, pp. 4298–4302, 2010.

[142] M.-H. Lin, H.-Y. Chen, and S. Gwo, "Layer-by-layer assembly of three-dimensional colloidal supercrystals with tunable plasmonic properties," *Journal of the American Chemical Society*, vol. 132, no. 32, pp. 11259–11263, 2010.

[143] S. Y. Heriot, H.-L. Zhang, S. D. Evans, and T. H. Richardson, "Multilayers of 4-methylbenzenethiol functionalized gold nanoparticles fabricated by langmuir–blodgett and langmuir–schaefer deposition," *Colloids and Surfaces A: Physicochemical and Engineering Aspects*, vol. 278, no. 1, pp. 98–105, 2006.

[144] M. K. Hossain, G. R. Willmott, P. G. Etchegoin, R. J. Blaikie, and J. L. Tallon, "Tunable SERS using gold nanoaggregates on an elastomeric substrate," *Nanoscale*, vol. 5, no. 19, pp. 8945–8950, 2013.

[145] G. Willmott, R. Chaturvedi, S. Cummins, and L. Groenewegen, "Actuation of tunable elastomeric pores: Resistance measurements and finite element modelling," *Experimental Mechanics*, vol. 54, no. 2, pp. 153–163, 2014.

[146] G. Kamita, M. Kolle, F. Huang, J. J. Baumberg, and U. Steiner, "Multilayer mirrored bubbles with spatially-chirped and elastically-tuneable optical bandgaps," *Optics Express*, vol. 20, no. 6, pp. 6421–6428, 2012.

[147] J. Turkevich, P. C. Stevenson, and J. Hillier, "A study of the nucleation and growth processes in the synthesis of colloidal gold," *Discussions of the Faraday Society*, vol. 11, pp. 55–75, 1951.

[148] J. Baumberg, F. Huang, and M. Millyard, "Optical device," May 16 2012. US Patent App. 14/117,876.

[149] L. Xu, G. Han, J. Hu, Y. He, J. Pan, Y. Li, and J. Xiang, "Hydrophobic coating-and surface active solvent-mediated self-assembly of charged gold and silver nanoparticles at water–air and water–oil interfaces," *Physical Chemistry Chemical Physics*, vol. 11, no. 30, pp. 6490–6497, 2009.

[150] S. Huang, G. Tsutsui, H. Sakaue, S. Shingubara, and T. Takahagi, "Experimental conditions for a highly ordered monolayer of gold nanoparticles fabricated by the langmuir–blodgett method," *Journal of Vacuum Science & Technology B: Microelectronics and Nanometer Structures Processing, Measurement, and Phenomena*, vol. 19, no. 6, pp. 2045–2049, 2001.

[151] A. M. Boies, P. Lei, S. Calder, W. G. Shin, and S. L. Girshick, "Hot-wire synthesis of gold nanoparticles," *Aerosol Science and Technology*, vol. 45, no. 5, pp. 654–663, 2011.

[152] V. A. Turek, M. P. Cecchini, J. Paget, A. R. Kucernak, A. A. Kornyshev, and J. B. Edel, "Plasmonic ruler at the liquid–liquid interface," *ACS Nano*, vol. 6, no. 9, pp. 7789–7799, 2012.

[153] T. Li, Z. Huang, Z. Suo, S. P. Lacour, and S. Wagner, "Stretchability of thin metal films on elastomer substrates," *Applied physics letters*, vol. 85, no. 16, pp. 3435–3437, 2004.

[154] M. Manzoor, P. Lemoine, D. Dixon, J. Hamilton, and P. Maguire, "Stretchable conducting gold films prepared with composite MWNT/PDMS substrates," *AIP Advances*, vol. 5, no. 10, p. 107237, 2015.

[155] S. P. Lacour, S. Wagner, Z. Huang, and Z. Suo, "Stretchable gold conductors on elastomeric substrates," *Applied Physics Letters*, vol. 82, no. 15, pp. 2404–2406, 2003.

[156] G. Lévêque and O. J. Martin, "Optical interactions in a plasmonic particle coupled to a metallic film," *Optics express*, vol. 14, no. 21, pp. 9971–9981, 2006.

[157] F. M. Huang, D. Wilding, J. D. Speed, A. E. Russell, P. N. Bartlett, and J. J. Baumberg, "Dressing plasmons in particle-in-cavity architectures," *Nano Letters*, vol. 11, no. 3, pp. 1221–1226, 2011.

[158] M. N. Mendis, H. S. Mandal, and D. H. Waldeck, "Enhanced sensitivity of delocalized plasmonic nanostructures," *The Journal of Physical Chemistry C*, vol. 117, no. 48, pp. 25693–25703, 2013.

[159] W. Park and J.-B. Lee, "Mechanically tunable photonic crystal structure," *Applied Physics Letters*, vol. 85, no. 21, pp. 4845–4847, 2004.

[160] Y.-K. Park, S.-H. Yoo, and S. Park, "Assembly of highly ordered nanoparticle monolayers at a water/hexane interface," *Langmuir*, vol. 23, no. 21, pp. 10505–10510, 2007.

[161] R. T. Hill, J. J. Mock, A. Hucknall, S. D. Wolter, N. M. Jokerst, D. R. Smith, and A. Chilkoti, "Plasmon ruler with angstrom length resolution," *ACS nano*, vol. 6, no. 10, pp. 9237–9246, 2012.

[162] C.-N. Lok, C.-M. Ho, R. Chen, Q.-Y. He, W.-Y. Yu, H. Sun, P. K.-H. Tam, J.-F. Chiu, and C.-M. Che, "Silver nanoparticles: partial oxidation and antibacterial activities," *JBIC Journal of Biological Inorganic Chemistry*, vol. 12, no. 4, pp. 527–534, 2007.

[163] Y. Han, R. Lupitskyy, T.-M. Chou, C. M. Stafford, H. Du, and S. Sukhishvili, "Effect of oxidation on surface-enhanced Raman scattering activity of silver nanoparticles: a quantitative correlation," *Analytical Chemistry*, vol. 83, no. 15, pp. 5873–5880, 2011.

[164] K. Awazu, M. Fujimaki, C. Rockstuhl, J. Tominaga, H. Murakami, Y. Ohki, N. Yoshida, and T. Watanabe, "A plasmonic photocatalyst consisting of silver nanoparticles embedded in titanium dioxide," *Journal of the American Chemical Society*, vol. 130, no. 5, pp. 1676–1680, 2008.

[165] Y. Luo, R. Zhao, and J. B. Pendry, "van der Waals interactions at the nanoscale: The effects of nonlocality," *Proceedings of the National Academy of Sciences*, vol. 111, no. 52, pp. 18422–18427, 2014.

[166] K. Isozaki, T. Ochiai, T. Taguchi, K.-i. Nittoh, and K. Miki, "Chemical coating of large-area Au nanoparticle two-dimensional arrays as plasmon-resonant optics," *Applied Physics Letters*, vol. 97, no. 22, p. 221101, 2010.

[167] M. P. Cecchini, V. A. Turek, J. Paget, A. A. Kornyshev, and J. B. Edel, "Self-assembled nanoparticle arrays for multiphase trace analyte detection," *Nature Materials*, vol. 12, no. 2, p. 165, 2013.

[168] K. J. Savage, M. M. Hawkeye, R. Esteban, A. G. Borisov, J. Aizpurua, and J. J. Baumberg, "Revealing the quantum regime in tunnelling plasmonics," *Nature*, vol. 491, no. 7425, p. 574, 2012.

[169] M. Hentschel, M. Saliba, R. Vogelgesang, H. Giessen, A. P. Alivisatos, and N. Liu, "Transition from isolated to collective modes in plasmonic oligomers," *Nano Letters*, vol. 10, no. 7, pp. 2721–2726, 2010.

[170] B. Luk'yanchuk, N. I. Zheludev, S. A. Maier, N. J. Halas, P. Nordlander, H. Giessen, and C. T. Chong, "The fano resonance in plasmonic nanostructures and metamaterials," *Nature Materials*, vol. 9, no. 9, p. 707, 2010.

[171] L. Zhao, K. L. Kelly, and G. C. Schatz, "The extinction spectra of silver nanoparticle arrays: influence of array structure on plasmon resonance wavelength and width," *The Journal of Physical Chemistry B*, vol. 107, no. 30, pp. 7343–7350, 2003.

[172] A. Kontogeorgos, D. R. Snoswell, C. E. Finlayson, J. J. Baumberg, P. Spahn, and G. Hellmann, "Inducing symmetry breaking in nanostructures: anisotropic stretch-tuning photonic crystals," *Physical Review Letters*, vol. 105, no. 23, p. 233909, 2010.

[173] M. G. Millyard, F. Min Huang, R. White, E. Spigone, J. Kivioja, and J. J. Baumberg, "Stretch-induced plasmonic anisotropy of self-assembled gold nanoparticle mats," *Applied Physics Letters*, vol. 100, no. 7, p. 073101, 2012.

[174] G. A. Rance, D. H. Marsh, S. J. Bourne, T. J. Reade, and A. N. Khlobystov, "Van der Waals interactions between nanotubes and nanoparticles for controlled assembly of composite nanostructures," *ACS Nano*, vol. 4, no. 8, pp. 4920–4928, 2010.

[175] S. Yamamoto and H. Watarai, "Surface-enhanced Raman spectroscopy of dodecanethiol-bound silver nanoparticles at the liquid/liquid interface," *Langmuir*, vol. 22, no. 15, pp. 6562–6569, 2006.

[176] C. L. Leverette and R. A. Dluhy, "Vibrational characterization of a planar-supported model bilayer system utilizing surface-enhanced Raman scattering (SERS) and infrared reflection–absorption spectroscopy (IRRAS)," *Colloids and Surfaces A: Physicochemical and Engineering Aspects*, vol. 243, no. 1, pp. 157–167, 2004.

[177] S. N. Singh, H. Bhatti, and R. Singh, "Vibrational spectra and assignments of 1-halonaphthalenes," *Spectrochimica Acta Part A: Molecular Spectroscopy*, vol. 34, no. 10, pp. 985–992, 1978.

[178] K. H. Michaelian, *Assignment of vibrational spectra of halogenated naphthalenes and n-heterocycles*. PhD thesis, 1970.

[179] C. G. Worley and R. W. Linton, "Removing sulfur from gold using ultraviolet/ozone cleaning," *Journal of Vacuum Science & Technology A: Vacuum, Surfaces, and Films*, vol. 13, no. 4, pp. 2281–2284, 1995.

[180] E. W. Elliott III, R. D. Glover, and J. E. Hutchison, "Removal of thiol ligands from surface-confined nanoparticles without particle growth or desorption," 2015.

[181] F. Benz, R. Chikkaraddy, A. Salmon, H. Ohadi, B. De Nijs, J. Mertens, C. Carnegie, R. W. Bowman, and J. J. Baumberg, "SERS of individual nanoparticles on a mirror: size does matter, but so does shape," *The journal of physical chemistry letters*, vol. 7, no. 12, pp. 2264–2269, 2016.

[182] Y.-K. Hong, H. Kim, G. Lee, W. Kim, J.-I. Park, J. Cheon, and J.-Y. Koo, "Controlled two-dimensional distribution of nanoparticles by spin-coating method," *Applied Physics Letters*, vol. 80, no. 5, pp. 844–846, 2002.

[183] K.-S. Chou, K.-C. Huang, and H.-H. Lee, "Fabrication and sintering effect on the morphologies and conductivity of nano-Ag particle films by the spin coating method," *Nanotechnology*, vol. 16, no. 6, p. 779, 2005.

[184] M. Retsch, Z. Zhou, S. Rivera, M. Kappl, X. S. Zhao, U. Jonas, and Q. Li, "Fabrication of large-area, transferable colloidal monolayers utilizing self-assembly at the air/water interface," *Macromolecular Chemistry and Physics*, vol. 210, no. 3-4, pp. 230–241, 2009.

[185] T. Ding, C. Rüttiger, X. Zheng, F. Benz, H. Ohadi, G. A. Vandenbosch, V. V. Moshchalkov, M. Gallei, and J. J. Baumberg, "Fast dynamic color switching in temperature-responsive plasmonic films," *Advanced Optical Materials*, vol. 4, no. 6, pp. 877–882, 2016.

[186] K. M. Mayer and J. H. Hafner, "Localized surface plasmon resonance sensors," *Chemical Reviews*, vol. 111, no. 6, pp. 3828–3857, 2011.

[187] S. Seo, M. R. Gartia, and G. L. Liu, "Vertically stacked plasmonic nanoparticles in a circular arrangement: a key to colorimetric refractive index sensing," *Nanoscale*, vol. 6, no. 20, pp. 11795–11802, 2014.

[188] L. Qin, S. Wu, J.-h. Deng, L. Li, and X. Li, "Tunable light absorbance by exciting the plasmonic gap mode for refractive index sensing," *Optics Letters*, vol. 43, no. 7, pp. 1427–1430, 2018.

[189] T. Endo, K. Kerman, N. Nagatani, H. M. Hiepa, D.-K. Kim, Y. Yonezawa, K. Nakano, and E. Tamiya, "Multiple label-free detection of antigen- antibody reaction using localized surface plasmon resonance-based core- shell structured nanoparticle layer nanochip," *Analytical Chemistry*, vol. 78, no. 18, pp. 6465–6475, 2006.

[190] W. Lewandowski, M. Fruhnert, J. Mieczkowski, C. Rockstuhl, and E. Górecka, "Dynamically self-assembled silver nanoparticles as a thermally tunable metamaterial," *Nature Communications*, vol. 6, p. 6590, 2015.

[191] D. Bloor, K. Donnelly, P. Hands, P. Laughlin, and D. Lussey, "A metal–polymer composite with unusual properties," *Journal of Physics D: Applied Physics*, vol. 38, no. 16, p. 2851, 2005.

[192] D. Bloor, A. Graham, E. Williams, P. Laughlin, and D. Lussey, "Metal–polymer composite with nanostructured filler particles and amplified physical properties," *Applied Physics Letters*, vol. 88, no. 10, p. 102103, 2006.

[193] Y. Kim, J. Zhu, B. Yeom, M. Di Prima, X. Su, J.-G. Kim, S. J. Yoo, C. Uher, and N. A. Kotov, "Stretchable nanoparticle conductors with self-organized conductive pathways," *Nature*, vol. 500, no. 7460, p. 59, 2013.

[194] M. Segev-Bar, A. Landman, M. Nir-Shapira, G. Shuster, and H. Haick, "Tunable touch sensor and combined sensing platform: Toward nanoparticle-based electronic skin," *ACS Applied Materials & Interfaces*, vol. 5, no. 12, pp. 5531–5541, 2013.

[195] M. P. Cecchini, V. A. Turek, A. Demetriadou, G. Britovsek, T. Welton, A. A. Kornyshev, J. D. Wilton-Ely, and J. B. Edel, "Heavy metal sensing using self-assembled nanoparticles at a liquid–liquid interface," *Advanced Optical Materials*, vol. 2, no. 10, pp. 966–977, 2014.

[196] S. Ayas, A. Cupallari, O. O. Ekiz, Y. Kaya, and A. Dana, "Counting molecules with a mobile phone camera using plasmonic enhancement," *ACS Photonics*, vol. 1, no. 1, pp. 17–26, 2013.